Some Aspects of Vibration Isolation and Feedback Control for Interferometric Gravitational Radiation Detectors

by

Caroline Agnes Cantley

Department of Physics and Astronomy
University of Glasgow.

ProQuest Number: 11008002

ProQuest 11008002

to my Family

Acknowledgements

Contents

3 Feedback Control and Damping of Double Pendulums

iv

Preface

Development of a prototype interferometric gravitational radiation detector of 10m arm length was initiated at Glasgow University in 1978. Development of this prototype still continues and over the past few years plans have been made to develop a long-baseline detector of 3km arm length (the GEO project). This project is proposed by a collaboration formed between various research groups including our own group at Glasgow University, a group at the University of Wales (College of Cardiff) and one at the Max-Planck Institute for Quantum Optics in Garching, Germany. This thesis is an account of the research carried out by the authoress between October 1987 and September 1990 as part of the development of the proposed detector, specifically in relation to certain aspects of vibration isolation and feedback control of the test masses in the detector.

Chapter 1 is a general introduction to the nature, sources and detection of gravitational radiation. The astrophysical sources which are most likely to be first detected and the two main types of Earth-based detectors currently under development are described (resonant bar detectors and laser interferometric detectors). The dominant sources of noise which limit the performance of laser interferometeric detectors are discussed. Most of this chapter is derived from the published literature.

Chapter 2 is an introduction to the vibration isolation methods commonly used in interferometric detectors. A brief introduction to the design and analysis of feedback control systems is also given in this chapter. Initial experimental investigations into the position control of a test mass suspended as a simple pendulum are then presented.

Chapter 3 presents some theoretical and experimental investigations carried out relating to the feedback position control and damping of a test mass suspended as a double pendulum.

Chapter 4 describes the analysis of, and experimental results from, a novel design of double pendulum suspension system incorporating frequency selective (split) feedback position control.

The work described in Chapters 2, 3 and 4 was carried out with the assistance of Dr. N.A. Robertson and Prof. J. Hough. The software package used for most of the feedback control loop analysis contained in this thesis was PC/MATLAB.

Chapter 5 presents the results obtained using the finite element method to predict the

level of vibration isolation obtainable in each dimension with the double pendulum system described in Chapter 4. The level of horizontal isolation of the system was measured experimentally to compare it with the theoretical prediction.

Chapter 6 describes a relatively detailed investigation into the limitations of the performance of vibration isolation stacks using finite element analysis. The finite element software used in Chapters 5 and 6 was MSC/NASTRAN.

The finite element analyses of Chapters 5 and 6 were carried out in collaboration with Mr. R.J.S. Greenhalgh (Rutherford Appleton Laboratory, Oxfordshire), and with the help of Prof. J.Hough and Dr. N.A. Robertson.

In Chapter 7 the conclusions are presented and the prospects for the future of gravitational radiation detection are discussed.

Appendix A is a simple calculation indicating the level of unwanted magnetic damping of a test mass suspended as a pendulum due to the feedback control transducers.

Appendix B is an example of an input data deck used for the finite element analysis of the vibration isolation stack model discussed in Chapter 6.

Appendix C contains some measurements of the spectrum of seismic ground tilt at two sites close to the prototype detector at Glasgow University. These data were obtained with the help of Prof. J. Hough.

Summary

Some Aspects of Vibration Isolation and Feedback Control for Interferometric Gravitational Radiation Detectors

Gravitational radiation, first predicted by Einstein in his General Theory of Relativity (1916), remains undetected despite considerable effort by researchers over the past few decades. Direct observation of gravitational radiation would not only provide a test of Einstein's theory, but would yield information on the astrophysical sources and processes involved in its production. Gravitational radiation is quadrupole in nature and it gives rise to a tidal strain in space. However its interaction with matter is very weak making it extremely difficult to detect. The prototype detector developed at Glasgow University is designed in such a way that it exploits the quadrupole nature of gravitational radiation by attempting to measure the differential change in length between two resonant cavities making up the orthogonal arms of an interferometer. Similar laser interferometric detectors are currently under development at various sites worldwide. Development of the 10m prototype detector at Glasgow was initiated about 13 years ago and plans are now well under way for the development of a more sensitive detector of 3km arm length (the GEO project) in collaboration with various other research groups including a group at the University of Wales (College of Cardiff) and one at the Max-Planck-Institute for Quantum Optics in Garching, Germany.

Chapter 1 is a general introduction to the nature of gravitational radiation and the astrophysical sources likely to produce detectable levels of this radiation at the Earth. The main features of the two most promising types of detector currently being developed - resonant bar detectors and laser interferometric detectors - are described. The ultimate sensitivity of any gravitational wave detector is limited by various sources of noise and the dominant noise sources which degrade the performance of interferometric detectors are discussed in some detail. It is shown here that the sensitivity of such detectors is likely to be severely limited by the effects of seismic noise at low frequencies (below

about 100Hz).

The test masses forming the arms of an interferometric gravitational wave detector must be isolated from all external influences, particularly the seismic background, and must be 'free' to move under the influence of a gravitational wave. Furthermore, in order to operate an interferometric detector efficiently the position and orientation of the test masses must be controlled to a very high degree of accuracy.

In Chapter 2 the level of seismic noise expected at a typical detector site is discussed. Some of the methods commonly used to seismically isolate the test masses in interferometric detectors are then described. A brief introduction to the concept of feedback control and the methods of analysis available for designing feedback systems is then presented. Finally, preliminary experimental investigations into the position control of a test mass suspended as a simple pendulum are described.

In order to achieve the required level of seismic isolation of the test masses in the planned 3km detector (GEO) (an isolation factor of $\sim10^{10}$ at ~100Hz) it is proposed to use double pendulum suspensions in conjunction with five-layer vibration isolation stacks and air mounts. Chapter 3 gives an account of various theoretical investigations carried out into feedback control and damping of a test mass suspended as a double pendulum. Experimental investigations into feedback control and damping of various double pendulum systems were also conducted and the results from these are presented.

On applying feedback control and damping signals to an isolated test mass it is important to avoid re-introducing displacement noise. Chapter 4 describes a novel design of double pendulum suspension system with frequency selective (split) feedback control. This system was designed specifically to attempt to reduce the level of displacement noise occurring at the test mass due to the application of the feedback signals. Two different split feedback control systems were designed and their perfomance was tested experimentally.

A finite element model was generated to predict the levels of isolation in the horizontal and vertical directions achievable with the double pendulum system described in Chapter 4. The horizontal isolation was measured experimentally to compare it with the theoretically predicted isolation. The theoretical and experimental results are presented in Chapter 5.

As mentioned already, vibration isolation stacks are commonly used in conjunction with pendulum suspensions to obtain the desired level of isolation for the test masses.

These multi-layer stacks consist of alternating layers of rubber and heavy material. Chapter 6 describes theoretical investigations into the limitations to the performance of such multi-layer stack systems using a finite element model. The results obtained illustrate clearly that cross-coupling effects which could degrade the predicted isolation performance can possibly take place in such multi-layer stacks. The results obtained from these analyses were used to establish various design criteria for the stack systems of the proposed 3km detector (GEO). These criteria attempt to ensure that the resulting motion of a test mass suspended from the top of such a stack system is reduced to a satisfactory level.

In Chapter 7 the conclusions are presented and the prospects for the future of gravitational radiation detection are discussed.

Appendix A contains a simple calculation which shows that unwanted magnetic damping of a test mass suspended as a pendulum might take place due to electromagnetic induction in the coil/magnet transducers which are commonly used to control the position and orientation of the test masses in interferometric detectors.

Appendix B contains an example of an MSC/NASTRAN data deck used for the frequency response analysis of the vibration isolation stack model discussed in Chapter 6.

It was shown in Chapter 6 that ground tilting motions might couple strongly to horizontal motion at the top of the vibration isolation stacks used in gravitational radiation detectors. Since relatively little information is available on the magnitude of ground tilt at the Earth's surface it seemed important to make a measurement of the ground tilt spectrum at a typical detector site. Appendix C presents some measurements of the spectrum of seismic ground tilt at two sites close to the 10m prototype detector.

Chapter 1

The Nature, Sources and Detection of Gravitational Radiation

1.1 Introduction

Gravitational waves were first predicted to exist by Einstein in his General Theory of Relativity (1916). Direct observation of gravitational waves remains one of the most challenging problems in 20th Century experimental physics. Over the past few decades much progress has been made in research towards their detection. Success in this field will be of considerable importance both in astronomy, where unique information about violent interactions in the Universe may be obtained, and in physics where fundamental aspects of relativistic theories may be checked.

Evidence for the existence of gravitational radiation has come from observation of the rate of orbital decay of the binary pulsar PSR1913+16 due to gravitational radiation reaction [Taylor *et. al.* 1979]. However as yet there has been no convincing direct observation of gravitational radiation. Experimental development has now advanced to the stage where the experts involved are confident that instruments can be constructed which are capable of detecting the levels of gravitational radiation predicted to be generated by astrophysical sources.

This chapter gives a brief introduction to the nature, sources and detection of gravitational radiation. More comprehensive reviews of these topics are given by Thorne [Thorne 1987] and Blair [Blair 1991].

1.2 The Nature of Gravitational Radiation

Gravitational waves are propagating ripples in the curvature of spacetime. They are produced by the acceleration of mass just as electromagnetic waves are produced by the acceleration of electric charge. Certain other features are common to both types of

1

radiation. Both are transverse, propagate at the speed of light and have a zero rest mass particle associated with them (the graviton and the photon). However significant differences exist. Mass, unlike charge, has only one sign and a change in the quadrupole moment of a system of particles is necessary for the generation of gravitational waves. The gravitational interaction is much weaker than the electromagnetic interaction (*e.g.* the gravitational force between two stationary protons is about 10^{36} times weaker than the electrostatic force). For these reasons, the most promising sources for producing detectable levels of gravitational radiation are astrophysical in nature (involving large masses moving with high accelerations).

Gravitational waves give rise to tidal forces, the dimensionless amplitude h of a wave being characterised in terms of the strain it induces in space. For example, a gravitational wave of wavelength λ_{gw} passing through a ring of test particles will cause the ring to oscillate as shown in Figure 1.1. The amplitude of the gravitational wave is defined as $h = \frac{2\Delta L}{L}$ where $L \ll \lambda_{gw}$. The amplitude falls off inversely with distance as the wave expands away from its source.

$$\vdash\!\!-\!\!L\!-\!\!\dashv \qquad \vdash\!L-\Delta L\dashv \qquad \vdash\!\!-\!\!L+\Delta L\!-\!\!\dashv$$
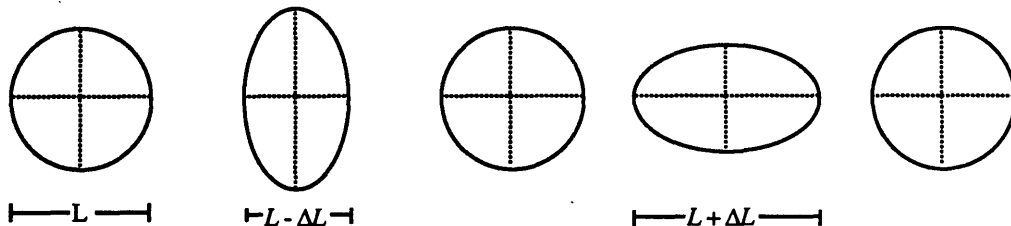
Figure 1.1   Effect of a gravitational wave on a ring of test particles. The wave is propagating perpendicular to the page and has "+" polarisation. The "×" polarisation produces the same effect but rotated 45^0 about the propagation axis.

Any gravitational wave can be described in terms of components of the two independent polarisation states ("+" (plus) and "×" (cross)) and gravitational waves detected at the Earth can be fully characterised by the time evolution of their two waveforms h_+ and $h_\times$ and by the direction (θ, ϕ) to their source.

Information on the amplitude, polarisation and velocity of these waves will provide

important tests of general relativity or other relativistic theories of gravity.

Since the predicted sources of gravitational waves involve compact concentrations of mass they may be shrouded by surrounding matter. Electromagnetic radiation is unable to escape from these high gravity regions without interacting strongly with this matter. However gravitational waves are highly penetrating. They should be virtually unaffected by the surrounding matter and should give unique information about the astrophysical sources and processes involved in their production. However the highly penetrative nature of gravitational radiation means that its interaction with any detector will be weak. The currently proposed detectors aim to be capable of measuring extremely small changes in strain: h of the order of 10^{-22} over millisecond time-scales.

Despite the fact that their interaction with matter is weak, gravitational waves carry very large energy fluxes. For a typical wave of frequency f at the sensitivity goal of currently proposed detectors the flux at the Earth is given by equation (1.1) [Schutz 1989]

$$\mathcal{F}_{gw} = 3.2 \times 10^{-3} \left[\frac{f}{1\text{kHz}}\right]^2 \left[\frac{h}{10^{-22}}\right]^2 \text{W m}^{-2} . \qquad (1.1)$$

This huge energy flux suggests that detectable gravitational wave events will be fairly infrequent.

The astrophysical sources of gravitational radiation which are most likely to produce gravitational waves within the frequency range of terrestrial detectors (from a few tens of hertz to a few kilohertz) are described in the next section.

1.3   Predicted Sources of Gravitational Radiation

It is useful to divide gravitational wave sources into two main categories according to the temporal behaviour of the waves they produce; those sources which produce bursts of gravitational waves and those sources which produce continuous gravitational waves. In addition to these two types of source it is believed that there is a stochastic background of gravitational radiation.

1.3.1   Burst Sources

Supernovae

The earliest designed gravitational wave detectors were optimised to look for signals from

stars collapsing as in supernovae. Supernovae can be divided into two categories depending on the composition of the original star. Type I supernovae are thought to occur when a white dwarf accretes matter from a companion star and undergoes nuclear explosion. The stellar core in this case may or may not collapse to form a neutron star. Type II supernovae occur when the radiation pressure from the nuclear reactions in the core of a highly evolved massive star is no longer sufficient to prevent rapid gravitational collapse. A neutron star or a black hole may be produced. If the collapse is non-symmetrical there will be a short burst of gravitational waves followed by a 'ringing' as the core recovers from the sudden collapse. Furthermore, if the initial angular momentum of the collapsing star is sufficiently high the collapsed core may become unstable, perhaps even bifurcating to produce two components. In this situation even greater levels of gravitational radiation can be emitted.   (in the form of gravitational waves)

The amplitude h produced by a burst source that emits an energy E in a time τ at a distance r and frequency f is given approximately by:

$$h \sim 5 \times 10^{-22} \left[\frac{E}{10^{-3} M_\odot c^2}\right]^{1/2} \left[\frac{1\mathrm{kHz}}{f}\right] \left[\frac{\tau}{1\mathrm{ms}}\right]^{-1/2} \left[\frac{15\mathrm{Mpc}}{r}\right] \tag{1.2}$$

where $M_\odot$ is the mass of the sun and 15Mpc is approximately the distance to the Virgo cluster [Hough et. al. 1987].

The exact level of gravitational radiation emitted by a supernova event depends on the asymmetry and rate of the collapse and therefore is not easy to predict. Numerical simulations to predict the shapes and amplitudes of the waveforms produced in supernovae events have been carried out by various people e.g. [Saenz and Shapiro 1981]. These simulations will be useful in aiding the interpretation of future observations.

Coalescing Compact Binaries

This type of source is currently believed to be the most promising for detection. Binaries are systems involving two objects orbiting each other under their mutual gravitational attraction. Such systems will emit continuous gravitational radiation at a frequency equal to twice their orbital frequency for the majority of their lifetime. Furthermore, binary systems made of compact objects such as neutron stars and/or black holes should eventually spiral together as a result of losing energy in the form of gravitational

radiation, until the stars or holes coalesce. In the last few seconds prior to the collision, a characteristic 'chirp' of gravitational waves will be produced where both the frequency and amplitude of the waveform sweep upwards towards a maximum.

The characteristics of the signal depend on only a few parameters. Consider a binary system with total mass m_T $M_\odot$ and reduced mass μ $M_\odot$, at a distance r_{100} from the Earth (measured in hundreds of Mpc) emitting waves at a frequency f_{100} (measured in hundreds of hertz). The amplitude $<h>$ of the signal (which is averaged over the source and detector orientations) produced by such a system of coalescing objects is given by equation (1.3) [Schutz 1986]:

$$<h> = 10^{-23} \ m_T{}^{2/3} \ \mu \ f_{100}{}^{2/3} \ r_{100}{}^{-1}. \tag{1.3}$$

Furthermore the frequency of the signal changes on the time scale [Schutz 1986]

$$\tau = \frac{f}{\dot{f}} = 7.8 \ m_T{}^{-2/3} \ \mu^{-1} \ f_{100}{}^{-8/3} \ \text{sec} \ . \tag{1.4}$$

It is very significant that the masses m_T and μ appear in both equations in such a way that they can be eliminated. The rate of change of frequency of the waveform can be measured as can the amplitude $<h>$ (using a network of three detectors). This gives a way of determining the distance to the binary coalescence event independent of any assumptions about the masses of the stars involved. If the coalescing binary system can also be detected optically this would provide a means of measuring the Hubble constant to a higher degree of accuracy than ever before [Schutz 1986].

1.3.2 Continuous Sources

Rotating Neutron Stars

Rotating neutron stars can emit gravitational waves at twice their frequency of rotation if they deviate from axisymmetry. The greater the deviation and the higher the rotation rate, the stronger the emission. The deviations from axisymmetry can be caused by various effects. For example, if the neutron star is a pulsar the crust may be deformed by the presence of a magnetic field which is misaligned with the rotation axis [Zimmerman 1978]. The crust or core of the neutron star could have lumps in it due to the occurrence of starquakes. If the neutron star is accreting matter from a companion star

5

and is rotating rapidly enough an instability can occur creating hydrodynamic waves in the mantle and crust travelling in the opposite direction to the star's rotation. Gravitational waves can be emitted strongly from such a star [Wagoner 1984].

1.3.3 The Stochastic Background

A random background of gravitational waves may exist due to the superposition of the emissions from many sources randomly distributed in time and space. Several possible sources of this gravitational wave background have been suggested. For instance, cosmic strings forming closed loops can oscillate producing gravitational waves over a wide range of frequencies as the loop size changes with time [Vachaspati and Vilenkin 1985]. These closed loops are predicted to seed the formation of galaxies and clusters. Observation of the background radiation might yield information on the process of galaxy formation.

It is also believed that the combined emission of all the existing binary stars should superpose to give rise to a stochastic background of radiation. However the peak amplitude of such radiation would lie at a frequency below about 10^{-2}Hz.

There may also be remnant radiation from the big-bang (primordial radiation) which originated at a very early stage in the history of the Universe. The peak amplitude of such radiation probably lies outwith the frequency range of terrestrial detectors.

Binary coalescence and black hole formation in a population of large pregalactic stars (known as population III stars) which evolved very rapidly would also contribute to the stochastic background of gravitational radiation. This class of source is controversial.

1.4 The Detection of Gravitational Radiation

Any method for directly detecting gravitational radiation will require making a measurement of the induced strain in space. Several research groups around the world are currently involved in the development of two distinct types of laboratory based instruments designed to be capable of measuring these minute strains; resonant bar detectors and laser interferometric detectors.

1.4.1 Resonant Bar Detectors

The resonant bar detector was first proposed and developed by Joseph Weber of the University of Maryland in the 1960's. Currently there are many research groups in the U.S.A., Europe and the Far East ∧(including Australia) developing resonant bar detectors.

The resonant bar detector essentially consists of a single bar (mass of a few tonnes) of low intrinsic loss metal (high quality factor Q) whose fundamental longitudinal frequency is at about a kilohertz and which may be cooled to a temperature of a few kelvin. A gravitational wave of suitable frequency, orientation and polarisation passing through such a detector will produce a strain which will give rise to potentially detectable movements of the ends of the bar at its fundamental modal frequency. The induced motions can be measured using some sort of transducer (*e.g.* a parametric transducer or a resonant transducer) whose signals are amplified and monitored. To reduce the damping of the internal quality factor (Q) of the bar it is suspended inside a vacuum chamber. Further isolation from external vibrations is provided using a series of mechanical filters to connect the suspension point to the ground.

The sensitivity of resonant bar detectors is limited by noise in the sensors (transducers and amplifiers) and also by thermal noise in the bar itself. The effects of thermal noise can be reduced by using large mass bars of high Q material cooled to very low temperatures. For example, the aluminium bar at Stanford University of mass 4800Kg has an internal Q of $\sim 5 \times 10^6$ and is cooled to liquid helium temperature (4.2K).

However there is a more fundamental limitation to the performance of bar detectors in the form of the Heisenberg Uncertainty Principle. This places a limit on the strain sensitivity of a typical bar of the order of 10^{-20} [Thorne *et. al.* 1979]. Techniques have been proposed for reducing this limit where the oscillating system is monitored without perturbing its quantum mechanical state ('quantum non-demolition' techniques). However considerable experimental development is needed before such techniques can be implemented.

The most sensitive bar detectors (*i.e.* those at Stanford University and CERN (University of Rome)) have achieved strain sensitivities of $\sim 10^{-18}$ for millisecond pulses. However it seems unlikely that the sensitivity of bar detectors could be improved to the level where gravitational radiation will be likely to be detected. Also bar detectors are restricted in their bandwidth of operation since they are only sensitive to gravitational

waves within a few tens of hertz of the frequency of the fundamental mode. However an array of bar detectors of different sizes could be used to achieve a broader bandwidth of operation.

1.4.2 Laser Interferometric Detectors

The interferometric method for detecting gravitational radiation was pioneered by Forward [Forward 1978] and Weiss [Weiss 1972]. The Michelson interferometer forms the basis for the two types of interferometric detectors currently being developed.

A simple Michelson interferometer is illustrated in Figure 1.2. A beamsplitter and two end mirrors form the arms of the interferometer. Laser light incident on the beamsplitter is split equally between the two arms. The light traversing each arm is returned by the end mirror (test mass) to be recombined at the beamsplitter. Any differential length change of the two arms will give rise to a change in the relative phase of the interfering beams. This produces a change in the intensity of the light detected by the photodiode at the output port.
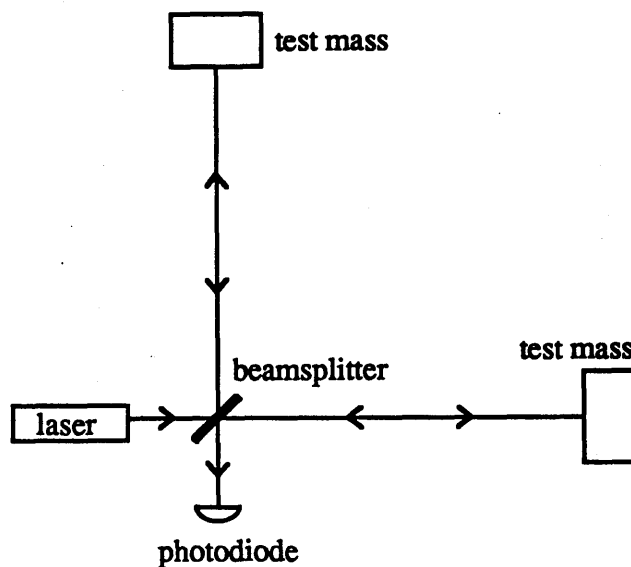
Figure 1.2 Schematic diagram of a Michelson Interferometer.

The test masses must be free to move under the influence of a gravitational wave without being disturbed by external influences such as ground vibrations and air pressure fluctuations. Interferometric detectors are operated under high vacuum (*e.g.* ~10^{-4} mbar) with the test masses and other optical components 'freely' suspended as pendulums to reduce such effects.

Interferometric detectors are well suited to the quadrupole nature of gravitational radiation since the strain in space introduced by a gravitational wave has opposite signs in two directions perpendicular to each other. An obvious advantage these separated mass detectors have over resonant bar detectors is that they can be used to detect signals over a wide frequency range. Furthermore since gravitational radiation gives rise to strains in space, the sensitivity of any detector can be increased by increasing its physical size, and interferometric detectors can be made physically very large compared to bar detectors. In fact, to obtain the maximum signal response from a detector, the length of each arm should be equal to one quarter of the wavelength of the gravitational wave being searched for. This means that for signals of about a kilohertz the optimum arm length would be close to 100km. An arm length of this order can effectively be obtained by folding the optical paths in each arm using either optical delay lines or resonant cavities.

Delay-Line Detectors

This type of detector was first proposed by Weiss [Weiss 1972]. There are a number of groups at present developing delay-line detectors including the group at the Max Planck Institute for Quantum Optics (MPQ) in Garching who have a prototype detector of 30m arm length [Winkler 1991]. Figure 1.3 is a schematic diagram of a delay-line interferometer. The geometries of the mirrors are designed so that the beams of light within each arm are spatially separated.

In the Garching prototype an argon laser is used as the light source. The phase difference between the returning beams at the output is maintained on a null by adjusting the phase of the light within each of the arms using electro-optic modulators (Pockels cells) placed between the beamsplitter and entrance mirrors in each arm. At the lower frequencies (<~30Hz) the coarse optical path length adjustment is achieved by controlling the positions of the two outboard mirrors using coil/magnet feedback transducers.

In principle, an interferometer can be made insensitive to laser frequency fluctuations if the arm lengths are identical. However light scattered within the arms (which might have a much longer optical path length than the main beam) can leak back
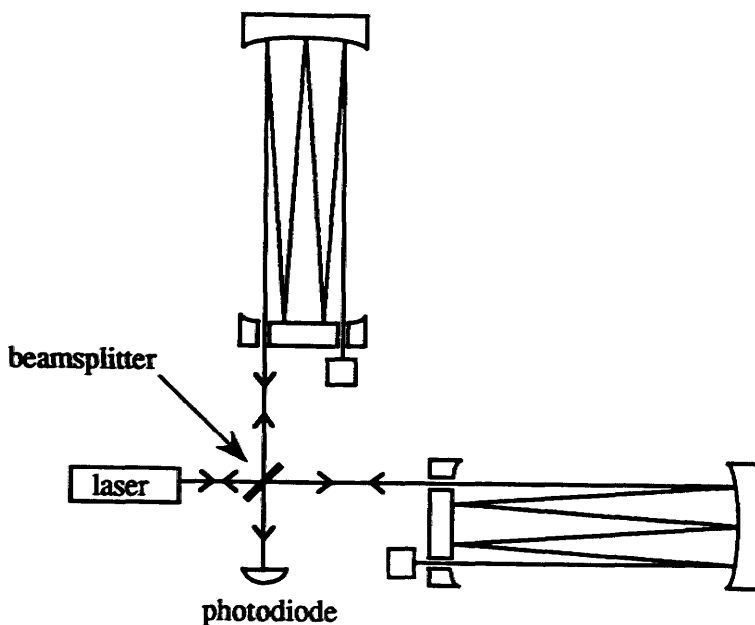
Figure 1.3   Schematic diagram of a delay-line interferometer.

towards the beamsplitter making the delay-line detector more sensitive to these laser frequency fluctuations. To reduce this effect the laser frequency is stabilised with respect to a reference cavity at low frequencies and with respect to the path length inside the interferometer at frequencies above about 10Hz.

The best *amplitude* sensitivity demonstrated so far on the Garching prototype is $1.1 \times 10^{-19}/\sqrt{Hz}$ (above 2kHz) [Shoemaker *et. al.* 1988]. (This is equivalent to a displacement sensitivity of ~3.3 × 10^{-18} $^m/\sqrt{Hz}$). This performance level is impressively close to the fundamental limit set by the uncertainty associated with counting the photons on the output of the interferometer (for the illuminating light power used). This sensitivity limit (photon shot noise) will be discussed in more detail in Section 1.5.2.

Resonant Cavity Detectors

The technique of using resonant cavities (Fabry-Perot cavities) to increase the effective arm length of an interferometric detector was first developed at Glasgow University and there are now a number of other research groups who have adopted the resonant cavity configuration. Figure 1.4 is a schematic diagram of a resonant cavity interferometer.

10
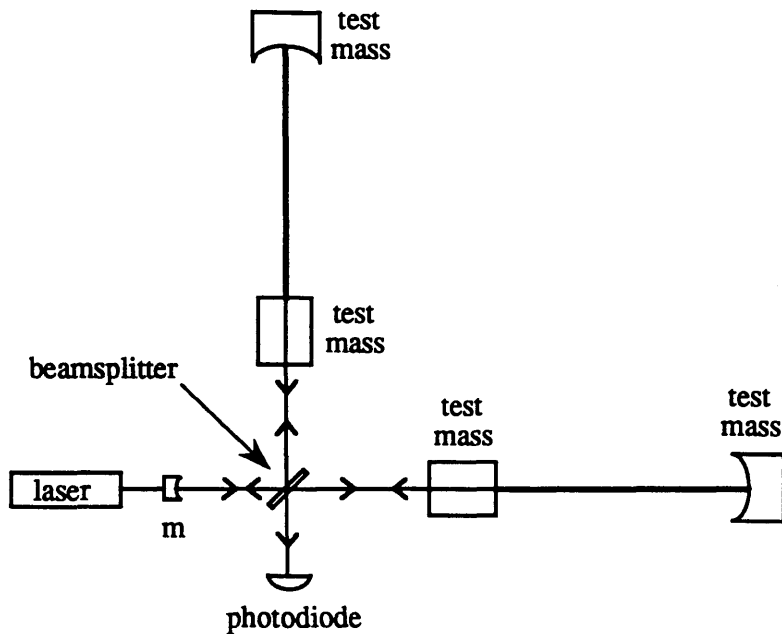
Figure 1.4   Schematic diagram of a resonant cavity interferometer.

The prototype detector at Glasgow has arms each of length 10m. Basically one of the cavities - the primary cavity - is held on resonance by locking the frequency of the laser light to the cavity at frequencies above a few hertz. At the lower frequencies the distance between the masses in the primary cavity is controlled with respect to the frequency of the laser. The length of the secondary cavity is then controlled to hold it on resonance with the highly stabilised light. A gravitational wave of suitable polarisation passing through the detector will induce a relative change of length in the two arms, or rather, will move the secondary cavity off resonance with the laser light. However this change is compensated for by the feedback loop holding the secondary cavity on resonance. The feedback signal for this cavity provides the signal for searching for gravitational waves.

The resonant cavity interferometer requires more sophisticated control systems than its delay-line counterpart since the two cavities must be held on resonance with the laser light. This requires precision control of the test masses forming the cavities.

The resonant cavity detector has the advantage that smaller mirrors can be used than in a delay-line detector. Furthermore scattered light is less likely to be a problem since a very high degree of laser frequency stabilisation is necessary to keep the cavities tightly enough on resonance to achieve the required level of performance.

11

The best displacement sensitivity demonstrated so far on the Glasgow prototype is $\sim 1.7 \times 10^{-18}$ $^m/\sqrt{Hz}$ (over a range between 1.5kHz and 2.5kHz) [Hough *et. al.* 1989]. This corresponds to an $_{\wedge}$ sensitivity of $\sim 1.7 \times 10^{-19}$ $/\sqrt{Hz}$.
amplitude

1.5   Limitations to the Sensitivity of Laser Interferometric Detectors

The ultimate sensitivity of a laser interferometric detector is limited by various sources of noise. In this section some of the more significant noise sources will be described. A more exhaustive description of the possible noise sources can be found in the proposals for long-baseline detectors submitted by the various research groups to their funding authorities [Blair *et. al.* 1989, Giazotto *et. al.* 1989, Vogt *et. al.* 1989 and Hough *et. al.* 1989] (the AIGO, VIRGO, LIGO and GEO projects respectively). The last of these proposals, for a detector of 3km arm length (GEO), was submitted by a collaboration formed between several groups including the research group at the Max-Planck Institute for Quantum Optics (MPQ) and our group at Glasgow University. The GEO proposal [Hough *et. al.* 1989] will be frequently referred to throughout the remainder of this thesis.

1.5.1   Heisenberg Uncertainty Principle

The Heisenberg Uncertainty Principle places the lowest limit on the accuracy of any measurement of the position of a free mass. The minimum detectable differential displacement of the two suspended end masses (each of mass m) of an interferometer at frequency f (over a bandwidth of Δf) is set by the uncertainty principle to be [Edelstein *et. al.* 1978]:

$$\Delta x_{up} = \left[\frac{\hbar}{m f^2 \pi^2}\right]^{1/2} {}^m/\sqrt{Hz} \tag{1.5}$$

where $\hbar$ is Plancks constant divided by 2π. This sets a limit to the minimum possible gravitational wave amplitude h an interferometer can detect of:

$$h \sim \frac{1}{L}\left[\frac{2\hbar}{m f^2 \pi^2}\right]^{1/2} /\sqrt{Hz} \tag{1.6}$$

where L is the arm length of the detector. From this one can see that the minimum detectable gravitational wave amplitude improves linearly with increasing detector arm length. It should be noted that for most practical designs of detector it seems that other limitations to the sensitivity will be more significant than that set by the uncertainty principle.

1.5.2 Photon Shot Noise

An induced phase shift between the light in the two arms will produce a change in the power of the light on the output of the interferometer. The minimum detectable phase shift and hence minimum detectable differential displacement in a time τ is determined by the minimum detectable change in light power. This is limited by the $\sqrt{n}$ uncertainty associated with counting an average of n photons at the photodiode in a time τ (photon shot noise). The limiting sensitivity due to photon shot noise as a function of frequency f is given by [Hough et. al.1989]:

$$h = \left[\frac{\pi \hbar \lambda}{\varepsilon I_0 c}\right]^{1/2} \frac{f}{\sin (\pi f \tau_s)} \ /\sqrt{\text{Hz}} \tag{1.7}$$

where λ is the light wavelength, I_0 is the light power, ε is the quantum efficiency of the photodiode, c is the velocity of light in vacuum and τ_s is the storage time of the light in the arms. From this equation one can see that the effect of shot noise can be reduced by increasing the light power. Equation (1.7) also shows that the sensitivity of the interferometer can be optimised by setting the storage time τ_s of the light in each arm equal to half the period of the gravitational wave being searched for. (In a resonant cavity interferometer the far mirror in each cavity is chosen to have very high reflectivity R; the reflectivity of the input mirror on each arm can be chosen to give the desired storage time.)

Various techniques can be used to reduce the effect of shot noise - for example, standard recycling. If the mirrors in the detector are very low loss, when the detector is operated on a null fringe, most of the illuminating light power will be returned towards the laser and will be wasted. This wasted light can be coherently added to the input light beam by careful positioning of a mirror (m) on the input port as shown in Figure 1.4. This increases the light power in the interferometer reducing the shot noise effect

13

[Drever *et. al.* 1983]. The limiting sensitivity due to photon shot noise as a function of frequency is then given by:

$$h = \left[\frac{\hbar \, \lambda f \, (1\text{-}R)}{\varepsilon \, I_0 \, L} \right]^{1/2} /\sqrt{Hz} \qquad (1.8)$$

where L is the arm length of the detector and the storage time of the light τ_s has been set equal to half the gravitational wave period [Hough *et. al.* 1989].

Another method of improving the sensitivity beyond the shot noise limit has been proposed where squeezed light is injected into the output port of the interferometer [Caves 1981]. However much development is required before this technique will become practical.

1.5.3 Thermal Noise

Thermal noise associated with the modes of the pendulum suspensions and modes of the test masses themselves can limit the sensitivity of an interferometric detector.

Consider a test mass m suspended as a simple pendulum with resonant frequency f_0 and quality factor Q. The thermal motion of the pendulum associated with the pendulum mode is peaked at the resonant frequency, which is typically about 1Hz. For frequencies f much higher than this it can be shown that the r.m.s. spectral displacement density of these thermal motions is given by [Weiss 1972]

$$x_{rms} = \left[\frac{k \, T f_0}{2 \, m \, Q \, \pi^3 f^4} \right]^{1/2} \, m/\sqrt{Hz} \qquad (1.9)$$

where kT is the thermal energy associated with the resonance, k being Boltzmann's constant and T the absolute temperature. This sets a limit to the minimum possible gravitational wave amplitude h an interferometer can detect of:

$$h \sim \frac{1}{L} \left[\frac{2 \, k \, T f_0}{m \, Q \, \pi^3 f^4} \right]^{1/2} /\sqrt{Hz} \qquad (1.10)$$

where L is the arm length of the detector.

In a similar way it can be show that in the case of the thermal motion associated

with the internal modes of the test masses, the r.m.s. spectral displacement density at frequencies below the internal resonant frequency f_0 given by [Weiss 1972]

$$x_{rms} = \left[\frac{kT}{2\,m\,Q\,\pi^3 f_0^3} \right]^{1/2} \text{m}/\sqrt{\text{Hz}} \qquad (1.11)$$

where Q is the internal quality factor of the mass m. This sets a limit to the minimum possible gravitational wave amplitude h an interferometer can detect of:

$$h \sim \alpha\, \frac{1}{L} \left[\frac{2\,kT}{m\,Q\,\pi^3 f_0^3} \right]^{1/2} /\sqrt{\text{Hz}} \qquad (1.12)$$

where α is some factor of the order of a few which accounts for the summation of the effects of a number of internal resonant modes.

It is clear from both equations (1.10) and (1.12) that apart from reducing the temperature T the thermal noise can be minimised by using high Q materials for the test masses and high Q pendulum suspensions. The detector can also become less sensitive to the thermal noise effects if the arm length L is made large. In the proposed 3km detector (GEO) we aim to use test masses with $Q \sim 10^6$-10^7 and pendulum suspensions with $Q \sim 10^7$-10^8 [Hough *et. al.* 1989].

1.5.4 Seismic Noise

Seismic noise is a significant problem for all terrestrial interferometric detectors, especially at low frequencies. The test masses and other optical components of an interferometer need to be isolated from ground vibrations in order to reduce the effects of seismic noise to an acceptably low level. This isolation can be achieved using various types of mechanical isolators *e.g.* pendulum suspensions, vibration isolation stacks and air springs, to couple the test masses and other sensitive components to the ground. However despite these measures seismic noise is likely to limit the sensitivity of earth-borne detectors at frequencies below about a few tens of hertz.

To a large extent this thesis is concerned with investigations into the performance of the passive isolation systems commonly used in interferometric detectors.

15

1.5.5 Other Sources of Noise

There are many other sources of noise which might limit the sensitivity of an interferometric detector. For example, fluctuations in the residual gas pressure of the vacuum can give rise to noise in the detector by varying the optical path lengths of the light beams. Frequency and intensity fluctuations of the laser light can limit the sensitivity of the detector and these need to be stabilised using feedback systems. Rotational and tilting motions of the suspended test masses can cause misalignment of the optical cavities leading to fluctuations in the intensity of the detected light and a reduction in sensitivity. The alignment of optical cavities must be maintained using local control of the orientation of the test masses. Such control systems are discussed in Chapter 4.

1.5.6 Summary of the Predicted Noise Levels

For reference, Figure 1.5 shows a graph of the predicted levels of noise in the proposed 3km detector (GEO) when it is optimised to search for burst sources of gravitational waves. The seismic noise curve was calculated here assuming that the test masses were isolated using passive air mounts, five-layer vibration isolation stacks and double pendulum suspensions. The photon shot noise curve was calculated assuming that standard recycling (Section 1.5.2) was being used. This graph is taken directly from the GEO proposal [Hough *et. al.* 1989] where further details can be obtained. From this graph one can see that the dominant noise source towards the higher frequencies is photon shot noise. At the lower frequencies (below about 100Hz) the sensitivity of the detector is severely limited by the effects of seismic noise.

h_{eff}

Seismic Noise

Neutron Star formation (Virgo) non – axisymmetrical

10^{-21}

Neutron Star binary coalescence (100 M pc)

Photon Noise : $\epsilon I_o = 50W$, $1 - R = 5 \times 10^{-5}$

Thermal Noise (suspensions) $Q_s = 10^8$, $m = 400$ kg

10^{-22}

3×10^5 (silicon)
1.5×10^6 (fused silica)

Thermal Noise (internal modes) : $Q_{INT} = $

10^{-23}

Uncertainty Principle : $m = 400$ kg

Vacuum Noise : 10^{-8} mbar – Fabry-Perot

10^{-24}

10   10^2 10^3 10^4

Frequency (Hz)
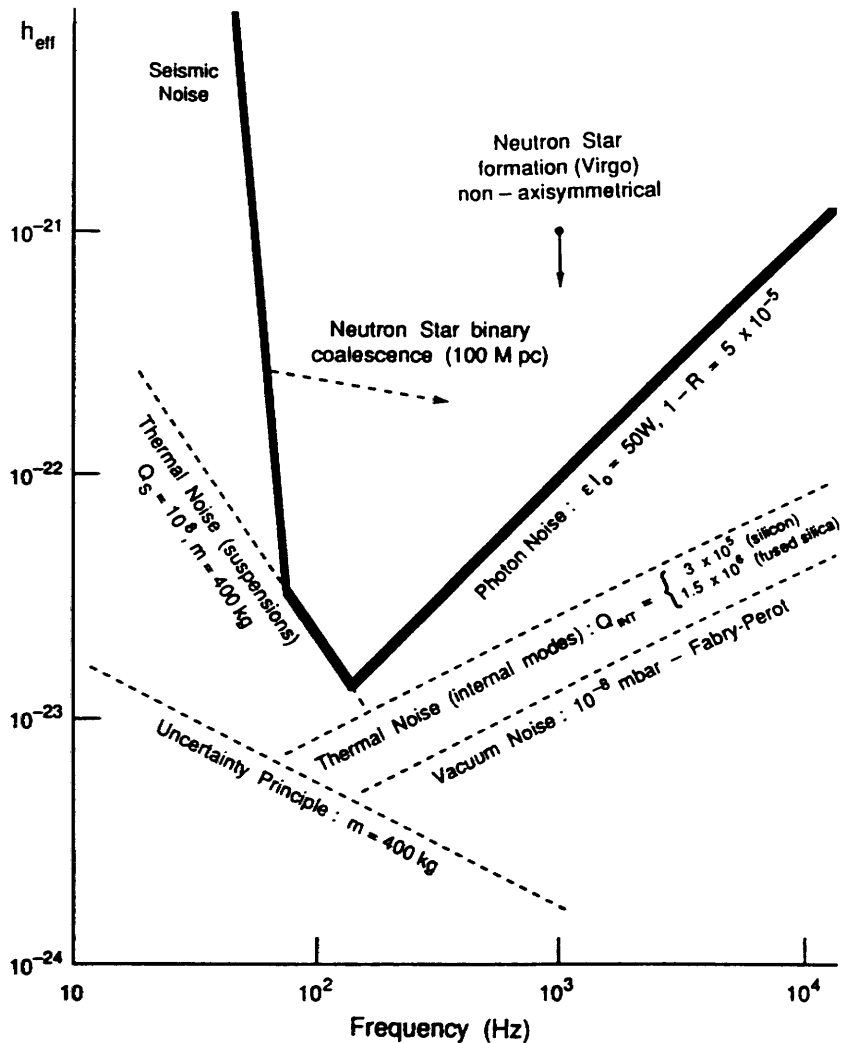
Figure 1.5 **The predicted levels of noise in the proposed 3km detector when optimised to search for burst sources of gravitational waves (such as neutron star formation and compact binary coalescences). The ordinate h_{eff} is the root-mean-squared amplitude for pulse signals of characteristic frequency f measured over a bandwidth of $f/2$. The seismic noise curve was determined here assuming that the test masses were isolated using passive air mounts, five-layer vibration isolation stacks and double pendulum suspensions. The photon shot noise curve was determined assuming that standard recycling was being used. The predicted amplitudes of two different types of burst source have been superimposed for comparison. This graph is taken directly from the GEO proposal [Hough et. al. 1989] where further details are given.**

Chapter 2

An Introduction to Test Mass Isolation and Feedback Control Techniques

2.1 Introduction

The ultimate sensitivity of an interferometric gravitational radiation detector is limited by various sources of noise some of which have spectra which rise towards lower frequencies as discussed in Chapter 1. This category includes thermal noise from the pendulum suspensions of the test masses and more particularly seismic noise. Since there are interesting sources of gravitational waves in the frequency region of ten to a few hundred hertz the test masses must be seismically isolated to a high level in order to ensure that the potential large bandwidth operation of an interferometric detector may be realised.

The problem of thermal noise can be alleviated by ensuring that the last stage of pendulum suspension of the test mass has a high quality factor Q ~10^7 or 10^8 [Hough *et. al.* 1989]. Regarding seismic noise, simple passive isolation techniques offer adequate performance in reducing the effects at frequencies above about 1kHz. However at lower frequencies, due to the inherently larger amplitude of seismic noise and generally speaking less effective performance of simple isolation systems, more sophisticated seismic isolation systems must be used. Furthermore, in order to control the position and orientation of the isolated mass to the high degree of accuracy necessary in a resonant cavity interferometer, high gain electronic feedback systems must be used. Feedback must also be used to electronically damp the high Q resonances of the pendulum system. However it is essential that the application of electronic feedback to the suspended mass does not compromise the level of isolation achieved by the suspension system.

2.2 Seismic Noise

The seismic background is an important source of noise for Earth-based gravitational radiation detectors. It gives rise to components of motion at the Earth's surface in the horizontal, vertical and rotational senses. These motions can be natural or man-made in origin, discrete or continuous in nature.

The most important region of the seismic spectrum in the context of gravitational wave detection is the high frequency region (> 0.5Hz). High frequency noise is mainly local in origin and the amplitude is commonly seen to increase during the daytime indicating that it is man-made. The coupling of the wind to trees or man-made structures is another major source of high frequency noise. Generally speaking the amplitude of noise in the horizontal and vertical directions is approximately the same. A common observation is that the linear spectral density of ground displacement attenuates as f^2 in both dimensions. However the amplitude of the seismic background can vary considerably from area to area by up to a few orders of magnitude. To illustrate this point consider the following observations which were made at various sites (in a bandwidth from ~10Hz to ~1kHz):

linear spectral density of ground displacement	*location*	*reference*
$\sim \dfrac{3 \times 10^{-7}}{f^2} \dfrac{m}{\sqrt{Hz}}$	Garching, W. Germany	[Shoemaker *et. al.* 1988]
$\sim \dfrac{1 \times 10^{-6}}{f^2} \dfrac{m}{\sqrt{Hz}}$	Pisa, Italy	[Giazotto 1987]
$\sim \dfrac{1 \times 10^{-7}}{f^2} \dfrac{m}{\sqrt{Hz}}$	Tentsmuir, Scotland	[Hough *et. al.* 1986]
$\sim \dfrac{1.5 \times 10^{-7}}{f^2} \dfrac{m}{\sqrt{Hz}}$	Pisa, Italy	[Del Fabbro *et. al.* 1988a]

In general the level of the noise is much greater at the surface of the Earth than at depth as illustrated by a measurement made down a zinc mine at a depth of ~0.5km in a frequency band between ~10Hz and 100Hz:

$\sim \dfrac{2 \times 10^{-9}}{f^2} \dfrac{m}{\sqrt{Hz}}$	Ogdensburg, U.S.A.	[Isacks and Oliver 1964]

In the proposed 3km detector we are aiming for a limiting gravitational wave amplitude due to seismic noise of $h \sim \frac{10^{-24}}{\sqrt{Hz}}$ or better at 100Hz [Hough *et. al.* 1989]. For a near surface based detector this implies that an isolation factor of about 10^{10} or better at 100Hz is required. Some passive methods of vibration isolation commonly used in gravitational wave detectors are described in the next section.

2.3 Passive Methods of Vibration Isolation

2.3.1 Simple Pendulum

Conceptually the simplest way of achieving passive isolation of a test mass is to suspend the mass as a pendulum. There will be some transfer of motion between the point of suspension and the mass, the amplitude of which is governed by the transfer function of the pendulum *i.e.*

$$transfer\ function = \frac{displacement\ of\ mass}{displacement\ of\ suspension\ point} \qquad (2.1)$$

Consider a point mass m suspended from the ground using a wire of length L and negligibly small mass as shown in Figure 2.1. Consider motions of the mass in the horizontal direction with respect to an arbitrary reference point. The mass will be subject to a restoring force F_r given by:

$$F_r = T \sin \theta \qquad (2.2)$$

where $\quad \theta \quad =$ the angle the suspension wire makes with the vertical axis,

$\qquad T \quad \sim \quad mg$ (for small θ)

and, $\quad g \quad =$ the acceleration due to gravity.

Assume that the mass is also subject to a velocity dependent damping force F_d given by:

$$F_d = b\,(\dot{x}_1 - \dot{x}_0) \qquad (2.3)$$

where $\quad b =$ the damping coefficient of the pendulum.
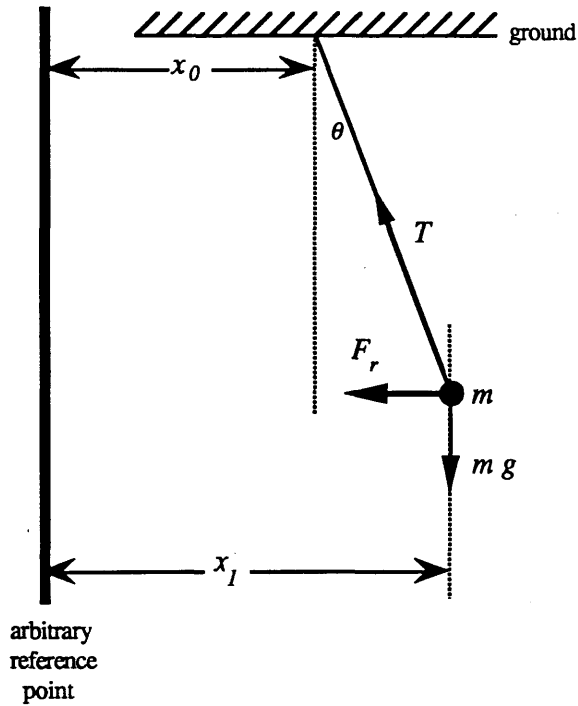
Figure 2.1 *Simple pendulum suspension of a point mass. The symbols used here are defined in the text which follows.*

For small displacements of the mass the approximation $\sin \theta \approx \dfrac{(x_1 - x_0)}{L}$ can be made and the equation of motion of the mass can be written as

$$m\ddot{x}_1 + \frac{mg}{L}(x_1 - x_0) + b(\dot{x}_1 - \dot{x}_0) = 0 \qquad (2.4)$$

Taking the Laplace transformation of this equation, assuming zero initial conditions, yields the transfer function for the pendulum (the magnitude of which gives the transmissibility T) in the frequency domain s:

$$\frac{x_1}{x_0} = \frac{\gamma s + \omega_0^2}{s^2 + \gamma s + \omega_0^2} \qquad (2.5)$$

where,

$s = j\omega$ (where $j^2 = -1$)

ω_0 = the natural angular resonant frequency of the pendulum = $2\pi f_0$

$\omega_0^2 = \dfrac{g}{L}$

$$\gamma = \text{the damping factor of the pendulum} = \frac{b}{m} = \frac{\omega_0}{Q}$$

and Q = the quality factor of the pendulum.

The form of equation (2.5) tells us that at frequencies below the natural resonant frequency f_0 of the pendulum the transmissibility is unity *i.e.* there is no isolation of the suspended mass. At the resonant frequency f_0, a peak occurs in the transfer function curve, the magnitude of which depends on the damping factor γ of the pendulum. Above this frequency isolation is obtained, the transfer function falling as f_0^2/f^2 until a frequency given by $f = f_0 Q$ (commonly referred to as the corner frequency) where the effects of the damping in the pendulum become apparent and the transfer function tends to behave as $f_0/Q f$.

As already mentioned in Chapter 1, with application to gravitational wave detectors, high Q (~10^7 or 10^8) pendulum suspensions for the test masses are necessary in order to try to minimise the random motions occurring due to thermal effects [Hough *et. al.*1989]. Typically the pendulums used in laser interferometers have a resonant frequency of ~1Hz. In such high Q, low resonant frequency systems the effects of damping are negligibly small with the corner frequency lying at about 10^4 or 10^5 kHz which is well outwith the frequency range of interest for the detection of gravity waves (up to about 10kHz). Note that under this condition ($\gamma \rightarrow 0$) the transfer function of the simple pendulum approximates to:

$$\frac{x_1}{x_0} \approx \frac{\omega_0^2}{s^2 + \omega_0^2} \qquad (2.6)$$

Essentially each stage of a typical pendulum suspension designed for use in a gravitational wave detector would behave as f_0^2/f^2 at frequencies above the resonant frequency of the pendulum. Thus for a 1Hz pendulum the horizontal transmissibility at 100Hz would be $T \sim 1 \times 10^{-4}$. It should be pointed out here that the isolation of a simple pendulum increases proportionally as the length of suspension wire increases. However in order to achieve a significant improvement in the isolation level achieved one would need to use unfeasibly long suspension wires.

Pendulum suspensions also provide some degree of isolation from vertical seismic motions, although not as effectively as in the horizontal direction. The vertical transfer

function for a single pendulum is similar in form to equation (2.5), the horizontal transfer function. However, in this case the natural frequency of oscillation and the isolation characteristics of the pendulum are governed by the elastic properties of the loaded suspension wire. The restoring force on the mass in the vertical z direction has the form

$$F_r = k_v z \tag{2.7}$$

where k_v is the vertical stiffness of the wire which is determined according to

$$k_v = \frac{EA}{L} \tag{2.8}$$

where,

$\qquad E = $ the Young's modulus for the wire material

and $\qquad A = $ the cross-sectional area of the wire.

The vertical resonant angular frequency of the pendulum is given by

$$\omega_v^2 = \frac{k_v}{m} . \tag{2.9}$$

For instance, a high Q pendulum consisting of a steel suspension wire loaded to within a factor of two from its breaking strain (which is $\sim 1.4 \times 10^{-2}$) and of horizontal resonant frequency 1Hz would have a vertical resonant frequency of ~12Hz. This pendulum would have a vertical transmissibility of $T \sim 1.4 \times 10^{-2}$ at 100Hz.

2.3.2 Multiple Pendulum

Increased isolation can be achieved by using two or more pendulums connected in series. Vibrations at the top of the multiple pendulum are then subject to several stages of attenuation in their journey down the system. The total attenuation will depend on the physical characteristics of each stage *i.e.* the lengths of wires (L_1, L_2,..*etc.*) and size of the masses (m_1, m_2,..*etc.*) suspended.
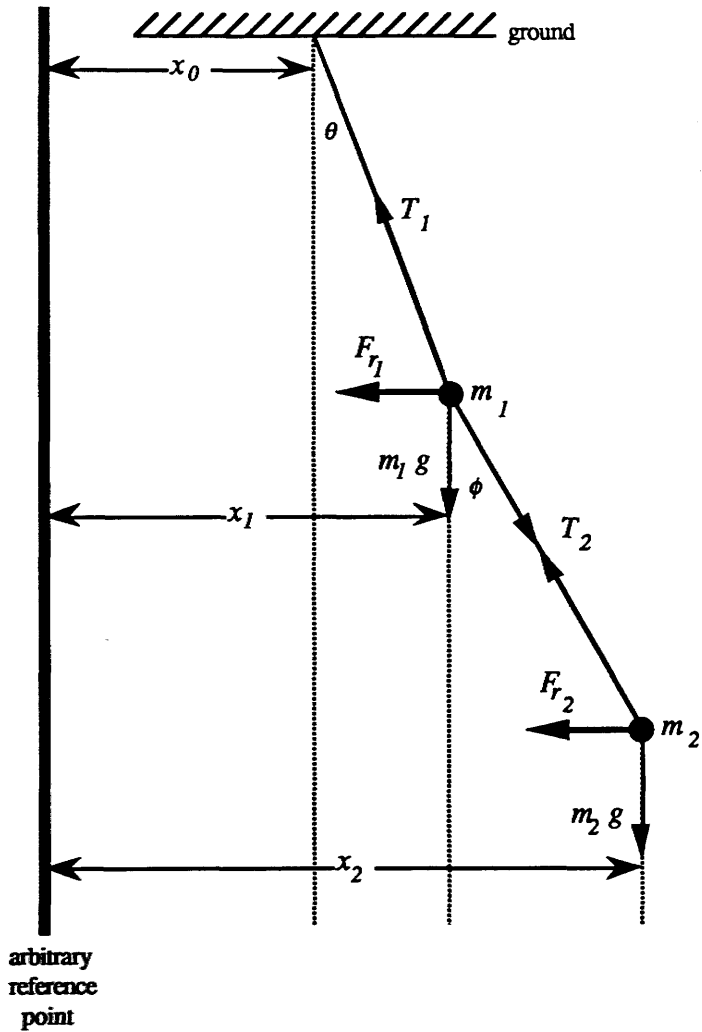
Figure 2.2 Double pendulum suspension of a point mass. The symbols used here are defined in the text.

Consider the double pendulum illustrated in Figure 2.2. The intermediate and lower masses will be subject to restoring forces as described below:

$$F_{r_1} = T_1 \sin\theta - T_2 \sin\phi \qquad (2.10)$$

$$F_{r_2} = T_2 \sin\phi \qquad (2.11)$$

Note that the restoring force acting on the intermediate mass m_1 depends on the total

mass in the chain below. Assume also that the masses are subject to velocity dependent damping forces given by

$$F_{d_1} = b_1 \, (\dot{x}_1 - \dot{x}_0) \tag{2.12}$$

$$F_{d_2} = b_2 \, (\dot{x}_2 - \dot{x}_1). \tag{2.13}$$

For small horizontal displacements the equations of motion of the masses are

$$m_1 \ddot{x}_1 + (m_1 + m_2) \frac{g}{L_1} \, (x_1 - x_0) - \frac{m_2 \, g}{L_2} \, (x_2 - x_1) + b_1 \, (\dot{x}_1 - \dot{x}_0) = 0 \tag{2.14}$$

and

$$m_2 \ddot{x}_2 + \frac{m_2 \, g}{L_2} \, (x_2 - x_1) + b_2 \, (\dot{x}_2 - \dot{x}_1) = 0 \tag{2.15}$$

Again by taking the Laplace transformation of these equations, assuming zero initial conditions, the transfer function to the lower mass can be derived *i.e.*

$$\frac{x_2}{x_0} = \frac{\gamma_1 \gamma_2 s^2 + \left[(1 + \alpha_m) \gamma_2 \omega_1^2 + \gamma_1 \omega_2^2 \right] s + (1 + \alpha_m) \omega_1^2 \, \omega_2^2}{s^4 + \left[\gamma_1 + \gamma_2 \right] s^3 + \left[(\omega_1^2 + \omega_2^2)(1 + \alpha_m) + \gamma_1 \gamma_2 \right] s^2 + \left[(1 + \alpha_m) \gamma_2 \omega_1^2 + \gamma_1 \omega_2^2 \right] s + (1 + \alpha_m) \omega_1^2 \, \omega_2^2} \tag{2.16}$$

where γ_1 = the damping factor for the first stage of the pendulum

  γ_2 = the damping factor for the second stage of the pendulum

and α_m = the mass ratio m_2/m_1 .

The natural resonances of the separate stages at angular frequencies $\omega_1 = \sqrt{g/L_1}$ and $\omega_2 = \sqrt{g/L_2}$ are coupled together giving two new natural frequencies of oscillation for the double pendulum at ω_L and ω_U (lower and upper resonances).

It is interesting to note here that it has been shown that for a double pendulum system consisting of two identical 1Hz pendulums (mass ~ 400Kg), one only requires the Q of the upper stage to be ~10^4, to keep the thermal noise level of a similar magnitude to that for a single 1Hz pendulum of Q~10^8 at frequencies greater than 10Hz [Robertson D.I. 1990]. The use of a relatively lower Q first stage has the advantage of reducing the amplitude of test mass motion at the resonant frequencies of the coupled system, easing the dynamic range requirements of any control system used to control the motions of the test mass.

The transfer function described in equation (2.16) can be re-written in the limit where γ for each stage is small (as is the case for the pendulums discussed here):

$$\frac{x_2}{x_0} \approx \frac{(1 + \alpha_m)\omega_1^2 \, \omega_2^2}{s^4 + \left[(\omega_1^2 + \omega_2^2)(1 + \alpha_m) \right] s^2 + (1 + \alpha_m)\omega_1^2 \, \omega_2^2}. \qquad (2.17)$$

The two resonant frequencies of the coupled system ω_L and ω_U are obtained by taking the roots of the denominator of this transfer function. One can immediately see that their values depend on the lengths and masses in each stage. For instance, for a double pendulum with identical masses and lengths in both stages (natural angular resonant frequencies ω_0) these resonances are at the frequencies given by $\omega_L = \sqrt{(2 - \sqrt{2})}.\omega_0$ and $\omega_U = \sqrt{(2 + \sqrt{2})}.\omega_0$.

At frequencies higher than the upper resonance (ω_U) of the coupled system, the transfer function approximates to:

$$\frac{x_2}{x_0} \approx \frac{\left(1 + \frac{m_2}{m_1}\right)\omega_1^2 \, \omega_2^2}{s^4} \qquad (2.18)$$

From this one can see that to achieve the best possible isolation with a high Q double pendulum one should aim for the condition $m_2 \leq m_1$. Comparing this to equation (2.6) one can see that the isolation increases as f^4 which is much better than for a single pendulum where the isolation increases only as f^2. For instance, a system of two identical 1Hz pendulums will have a horizontal transmissibility of $T \sim 2 \times 10^{-8}$ at 100Hz.

Obviously even higher levels of isolation can be achieved by increasing the number of pendulum stages connected in series. However this results in an increase in the number of degrees of freedom of the system i.e. an increase in the number of natural modes of oscillation. Since we are dealing with high Q pendulums, the phase changes associated with each pendulum resonance will be very rapid. Therefore any feedback system used to control the position of the lower mass of such a high Q multiple-stage pendulum would have to compensate for these fast phase changes in the pendulum transfer function in order to maintain stability in the closed feedback loop. Furthermore, the resulting increase in the number of degrees of freedom of the system can aggravate the problem of linear and non-linear cross-coupling of modes (see Section 2.3.3). A way

of minimising these problems is to use as few stages of isolation as possible consistent with achieving the required isolation level.

It is proposed to use double pendulum suspensions for the test masses in the 3km detector (GEO). Chapter 4 describes a novel design of double pendulum suspension system which was developed for use in such an interferometric detector.

Double pendulum suspensions are currently used in the 30m prototype detector at MPQ, Garching [Shoemaker *et. al.* 1988]. The upper stage of each double pendulum consists of a plate suspended using four vertical springs. The test mass is then suspended from the plate using a single wire loop. An alternative design of double pendulum suspension which is based on similar ideas to the system used at MPQ and that described in Chapter 4 is currently being developed at MIT [Stephens *et. al.* 1991]. Here the test mass is suspended inside a hollow cylindrical shell mass using a single wire loop. The shell itself is then suspended from a support plate using four vertical springs. Note that the use of vertical springs in the upper stage of each of these double pendulum systems increases the isolation of the test mass to vertical and tilting motions at the top suspension point.

It is interesting to note here that a research group at the INFN laboratory in Pisa have designed and constructed a 'seven-stage super attenuator' for use in interferometric detectors operating down to as low a frequency as ~10Hz. This super-attenuator which provides isolation in the three dimensions consists of a seven-stage pendulum for attenuation in the horizontal plane and seven gas springs for attenuation in the vertical direction. This system is capable of supporting a large (400kg) test mass for use in the proposed VIRGO long-baseline interferometer. The highest frequency vertical mode of this compound suspension system is at about 6.0Hz, with the highest frequency horizontal mode at about 3.3Hz. It has already been demonstrated that this system can reduce the seismic noise by at least a factor of $\sim 2 \times 10^8$ above 10Hz [Del Fabbro *et. al.* 1988b].

2.3.3 Limitations to the Isolation Achievable with Pendulums

In deriving the transfer functions for the pendulum systems described in Sections 2.3.1 and 2.3.2, two assumptions were made which are in general not totally justifiable. The first of these was that the suspended mass was point-sized. In reality a suspended mass will be finite in size and therefore will have internal modes of oscillation. Generally

speaking, for the size of mass typically used in prototype gravity wave detectors (<10kg) the lowest of these modes lies at a frequency outwith the upper detection frequency for gravity waves (a few tens of kHz). If the intrinsic Q of the mass is sufficiently high then thermal noise associated with these modes will not limit the sensitivity of the detector (see Section 1.5.3). Intrinsic Q's of ~10^6 or better are required for the 3km gravitational radiation detector [Hough et. al. 1989].

Another consequence of the suspended mass having finite size is that its tilting and rotational motions can couple to horizontal motion at the mirrored surface of the mass. In order to minimise this effect, the frequencies of the tilting and rotational modes should be made as low as possible relative to the fundamental pendulum mode. In the case of the tilting mode this can be achieved by attempting to ensure that the positioning error of the breakaway point from the centre of mass is as small as possible. It is also possible to electronically damp these modes to an acceptable level (refer to Section 2.4). However great care must be taken that the electronic damping systems do not re-introduce displacement noise to the isolated test mass. Chapter 4 describes a test mass isolation and feedback control system designed specifically to minimise such effects.

A second and possibly more serious invalid assumption in the analysis of the pendulum was that the suspension wire of the pendulum was of negligible mass. In practice the internal modes of the taut wire (commonly referred to as 'violin-modes') are a significant limitation to the isolation obtained with a pendulum suspension. If one considers the motion of the suspended mass (m) in a single pendulum of length L to be due to a travelling wave in the wire then, in the absence of damping, the transfer function as a function of angular frequency ω is [Robertson N.A. 1981]:

$$\frac{x_1}{x_0} = \frac{1}{\cos\left(\frac{\omega L}{c}\right) - \frac{\omega c}{g}\sin\left(\frac{\omega L}{c}\right)} \qquad (2.19)$$

where,

c = the propagation velocity of the wave in the wire = $\sqrt{T/\rho_L}$

with, T = the tension in the wire = mg

and ρ_L = the linear density of the wire.

The first resonance of this system can be obtained by setting $\omega L/c \ll 1$. Equation (2.19) then approximates to equation (2.6) for the single pendulum with no damping which was derived ignoring the internal modes of the wire. The first resonant frequency is therefore

at ω_0, the natural frequency of the pendulum. All of the other violin resonances fall into a series ω_n such that:

$$\lambda_n \approx \frac{2L}{n} \qquad (2.20)$$

where $n = 1,2,3,\dots\text{etc.}$

The higher the value of n the less approximate this relation becomes.

In the case of steel piano wire (breaking stress 3×10^9 Nm^{-2}; density 7800kgm^{-3}) loaded to within a factor $N = 2$ of its breaking stress, these resonances are at frequencies given by [Robertson N.A. 1991]:

$$f_n \approx 880 \left(\frac{2}{N}\right)^{\frac{1}{2}} \left(\frac{n}{1}\right) \left(\frac{f_0}{1\text{Hz}}\right)^2 \text{ Hz} \qquad (2.21)$$

Hence the first few of these resonances will fall within the working frequency range of a typical gravitational wave detector (up to a few kilohertz).

Note also from equation (2.19) that at best the isolation is ω/g, the transmissibility curve falling as f instead of f^2 as predicted in the absence of the violin modes. Hence the presence of violin modes in the wire has two negative effects on the isolation properties of a pendulum. Firstly there is a reduction in the isolation at the violin mode frequencies (these tend to be fairly high Q of the order of about 10^4 [Shoemaker 1987]). Secondly the isolation of the pendulum increases only as f instead of f^2 at frequencies above the first violin mode. Fortunately this transition should occur at a high enough frequency that the detector sensitivity should not be affected.

2.3.4 Vibration Isolation Stacks

Another system commonly used to achieve isolation of the test masses in gravitational wave detectors is the vibration isolation stack. Stacks are commonly used in conjunction with pendulum suspension systems to enhance the isolation levels obtained. A one-stage stack consists of a layer of a heavy material (*e.g.* lead) supported by an elastic material (*e.g.* rubber) as shown in Figure 2.3.
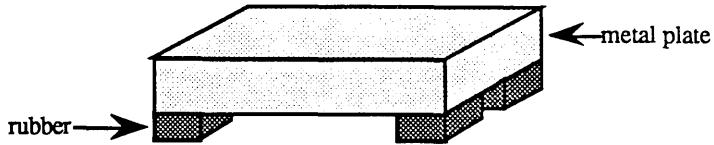
Figure 2.3   Schematic diagram of a one-stage vibration isolation stack.

This system behaves in each dimension like a mass connected to a damped spring. Shear motions of the rubber give the stack horizontal spring and damping whilst compressional motions of the rubber give the stack vertical spring and damping. This system is analogous to the one-stage pendulum discussed in Section 2.3.1 where the gravitational restoring force on the mass gives the pendulum horizontal stiffness and stretching of the wire gives the pendulum vertical stiffness.

   The transfer functions for a one-stage stack in each dimension can be derived using simple dynamical theory. For instance, to obtain the horizontal transfer function the simple spring / damper model illustrated in Figure 2.4 can be used to represent the stack.
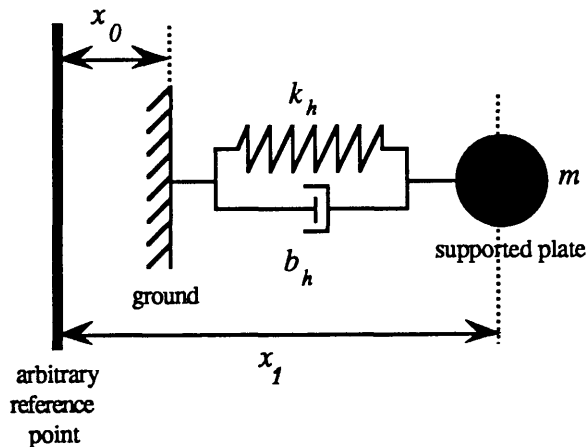
Figure 2.4   Simple spring/damper model representing the horizontal dynamical behaviour of a one-stage vibration isolation stack.

The transfer function in the horizontal direction is then:

$$\frac{x_1}{x_0} = \frac{\gamma_h s + \omega_h^2}{s^2 + \gamma_h s + \omega_h^2} \qquad (2.22)$$

29

which is identical in form to equation (2.5) for the simple pendulum, falling as f^2 until the corner frequency where $f \sim f_h Q$ where it tends to fall as f. However in this case the horizontal resonant angular frequency is given by:

$$\omega_h^2 = \frac{k_h}{m} \qquad (2.23)$$

and the damping factor by:

$$\gamma_h = \frac{b_h}{m} = \frac{\omega_h}{Q_h} \qquad (2.24)$$

Here the horizontal stiffness k_h is related to the Shear modulus G of the rubber by the equation

$$k_h = \frac{GA}{z} \qquad (2.25)$$

with,

$\quad\quad A$ = the total loaded area of the rubber support

and $\quad z$ = the height of the rubber supports.

For instance, it has been demonstrated that a stack with a 6kg mass supported by 'neoprene' rubber of cross-sectional area ~4cm^3 and thickness ~0.6cm has a horizontal resonant frequency of $f_h \sim$7Hz. According to equation (2.22), and assuming a quality factor of $Q_h \sim 5$ *, the transmissibility of this system at 100Hz will be $T \sim f_h/Qf \sim 1.4 \times 10^{-2}$. This is much larger than for a typical one stage pendulum due to the higher frequency of the resonance and lower Q value (lower corner frequency).

Similar equations to (2.22), (2.23) and (2.24) can be derived for the vertical direction where the vertical stiffness is related to the Young's modulus E by

$$k_v = \frac{EA}{z}. \qquad (2.26)$$

For a one-stage stack of the dimensions described above, it has been demonstrated that the vertical resonant frequency will be of the order of $f_v \sim$17Hz. Assuming a quality factor of $Q_v \sim 15$ * such a system would give a transmissibility at 100Hz of $T \sim 2.9 \times 10^{-2}$.

One of the main advantages of stack systems compared to pendulum systems is that they can be physically much more compact in size. Furthermore, since they are low Q systems the motions which occur at the resonant frequencies are much smaller than for

---

* Based on previous measurements made with silicone rubber.

high Q pendulum systems.

Conversely a major disadvantage is that a one-stage stack will produce more thermal noise than a one-stage pendulum due to the much higher level of damping occurring in a stack. However, since stacks are commonly used in conjunction with pendulum suspensions, usually being placed somewhere between the ground and the point of pendulum suspension, any thermally generated displacements at the top of the stack should be attenuated to an acceptable level by the time they reach the suspended test mass.

On extending the analysis to a two-stage stack, the horizontal transfer function from motion at the ground x_0 to motion at the centre of mass of the top plate of the stack x_2 is given by:

$$\frac{x_2}{x_0} = \frac{\gamma_1\gamma_2 s^2 + \left[\gamma_2\omega_1^2 + \gamma_1\omega_2^2\right]s + \omega_1^2\,\omega_2^2}{s^4 + \left[\gamma_1 + \gamma_2 + \frac{b_2}{m_1}\right]s^3 + \left[\omega_1^2 + \omega_2^2 + \gamma_1\gamma_2 + \frac{k_2}{m_1}\right]s^2 + \left[\gamma_2\omega_1^2 + \gamma_1\omega_2^2\right]s + \omega_1^2\,\omega_2^2} \qquad (2.27)$$

where the subscripts refer to layers one and two. At frequencies above the resonant frequencies and before the effects of damping become apparent this equation approximates to

$$\frac{x_2}{x_0} \approx \frac{\omega_1^2\,\omega_2^2}{s^4} \qquad (2.28)$$

Comparing this to equation (2.18) one can see that there is a fundamental difference in the horizontal isolation characteristics of the two-stage stack compared to the two-stage pendulum. In the case of the multi-stage pendulum the horizontal restoring force acting on each mass depends on the total mass in the chain below as illustrated by equation (2.14). However in a multi-layer stack system, to first order, the horizontal restoring forces acting on any mass depends solely on the elastic properties of the rubber. Both systems do however behave similarly in the vertical sense.

2.3.5 Limitations to the Isolation Achievable with Stacks

The level of horizontal isolation predicted using the simple spring/damper model as shown in Figure 2.4 may not be achievable in practice due to cross-coupling effects which might take place in stacks due to their extended geometry. A detailed investigation

of the limitations to the performance of vibration isolation stacks due to the effects of coupling is described in Chapter 6.

2.4 Orientation and Position Control of the Test Masses in Laser Interferometers

In resonant cavity interferometers it is essential to control both the position and orientation of the test masses to a high degree of accuracy. However it is very important that the application of feedback to the test masses does not degrade the detector performance.

Axial control of the test masses must be provided in order to control the absolute lengths of the cavities. As discussed in Section 1.4.2, a control system is used to stabilise the laser frequency to the length of the primary cavity in the 10m prototype detector. However it is unreasonably demanding to expect such a feedback system to have enough dynamic range to compensate for the large low frequency motions of the suspended test masses. Therefore the distance between the masses in the primary cavity must be locked to the laser frequency at low frequencies (below a few hertz) by applying feedback to the test masses. Similarly feedback must also be applied to the test masses of the secondary cavity in order to control the length of this cavity with respect to the length of primary cavity and the frequency of the laser light *i.e.* to operate the detector on a null fringe, providing the main output signal of the detector. Furthermore, these axial control systems must also electronically damp the high Q pendulum modes sufficiently well to maintain stability in the feedback loops and to avoid excessive motions at the pendulum modal frequencies.

If the cavities and the laser are held exactly on resonance producing a null fringe in the detector output, the system will be insensitive to fluctuations in the laser intensity. However any offset Δx in the length of a cavity (of length L) from its correct locking point will lead to a reduction in the detector sensitivity due to such fluctuations. Suppose that the fluctuations in the light intensity I are of the order of $\left(\frac{\Delta I}{I}\right) \sim 10^{-7}/\sqrt{\text{Hz}}$ and that we are aiming for a detector sensitivity of $h \sim 10^{-24}/\sqrt{\text{Hz}}$ at 100Hz. In the presence of an offset Δx, the detector sensitivity h as a function of the laser intensity fluctuations is given by [Hough *et. al.*1986]

$$h = \left(\frac{\Delta I}{I}\right)\left(\frac{\Delta x}{L}\right) \tag{2.29}$$

Up to frequencies of a few hertz, when in the unlocked state, one might expect Δx to be a few microns. Over an arm length of 3km this would mean that a feedback gain of about 10^7 or 10^8 would be necessary in this low frequency region in order to reduce Δx to the required level at the higher frequencies. This indicates that control systems of bandwidth of a few kHz are required for locking the arms. Note that if recycling is used in the detector (Section 1.5.2) then the locking requirements would be less demanding since this technique reduces the intensity noise (photon shot noise) of the light detected at the output of the interferometer.

Orientation control of the test masses must be used in order to control precisely the directions of the optical axes of the cavity mirrors. The pointing accuracy must be sufficiently high and stable for the cavities to be aligned in such a way as to optimise the detector efficiency. Any misalignment of the optical axes of the mirrors with the laser beam would cause the fundamental transverse mode amplitude of the cavity to decrease leading to a reduction in the sensitivity of the detector. For instance, it has been calculated that the misalignment angle must be less than about 10^{-7} rad in order to retain 95% of the gravitational wave signal [Hough et. al.1986].

Furthermore, if the beamsplitter is not symmetrical between the two interferometer arms but deviates by some angle then a lateral beam jitter δx will produce a phase fluctuation in the detected light. This is equivalent to fluctuations in the relative lengths of the cavities. If two beams interfere at an angle α and displace laterally by a distance δx with respect to each other, a phase fluctuation of

$$\delta\phi = \frac{2\pi \; \alpha \; \delta x}{\lambda} \qquad (2.30)$$

is induced between the two beams, where λ is the wavelength of the argon ion laser light (514nm). For a misalignment angle of say $\alpha = 10^{-5}$ rad, this places a limit on the positional fluctuations of light returning towards the beamsplitter of the order of $\sim 10^{-12}$ $\mathrm{m}/\sqrt{\mathrm{Hz}}$. For a cavity length of 3km this corresponds to an angular stability of the test masses of about 3×10^{-16} $\mathrm{rad}/\sqrt{\mathrm{Hz}}$ [Hough et. al. 1986].

It is important that the orientation control systems for the test masses do not couple the stabilised tilting and rotational modes to the fundamental pendulum mode. Noise in the feedback signals for the orientation control could then drive motions of the test mass in the longitudinal test direction. This can be minimised by using narrow bandwidth

feedback loops for damping of these modes. However as mentioned earlier, care should be taken that the high Q's of the pendulum suspensions and the test masses are not be reduced by the presence of the orientation control transducers. This is discussed in Chapter 4.

2.5 The Design and Analysis of Feedback Control Systems

2.5.1 Negative Feedback Control Systems

Negative feedback control systems are used to control the position and orientation of the test masses in laser interferometric gravitational wave detectors. A negative feedback control system is a closed-loop system which produces an output signal to cancel a selected input signal which might be varying. Figure 2.5 is a loop diagram representing a simple closed-loop negative feedback control system.
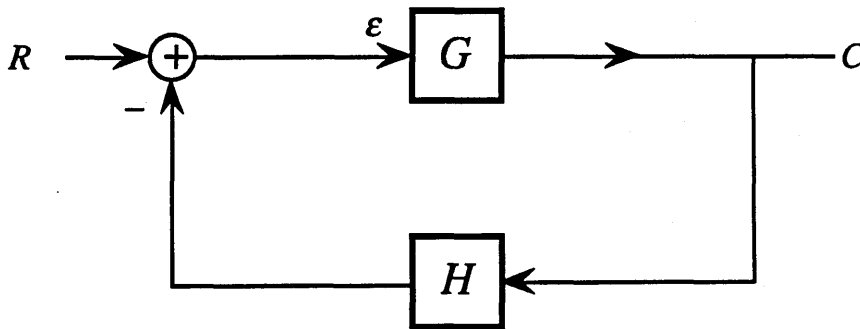
Figure 2.5 Block diagram representation of a simple closed-loop negative feedback system. The symbols used are defined in the text.

Here G is the forward transfer function for the system to be controlled and H is the feedback transfer function. The open-loop transfer function is defined as GH and the closed-loop transfer function is defined as $\frac{C}{R} = \frac{G}{1+GH}$.

The magnitude of the error point signal ε (the difference between the reference input signal R and the feedback signal CH) is a measure of how well the system performs. When operating correctly, the closed-loop system should behave in such a way that the error signal ε is minimised.

34

There are some fundamental requirements which the feedback systems used for the position and orientation control of the test masses in resonant cavity interferometers must fulfil . The closed-loop system should be stable, that is, under excitation it should settle to a steady value, its oscillations decaying in amplitude reasonably rapidly. Furthermore, this steady state value should be as close to zero as possible. The system should also have high enough gain that it exhibits satisfactory behaviour over the specified frequency range *i.e.* good dynamic accuracy and large bandwidth.

When analysing such linear control systems one begins by forming a mathematical description of the physical system in the time domain t in the form of an nth order linear differential equation relating the output of the system $C(t)$ to the input of the system $R(t)$. In order to determine the behaviour of the closed-loop system this equation must be solved. To do this the Laplace transform of the differential equation in the time domain t can be taken to give the corresponding algebraic equation in the frequency domain s. This yields polynomial expressions for the open and closed-loop transfer functions in the frequency domain. The behaviour of the closed-loop system can then be predicted by analysing these functions using various techniques.

2.5.2 Stability of a Closed-Loop Control System

Absolute Stability

The characteristic equation by which the absolute stability of a closed-loop system can be assessed is obtained by setting the denominator of the closed-loop transfer function equal to zero *i.e.*

$$1 + GH = 0 \tag{2.31}$$

The roots of the characteristic equation give the closed-loop poles (resonances) of the system where the transfer function becomes infinite. Correspondingly, the roots of the numerator of the closed-loop transfer function give the zeros (nulls) of the system where the transfer function becomes zero. The poles and zeros of the closed-loop transfer function can be real or complex. If they are complex they must appear as conjugate pairs since the polynomials describing the closed-loop transfer function are real.

By way of an example consider the closed-loop transfer function shown below:

$$X(s) = \frac{1}{(s-a)(s-b)(s-c)} \tag{2.32}$$

35

where a and b are the complex poles given by $a = (\sigma + j\omega)$, $b = (\sigma - j\omega)$ and c is a purely real pole. Mathematically, the meaning of the poles can be understood by taking the inverse Laplace transformation to give the time solution of the transfer function

$$X(t) = A\, e^{(\sigma+j\omega)t} + B\, e^{(\sigma-j\omega)t} + C\, e^{ct} \qquad (2.33)$$

where A, B and C are constants. Hence the locations of the poles in the complex s-plane $i.e.$ the magnitudes of c, σ and ω determine the time response of the closed-loop system. Note that if the imaginary parts are non-zero and the real parts are equal to zero then the response of the system is purely oscillatory. If the real parts are negative and the imaginary parts are non-zero the oscillations will decay exponentially with time. Conversely, if the real parts are positive and the imaginary parts are non-zero the oscillations will grow exponentially with time. Therefore the condition for absolute stability is that the real parts of the poles of the closed-loop transfer function are negative. If the real parts are zero the system is classified as marginally stable. Hence the exact locations of the poles on the s-plane also indicate the relative stability of the system.

Relative Stability

The relative stability of a closed-loop control system can be assessed by measuring the gain margin and phase margin of the system. In order to understand the meaning of these terms consider once more the simple control-loop shown in Figure 2.5 with closed-loop transfer function $\frac{G}{1+GH}$ and open-loop transfer function GH. It is clear that if $|GH| = 1$ and the phase of this transfer function is -180^0 then the closed-loop transfer function becomes infinite and the closed-loop system is unstable. This is undesirable and how close the system is to this condition defines the relative stability.

The 'gain margin' is defined as the magnitude of the reciprocal of GH evaluated at the phase cross-over frequency ω_π at which the phase angle ϕ of GH is -180^0 (or in other words the factor by which the gain must be increased in order to just produce instability).

The 'phase margin' is defined as 180^0 plus the phase angle ϕ of GH at the gain cross-over frequency (or unity gain frequency) ω_j at which $|GH| = 1$ (or in other words the amount of phase shift at ω_j which would just produce instability).

36

2.5.3 Some Methods of Analysis

Some methods of analyses commonly used to predict the behaviour and relative stability of closed-loop control systems are described here. The first of these, namely 'root locus analysis' can be used to determine the transient response of the system; the other methods namely 'Nyquist analysis' and 'Bode analysis' are useful for determining the frequency response of the system. These methods of analysis were applied at various stages in order to design and analyse the feedback control systems described in Chapters 3 and 4.

Root Locus Analysis

This method enables one to study the effects of varying the open-loop characteristics on the closed-loop transient response of the system. For instance, the locations of the closed-loop poles on the complex s-plane change as the open-loop gain factor is varied. A locus of these pole locations on the s-plane as a function of gain is called a root-locus. (An example of a root locus plot is given in Section 3.2.2, Figure 3.6). As the open-loop gain factor is increased from zero to infinity, the closed-loop poles originate from the open-loop poles and proceed towards the open-loop zeros.

Once the root-locus for the system is plotted a value for the gain can be chosen such that the behaviour of the closed-loop control system is satisfactory with respect to stability and transient response performance.

Nyquist Analysis

A Nyquist curve is a polar plot of the gain and phase of the open-loop transfer function *GH*. A system is defined to be stable if the Nyquist curve does not encircle the (-1,0) point ('Nyquist Stability Criterion'). To illustrate this consider the Nyquist curves for the two open-loop transfer functions shown in Figure 2.6. The open-loop transfer function represented by the dashed curve encloses the point (-1,0) so there exist roots of the characteristic equation (denominator of the closed-loop transfer function) with positive
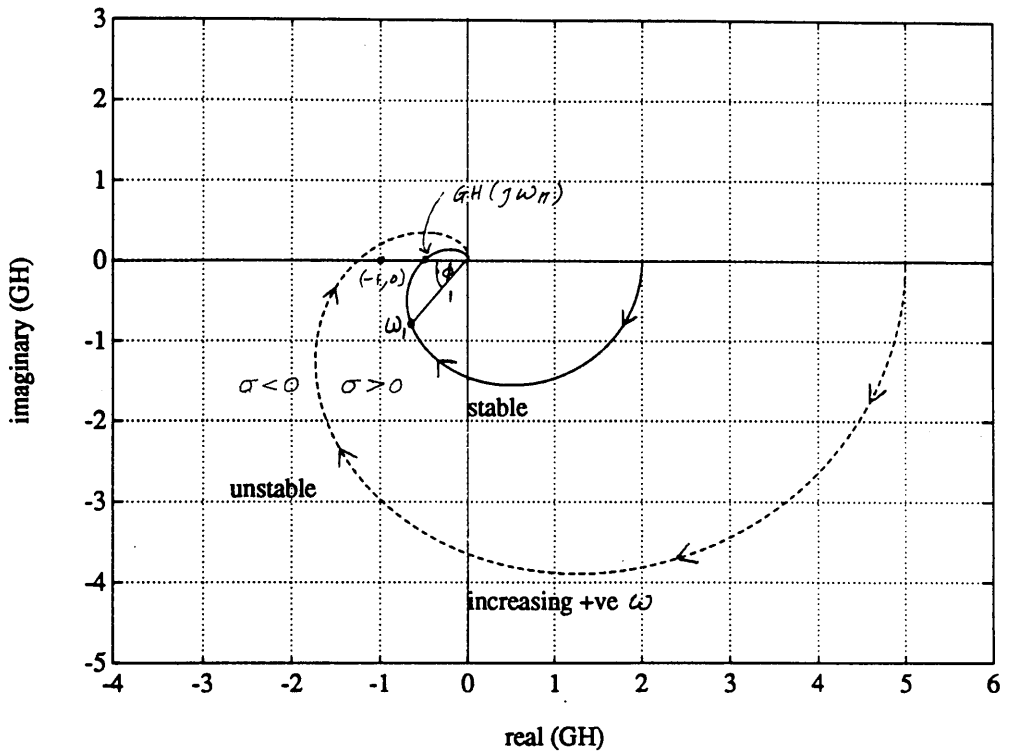
Figure 2.6 **Examples of Nyquist plots (polar plots of the gain and phase of the open-loop transfer function GH). The point (-1,0) indicates a unity gain at a phase shift of -180 ^{o}. The open-loop transfer function represented by the dashed curve encloses the po _____ (-1,0) and hence the system is unstable (regions to the right hand side of the +ve ω curve plotted correspond to $\sigma > 0$). The system represented by the solid curve is stable since it does not enclose the point (-1,0) (regions to the left hand side of the +ve ω curve plotted correspond to $\sigma < 0$). The relative stability of this system can be assessed by measuring the gain and phase margins. The gain margin is the reciprocal of GH evaluated at the phase cross-over frequency ω_π at which the phase angle ϕ of GH is -180 ^{o}. The phase margin is defined as 180 ^{o} plus the phase angle ϕ of GH at the unity gain frequency ω_1.**

real parts and the system is therefore unstable. In contrast the system represented by the solid curve is stable since the curve does not enclose the point (-1,0). The relative stability can be assessed by measuring the gain and phase margins as indicated in Figure 2.6.

Bode Analysis

Bode plots are complementary graphs of the magnitude of *GH* against frequency and the phase of *GH* against frequency. The phase shift and the rate of change of gain of a transfer function are usually interdependent. A slope of -6dB/octave on the Bode magnitude plot indicates a phase lag of 90^0. A slope of -12dB/octave indicates a phase lag of 180^0. Thus for the system to be stable, the magnitude of the slope of the Bode magnitude curve must not exceed -12dB/octave at the unity gain frequency ω_1. The relative stability can be assessed by measuring the gain and phase margins from these plots. Examples of a Bode magnitude and phase plots are shown in Section 4.3, Figures 4.6 & 4.7.

2.6 Position Control of a Test Mass Suspended as a Simple Pendulum

As mentioned in Section 2.4 axial control of the suspended test masses forming the cavities in a laser interferometric gravitational wave detector must be provided in order to keep the cavities on resonance with the laser light. Furthermore, the relative lengths of the two cavities must also be stabilised in order to operate the detector on a null interference fringe.

Preliminary investigations into the axial position control and electronic damping of a suspended test mass by the application of negative feedback are presented in this section. To achieve the required isolation level it is intended to use double pendulum suspensions for the test masses in the 3km gravitational wave detector. However for the purpose of these initial investigations, the test mass to be controlled here was suspended as a simple pendulum. The control and damping of double pendulum suspension systems by the application of feedback is discussed in Chapters 3 and 4.

2.6.1 Components of the Position Sensing and Feedback Control System

Position Sensing

The position of the test mass to be controlled was sensed with respect to a reference point using the Michelson interferometer arrangement shown in Figure 2.7. The reference point used here was a reference mirror mounted on the ground. However in a gravitational wave detector the reference point would be another suspended test mass/mirror which is isolated from ground vibrations.
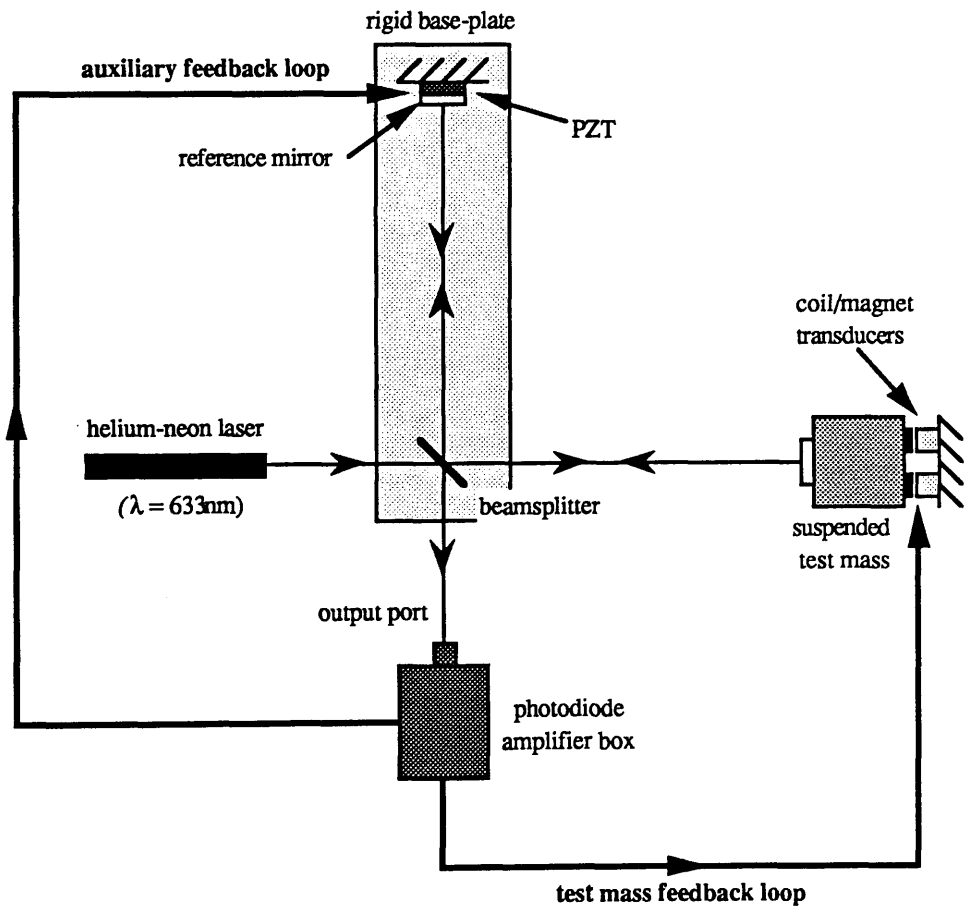
Figure 2.7 Michelson interferometer position sensing and feedback control system.

A mirror was mounted on the front face of the test mass and in conjunction with the beamsplitter (which would also be seismically isolated in a laser interferometric gravitational wave detector) this formed one arm of the Michelson interferometer. The reference mirror and the beamsplitter formed the second arm of the interferometer. Note that since these two components were mounted on a rigid base-plate, the length of this arm was essentially unaffected by ground vibrations.

By illuminating the interferometer with helium-neon laser light and detecting the fringe signal of the interfered beams at the output port, any changes in the relative lengths of the interferometer arms could be monitored.

Test Mass Feedback Loop

A photodiode was used to detect the fringe intensity signal on the output of the interferometer and convert it to a voltage signal. This signal could then be suitably amplified and filtered and fed to coil/magnet transducers acting between the suspended test mass and the ground in such a way as to minimise the changes in the relative lengths of the two arms (see Figure 2.7).

Note that in a gravitational wave detector the feedback coils acting on the test mass would be seismically isolated in order to avoid electromagnetic coupling of ground motions directly to the test mass. However for the preliminary investigations into feedback position control presented here it seemed sensible to avoid suspending the feedback coils at this early stage since this would introduce further complexity to the control loop. Test mass feedback control systems incorporating feedback coils mounted on a suspended reaction mass are discussed in Chapters 3 and 4.

Auxiliary Feedback Loop (PZT)

A second feedback loop was introduced to the system by placing a PZT (piezo-electric transducer) between the reference mirror and its ground based mount. This was a useful addition to the system for various reasons. In its pre-locked state, the low frequency motions of the freely swinging test mass with respect to the ground-borne reference mirror would be relatively large (a few microns perhaps) and there would be a high rate of fringe passage observed on the output of the interferometer. If an amplified voltage signal proportional to the detected fringe intensity signal was fed back to the PZT in such a way as to make the reference mirror follow the large low-frequency motions of the test mass, then this would effectively slow down the rate of fringe passage. This would then

make it much easier for the test mass feedback loop to initially acquire lock and having done so the gain in the auxiliary loop could then be turned down if desired.

Another advantage of having the PZT present in the system was that it provided a means for introducing displacement noise of known amplitude to the reference mirror, making it possible to measure the open-loop gain in the test mass feedback loop. The method used for this is described in more detail in the next section.

2.6.2 Behaviour of the Two-Loop System

The loop diagram representing the two-loop system is shown in Figure 2.8. Note that all displacements shown here are measured with respect to an arbitrary reference point.
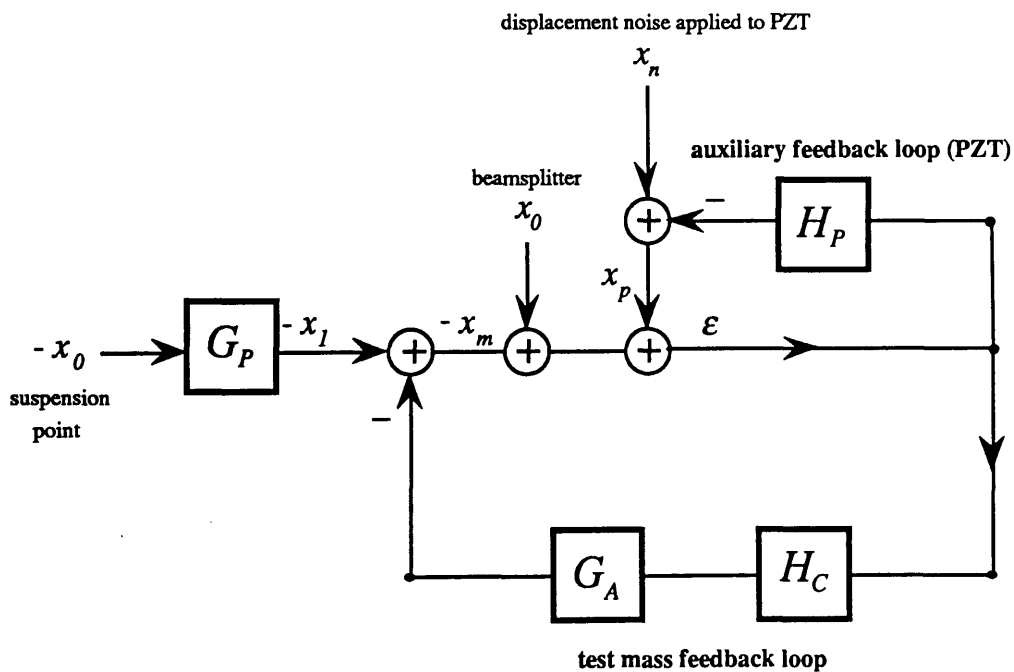
Figure 2.8 Loop diagram representation of the two-loop control system (where the symbols have the definition given in the text).

The symbols used in Figure 2.8 have the definitions given below:

x_0 = the displacement of the beamsplitter / suspension point due to ground noise

41

x_1 = the resulting displacement of the test mass due to ground noise x_0 at the pendulum suspension point

x_m = the residual displacement of the test mass with the test mass feedback loop closed

x_n = the displacement noise introduced to the reference mirror by applying a voltage signal across the PZT

x_p = the residual displacement of the reference mirror with the auxiliary feedback loop closed

ε = the error point signal with the loops closed

    = the 'residual locked fringe signal'

    = $x_p - x_m + x_0$

(note that with the feedback loops open this becomes $\varepsilon = x_n - x_1 + x_0$)

G_p = the passive transfer function for the simple pendulum of resonant angular frequency ω_0, assuming that it has negligible natural damping (equation (2.6))

$$G_p = \frac{x_1}{x_0} = \frac{\omega_0^2}{s^2 + \omega_0^2}$$

H_C = the transfer function for the conversion of the detected fringe signal ε in terms of displacement, to the acceleration produced by the coil/magnet feedback transducers. The frequency dependence of this function is determined by the form of the electronics used for amplification/filtering. Note also that this function has the dimensions of sec^{-2}.

G_A = the transfer function for the conversion of the acceleration produced by the coil/magnet feedback transducers to the resulting test mass displacement *i.e.*

$$G_A = \frac{1}{s^2 + \omega_0^2} \qquad (2.34)$$

Note that this function has dimensions of sec^2.

and

H_p = the transfer function for the conversion of the detected fringe signal ε in

42

terms of displacement, to the displacement of the reference mirror produced by the PZT. The frequency dependence of this function depends on the form of the electronics used for amplification/filtering.

Consider the situation where the amplitude of motion of the beamsplitter and the test mass produced by ground noise x_0 is negligible compared to the amplitude of motion of the reference mirror due to an applied noise signal x_n. The loop diagram then simplifies to that shown in Figure 2.9.
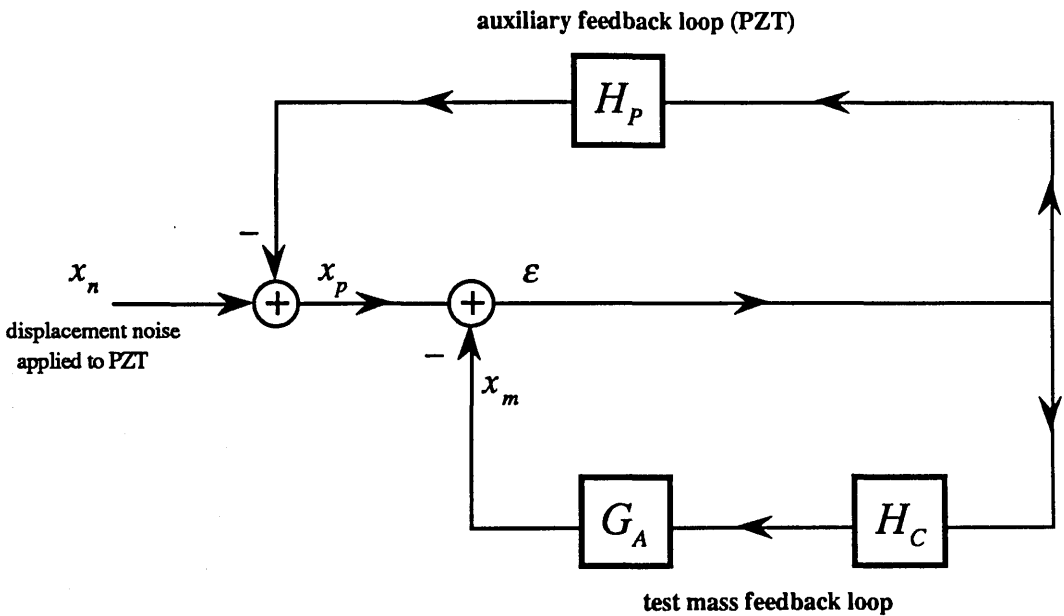
Figure 2.9 *Simplified loop diagram representation of the two-loop control system (where the symbols have the definitions given in the text).*

The error point signal ε for this closed-loop system will now be given by $\varepsilon = x_p - x_m$. On analysing this loop diagram the closed-loop transfer function can be derived (see Section 2.5.1):

$$closed\text{-}loop\ transfer\ function = \frac{\varepsilon}{x_n} = \frac{1}{1 + H_P + H_C G_A} \qquad (2.35)$$

Substituting for G_A gives the closed-loop transfer function in terms of the feedback

43

transfer functions H_C and H_P

$$\frac{\varepsilon}{x_n} = \frac{s^2 + \omega_0^2}{s^2(1 + H_P) + \left[H_C + (1 + H_P)\omega_0^2\right]} \tag{2.36}$$

In order to investigate the behaviour of the test mass feedback loop, it is desirable to reduce the gain in the auxiliary feedback loop to as low a setting as possible after the test mass feedback loop has acquired lock. (Also in a gravitational wave detector any equivalent auxiliary loop used to ease the acquisition of lock of the main feedback loop might introduce noise to the test mass, degrading the detector sensitivity.) Under this condition ($H_P = 0$ and $x_p = x_n$) the closed-loop transfer function simplifies to:

$$\frac{\varepsilon}{x_n} = \frac{s^2 + \omega_0^2}{s^2 + \left(H_C + \omega_0^2\right)} \tag{2.37}$$

From this equation one can see that the application of negative feedback to the test mass in this way forces the natural resonance of the pendulum to a higher frequency given by $\omega = \sqrt{H_C + \omega_0^2}$.

The open-loop transfer function (open-loop gain) of the test mass feedback loop $H_C G_A$ is given by (refer to Section 2.5.1):

$$H_C G_A = \frac{H_C}{s^2 + \omega_0^2} \tag{2.38}$$

By setting $|H_C G_A| = 1$ in this equation one can see that the unity gain frequency of the feedback loop is at $\omega = \sqrt{H_C - \omega_0^2}$. The relative motion of the test mass and the reference mirror is reduced by the application of feedback up to this frequency. Note that the unity gain frequency is approximately equal to the new resonant frequency of the pendulum if $H_C \gg \omega_0^2$.

As well as being forced to a higher frequency, the new resonance of the pendulum can also be electronically damped by the application of feedback. This can be achieved by using differentiation in the test mass feedback transfer function *i.e.* if H_C has the form $H_C = H_{C0}(1 + \tau_c s)$. Here τ_c is the time constant of the differentiator. The corner frequency f_c for this differentiation is related to τ_c by:

$$f_c = \frac{1}{2\pi\tau_c} \qquad (2.39)$$

The closed-loop transfer function then becomes

$$\frac{\varepsilon}{x_p} = \frac{1}{1 + H_C G_A} = \frac{s^2 + \omega_0^2}{s^2 + H_{C0}\, \tau_c\, s + (H_{C0} + \omega_0^2)}. \qquad (2.40)$$

The damping factor γ for the pendulum is determined according to the relationship $\gamma = \tau_c H_{C0}$. Thus the Q value of the new pendulum resonance can be controlled by varying the size of the test mass feedback gain H_{C0} and the time constant τ_c according to the relationship:

$$Q = \frac{1}{\tau_c \sqrt{H_{C0}}}. \qquad (2.41)$$

(under the condition $H_{C0} \gg \omega_0^2$).

Note that when differentiation is used to damp the pendulum resonance in this way, the unity gain frequency of the feedback loop will increase. For instance, with feedback of the form $H_C = H_{C0}(1 + \tau_c s)$ where τ_c is chosen to achieve critical damping ($Q=0.5$), it can be shown that the unity gain frequency will occur at $\omega = \sqrt{(2+\sqrt{5})H_{C0}}$ (under the condition $H_{C0} \gg \omega_0^2$).

It is useful to know the value of the unity gain frequency of the test mass feedback loop since it indicates the bandwidth over which the position of the test mass is being controlled effectively. Referring to Figure 2.9, the open-loop gain of the test mass feedback loop $H_C G_A$ as a function of frequency can be measured by studying the behaviour of the closed-loop system since

$$\frac{x_p}{\varepsilon} = 1 + H_C G_A \qquad (2.42)$$

Note that this relationship holds whether the auxiliary feedback loop is closed or not since it is the residual displacement of the reference mirror x_p which is observed.

Figure 2.10 shows an example of an experimentally measured loop gain curve of $H_C G_A$ versus frequency. The feedback amplifier circuits used in the two loops are shown in Figure 2.11. Note that the differentiation time constant τ_c was chosen to be small here so that the electronic damping of the pendulum would be small $i.e.$ $H_C \sim H_{C0}$.
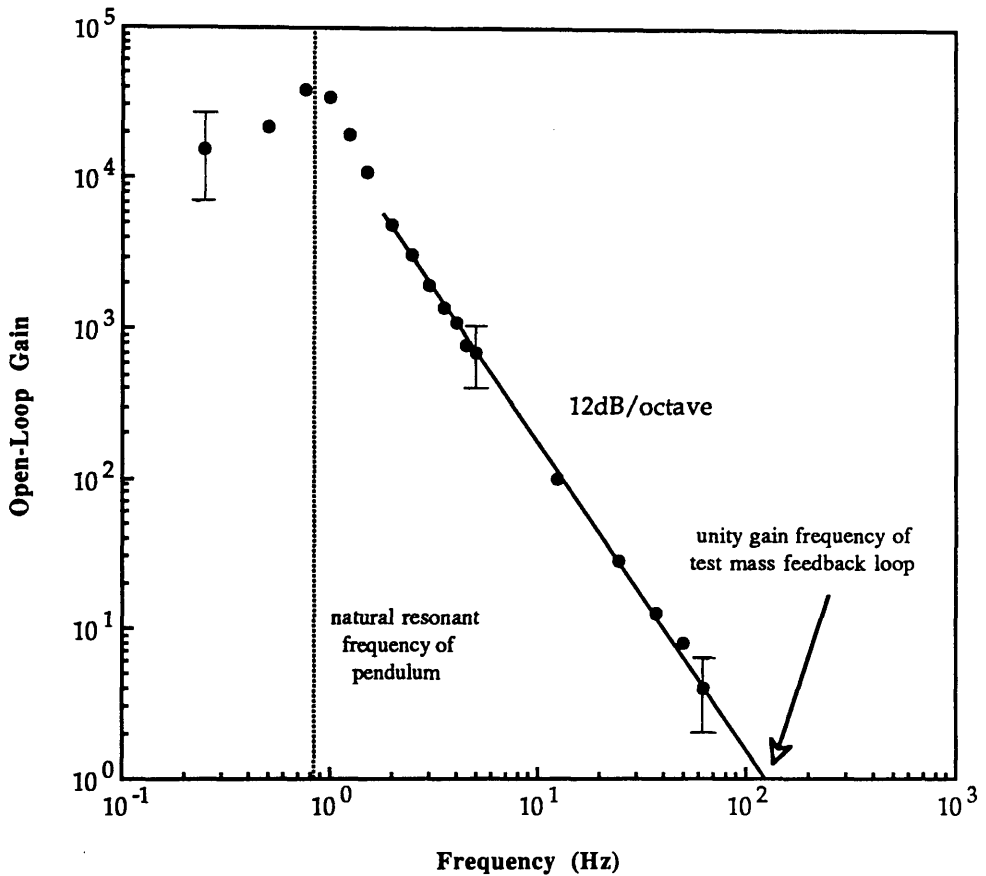
Figure 2.10 *Open-loop gain of the test mass feedback loop* $(H_C G_A)$ *as a function of frequency (typical error bars are shown).The measurements were made using white noise as the test signal applied to the PZT.*

It was hoped that this would enable an observation to be made of the the new resonance peak in the residual locked fringe signal spectrum. It was believed that stability would be maintained in the closed-loop by the existence of some small degree of natural damping in the pendulum.

The data shown in Figure 2.10 were obtained using the following method. Firstly the fringe intensity signal was D.C. biased to be symmetrical about zero volts. This ensured that the error point signal of the locked system would contain information on the
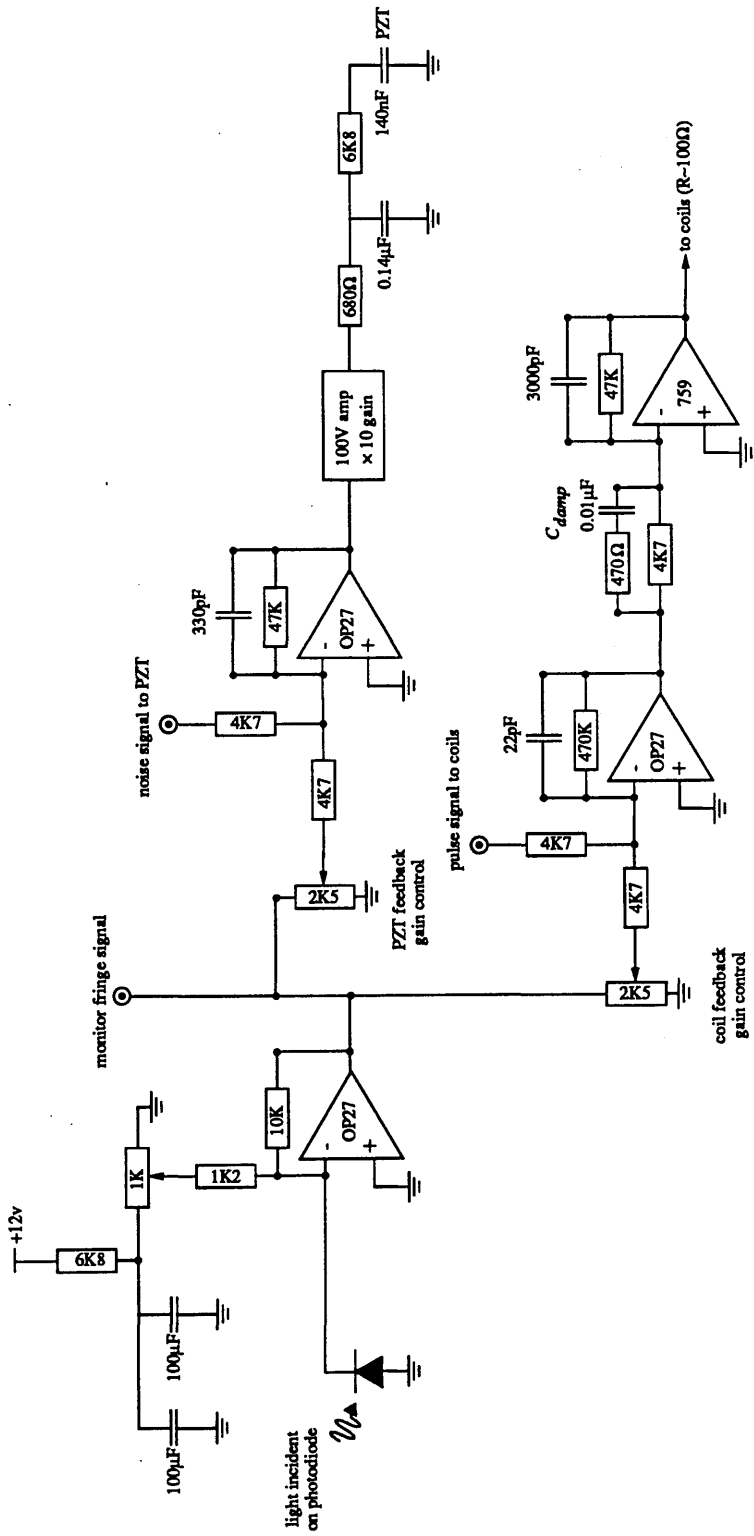
Figure 2.11 The circuit for the PZT and coil feedback loops.

relative direction of movement of the reference mirror and the test mass. The gain in the auxiliary loop was then increased to slow down the rate of fringe passage. The test mass feedback loop was then locked to the side of a fringe and the gain in the auxiliary loop was reduced to as low a value as possible without the system losing lock. A displacement noise signal x_n was introduced to the closed-loop system by applying a test signal ('white' voltage signal) to the PZT (see Figures 2.9 and 2.11). The magnitudes of the residual displacement signal x_p at the PZT and the 'residual locked fringe signal' ε were then observed over a range of frequencies (see Figure 2.9).

The residual locked fringe voltage signal was converted to a relative displacement ε using the relationship:

$$\frac{\delta x}{\delta V} = \left(\frac{2}{\Pi} \times \frac{\lambda}{4} \times \frac{1}{F_{vpp}} \right) \frac{m}{v} \qquad (2.43)$$

where F_{vpp} is the fringe peak to peak voltage amplitude before locking (see Figure 2.12).
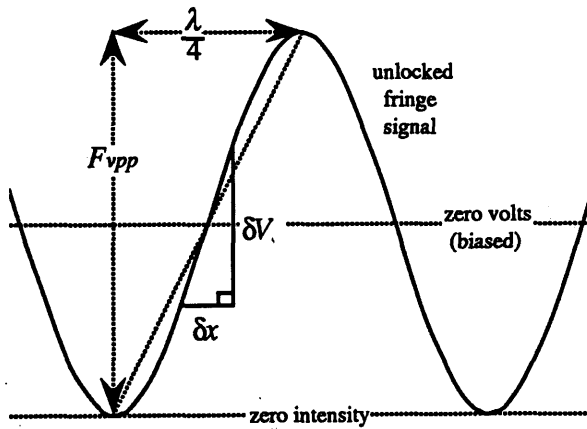
Figure 2.12   Conversion of the fringe intensity signal to a relative displacement signal when locking to the side of a fringe. The symbols used have the definitions given in the text.

The residual voltage signal observed at the PZT was converted to a residual displacement signal x_p using the calibration factor for the PZT which was measured to be $\sim 3.9 \times 10^{-7}$ mV^{-1}.

The loop gain curve shown in Figure 2.10 has the form predicted by equation (2.38) falling at 12dB/octave at frequencies above the natural pendulum frequency f_0 which is seen here as a peak at ~0.9Hz. By extrapolation the unity gain frequency of the test mass feedback loop is seen here to be at $\omega = \sqrt{H_{C0} - \omega_0^2}$ ~110Hz. This yields a value for H_{C0} of ~ 4.8×10^5 rads^{-2}. Using equation (2.38) and substituting for H_{C0}, the gain at low frequencies where $s \ll \omega_0^2$ was calculated to be ~1.5×10^4. This agrees reasonably well with the value extrapolated from the curve within the limits of the errors.

Notice however that the open-loop gain curve appears to pass through the unity gain point with a gradient of approximately 12dB/octave indicating that the pendulum had very little natural damping. According to the Nyquist Stability Criterion (refer to Section 2.5.2) the closed-loop system should therefore be verging on instability.

However when these measurements of open-loop gain were made the auxiliary loop had non-zero gain. The closed-loop response of the system therefore depends on the behaviour of both the feedback loops according to equation (2.36). From the circuit diagram shown in Figure 2.11, the feedback transfer function for the auxiliary loop H_P involved an integration with a relatively large time constant τ_p i.e. had the form:

$$H_P = \frac{H_{P0}}{(1 + \tau_p s)} \tag{2.44}$$

with the corner frequency f_c for the integration (roll-off) of the auxiliary feedback signal given by

$$f_c = \frac{1}{2\pi\tau_p}. \tag{2.45}$$

On substituting equation (2.44) into equation (2.36) one obtains the more explicit version of the closed-loop transfer function shown below

$$\frac{\varepsilon}{x_n} = \frac{\tau_p s^3 + s^2 + \tau_p \omega_0^2 s + \omega_0^2}{\tau_p s^3 + (1 + H_{P0})s^2 + (\tau_p \omega_0^2 + \tau_p H_{C0})s + (\omega_0^2 + H_{P0}\omega_0^2 + H_{C0})}. \tag{2.46}$$

Recall from Section 2.5.2, equation (2.31) that the roots of the denominator (characteristic equation) give the poles or resonances of the closed-loop system.

The magnitude of H_{P0} in the auxiliary loop was calculated to be ~5.3 with

48

$\tau_p \sim 9.4 \times 10^{-4}$ s. On substituting values for the various other parameters into equation (2.46) and taking the roots, the new resonant frequency of the pendulum was calculated to be at ~44Hz with a corresponding quality factor of the pendulum of $Q \sim 5$. Hence, according to equation (2.46), the integration in the auxiliary feedback loop of time constant τ_p provides damping of the pendulum resonance.

This concept was verified experimentally by applying a stepped 10mV pulse across the feedback coils in the closed-loop state (see Figure 2.11) and observing the decaying oscillation in the residual fringe signal with a storage scope. Figure 2.13 shows an example of such an observed step response.
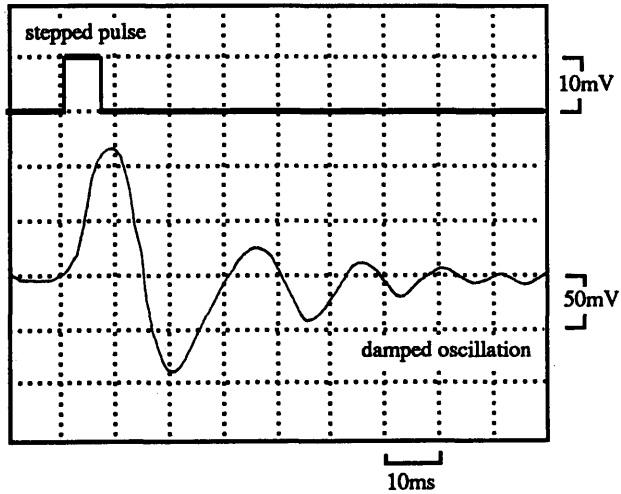
Figure 2.13 *Measured transient response of the closed two-loop system. The step function used here had an amplitude of ~10mV and a duration of ~7ms. The average frequency observed over the first two cycles is $f \sim 43Hz$, with a corresponding Q of ~4.*

In conclusion, in the absence of electronic damping (differentiation) in the test mass control loop, stability is maintained in the closed-loop by the presence of an integration in the auxiliary loop feedback transfer function. The action of the auxiliary feedback loop had the effect of reducing both the magnitude, and the Q of the new pendulum resonance as illustrated in Figure 2.13.

2.6.3 Conclusion

It has been shown here that the position of a test mass suspended as a simple pendulum of high Q can be controlled with respect to a reference point using negative feedback. In applying feedback to the test mass in this way, the natural resonant frequency of the pendulum is forced to a higher value approximately equal to the unity gain frequency of the feedback loop. The unity gain frequency indicates the bandwidth over which the feedback system is controlling the mass effectively, and this can be increased by increasing the open-loop gain of the feedback loop. The undesirably large motions of the suspended test mass at the resonant frequency of the high Q pendulum can also be electronically damped by introducing a differentiation stage of the appropriate time constant in the feedback electronics.

It was also interesting to observe here for this two-loop feedback system, that electronic damping of the high Q pendulum resonance could also be provided by introducing an integration stage with the appropriate time constant in the feedback electronics of the auxiliary loop. The action of this auxiliary feedback loop also had the effect of reducing the value of the new resonant frequency of the pendulum.

In Chapter 3 theoretical and experimental investigations into the feedback position control and damping of a test mass suspended as a double pendulum are discussed.

Chapter 3

Feedback Control and Damping of Double Pendulums

3.1 Introduction

In order to achieve the required level of isolation from seismic and mechanical noise ($T\sim 10^{-10}$ or better at 100Hz) it is proposed to use double pendulum suspensions for the test masses in the 3km detector [Hough *et. al.* 1989]. In conjunction with the five-layer vibration isolation stacks and air springs used to connect the double pendulums to the ground, it is believed that the levels of isolation achievable will be more than adequate at frequencies $\geq$ 100Hz.

As well as providing better isolation, there are other advantages in using double pendulum suspensions. As discussed in Chapter 2, the test masses of a laser interferometer must be controlled in both position and orientation. Furthermore, the natural modes of oscillation of the suspended masses must be electronically damped to avoid large motions at the various resonant frequencies. By using double pendulum suspensions, the position control of the test masses at low frequencies can be implemented by applying feedback signals to the intermediate pendulum masses. Chapter 4 discusses the analysis and implementation of such feedback control systems where the low frequency portion of the position control signal is applied to the intermediate mass, the higher frequency signals being applied to the test mass.

These low frequency feedback signals are inherently larger in amplitude than the higher frequency signals due to a combination of the fact that seismic noise is larger at low frequencies and also passive isolation is poorer. Therefore applying the large low frequency feedback signals to the intermediate mass in this way reduces the possibility of high frequency displacement noise being introduced to the test mass *via* non-linear conversion of low frequency signals in the feedback electronics or transducers. At

frequencies greater than the natural resonant frequency of the high Q lower pendulum stage, any such displacement noise at the intermediate mass will be attenuated by 12dB/octave in its transmission to the test mass.

In the 3km detector it has been proposed that the orientation of the test masses will be controlled using double-loop suspension wires for the test masses and applying suitable low frequency, narrow bandwidth feedback signals to the intermediate masses.

There are however some disadvantages associated with double pendulum suspensions as discussed in Chapter 2. The number of degrees of freedom of the system will increase by a factor of two giving rise to an increase in the number of resonances which must be electronically damped. The linear and non-linear cross-coupling of modes may be aggravated by the increase in the number of degrees of freedom. However, if care is taken in the design and construction these effects can be reduced to an acceptably low level.

In Section 2.6 it was shown that the position of a test mass suspended as a simple pendulum can be controlled by sensing the position of the mass and applying a feedback signal directly to the mass. The test mass can also be damped electronically by the feedback signal enabling a suspension of high natural Q to be used without giving rise to undesirably large motion at the new pendulum resonant frequency.

This present chapter is concerned with investigations into the position control and electronic damping of a test mass suspended as a double pendulum. Some theoretical analyses conducted on the possibilities of controlling the position of the test mass whilst damping both of the natural pendulum resonances by sensing the position of the test mass and feeding back to this mass are presented. An evaluation is made of the resulting amplitude of test mass motion at each of the pendulum resonances in order to assess their relative significance as regards the effective operation of a laser interferometric gravitational wave detector. Damping of the resonances by sensing the acceleration of, and feeding back a signal to, the intermediate mass was also investigated theoretically. The closed-loop response of the pendulum with both of these types of feedback in operation was then analysed to see if both large bandwidth position control and critical damping of the resonances could be achieved simultaneously.

Experimental results from investigations into the position control and electronic damping of a test mass suspended as a double pendulum are presented. It is shown that, to avoid coupling seismic noise to the test mass, it is necessary to isolate the feedback transducers. Finally, the results from a balanced double pendulum system incorporating

52

suspended feedback coils are described. The results presented here were then used as a basis for the design of the nested double pendulum isolation system discussed in Chapter 4.

3.2 Position Control and Damping by the Application of Feedback to the Lower Mass

It is the purpose of this section to examine theoretically the degree to which the coupled resonances of a high Q double pendulum can be electronically damped whilst controlling the position of the lower mass, by sensing the position of, and applying a feedback signal to, the lower mass. The aim here is to reduce the amplitude of motion of the lower mass (test mass in a laser interferometric detector) to an acceptable level at both of the pendulum resonant frequencies and to achieve large bandwidth position control. Large bandwidth position control is required in a laser interferometric detector to keep the Fabry-Perot cavities on resonance and to operate the detector on a null fringe (refer to Section 2.4). The implementation of electronic damping avoids any undesirably large motions of the test mass which might reduce the overall detector sensitivity or cause loss of lock.

3.2.1. The Closed-Loop System

Consider a double pendulum similar to that illustrated in Figure 2.2, Chapter 2. It is assumed here that the natural damping present in each stage of the pendulum is negligibly small (*i.e.* high Q pendulum stages, γ_1, $\gamma_2 \rightarrow 0$) since we are here concerned with the possibility of damping the pendulum exclusively by the application of feedback.

Consider the situation where the position of the lower mass m_2 is sensed relative to some arbitrary point x_3. A feedback force of the form $F_2=m_2k(x_3-x_2)$ can then be applied to the lower mass to hold the position of the mass fixed relative to the reference point x_3. Here k is the transfer function for the conversion of the sensed displacement to the feedback acceleration produced by the coils. The frequency dependence of this function depends on the form of the electronics used for amplification and filtering.

If one assumes that the reference point x_3 is absolutely stationary at all frequencies (for instance, the reference point is the fixed stars, or a very highly isolated test mass), then one can set $x_3=0$. The equations of motion for the two pendulum masses can then

be derived in a similar way to those in Section 2.3.2, yielding the transfer function from motion of the top of the pendulum x_0, to motion of the test mass x_2, as a function of s, in the closed-loop state *i.e.*

$$\frac{x_2}{x_0} = \frac{M\omega_1^2\omega_2^2}{m_1s^4 + \left[M(\omega_1^2 + \omega_2^2) + km_1\right]s^2 + k\left[M\omega_1^2 + m_2\omega_2^2\right] + M\omega_1^2\omega_2^2}. \tag{3.1}$$

Here M is the total mass of the system *i.e.* $M = m_1 + m_2$, with ω_1 and ω_2 representing the natural angular resonant frequencies of the separate stages of the pendulum. Equation (3.1) is similar in form to equation (2.16) if one sets $\gamma_1 = \gamma_2 = 0$; note however that equation (3.1) also involves the feedback transfer function k. The loop diagram representation of this closed-loop system is shown in Figure 3.1.
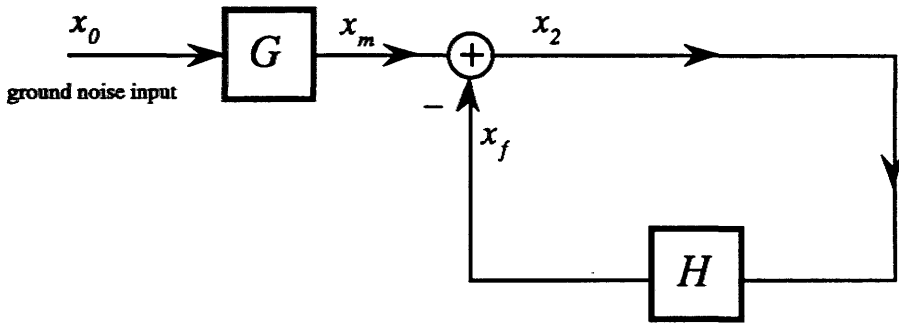
Figure 3.1 Loop diagram for the position control and electronic damping of a double pendulum via the lower mass.

In Figure 3.1 the symbols have the definitions given below, where all displacements are measured with respect to an arbitrary reference point:

x_0 = the displacement of the suspension point due to ground noise

x_m = the displacement of the lower mass due to ground noise at the suspension point

x_f = the displacement of the lower mass due to the applied feedback signal

x_2 = the residual displacement of the lower mass with the feedback loop closed

G = the passive transfer function for the double pendulum (see equation (2.17)):

$$\frac{x_m}{x_0} = \frac{M\omega_1^2\omega_2^2}{m_1s^4 + M(\omega_1^2 + \omega_2^2)s^2 + M\omega_1^2\omega_2^2} \tag{3.2}$$

54

H = the transfer function for the conversion of the detected displacement x_2 to the resulting displacement of the lower mass due to the applied feedback signal. The precise form of this will depend on the form of the feedback electronics used for amplification and filtering *i.e.* the form of k used. Note that H is the open–loop transfer function.

On analysing this loop one can see that the closed-loop transfer function for this system is in fact given by $\frac{G}{1+H}$ which is equal to equation (3.1). From this, and equation (3.2) which describes G, the passive pendulum transfer function, the explicit version of the open-loop transfer function H can be obtained, as shown in equation (3.3).

$$H = \frac{k\,m_1 s^2 + k\,(M\omega_1^2 + m_2\omega_2^2)}{m_1 s^4 + M(\omega_1^2 + \omega_2^2)s^2 + M\omega_1^2\omega_2^2} \tag{3.3}$$

In conjunction, the closed-loop transfer function (equation (3.1)) and the open-loop transfer function (equation (3.3)) contain all of the information necessary for quantitatively assessing the behaviour of the closed-loop system for various types of feedback transfer function k.

Recall that the root-locus method described in Section 2.5.3 enables the direct observation of the pole positions of the closed-loop transfer function of a system on the complex s-plane, as the open-loop transfer function characteristics are varied. It is therefore useful to employ this method to determine the levels of damping of the normal modes of the double pendulum for various forms of feedback transfer function k.

Firstly it is informative to determine the poles (resonances) and zeros of the open-loop system using equation (3.3). The pendulum was modelled to have identical masses ($m_1 = m_2 = 2$kg; $M = 4$kg) and identical natural resonant frequencies for each stage ($\omega_1 = \omega_2 = 6$rads[-1]). With these parameters, the open-loop system was found to have two poles (resonances) at $\omega = 4.59$rads[-1] and $\omega = 11.09$rads[-1]. The system also had one zero at $\omega = 10.39$rads[-1]. The lower resonance of the double pendulum is the mode where the masses move in phase as shown schematically in Figure 3.2. The upper resonance is also shown in Figure 3.2 and here the masses move in antiphase. Note that the frequency at which the zero occurs ($\omega = 10.39$rads[-1]), agrees exactly with that calculated by considering the dynamics of the intermediate mass when the lower mass is pinned vertically below the suspension point *i.e.* $\omega_{zero} = \sqrt{3}\,\omega_0$ (where $\omega_0 = 6$rads[-1]).

55

lower resonance

(the two masses move in phase)

upper resonance

(the two masses move in antiphase)
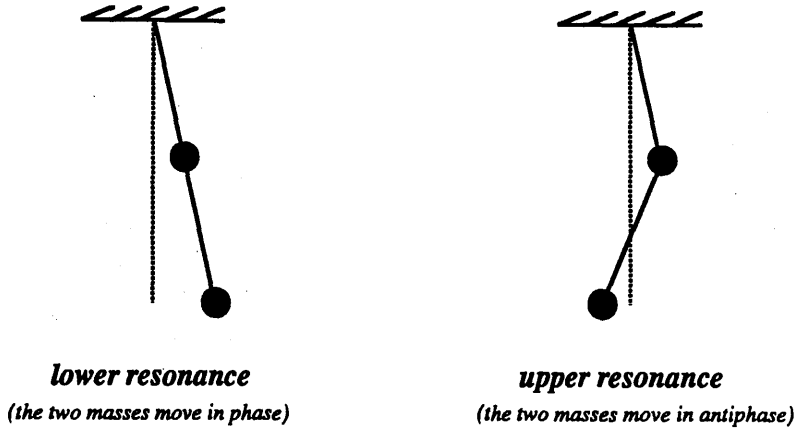
Figure 3.2 *Snapshot in time showing the two resonances of the passive double pendulum.*

As the feedback gain is increased, the closed-loop poles will originate from the open-loop poles and tend towards the open-loop zeros of the system. Therefore with feedback, one of the two new pendulum resonances will occur at a frequency of ω=10.39rads^{-1} (the frequency of the natural open-loop zero), corresponding to the situation where the lower mass is pinned below the suspension point. The second new resonance of the double pendulum will occur at a frequency governed by the feedback transfer function gain and phase characteristics.

It was shown in Section 2.6 that the resonance of a single pendulum can be electronically damped by using differentiation in the position control feedback electronics (equations (2.40) & (2.41)). In a similar way the coupled resonances of a double pendulum can be damped to varying degrees by the use of differentiation.

3.2.2 Levels of Damping Achievable

Consider the case where the transfer function k involves both spring (for position control) and damping terms *i.e.* $k = k_0(1 + s\tau_1)$, (refer to Section 2.6). When the feedback involves differentiation in this way, the closed-loop transfer function (equation (3.1)) can be re-written as:

$$\frac{x_2}{x_0} = \frac{(1+\alpha_m)\omega_1^2\omega_2^2}{(s^2 + \gamma_L s + \omega_L^2)(s^2 + \gamma_U s + \omega_U^2)} \qquad (3.4)$$

56

where α_m is the mass ratio m_2/m_1. Here ω_L and ω_U are the angular frequencies for the new lower and upper resonances (poles), with corresponding damping factors γ_L and γ_U, respectively. It can be shown that the quality factor Q for either of these resonances $(\sigma_i \pm j\omega_i)$ can be determined from the root-locus plot using the relationship $\tan\theta = \sqrt{(4Q^2 - 1)}$ where $\tan\theta = \omega_i/\sigma_i$. Thus as a pole locus tends towards the real axis it becomes more heavily damped. Critical damping occurs when the complex conjugate roots of a pole intersect the real axis.

Using the commercial package MATLAB, the poles of the closed-loop transfer function (equation (3.1)) were plotted for various values of τ_1 as a function of gain k_0. Figure 3.3 shows the loci of the positive roots obtained for some selected cases. The corresponding negative roots have loci which are the mirror image of these about the real axis.

These loci plots show that one of the natural resonances of the pendulum is forced to a higher frequency by the application of feedback and that this can be critically damped if the correct combination of k_0 and τ_1 is chosen (this resonance will be referred to as the new upper resonance here). Recall from Section 2.6.2 that the unity gain frequency of the feedback loop (which indicates the bandwidth of control) is related to the gain k_0 by $\omega \sim \sqrt{(2+\sqrt{5})k_0}$ when this new upper resonance is damped critically. Figure 3.4 is an enlargement of the first plot showing more clearly the loci for the new lower resonance of the system. Note that in using this simple type of feedback transfer function, the new lower resonance can never be critically damped. This is a consequence of the presence of the natural open-loop zero at $\omega = 10.39$rads^{-1}. One of the natural poles must ultimately tend towards this zero with increasing gain.

However, for relatively low values of gain, the Q factor of the new lower resonance can be set to an optimally low value. Note also that by using the relatively large gain required to critically damp the new upper resonance, the Q of the new lower resonance becomes higher than its minimum value. From Figure 3.3, one can see that the new upper resonance originates from either the natural lower resonance or the natural upper resonance depending on the frequency at which the differentiation begins *i.e.* on the value of τ_1 chosen. Figure 3.5 is a table illustrating some of the Q values achieved for both resonances as a function of τ_1 and k_0.
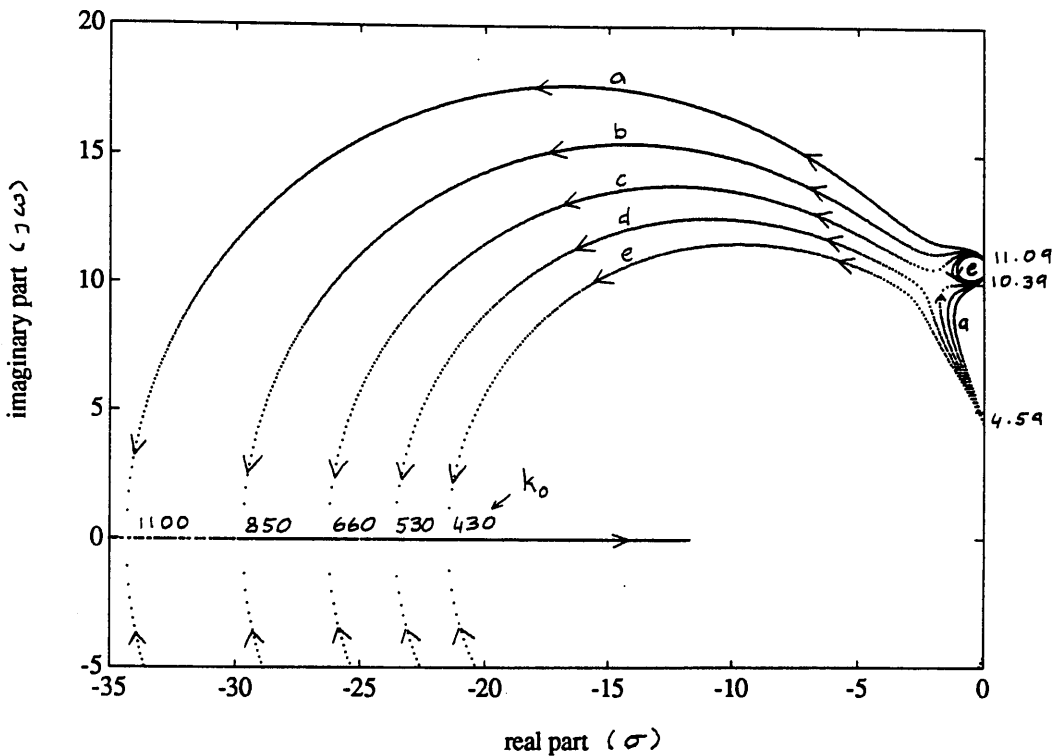
Figure 3.3 *The loci of the two positive roots of equation (3.1) with a feedback transfer function of the form $k=k_0(1+s\tau_1)$. The roots are plotted as a function of gain k_0 and time constant τ_1. The pairs of loci are labelled a,b,c,d and e corresponding to $\tau_1= 0.06s, 0.07s, 0.08s, 0.09s$ and $0.1s$. The arrows show the direction of increasing gain k_0. One of the poles tends towards the zero at $\omega \sim 10.39 rads^{-1}$ whilst the other tends towards the zero at $-1/\tau_1$. The origin of the pole which tends towards this zero depends on the τ_1 value chosen. The k_0 value at which the new upper resonance becomes critically damped is shown.*
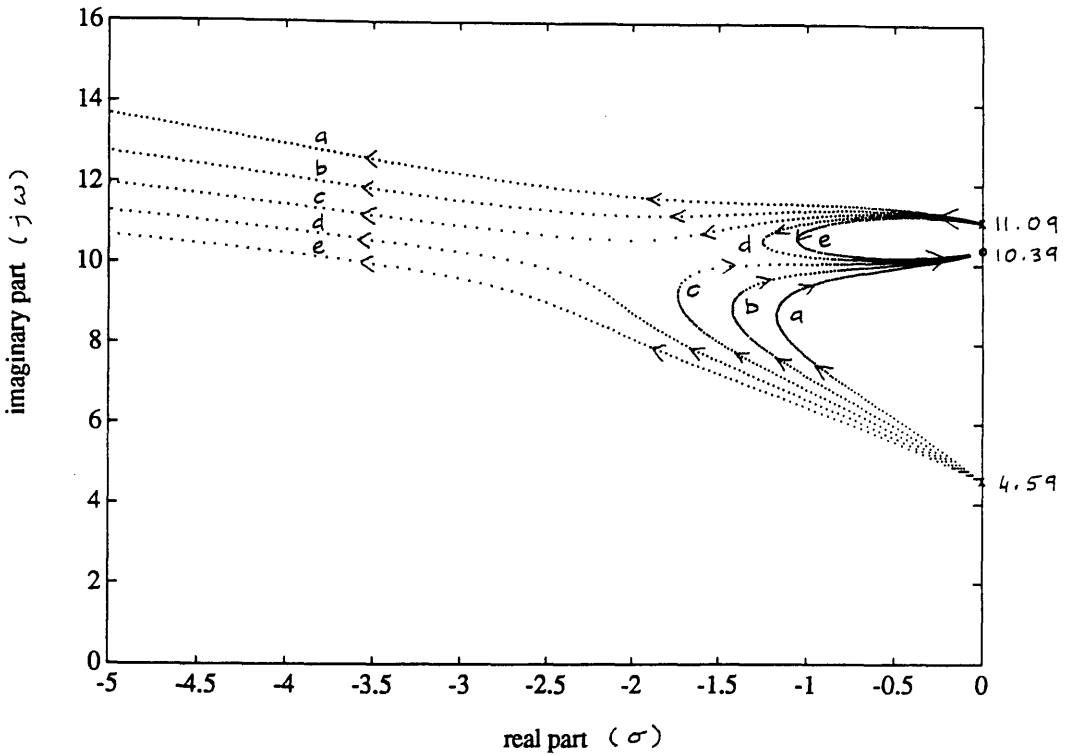
Figure 3.4   *Enlargement of Figure 3.3 showing more clearly the loci for the new lower resonance. The roots are plotted as a function of gain k_0 and time constant τ_1. The arrows show the direction of increasing gain k_0. The origin of the pole which tends towards the zero at $10.39 rads^{-1}$ depends on the value of τ_1 chosen. The pairs of loci are labelled* a,b,c,d *and* e *corresponding to* $\tau_1 =$ 0.06s, 0.07s, 0.08s, 0.09s *and* 0.1s.

τ_I (sec)	$\sim k_0$ (sec^{-2})	$\sim Q$ lower	$\sim Q$ upper
0.005	60	46	94
	1.6×10^5	2.6×10^5	0.5
0.01	60	23	47
	4.0×10^4	3.2×10^4	0.5
0.06	60	4	8
	1.1×10^3	190	0.5
0.08	70	3	5
	660	97	0.5
0.09	80	4	2
	530	75	0.5
0.2	40	9	1
	130	22	0.5

Figure 3.5 Table showing the Q values achieved for both pendulum resonances with feedback transfer function $k = k_0(1 + s\tau_I)$ for different values of time constant τ_I and gain factor k_0. For a given τ_I the first k_0 value stated is that necessary to optimally damp the new lower pendulum resonance; the second stated is that necessary to critically damp the new upper pendulum resonance. (Some of the cases considered here are illustrated in Figures 3.3 and 3.4).

From this table one can see that when the new lower resonance is optimally damped by choosing a relatively low gain factor k_0 (resulting in relatively narrow bandwidth position control of the mass), the corresponding Q factor of the new upper resonance is reduced to a comparable level *e.g.* with $\tau_I = 0.09$ s and $k_0 \sim 80$ s^{-2} then $Q_L \sim 4$ and $Q_U \sim 2$.

However one would like to force the new upper resonance to as high a frequency as possible (using high gain feedback), ensuring large bandwidth position control of the lower mass. Furthermore, it would be desirable to critically damp both new pendulum resonances simultaneously.

With this objective various other forms of feedback transfer function k were investigated in a similar way to that described above. These were designed to have a larger low frequency phase lead than for the above example, without increasing the gain and phase lead at higher frequency. The aim was to achieve better damping of the lower resonance whilst critically damping the upper resonance and forcing it to a relatively high

frequency. This was attempted using transfer functions involving both differentiation and integration terms of the form $k = k_0.\frac{(1 + s\tau_1)(1 + s\tau_2)}{(1 + s\tau_3)}$ (where the τ's are time constants).

For instance, a root-locus plot for the feedback transfer function $k = k_0.\frac{(1 + s\tau_1)(1 + s\tau_2)}{(1 + s\tau_3)}$ is shown in Figure 3.6. This plot shows the locus of the upper pole as a function of gain k_0 where the time constants were $\tau_1 = \frac{1}{20}$ s; $\tau_2 = \frac{1}{150}$ s and $\tau_3 = \frac{1}{100}$ s. The locus of the lower pole can't be seen on this plot due to the limited resolution, however it tends towards the open-loop zero at $\omega = 10.39$ rads^{-1} as the gain is increased. Figure 3.7 is a table showing the Q values obtained for each resonance as a function of gain k_0. The corresponding upper pole positions for each gain k_0 considered are shown on Figure 3.6.

From Figure 3.7 one can see that with a relatively low gain of $k_0 \sim 60$ s^{-2}, the Q of the lower resonance can be reduced to $Q_L \sim 5$ with the upper at $Q_U \sim 10$. Using a higher gain of $k_0 \sim 1.2 \times 10^4$ s^{-2} (giving a unity gain frequency of $\omega \sim 420$ rads^{-1} (computed using MATLAB)) the new upper resonance becomes critically damped. The corresponding Q of the lower resonance with this particular gain is $Q_L \sim 2.6 \times 10^3$. Compare this to the previous form of feedback described in Figure 3.5 where a unity gain frequency of $\omega \sim \sqrt{(2 + \sqrt{5})k_0} \sim 410$ rads^{-1} was achieved when $\tau_1 = 0.01$s and $k_0 \sim 4.0 \times 10^4$ s^{-2}. This gave a Q for the lower resonance of $Q_L \sim 3.2 \times 10^4$. Hence this second design of feedback transfer function reduces the Q of the lower resonance by more than a factor of 10, without compromising the bandwidth of the position control signal.

It was not possible to derive any form of feedback transfer function of this simple form (which introduced real open-loop zeros to the system), which achieved critical damping of both of the pendulum resonances simultaneously.

3.2.3 Amplitude of Motion of the Lower Mass at the New Resonant Frequencies

In the previous section it was shown that it is possible to damp both of the resonances of a double pendulum to a relatively high degree by sensing the position of, and applying a relatively low gain (narrow bandwidth) feedback signal to the lower mass. This gave Q's of a few for each resonance. Using higher gain (larger bandwidth feedback) it was shown that it was possible to critically damp the new upper resonance which was forced to a higher frequency by the feedback. However, increasing the bandwidth in this way

59
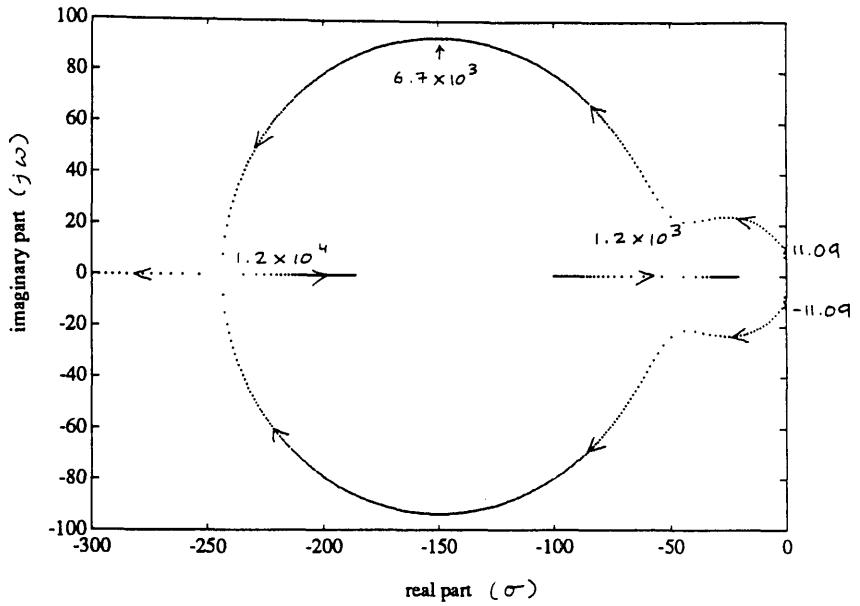
Figure 3.6 *The loci of the roots corresponding to the new upper pole (resonance) of equation (3.1) with a feedback transfer function of the form* $k = k_0 \cdot \frac{(1+s\tau_1)(1+s\tau_2)}{(1+s\tau_3)}$. *The time constants have the values* $\tau_1 = \frac{1}{20}$ s, $\tau_2 = \frac{1}{150}$ s *and* $\tau_3 = \frac{1}{100}$ s. *The arrows show the direction of increasing gain* k_0. *A few* k_0 *values are labelled for reference.*

k_0 (sec^{-2})	Q lower	Q upper
1.2×10^4	2600	0.5
6700	1400	0.6
1200	240	0.6
60	5	10

Figure 3.7 *Table showing the Q values achieved for both pendulum resonances with feedback transfer function* $k = k_0 \cdot \frac{(1 + s\tau_1)(1 + s\tau_2)}{(1 + s\tau_3)}$ *for different gain factors* k_0. *Here* $\tau_1 = \frac{1}{20}$ s, $\tau_2 = \frac{1}{150}$ s *and* $\tau_3 = \frac{1}{100}$ s. *The first* k_0 *value stated is that necessary to critically damp the new upper pendulum resonance; the fourth stated is that necessary to optimally damp the new lower pendulum resonance. The upper pole positions for the gain values shown are indicated on Figure 3.6.*

reduced the level of damping of the new lower resonance (to a Q of the order of few thousand). In order to understand the implications of these results for the operation of a gravitational radiation detector, the relative amplitude of the motion of the lower mass (test mass) must be evaluated at each of the new resonant frequencies.

It was shown in Section 2.5.2. that the transient behaviour of a closed-loop system can be determined by taking the inverse Laplace transform of the closed-loop transfer function. In order to find the time solution for the closed-loop system of Section 3.2.2, the closed-loop transfer function (as given in equation (3.4)) can be re-written in partial fraction form *i.e.*

$$\frac{x_2}{x_0} = \frac{(1+\alpha_m)\omega_1^2\omega_2^2}{(s^2 + \gamma_L s + \omega_L^2)(s^2 + \gamma_U s + \omega_U^2)} = \frac{As+B}{s^2 + \gamma_L s + \omega_L^2} + \frac{Cs+D}{s^2 + \gamma_U s + \omega_U^2} \qquad (3.5)$$

where A,B,C and D are constants. The inverse Laplace transformation of this expression is then:

$$Ae^{-\gamma_L t/2}\cos\omega_L' t + \left[\frac{B}{\omega_L'} - \frac{A\gamma_L}{2\omega_L'}\right]e^{-\gamma_L t/2}\sin\omega_L' t + Ce^{-\gamma_U t/2}\cos\omega_U' t + \left[\frac{D}{\omega_U'} - \frac{C\gamma_U}{2\omega_U'}\right]e^{-\gamma_U t/2}\sin\omega_U' t$$

$$(3.6a)$$

where,
$$\omega_L' = \omega_L \sqrt{1 - \frac{1}{4Q_L^2}} \qquad (3.6b)$$

etc.

This can be re-written as:

$$X_L\, e^{-\gamma_L t/2}\sin(\omega_L' t + \alpha_L) + X_U\, e^{-\gamma_U t/2}\sin(\omega_U' t + \alpha_U) \qquad (3.7)$$

where the amplitudes of the damped lower and upper resonances X_L and X_U are given by:

$$X_L = \left[A^2 + \left(\frac{B}{\omega_L'} - \frac{A\gamma_L}{2\omega_L'}\right)^2\right]^{1/2} \qquad (3.8)$$

and

$$X_U = \left[C^2 + \left(\frac{D}{\omega_U'} - \frac{C\gamma_U}{2\omega_U'}\right)^2\right]^{1/2} \qquad (3.9)$$

with the initial phases
$$\alpha_L = \tan^{-1}\left(\frac{A}{B}\right) \qquad (3.10)$$

and
$$\alpha_U = \tan^{-1}\left(\frac{C}{D}\right) \qquad (3.11)$$

respectively.

For instance, consider the situation where $k = k_0(1 + s\tau_1)$ with $\tau_1 = 0.09$ s and

$k_0 = 80\,\text{s}^{-2}$. Recall from Figure 3.5 that this form of feedback transfer function yielded quality factors of $Q_L \sim 4$ and $Q_U \sim 2$. Figure 3.8 shows a plot of the closed-loop transfer function given in equation (3.1) both with feedback and with $k = 0$. With $k = 0$ two large peaks corresponding to the coupled undamped pendulum resonances are clearly visible at $\omega \sim 4.59\,\text{rads}^{-1}$ and $\omega \sim 11.09\,\text{rads}^{-1}$. Above these resonances, natural isolation of the suspended test mass occurs with the ratio x_2/x_0 becoming smaller in magnitude. With the feedback applied, the motion of the test mass is reduced up to approximately the new upper resonant frequency of the system. The two new resonances occur at similar frequencies giving rise to one damped peak in the closed-loop transfer function curve.

Using the impulse response facility in MATLAB, the amplitude of test mass motion at the two resonant frequencies was observed as a function of time. The impulse response plots for the two damped resonances are shown separately in Figure 3.9. From this we can see that the amplitudes of oscillation are roughly equal, however the oscillation corresponding to what ends up as the uppermost of the two resonances with increasing gain is slightly better damped as one would expect.

Since the amplitude of test mass motion is approximately equal at the two resonant frequencies it would seem important to damp both resonances to a similarly high degree. The upper resonance, if pushed to a much higher frequency, might coincide with the frequency of a gravitational wave signal and obviously it would be necessary to critically damp this resonance. Furthermore, both resonances should be critically damped since it is undesirable to have large motions of the test mass at any frequency due to the possibility of cross-coupling of modes. Such an effect might lead to the misalignment of the reflected laser light with the cavity axis causing reduced sensitivity or loss of lock.

3.2.4 Conclusions

If aiming for large bandwidth position control, it appears to be necessary to damp the new lower resonance by some other means than *via* the position control signal to the lower mass. Another scheme whereby the resonances of a double pendulum are damped by sensing the acceleration of, and applying a feedback signal to the intermediate mass, is discussed in Section 3.3.
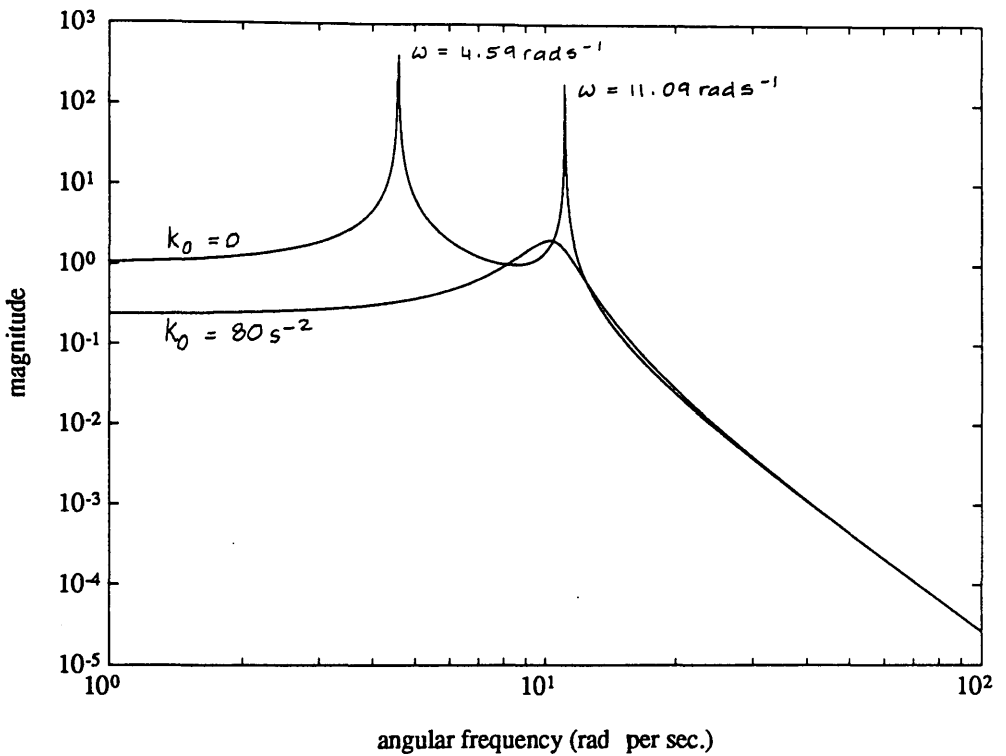
Figure 3.8 *A plot of the closed-loop transfer function given by equation (3.1) with $k=k_0(1+s\tau_1)$. Here $\tau_1 = 0.09s$ and $k_0 = 80s^{-2}$. With feedback of the described form, the new resonant frequencies are at $\omega \sim 10.5$ rads^{-1} and $\omega \sim 9.7$ rads^{-1} with Q's of 4 and 2 respectively (lower curve). Superimposed is the corresponding plot with $k_0 = 0$ (upper curve).*
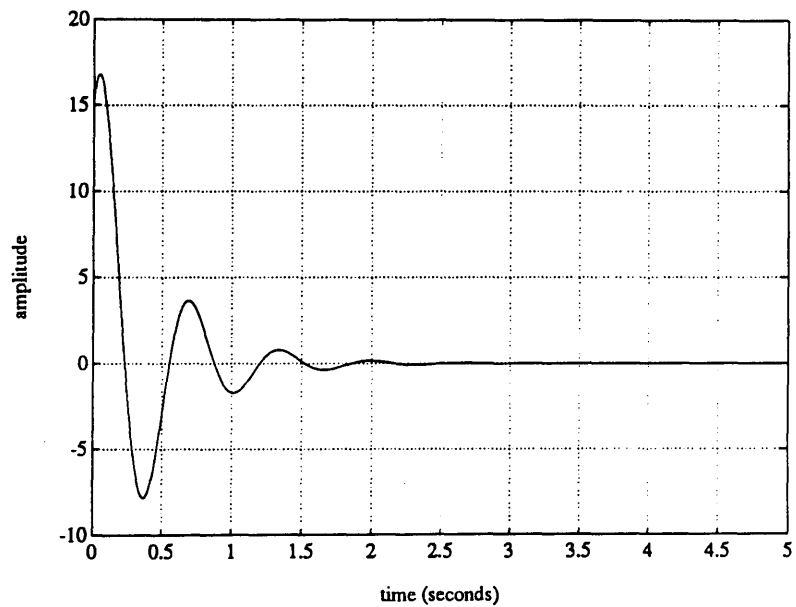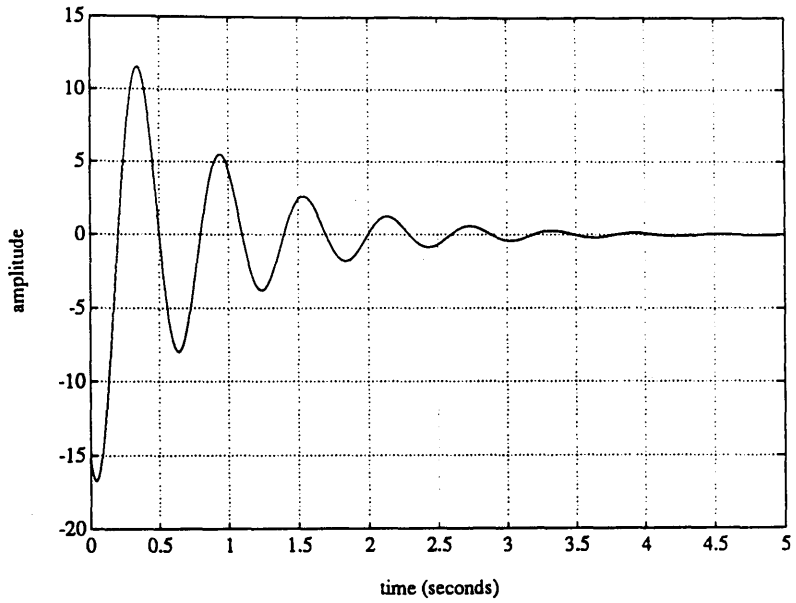
Figure 3.9 *Impulse response plots with feedback transfer function of the form $k = k_0(1 + s\tau_1)$ with $\tau_1 = 0.09s$ and $k_0 = 80s^{-2}$. The new resonant frequencies are at $\omega \sim 10.5$ rads^{-1} and 9.7 rads^{-1} with Q's of 4 and 2 (upper and lower plots) respectively.*

3.3 Damping by the Application of Feedback to the Intermediate Mass

It is the purpose of this section to examine the degree to which the coupled resonances of a high Q double pendulum can be damped by sensing the acceleration of, and applying a feedback signal to the intermediate mass. Ideally one would like to be able to critically damp both of the pendulum resonances simultaneously. This feedback system could then be used to reduce the motion of the lower mass (test mass) to a low level, reducing the dynamic range requirements of the main position control feedback loop.

3.3.1 The Closed-Loop System

Consider once more the double pendulum shown in Figure 2.2. Consider the situation where a damping feedback force of the form $F_1 = b_1 \dot{x}_1$ is applied to the intermediate mass where b_1 is some gain factor.

The equations of motion of the two masses can be derived to yield the transfer function from motion at the top of the pendulum x_0, to motion at the test mass x_2, as a function of frequency s, in the closed-loop state *i.e.*

$$\frac{x_2}{x_0} = \frac{(1 + \alpha_m)\omega_1^2 \omega_2^2}{s^4 + \gamma_1 s^3 + \left[(1 + \alpha_m)(\omega_1^2 + \omega_2^2)\right]s^2 + \gamma_1 \omega_2^2 s + (1 + \alpha_m)\omega_1^2 \omega_2^2} \qquad (3.12)$$

Here α_m is the mass ratio m_2/m_1 and ω_1 and ω_2 are the natural angular resonant frequencies of the two separate stages of the pendulum. Note also that here γ_1 is the electronic damping factor given by $\gamma_1 = b_1/m_1$.

As mentioned in Section 2.5.2, the roots of the denominator of a closed-loop transfer function *i.e.* the roots of the characteristic equation, give the positions of the poles of the closed-loop system on the complex s-plane. Thus the levels of damping of the two resonances can be assessed by observing the positions of the roots of the denominator of equation (3.12) as a function of b_1 (or γ_1).

Figure 3.10 is a root-locus plot showing the pole positions as a function of γ_1 for the case where the two stages of the double pendulum had identical mass and length *i.e.* $m_1=m_2=2$kg and $\omega_1=\omega_2=6$rads^{-1}. From this one can see that the lower frequency resonance of the pendulum corresponding to the first sketch shown in Figure 3.2 at

ω=4.59 rads^{-1}, is pushed to a slightly higher frequency by the feedback. With large γ_l, this resonance ends up at ω= 6rads^{-1}. This frequency corresponds to the situation where the intermediate mass is essentially pinned vertically below the suspension point and the lower stage of the pendulum oscillates as if it were uncoupled from the upper stage. This resonance cannot be critically damped by applying feedback of this type. The new upper resonance of the system (which originates from the pole at ω=11.09 rads^{-1}) can be critically damped using a gain factor of b_l~38 Nsm^{-1} (γ~19 s^{-1}), the frequency of oscillation becoming increasingly smaller as the level of damping is increased. This form of feedback also damps the lower resonance to a fairly low Q i.e. Q_L~3.4.

Figure 3.11 shows the corresponding plot of the closed-loop transfer function x_2/x_0 (given in equation (3.12)) for this system as a function of angular frequency ω, both with and without the described feedback applied. Without feedback, the two peaks corresponding to the coupled undamped pendulum resonances are clearly visible at ω=4.59rads^{-1} and ω=11.09rads^{-1}. Above these resonances, isolation of the suspended test mass occurs with the ratio x_2/x_0 becoming smaller in magnitude. With the feedback applied the resulting motion of the test mass at the resonant frequencies is greatly reduced. The new lower resonance is pushed to a frequency of ω ~ 5.6 rads^{-1} and its Q is reduced to Q_L~3.4. Correspondingly, the new upper resonance becomes critically damped.

An investigation was made to see if better simultaneous damping of the two resonances could be achieved by varying the relative length and mass ratios of the two pendulum stages. A marginal improvement in the relative damping ratios was obtained using a pendulum whose upper stage was twice the length of its lower stage, with the lower mass twice the intermediate mass. For m_1=1kg, m_2=2kg, ω_1=6rads^{-1}, ω_2=8.5rads^{-1}, critical damping of the upper resonance was achieved for γ_l=29 s^{-1} (b_l=29 Nsm^{-1}), and this gave a corresponding quality factor for the lower resonance of Q_L ~ 1.4.

3.3.2 Conclusions

It has been shown here that by applying inertial damping to the intermediate mass of a high Q double pendulum, the resulting motion of the lower mass at the pendulum resonant frequencies can be reduced to a very low level. The use of such a feedback system would reduce the dynamic range requirements of any separate servo-system used
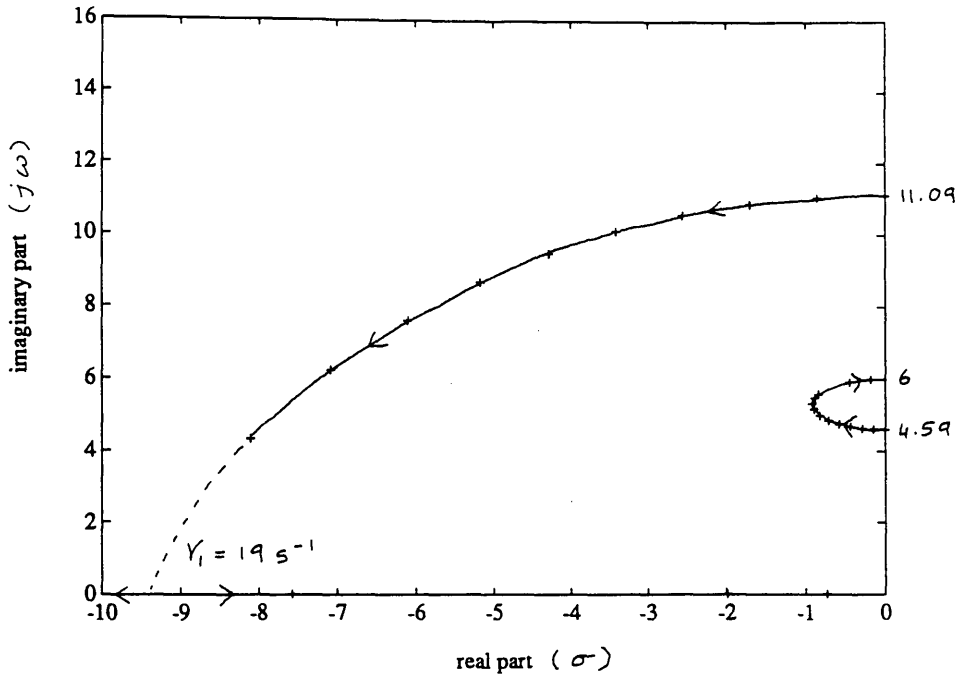
Figure 3.10 *The loci of the two positive roots of equation (3.12) as a function of γ_I. The arrows show the direction of increasing γ_I.*
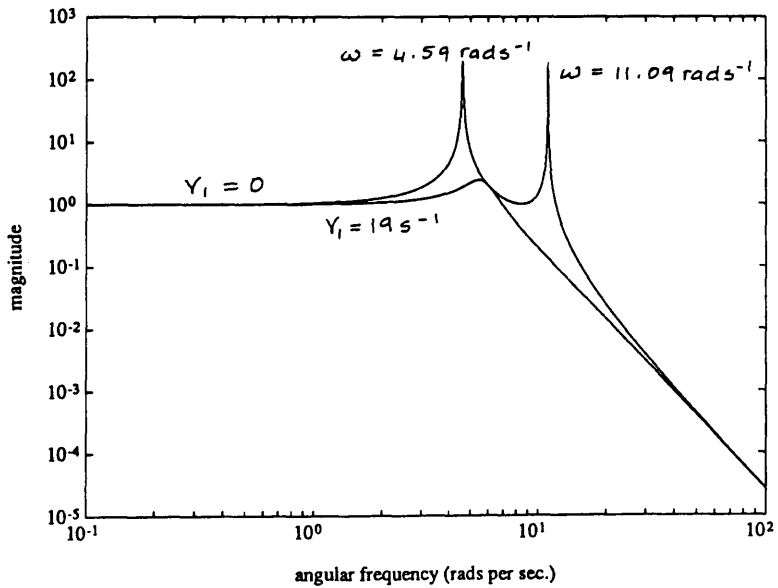
Figure 3.11 *The corresponding plot of the closed-loop transfer function (lower curve). The new lower resonance is at $\omega_L \sim 5.6 rads^{-1}$ with a corresponding Q value of $Q_L \sim 3.4$. The upper resonance is critically damped. The upper curve shows the equivalent plot with $\gamma_I = 0$ (no feedback).*

to control the position of the lower mass. Furthermore, this feedback loop would provide damping for the lower frequency resonance when the main position control loop is locked. (It was shown in the previous section that poor damping of this resonance is achieved by the position control feedback loop, if it has to operate over a relatively large bandwidth.) The performance of such a combined feedback system is analysed in the next section.

3.4 Position Control and Damping by the Application of Feedback to Both Masses

It is the purpose of this section to examine the level to which the coupled resonances of a high Q double pendulum can be damped and the position of the lower mass controlled, by applying feedback to both masses simultaneously. The feedback signal to the intermediate mass is derived by sensing the acceleration of the intermediate mass, whilst the feedback signal to the lower mass is derived by sensing the position of the lower mass relative to an arbitrary reference point (*e.g.* another highly isolated test mass in a laser interferometric detector). This analysis is based on the results of the previous two sections. The aim here is to produce a combined feedback system which controls the position of the lower mass over a relatively large bandwidth whilst critically damping both of the new pendulum resonances.

3.4.1 The Closed-Loop System

Consider once more the double pendulum shown in Figure 2.2 with identical length and mass in each stage ($m_1 = m_2 = 2\text{kg}$ and $\omega_1 = \omega_2 = 6\text{rads}^{-1}$). Consider the situation where feedback forces of the form $F_1 = b_1\dot{x}_1$ and $F_2 = m_2k(x_3-x_2)$ are applied to the intermediate and lower masses respectively (where b_1 and k are gain factors and the other symbols have their usual meanings). If one assumes that the reference point x_3 is absolutely stationary at all frequencies, then by setting $x_3 = 0$ and considering the equations of motion of the two masses, one can derive the transfer function from the motion at the top of the pendulum x_0 to motion of the lower mass x_2 *i.e.*

$$\frac{x_2}{x_0} = \frac{(1 + \alpha_m)\omega_1^2\omega_2^2}{s^4 + \gamma s^3 + \left[(1 + \alpha_m)(\omega_1^2 + \omega_2^2) + k\right]s^2 + (\omega_2^2 + k)\gamma s + \left[(1 + \alpha_m)\omega_1^2 + \alpha_m\omega_2^2\right]k + (1 + \alpha_m)\omega_1^2\omega_2^2}$$

(3.13)

Here the symbols have their usual meaning. Note that when $\gamma = {}^{b_1}/_{m_1} = 0$, equation (3.13) reduces to equation (3.1); also when $k = 0$ it reduces to equation (3.12) as expected. The positions of the poles on the complex s-plane (the roots of the denominator of equation (3.13) were observed for various forms of γ and k to see how well both of the resonances could be damped and to observe the new resonant frequencies. For instance, with $k = k_0(1 + \alpha s)$ where $k_0 = 10^6$ s^{-2} and $\alpha = 0.001$ s, with $\gamma = 8$ s^{-1}, the new lower and upper resonances were at angular frequencies $\omega_L \sim 9.6$rads^{-1} and $\omega_U \sim 870$rads^{-1} with quality factors of $Q_L \sim 1.3$ and $Q_U \sim 1.0$ respectively. Figure 3.12 shows the closed-loop transfer function curve both with and without the feedback loops closed. The position of the lower mass is being controlled approximately up to the new upper resonant frequency of the double pendulum.

It is desirable to operate the damping feedback to the intermediate mass over a restricted bandwidth to reduce the possibility of introducing noise to the test mass at higher frequencies. Figure 3.12 also shows the transfer curve where the feedback signal to the intermediate mass had three integrations with corner frequencies of $\omega = 30$rads^{-1} i.e. the feedback force was of the form $F_1 = {}^{m_1 \gamma x_1 s}/_{(1 + s\tau_1)^3}$ with $\tau_1 = \frac{1}{30}$ s. Three integrations were used here so that a 12dB/octave roll-off of the intermediate feedback signal was achieved (stability was maintained by the differentiation in the feedback to the lower mass). This resulted in the Q of the lower resonance increasing to about $Q_L \sim 7$. There is a trade-off between the damping achieved for the lower resonance and the bandwidth of the intermediate mass feedback loop, and some suitable compromise must be adopted.

In order to operate the position control loop over an even larger bandwidth and maintain critical damping of the new upper resonance, a larger gain factor k_0 with a correspondingly smaller differentiation time constant α could be used.

3.4.2 Conclusions

From Figure 3.12 one can see that the position of the lower mass is being controlled over a relatively large bandwidth and that both new resonances are being close to critically
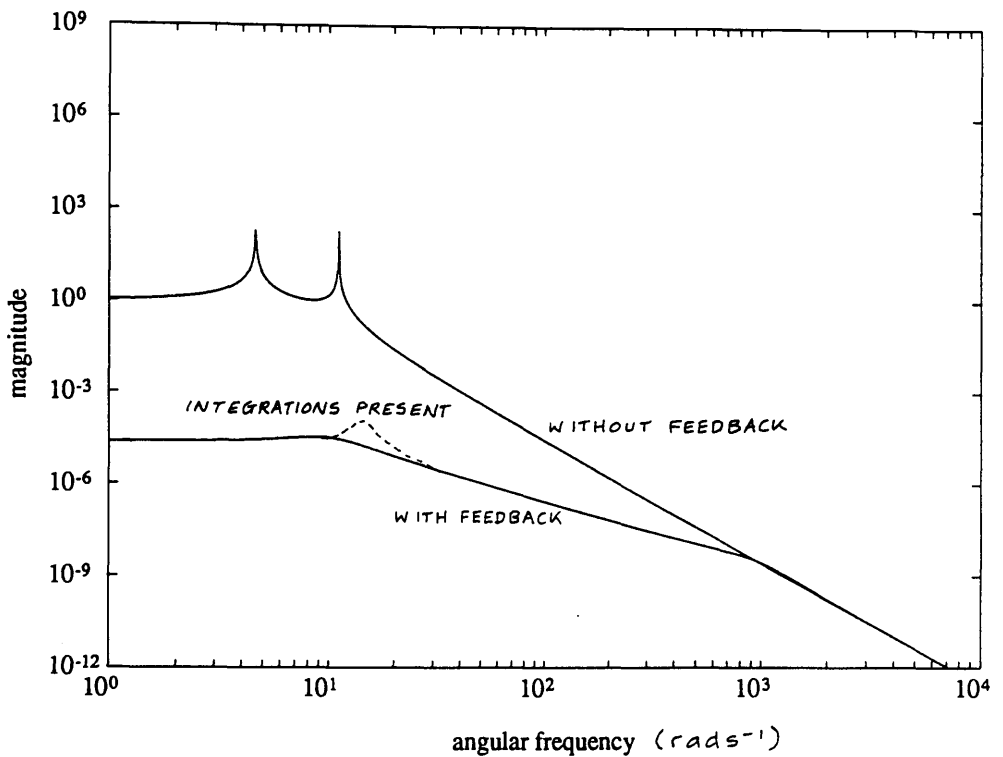
Figure 3.12 *A plot of the closed-loop transfer function given in equation (3.13). The two lower curves correspond to the case where feedback is applied to both of the masses. The feedback transfer function for the test mass has the form $k=k_0(1+\alpha s)$ with $k_0=10^6 s^{-2}$ and $\alpha=0.001 s$, while damping feedback is applied to the intermediate mass with $\gamma=8 s^{-1}$. The Q of the lower resonance increases to $Q\sim7$ when integrations are introduced in the intermediate mass feedback loop as detailed in the text. Superimposed is the corresponding plot with $k_0=0$ and $\gamma=0$ (no feedback).*

damped. The lower mass feedback loop is providing damping of the new upper resonance of the double pendulum. The new lower frequency resonance, where the lower mass is held fixed by the lower mass feedback and the intermediate mass essentially moves freely, is being damped by the feedback applied to the intermediate mass.

3.5 Experimental Investigations into the Position Control and Damping of a Double Pendulum

Experimental investigations into the position control and damping of a test mass suspended as a double pendulum, *via* feedback applied to the test mass initially using ground-based feedback coils and latterly using suspended feedback coils, are presented. Experimental investigations into the damping and position control of a double pendulum system *via* feedback applied to the intermediate mass are discussed in Chapter 4.

3.5.1 Characteristics of the Closed-Loop System

Consider a double pendulum where the position of the lower mass is being sensed with respect to an arbitrary reference point using the Michelson interferometer arrangement discussed in Section 2.6.1 and shown schematically in Figure 2.7. As for the single pendulum of Section 2.6, the feedback signal here is applied to the test mass *via* ground based feedback coils for simplicity. The simplified loop diagram for this system, under the condition where $x_0=0$, is identical to that for the single pendulum system as shown in Figure 2.9. However, in this instance G_P (see Figure 2.8) describes the passive transfer function for the double pendulum (equation (2.17)). Furthermore, the transfer function for the conversion of the acceleration produced by the coil/magnet feedback transducers to the resulting test mass displacement, G_A, is now given by:

$$G_A = \frac{s^2 + (1 + \alpha_m)\omega_1^2 + \alpha_m \omega_2^2}{s^4 + (1 + \alpha_m)(\omega_1^2 + \omega_2^2)s^2 + (1 + \alpha_m)\omega_1^2 \omega_2^2} \qquad (3.14)$$

where the symbols have their usual meaning.

The closed-loop transfer function for this system, as given in equation (2.35), can be expressed in terms of the feedback transfer functions for the test mass feedback loop and the auxiliary loop, H_C and H_P, respectively *i.e.*

$$\frac{\varepsilon}{x_n} = \frac{s^4 + (1+\alpha_m)(\omega_1^2 + \omega_2^2)s^2 + (1+\alpha_m)\omega_1^2\omega_2^2}{(1+H_P)s^4 + [(1+H_P)(1+\alpha_m)(\omega_1^2+\omega_2^2) + H_C]s^2 + (1+H_P)(1+\alpha_m)\omega_1^2\omega_2^2 + H_C[(1+\alpha_m)\omega_1^2 + \alpha_m\omega_2^2]} \quad (3.15)$$

Recall from equation (2.42) that the open-loop transfer function $H_C G_A$, or open-loop gain of the test mass feedback loop, can be measured as a function of frequency by studying the behaviour of the closed-loop system. If H_C is constant in the frequency range considered, then according to equation (3.14), the open-loop gain, $H_C G_A$, should fall at 12dB/octave at frequencies above the upper natural resonant frequency of the double pendulum.

3.5.2 Observed Behaviour of the Closed-Loop System

A double pendulum with identical stages was constructed where $m_1 = m_2 \sim$ 3kg and $\omega_0 \sim$ 5.7rads^{-1} for each stage. The coupled resonances of the double pendulum were calculated to be at angular frequencies $\omega_L \sim$ 4.4rads^{-1} and $\omega_U \sim$ 10.6rads^{-1} (refer to Section 2.3.2).

The position of the test mass was sensed with respect to the reference mirror shown in Figure 2.7 and the test mass feedback loop was locked with the aid of a small amount of gain in the auxiliary loop. The amplifier circuits used for the two loops are shown in Figure 2.11 where the damping capacitor in the test mass feedback loop had the value C_{damp}=0.1µF. The gain in the auxiliary loop was then reduced to a low level.

In the locked state, a peak corresponding to the new lower resonant frequency of the pendulum was observed in the residual fringe spectrum at $\omega_L \sim$ 9.8rads^{-1}. This agreed well with that predicted from theory i.e. $\omega_L \sim \sqrt{3}\omega_0 \sim$ 9.9rads^{-1} (Section 3.2.1).

The open-loop gain of the test mass feedback loop was measured as in Section 2.6.2 by observing the magnitude of the residual displacement signal x_p at the PZT and the residual locked fringe signal ε, over a range of frequencies (see Figure 2.9 and equation (2.42)). The observed voltage signals were converted to displacements using the calibrations given in Section 2.6.2.

Figure 3.13 shows the measured open-loop gain as a function of frequency. As predicted the gain falls at approximately 12dB/octave since we are at frequencies greater than the upper resonant frequency of the passive pendulum ($\omega_U \sim$ 10.6rads^{-1}). However, the gradient of the curve (and hence the phase margin) on approaching the unity gain frequency is not obvious from the data because of the large uncertainties in the
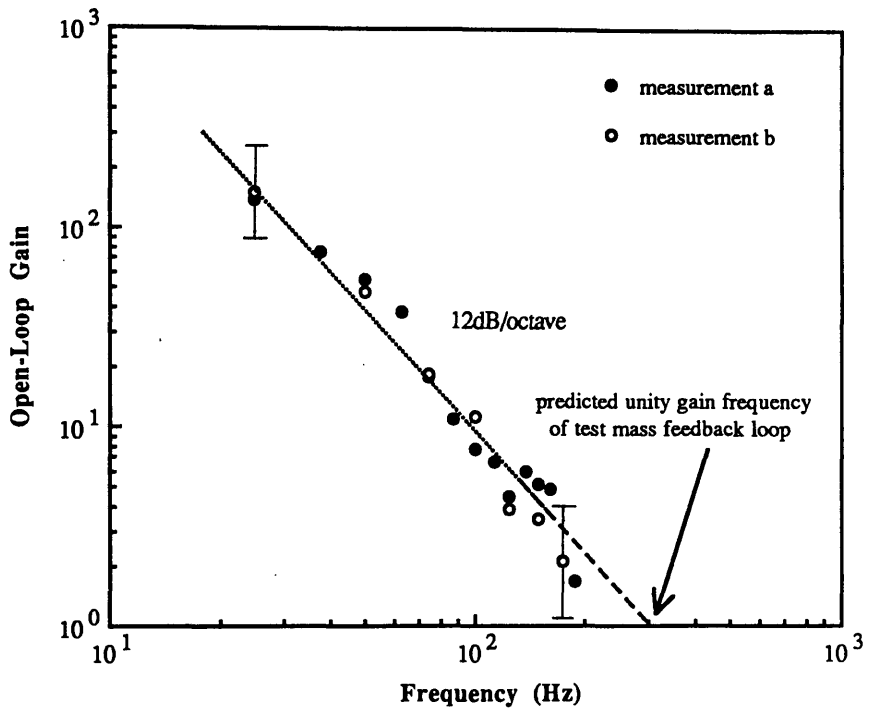
Figure 3.13 *Open-loop gain of the test mass feedback loop* $(H_C G_A)$ *as a function of frequency for the double pendulum with ground based feedback coils. Typical error bars are shown.*

measurements.

To predict the phase of $H_C G_A$ at the unity gain frequency, the open-loop response was modelled using MATLAB. The transfer function H_C was approximated to $H_C = H_{C0}(1+s\tau)$ where τ was the corner frequency for the differentiation at ~340Hz (due to the presence of C_{damp}=0.1µF). The calibration for the volts produced at the photodiode per unit displacement of the test mass was $\Delta V/\Delta x \sim 1.3\times10^3$ V/mm and the displacement of the test mass per volt across the feedback coils was $\Delta x/\Delta V \sim 0.14$ mm/V. From considerations of the loop, the loop gain at zero frequency was calculated to be of the order ~9×10^4. Using equation (3.14), H_{C0} was calculated to be ~2×10^6 s^{-2}. (Note that both of these values are dependent on the setting of the gain control knob in the feedback loop.) The model predicted the gradient of the loop gain curve to be ~9dB/octave around the unity gain frequency which was at $\omega \sim 1.8\times10^3$ rads^{-1} ($f\sim$290Hz), with a corresponding phase margin of ~40°. The corner frequency for the transition from a gradient of 12dB/octave to 9dB/octave was at the relatively high frequency of $\omega \sim$800rads^{-1} ($f\sim$130Hz). This is consistent with the experimental data in Figure 3.13, where the errors are large at this frequency. The model also predicted that the new upper resonance was being damped to a $Q_U \sim$1.5 due to this feedback.

3.5.3 Noise Introduced to the Test Mass *via* the Feedback Coils

Since coil/magnet feedback transducers are used to control the motions of the test mass, it is possible that these might re-introduce noise, degrading the isolation obtained by suspending the mass. For instance, motions of the ground based coils, due to say the seismic background, might give rise to displacement noise of the test mass *via* electromagnetic coupling between the coils and magnets. At frequencies within the bandwidth of the position control loop, relatively large currents are driven through the coils and this effect could be large. At frequencies above the unity gain point of the feedback loop, this effect would be reduced depending on how fast the feedback signal is rolled-off above unity gain. It is therefore important to consider this electromagnetic coupling effect.

Consider the magnet to be a magnetic dipole of moment P which is aligned with the axis of a circular current loop of radius a, carrying current I (as shown in Figure 3.14).
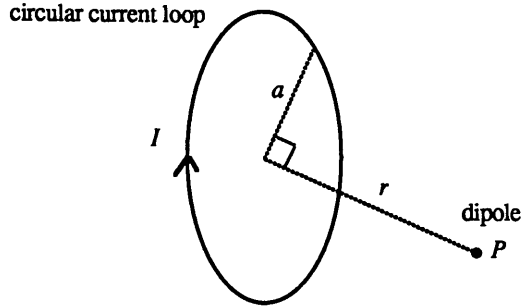
Figure 3.14 **Dipole aligned with the axis of a current loop.** The dipole of moment P is displaced a distance r along the axis of the coil loop of radius a and carrying current I.

The force on the dipole is given by:

$$F_r = P \left(\frac{dB_r}{dr} \right)_{coil} \tag{3.16}$$

For a circular coil of radius a, carrying current I and of N turns (assuming negligible length), the magnetic field along the axis of the coil is given by:

$$B_r = \frac{\mu_0 I N a^2}{2(a^2 + r^2)^{3/2}} \tag{3.17}$$

where μ_0 is the permeability of free space. Thus according to equation (3.16) the force on the dipole as a function of the relative separation r is given by:

$$F_r = \frac{3\mu_0 I P N a^2 r}{2(a^2 + r^2)^{5/2}} \tag{3.18}$$

The optimum separation r for the coil/magnet pairs would be where the force is independent of small relative motions $i.e.$

69

$$\left(\frac{dF_r}{dr}\right) = 0 \qquad (3.19)$$

This condition holds when the separation is $r \sim 0.5a$ *i.e.* when the magnet is situated at half a coil radius from the coil. In this situation, to first order, small variations in the relative separation of the coils and magnets will not couple displacement noise to the test mass. However, if the separation is not optimised in this way, then relative motions between the two components will result in displacement noise at the test mass.

(A more rigorous calculation has been carried out taking account of the finite size of the coils and magnets. This calculation showed that the position of constant field gradient might in fact lie closer to the end of the coil. However this depends critically on the precise dimensions of the system under consideration [Mackenzie 1989] .)

For instance, consider the case where the coils are situated at one coil radius from the magnets *i.e.* $r = a$. From equation (3.18), the magnitude of the field gradient will be

$$\left|\frac{dF_r}{dr}\right| = F_0 \left(\frac{3}{2a}\right) \qquad (3.20)$$

where F_0 is the static force generated between the coils and the magnets.

Using typical values *e.g.* $a \sim 1\text{cm}$, $F_0 \sim 5 \times 10^{-3}$ N, then at a frequency of 100Hz, where the seismic background will have an amplitude typically of $\delta r \sim 10^{-11}\ \text{m}/\sqrt{\text{Hz}}$ (refer to Section 2.2), this would result in a noise force of $\delta F \sim 7.5 \times 10^{-12}\ \text{N}/\sqrt{\text{Hz}}$ at the test mass. At 100Hz, this would give rise to a displacement noise of the freely suspended mass (3kg) of approximately $\delta x \sim \delta F/m\omega^2 \sim 6 \times 10^{-18}\ \text{m}/\sqrt{\text{Hz}}$ which is larger than the displacement transmitted to the test mass *via* its double pendulum suspension (refer to Section 2.3.2). Hence for the effective low frequency operation of a laser interferometric detector, it is sensible to take the precautionary measure of isolating the feedback coils from seismic motions.

3.5.4 Feedback *via* Suspended Transducers

To reduce the coupling of seismic noise directly to the test mass, the feedback coils were mounted on a reaction mass ($m \sim 3\text{kg}$) suspended as a high Q pendulum of angular resonant frequency $\omega = 4.0\ \text{rads}^{-1}$ as shown schematically in Figure 3.15.
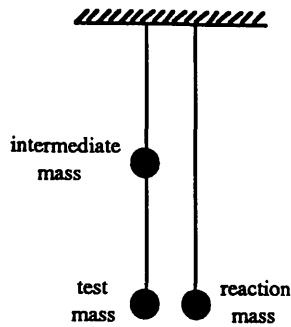
Figure 3.15 Schematic diagram of the double pendulum with feedback supplied via a suspended reaction mass.

The open-loop gain of the test mass position control loop was then measured. This was done using the usual method where a test signal was applied to the PZT (reference mirror) and the residual fringe signal with the position control loop locked was observed. A small amount of gain was also used in the auxiliary loop (feeding back to the reference mirror). The circuits used for the test mass and auxiliary loops are as shown in Figure 2.11, where the damping capacitor had a value of C_{damp}=0.1μF. The loop gain curve obtained was of a similar form to that shown in Figure 3.13. The maximum unity gain frequency observed was ~290Hz. However the resonance of the reaction pendulum was observed to electromagnetically couple to the test mass giving rise to a large peak in the residual fringe spectrum at ω~4 rads^{-1}. It was therefore necessary to electronically damp the reaction mass to the ground over a restricted bandwidth. Any displacement noise introduced to the reaction mass *via* electromagnetic coupling to the ground would only occur, to first order, at frequencies within this bandwidth (say below a few tens of hertz).

3.5.5 Shadow Sensor Servo-Systems

The electronic damping of the reaction mass to the ground at low frequencies was achieved using 'shadow sensor' coil/magnet assemblies. These are self-contained position sensing and feedback control elements which were originally implemented in the delay line detector at the Max-Planck-Institute [Shoemaker 1987].

Two magnets were mounted on the rear face of the reaction mass at positions

71

directly opposite two feedback coils rigidly mounted on the ground. A small flag was mounted perpendicular to the surface of each magnet. Each coil contained a light emitting diode and silicon photodiode placed directly opposite each other on the coil circumference. In each unit the flag partially interrupted the light incident on the photodiode, and a signal was developed which was proportional to the relative displacement of the flag and the detector/emitter pair. This signal was then suitably amplified and filtered and fed to the coil in such a way as to damp the motion of the reaction mass with respect to the ground.

Figure 3.16 shows the circuit used for each shadow sensor device on this occasion. The corner frequencies for the integrations were set at about 35Hz and 70Hz with the damping capacitors of value $C=0.47\mu F$. To observe how well the reaction pendulum was being damped due to the feedback, white noise was applied in each circuit at the point shown in Figure 3.16 to drive the reaction pendulum whilst the feedback loops were closed. Figure 3.17 shows the spectrum of the light intensity signal detected at one of the monitor points (see Figure 3.16) for different feedback gains. This shows clearly that as the gain is increased, the resonance of the reaction pendulum is both damped and forced to a slightly higher frequency by the action of the feedback.

3.6 A Prototype Balanced Double Pendulum Suspension System

Since the reaction mass and the test mass will have a force acting between them when the position control feedback loop is closed, if the system is not properly balanced, it is possible that there might be some net reaction at the points of suspension of the two masses. This might lead to the excitation of resonances in the support structure of the isolation system which could couple displacement noise to the test mass and potentially limit the gain and bandwidth of operation of the control loop.

One way of reducing the likelihood of this effect is to suspend both the test mass and reaction mass from a common intermediate mass, forming a balanced double pendulum arrangement as shown in Figure 3.18. The test mass and reaction mass are symmetrically suspended in such a way as to make the net reaction at the intermediate mass due to their interaction zero. Since the intermediate mass is itself suspended, the effect on the support structure of any slight imbalance in the lower stages will be reduced.

Furthermore, since the reaction mass is isolated to the same high level as the test

SKETCHES OF THE BODE MAGNITUDE PLOTS SHOWING
CORNER FREQUENCIES FOR FINAL AMPLIFIER STAGES

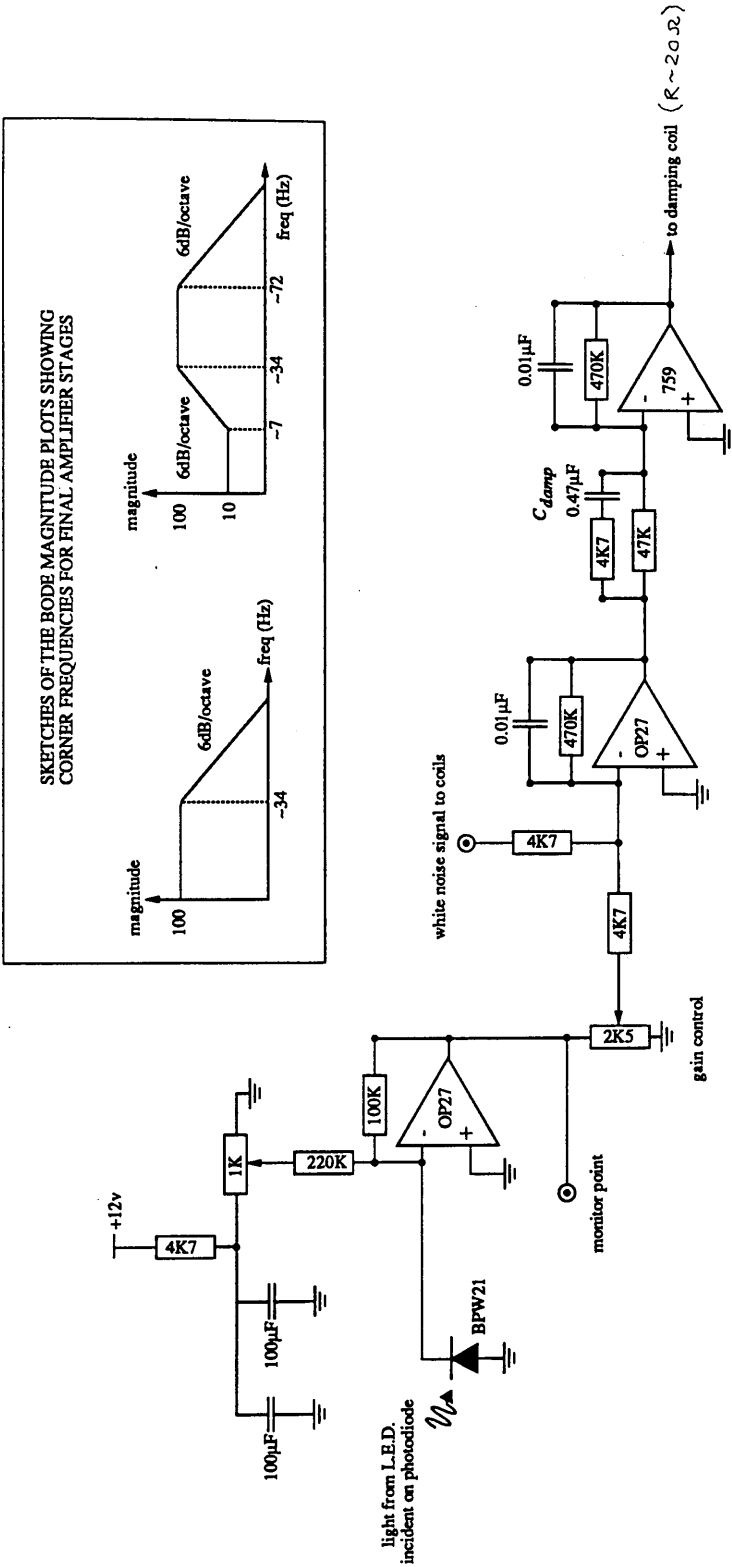*Figure 3.16 The circuit for the shadow sensor damping servos.*
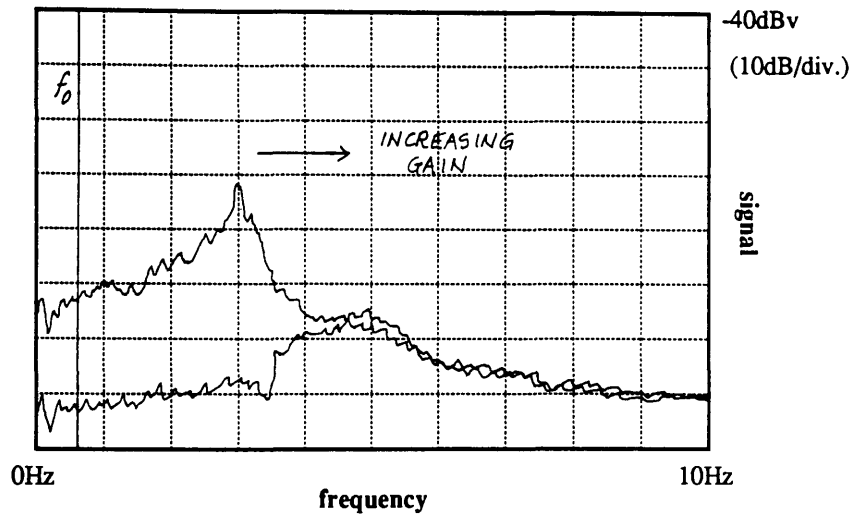
Figure 3.17 *The light intensity signal at the output of one of the shadow sensor photodiodes with different feedback gain settings. As the gain is increased the resonance of the reaction pendulum is both damped and forced to a higher frequency. The natural resonant frequency of the pendulum is $f\sim0.64Hz$ ($\omega\sim4rads^{-1}$).*

support plate

two stage vibration
isolation stacks

L_1

reference point

m_1

L_2

sense
(see Figure 2.7)

m_2 m_3

local damping of reaction
mass to ground using
shadow sensor servos
(refer to Section 3.5.5)

feedback signal
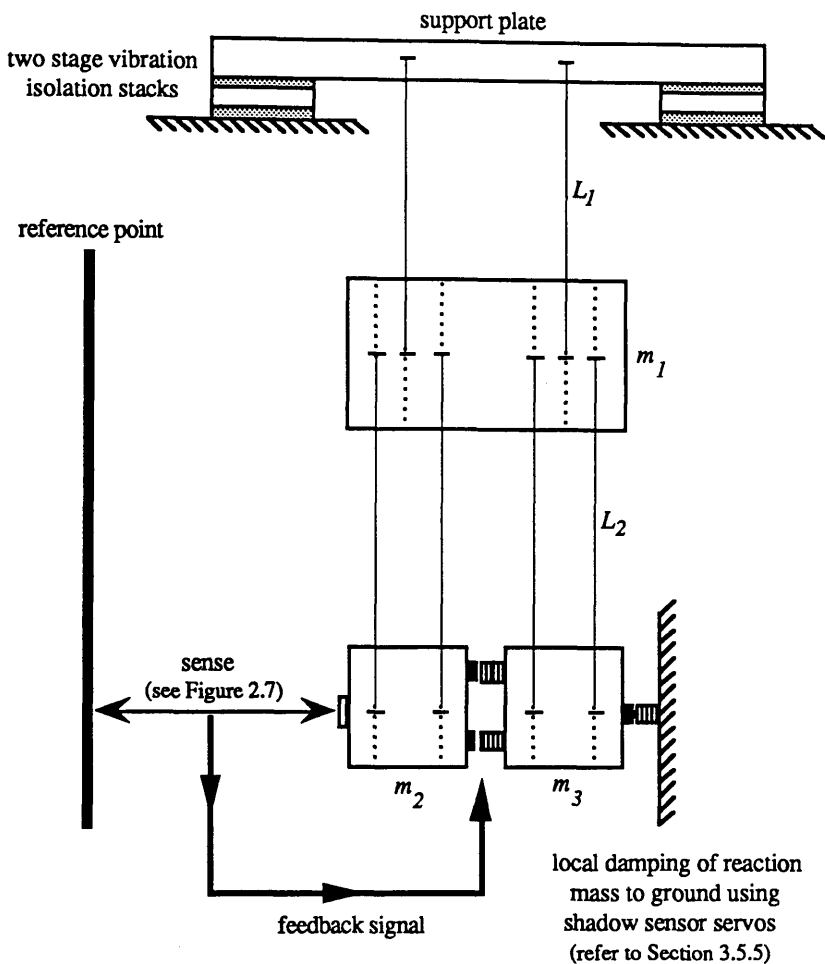
intermediate mass	$m_1 \sim 11\text{kg}$	upper stage	$L_1 \sim 0.28\text{m}$
		wire diameter	$d_1 = 0.31\text{mm}$
test mass	$m_2 \sim 3\text{kg}$	lower stages	$L_2 \sim 0.42\text{m}$
reaction mass	$m_3 \sim 3\text{kg}$	wire diameter	$d_2 = 0.23\text{mm}$

Figure 3.18   *Schematic diagram of the balanced double pendulum suspension system with feedback control. The position of the test mass is locked to the reference point (reference mirror) using coil/magnet transducers acting between the test mass and reaction mass. The resonance of the reaction pendulum is damped electronically to the ground.*

mass, seismic noise of significant magnitude cannot be re-introduced to the test mass *via* electromagnetic coupling effects in the feedback transducers, as described in Section 3.5.3.

Such a balanced double pendulum was constructed in order to experimentally investigate some of the aspects of its control and damping using feedback signals applied between the test mass and reaction mass which was damped to the ground over a restricted bandwidth.

3.6.1 Physical Description

Figure 3.18 shows the dimensions of the constructed balanced double pendulum. The support plate (1" thick aluminium) for the pendulum was connected to a ground–borne "dexion" support structure *via* two stage isolation stacks used to provide some extra isolation. Note that in an interferometric detector, both the support plate for the pendulum and the support structure would be carefully designed to have very low Q internal resonances to avoid introducing noise to the test mass.

Double loop suspension wires (steel piano wires) were used for each of the three pendulum masses in order to make it easier for the system to lock without the aid of tilt and rotational damping servo-systems. However, it would be more desirable to use a single loop suspension wire for the upper stage to avoid directly coupling low frequency ground tilting motions to the pendulum. For the dimensions of wires chosen the lowest frequency violin resonances were calculated to be at $f\sim480$Hz and $f\sim180$Hz for the upper and lower stages respectively (refer to Section 2.3.3).

An aluminium bar of mass $m_1\sim11$kg was used in the intermediate stage. The test mass and reaction mass were aluminium bars of similar dimensions ($m_2\sim m_3\sim3$kg). The use of a relatively heavier intermediate mass gives better isolation (equation (2.18)).

As in the previous experiments, the position of the test mass was sensed using the Michelson interferometer arrangement described in Section 2.6 and illustrated in Figure 2.7. Four coils were mounted on the front face of the reaction mass adjacent to four double magnets mounted on the rear face of the test mass. The main position control feedback signal could then be fed to these transducers to lock the position of the test mass to the reference mirror. To minimise the motion of the reaction mass at its pendulum resonant frequency, two shadow sensor coil/magnet arrangements were used to damp the reaction mass to the ground in the same way as described in Section 3.5.5 with slightly

larger damping capacitors of $C=1\mu F$ (refer to Figure 3.16).

3.6.2 Behaviour of the Closed-Loop System

The passive pendulum had three separate suspension stages and therefore three coupled pendulum modes. For the dimensions discussed these were calculated to be at $\omega \sim 4.2 \text{rads}^{-1}$, $\omega \sim 4.8 \text{rads}^{-1}$ and $\omega \sim 8.5 \text{rads}^{-1}$. However, since the reaction pendulum was locked to the ground by its damping servo loops (up to a few tens of hertz), and the intermediate mass was much larger than the test mass, the lower resonant frequency of this multiple system was predicted to closely correspond to the uncoupled natural resonant frequency of the test mass pendulum which was at $\omega \sim 4.8 \text{rads}^{-1}$. The new lower resonance with the position control feedback loop locked was predicted to correspond closely to the situation where the test mass was fixed in its static position with the intermediate mass oscillating relatively freely. This new lower resonance was predicted to be at $\omega \sim 7.8 \text{ rads}^{-1}$.

With the reaction mass damped to the ground, and the test mass and auxiliary feedback loops closed, a peak was observed in the residual locked fringe signal at $\omega \sim 8.2 \text{ rads}^{-1}$ corresponding to the new lower resonance of the pendulum. This agrees fairly well with the prediction. The new upper resonance was not clearly visible in the residual fringe spectrum, even with the damping capacitor removed from the test mass feedback loop, since it was being damped by the integration present in the auxiliary loop (feeding back to the reference mirror) (refer to Section 2.6.2). An integration was introduced to the test mass feedback loop at about 70Hz, to try to reduce this damping effect by cancelling out the 170Hz integration in the auxiliary feedback loop. The new upper resonance peak observed in the residual fringe spectrum was observed to increase in Q as predicted. The maximum observed upper resonant frequency with both loops closed was at about 250Hz. This extra integration was subsequently removed from the circuit.

The transfer function, G_A, for the conversion of the acceleration produced by the coil/magnet feedback transducers to the resulting test mass displacement, will have slightly different form from equation (3.14) since the reaction mass is suspended from the common intermediate mass in this system. It can be shown that G_A has the form

$$G_A = \frac{m_1 s^4 + (m_1 \omega_3^2 + M\omega_1^2 + m_2 \omega_2^2 + m_3\omega_3^2)s^2 + M\omega_1^2\omega_3^2}{m_1 s^6 + \left[m_1(\omega_2^2+\omega_3^2) + M\omega_1^2 + m_2\omega_2^2 + m_3\omega_3^2\right]s^4 + M\left[\omega_1^2\omega_2^2 + \omega_1^2\omega_3^2 + \omega_2^2\omega_3^2\right]s^2 + M\omega_1^2\omega_2^2\omega_3^2}$$

$$(3.21)$$

with $M=m_1+m_1+m_1$ and $\omega_1,\omega_2,\omega_3$, the natural angular frequencies for the intermediate, test and reaction mass stages respectively.

This transfer function, though complicated in appearance, when plotted looks like that for a single pendulum with feedback from an identically suspended mass (the lower stages of the balanced system). The two zeros in the numerator cancel with two of the poles in the denominator. Thus at frequencies above the resonance of the test mass pendulum ($\omega \sim 4.8 \text{rads}^{-1}$), the open-loop transfer function, $H_C G_A$, will fall at 12dB/octave if H_C is constant in the frequency range considered.

The open-loop gain of the coil feedback loop was measured using the standard method employed in previous measurements (refer to Section 2.6). However, in order to be able to increase the amplitude of the test signal introduced to the reference mirror (auxiliary loop) at any given frequency (thus reducing the error in the measurements), a sine wave signal of a single frequency was used instead of a white noise signal. The circuits for the two feedback loops are shown in Figure 3.19 where the damping capacitor in the test mass circuit was relatively small (C_{damp}=100pF). Stability was maintained in the combined loop by the action of the auxiliary feedback to the reference mirror (as described in Section 2.6.2).

Figure 3.20 shows two sets of open-loop gain data obtained with different coil feedback gain settings. Both curves fall at 12dB/octave in the observed frequency range, as predicted. Furthermore, the unity gain frequency is observed to increase as the test mass feedback gain is increased as one would expect. By extrapolation, the highest unity gain frequency for this loop is at about 900Hz as shown in Figure 3.20 .

3.6.3 Interaction of the Test Mass and Auxiliary Feedback Loops

It is interesting to note that since both the auxiliary (feeding back to the reference mirror) and the test mass feedback loops were closed, the unity gain frequency of the test mass feedback loop does not dictate the new upper resonant frequency of the pendulum which was of the order of a few hundred hertz (refer to Section 2.6.2).
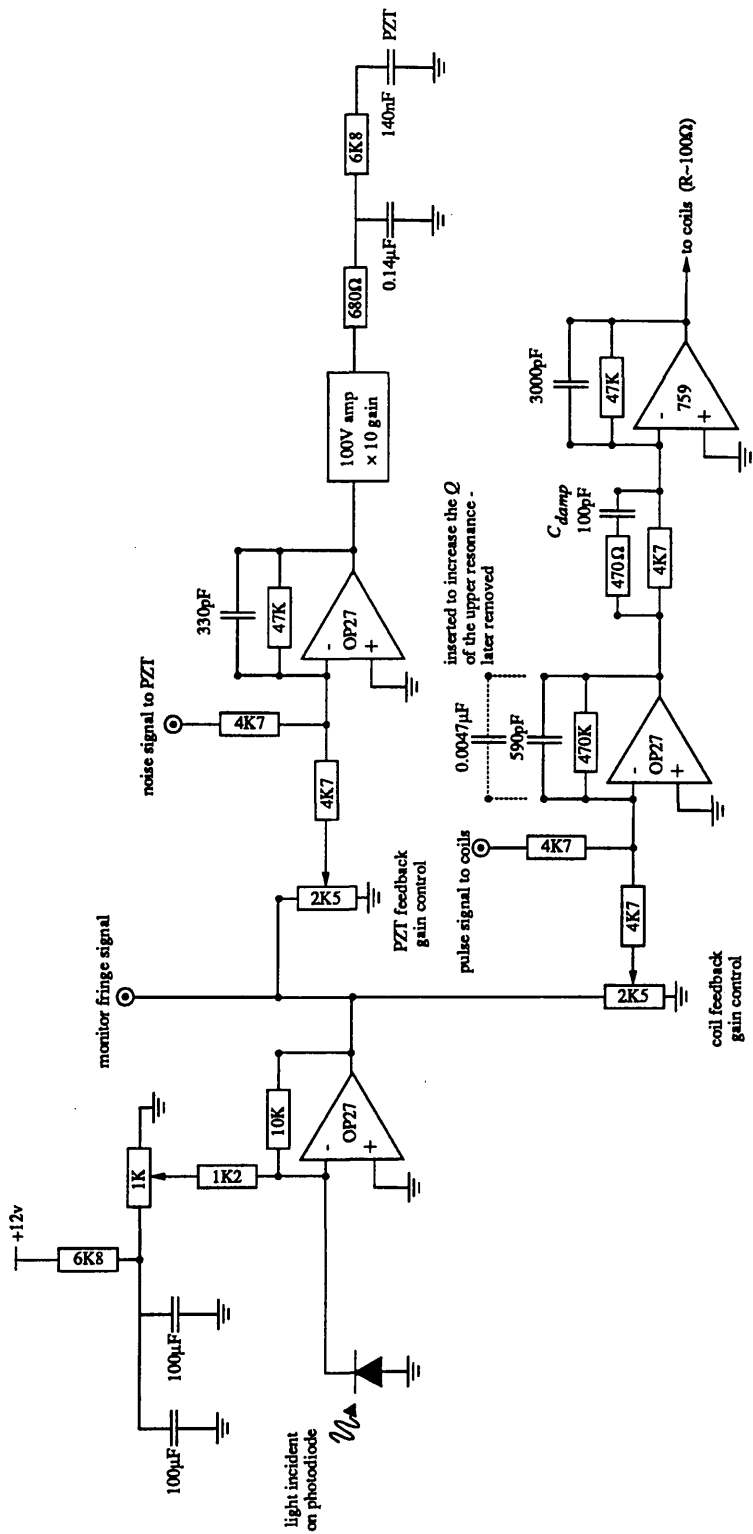
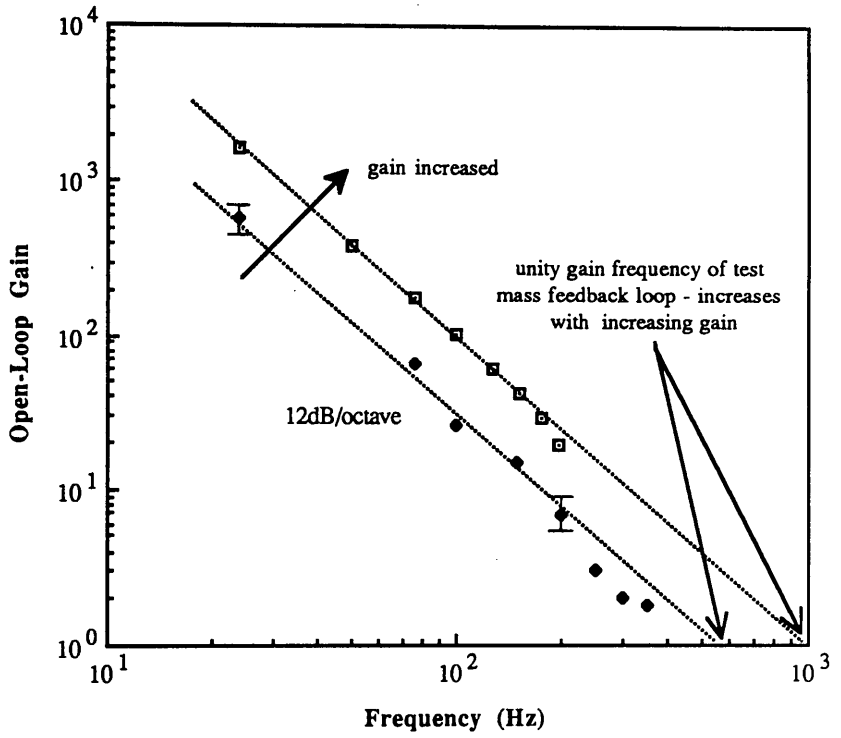*Figure 3.19   The circuit for the PZT and coil feedback loops.*

Figure 3.20 *Open-loop gain of the test mass feedback loop ($H_C G_A$) as a function of frequency for the balanced double pendulum with two different feedback gain settings. Typical error bars are shown.*

To demonstrate the effect of the interaction of the loops on the new upper resonant frequency, a simple experiment was conducted. White noise was fed into the auxiliary loop at the point shown in Figure 3.19. The loop diagram in this situation had the form shown in Figure 3.21.

auxiliary feedback loop (PZT)

test mass feedback loop
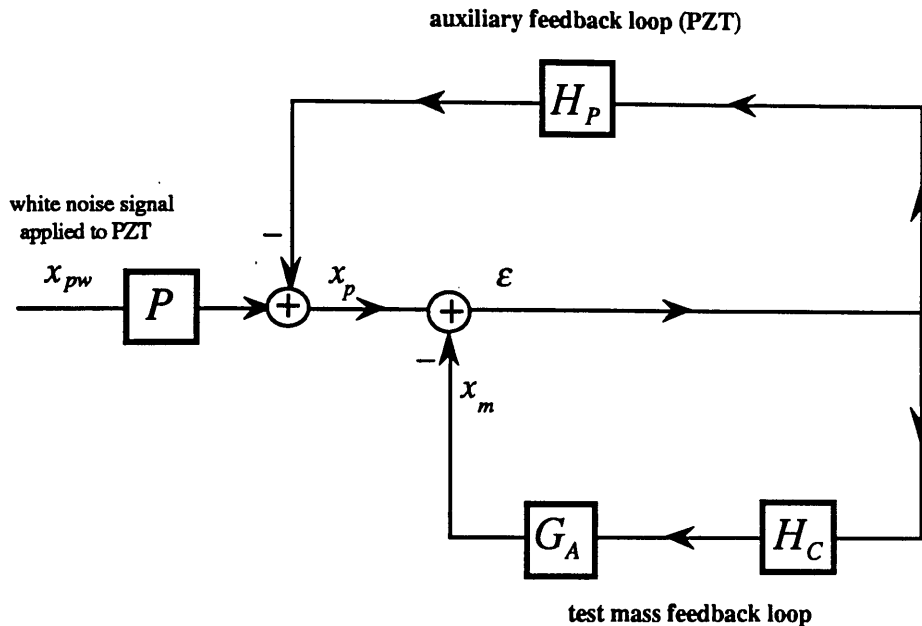
Figure 3.21   Loop diagram for the analysis of the unity gain frequencies of the two loops (with symbols as defined in text).

where x_{pw} is the white noise signal being applied and P is the electronic transfer function for the amplifier stages between the input port and the PZT. The transfer function from the acceleration produced by the feedback coils to the test mass displacement, G_A, is given by equation (3.21). All of the other symbols have their usual meaning (refer to Section 2.6.2). From this loop diagram it can be shown that:

$$\frac{x_p}{x_{pw}} = \frac{P(1 + H_C G_A)}{(1 + H_P + H_C G_A)} \tag{3.22}$$

where x_p is the signal measured directly on the PZT with both loops closed and the white noise applied. Note that the zero of this transfer function is at the unity gain frequency of the test mass feedback loop alone and that the pole of this transfer function

76

(the new upper resonant frequency of the pendulum) is at the unity gain frequency of the combined loops.

Figure 3.22 shows two experimentally measured spectra of the transfer function x_P/x_{pw} with fixed auxiliary loop gain and two different test mass feedback gain settings. These transfer functions were obtained by monitoring the voltage signals at the appropriate points in the loop (refer to Figure 3.21).

The transfer function x_P/x_{pw} was then modelled using MATLAB by considering the form of each of the separate transfer functions on the right hand side of equation (3.22). Figure 3.23 shows the two plots of x_P/x_{pw} which correspond to the experimentally measured spectra in Figure 3.22. The modelled transfer functions agree fairly well with the measured transfer functions at the two different gain settings. Note that each curve exhibits a null and a damped resonance peak as predicted, the damping being provided by the integration at $f\sim170$Hz in the auxiliary loop.

From these results we can see that the unity gain frequency of the combined loops (new upper resonant frequency) does indeed occur at a lower frequency than the unity gain frequency of the test mass feedback loop alone, as observed experimentally. Furthermore, the new upper resonance is being damped by the action of the auxiliary loop as predicted.

3.7 Conclusions

In this chapter it has been demonstrated, both theoretically and experimentally, that it is possible to control the position of a test mass suspended as a double pendulum over a large bandwidth (up to about a kilohertz or more), by sensing the position of, and applying a feedback signal directly to, the test mass.

As a consequence of using such large bandwidth feedback control, one of the resonances of the pendulum is forced to a much higher frequency which might lie within the detection frequency range of the proposed interferometric detector (in the region of about 100Hz to a few kilohertz). However, it has been shown that it is possible to electronically damp this resonance to a very high degree by incorporating a differentiation stage with the appropriate time constant in the feedback loop. Unfortunately, it is not possible to simultaneously damp the new lower resonance of the pendulum to a satisfactory level using the same feedback signal. To avoid dynamic range problems or the possibility of cross-coupling effects in the suspension, this lower frequency
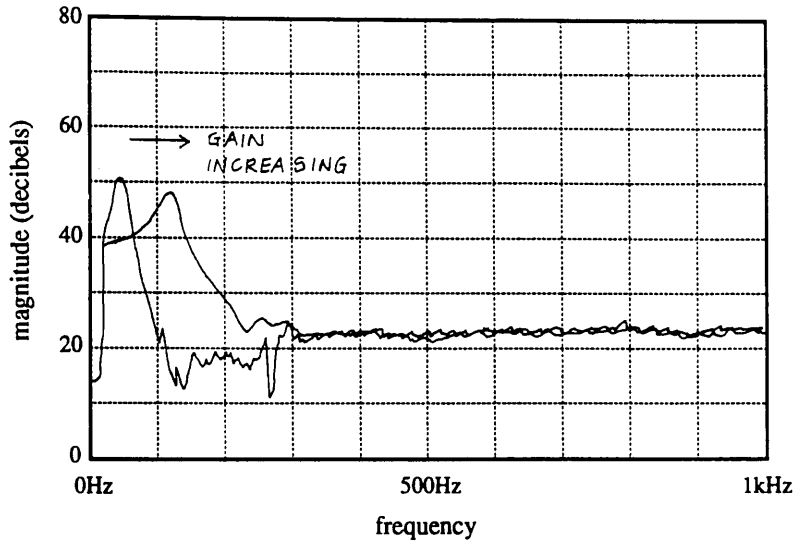
Figure 3.22 *Experimentally measured transfer function x_P/x_{pw} with two different test mass feedback gain settings. Both spectra exhibit a resonance and a null.*
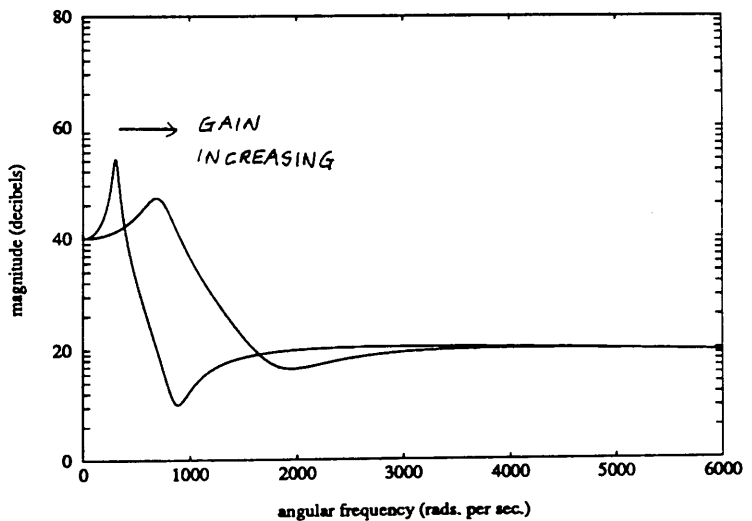

Figure 3.23 *Modelled transfer function x_P/x_{pw} with the two different feedback gain settings. The x-axis of this plot (given in units of rads^{-1}) is scaled to match Figure 3.22. The modelled curves compare well with the experimentally measured transfer functions.*

resonance must be damped by some other means *e.g.* by sensing the acceleration of, and feeding a signal to, the intermediate mass. Incorporating such a subsidiary damping loop in the suspension system has a secondary advantage in that it reduces the dynamic range requirements of the test mass position control loop, making it much easier for this loop to initially acquire lock.

It was also shown here that it is sensible to isolate the feedback transducers acting on the test mass to avoid the possibility of re-introducing seismic noise, shorting-out the passive isolation obtained by using the double pendulum suspension. Large bandwidth position control of a test mass suspended as part of a balanced double pendulum system has been demonstrated experimentally and there were no obvious problems with stability due to the introduction of the extra reaction pendulum stage.

It is possible in theory to design stable feedback systems whereby the motion of the lower mass of a double pendulum can be controlled by sensing the position of the lower mass and applying feedback signals solely to the intermediate mass. For instance this can be done by using three differentiation stages in the feedback electronics, or by using a feedback system similar to the 'Type I' system which is described later in this chapter. However it is believed that since large bandwidth control of the test mass is required (for the operation of laser interferometric detectors) such feedback systems would not operate satisfactorily in practice due to the unreasonable dynamic range requirements placed on the differentiating amplifiers. This would lead to instability at the higher frequencies. This subject is likely to be discussed more fully in a future publication.

Chapter 4

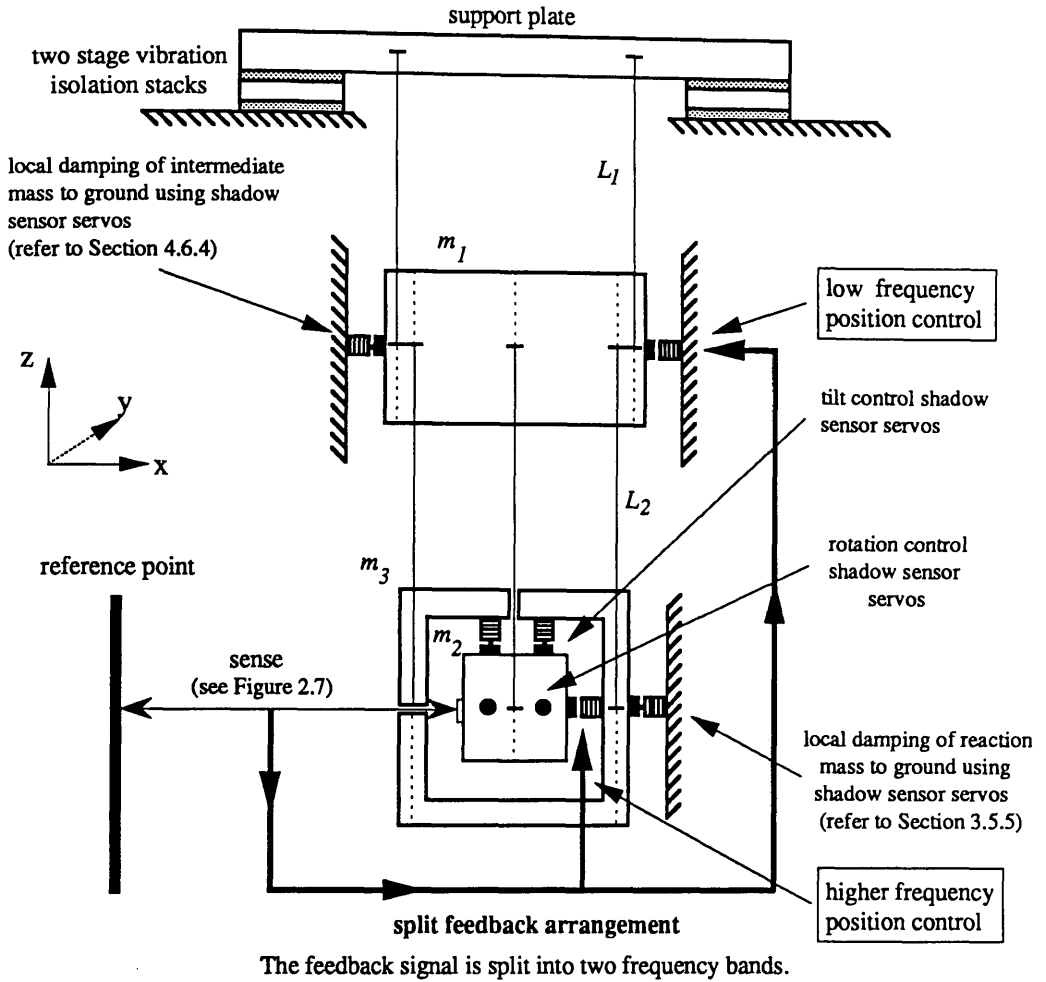# A Nested Double Pendulum System with Split Feedback Control

4.1 Introduction

A nested double pendulum suspension system with split (frequency selective) feedback control has been developed based on the theoretical and experimental investigations described in Chapters 2 and 3. This system has several special design features aimed at attempting to reduce the level of displacement noise occurring at the test mass due to the application of feedback control and damping signals.

The nested system essentially consists of a 'three-stage' double pendulum whose intermediate mass supports a test and reaction mass, on independent parallel suspensions, in such a way that the test mass is totally enclosed by the box-shaped reaction mass. This configuration enables the position and orientation of the test mass to be controlled *via* coil/magnet transducers coupling the test mass to the surrounding reaction mass (see Figure 4.1).

To reduce the level of displacement noise occurring at the test mass it would be desirable to avoid applying position control feedback signals directly to the test mass as discussed in Section 3.1. Initial investigations were conducted to see whether it would be possible in theory to control the motion of the lower mass of a double pendulum over a large bandwidth by applying feedback signals solely to the intermediate mass. In theory this appeared to be possible. However it seems highly unlikely that such a system would perform satisfactorily in practice due to the unreasonable dynamic range requirements placed on the electronics necessary for amplification and filtering.[*]

A reasonable compromise is to consider a split-feedback arrangement where the lower frequency feedback signals are applied to the intermediate mass, the higher frequency signals being applied to the test mass. Seismic noise is larger at low frequencies (see Section 2.2) and passive isolation is poorer (see Section 2.3), hence the

support plate

two stage vibration
isolation stacks

local damping of intermediate
mass to ground using shadow
sensor servos
(refer to Section 4.6.4)

L_1

m_1

low frequency
position control

tilt control shadow
sensor servos

z

y

x

L_2

rotation control
shadow sensor
servos

reference point

m_3

m_2

sense
(see Figure 2.7)

local damping of reaction
mass to ground using
shadow sensor servos
(refer to Section 3.5.5)

split feedback arrangement

higher frequency
position control

The feedback signal is split into two frequency bands.

intermediate mass	$m_1 \sim 11.0$kg	upper stage	$L_1 \sim 0.28$m	
		wire diameter	$d_1 = 0.31$mm	
test mass	$m_2 \sim 3.3$kg	lower stages	$L_2 \sim 0.45$m	
reaction mass	$m_3 \sim 2.3$kg	wire diameter	$d_2 = 0.23$mm	

Figure 4.1 **Schematic diagram of the nested double pendulum suspension system illustrating the split feedback control arrangement. In this system the test mass and surrounding reaction mass are independently suspended from the intermediate mass. The split feedback control arrangement is explained in more detail in Section 4.3.**

largest control signals are associated with these low frequency corrections. It is possible that if these low frequency signals are applied directly to the test mass they might give rise to higher frequency displacement noise at the test mass *via* non-linear conversion in the feedback electronics or transducers. However such noise imposed on the intermediate mass by application of the large low frequency control signals will be attenuated by the high Q suspension in its effect on the test mass.

Two split-feedback systems ("Type I" and "Type II", which involved different feedback bandwidths to the two masses) were designed for application to the nested double pendulum. Initially the behaviour of the nested pendulum with feedback applied solely to the test mass was investigated experimentally to ensure that there were no obvious problems associated with the novel pendulum design. Each of the split-feedback systems were then tested experimentally to assess their performance.

4.2   Design Philosophy

The nested double pendulum system is illustrated schematically in Figure 4.1. This system incorporates a top supporting plate mounted on two stages of isolation stack. The 'three-stage' double pendulum is then suspended from this isolated plate. The intermediate mass is suspended using double loops. Ideally single loop suspension should be used for this mass to reduce the possibility of ground tilts coupling to the pendulum. The reaction (box) mass in this system is also suspended using double loops. The test mass is suspended using a single loop to enable the orientation of the test mass in tilt (about the y-axis) and rotation (about the z-axis) to be controlled by way of shadow sensor coil/magnet assemblies coupling the test mass to the reaction mass. For the dimensions of wires chosen, the lowest frequency violin resonances were calculated to be at $f{\sim}470$Hz, 150Hz and 250Hz for the intermediate, reaction and test mass suspensions respectively.

The separation of all coil/magnet pairs is chosen such that the magnets lie in the position of constant coil field gradient, reducing spurious coupling effects (see Section 3.5.3). However, it is shown in Appendix A that electromagnetic coupling effects can take place between these coil/magnet pairs possibly damping the high Q pendulum to what might be an unacceptably low level. To reduce the level of damping of the test mass in the test direction due to this effect the axes of the tilt and rotation control coils in the nested system are arranged to lie perpendicular to the horizontal test direction

(see Figure 4.1).

Another important design feature of this system is of course the split (frequency selective) feedback arrangement as shown in Figure 4.1. The error point signal ε sensed between the test mass and the reference point can be split into two frequency bands. The lower frequency signals can be fed back to the intermediate mass (by way of coils mounted on the ground, though ideally these coils would be connected to the top of the stacks), with the higher frequency signals being fed to the test mass *via* longitudinal driving coils mounted on the suspended reaction mass. This reduces the noise imposed on the test mass due to the feedback control signals as discussed in Section 4.1.

Furthermore, as a consequence of limiting the feedback between the test mass and reaction mass to the higher frequency smaller magnitude signals, less flux linkage is required for the coil/magnet position controlling transducers. This reduces the magnitude of the damping of the suspended test mass due to electromagnetic induction (see Appendix A).

The reaction mass in this system is damped electronically to the ground using shadow sensor feedback systems (see Section 3.5.5) and latterly, the intermediate mass was also damped electronically to the ground (see Section 4.6.4).

4.3 Split Feedback Control

It was shown in Chapter 3 that it is relatively straightforward to maintain stability in the closed-loop system when sensing the position of, and feeding signals directly to, the lower mass of a double pendulum if differentiation is used in the feedback electronics. The use of differentiation ensures that the open-loop transfer function has a phase greater than -180° at frequencies where the gain is close to unity, avoiding the possibility of positive feedback. The ease of achieving stability in such a double resonance system is largely due to the fact that the open-loop transfer function contains a zero which lies at a frequency between the two natural poles (pendulum resonances) each having an associated -180° phase change. This zero provides a +180° phase change after the first resonance which ensures that the Nyquist curve for the system does not enclose the point (-1,0) and hence is stable (see Section 2.5.3). The relative stability is of course determined by the degree of differentiation used in the feedback electronics. However when feeding back to the intermediate mass in such a system, there is a fundamental difference in the open-loop transfer function which makes it much less simple to maintain

stability in the feedback loop, as will be illustrated below.

Consider the nested double pendulum where feedback forces are applied to the masses in both stages simultaneously, as shown in Figure 4.2.
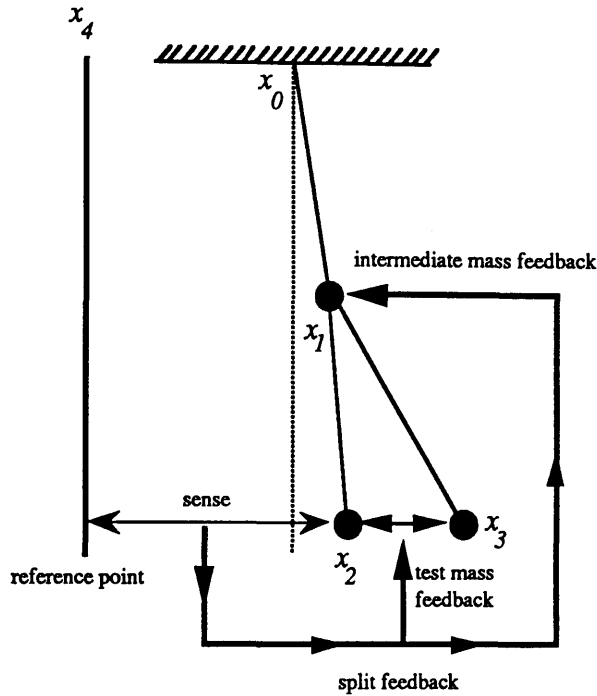

Figure 4.2 Sketch of the nested double pendulum with split-feedback control. The position of the test mass is sensed with respect to the reference point. The feedback signal is then split into two frequency bands with the low frequency signals being applied to the intermediate mass and the higher frequency signals being applied to the test mass.

The upper stage of the nested pendulum has natural angular resonant frequency $\omega_1 \sim 5.9 \text{rads}^{-1}$, with the two identical lower stages having frequency $\omega_2 = \omega_3 \sim 4.7 \text{rads}^{-1}$ (test mass and reaction mass stages respectively). The position of the test mass x_2 is sensed relative to an arbitrary reference point x_4 and the feedback forces acting on the intermediate and test masses are of the form $F_1 = m_1 H_1 (x_4 - x_2)$ and $F_2 = m_2 H_2 (x_4 - x_2)$ respectively.

The loop diagram representation of this split-feedback system is shown in Figure 4.3, assuming that the motion of the suspension point is zero i.e. $x_0 = 0$:
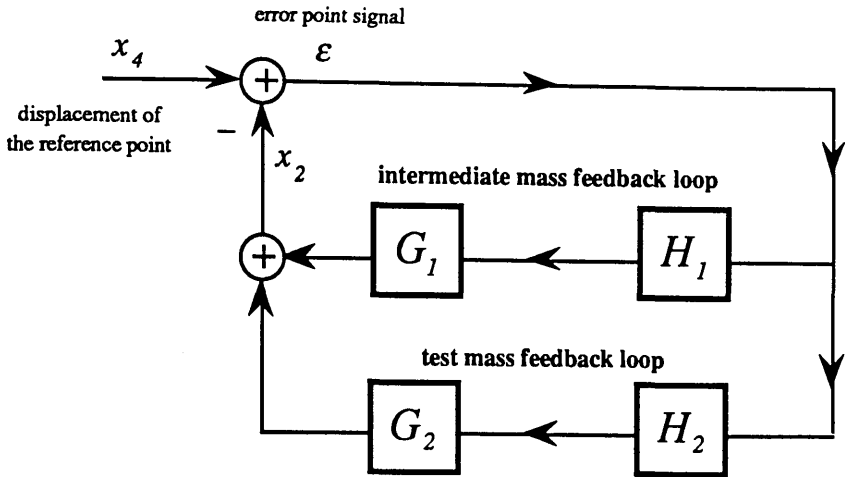
Figure 4.3 *Loop diagram for the split-feedback arrangement applied to the nested double pendulum (symbols as defined in text).*

This can be simplified to the single loop equivalent shown in Figure 4.4:
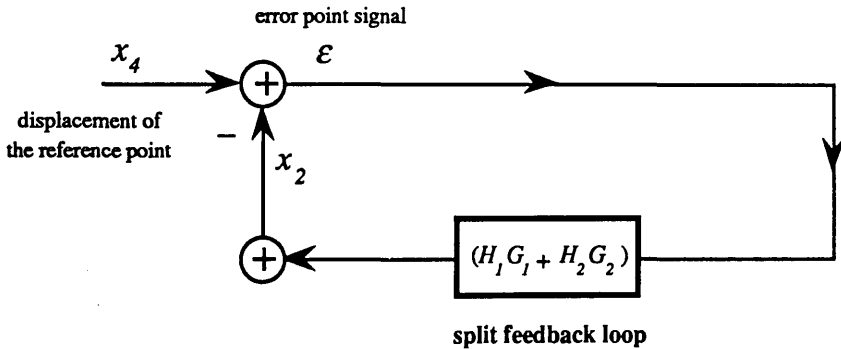

split feedback loop

Figure 4.4 *Simplified loop diagram for the split-feedback arrangement applied to the nested double pendulum (symbols as defined in text).*

where,

x_4 = the motion of the reference point (reference mirror (see Section 2.6.))

x_2 = the displacement of the test mass with both of the feedback loops closed

ε = the error point signal with the feedback loops closed = $x_4 - x_2$

H_1 = the transfer function for the conversion of the detected fringe signal ε in terms of displacement, to the acceleration produced by the coil/magnet

83

feedback transducers acting on the intermediate mass. The frequency dependence of this function is determined by the form of the electronics used for amplification/filtering. Note also that this function has dimensions of sec^{-2}.

H_2 = similar to H_1, except refers to the transducers acting between the test mass and the reaction mass (dimensions of sec^{-2}).

G_1 = the transfer function for the feedback acceleration of the intermediate mass, to the resulting test mass displacement (dimensions of sec^2) i.e.

$$G_1 = \frac{\omega_2^2(s^2 + \omega_3^2)}{s^6 + [A\omega_1^2 + B\omega_2^2 + C\omega_3^2]s^4 + A(\omega_1^2\omega_2^2 + \omega_1^2\omega_3^2 + \omega_2^2\omega_3^2)s^2 + A\omega_1^2\omega_2^2\omega_3^2} \quad (4.1)$$

G_2 = similar to G_1 except refers to the feedback acceleration of the test mass (dimensions of sec^2) i.e.

$$G_2 = \frac{s^4 + (A\omega_1^2 + \alpha_2\omega_2^2 + C\omega_3^2)s^2 + A\omega_1^2\omega_3^2}{s^6 + [A\omega_1^2 + B\omega_2^2 + C\omega_3^2]s^4 + A(\omega_1^2\omega_2^2 + \omega_1^2\omega_3^2 + \omega_2^2\omega_3^2)s^2 + A\omega_1^2\omega_2^2\omega_3^2} \quad (4.2)$$

The open-loop transfer function $(H_1G_1 + H_2G_2)$ is therefore given by:

$$(H_1G_1 + H_2G_2) = \frac{H_1\omega_2^2(s^2 + \omega_3^2) + H_2[s^4 + (A\omega_1^2 + \alpha_2\omega_2^2 + C\omega_3^2)s^2 + A\omega_1^2\omega_3^2]}{s^6 + [A\omega_1^2 + B\omega_2^2 + C\omega_3^2]s^4 + A(\omega_1^2\omega_2^2 + \omega_1^2\omega_3^2 + \omega_2^2\omega_3^2)s^2 + A\omega_1^2\omega_2^2\omega_3^2}$$
$$(4.3)$$

where the coefficients $A = (1+\alpha_2+\alpha_3)$, $B = (1+\alpha_2)$ and $C = (1+\alpha_3)$, with the mass ratios $\alpha_2 = m_2/m_1$ and $\alpha_3 = m_3/m_1$. The corresponding closed-loop transfer function $\frac{1}{1 + (H_1G_1 + H_2G_2)}$ can be derived easily using equation (4.3).

This pendulum has three natural modes of oscillation as shown in Figure 4.5.
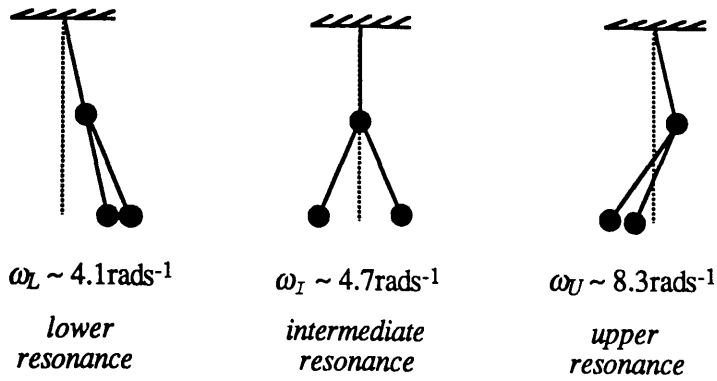
$\omega_L \sim 4.1 \text{rads}^{-1}$ $\omega_I \sim 4.7 \text{rads}^{-1}$ $\omega_U \sim 8.3 \text{rads}^{-1}$

lower *intermediate* *upper*
resonance *resonance* *resonance*

Figure 4.5 ***The three natural resonances of the nested double pendulum.***
The presence of the reaction mass pendulum in parallel with the test mass pendulum gives rise to the additional resonance at ω_I.

From equation (4.3), one can see that when $H_1 = 0$ and feedback is applied solely to the test mass from the suspended reaction mass, the open-loop transfer function has two zeros and three poles. Two of these poles are in fact cancelled by the two zeros leaving one remaining pole corresponding to the natural resonance of the lower stages of the system ($\omega_I = \omega_2 = \omega_3 \sim 4.7 \text{rads}^{-1}$) as shown in Figure 4.5. This loop is similar in form to that for a simple pendulum with feedback applied from an uncoupled point *e.g.* the ground. It is therefore fairly straightforward to achieve stability by using differentiation in the feedback electronics. When $H_2 = 0$ and feedback is applied solely to the intermediate mass (from an uncoupled point), there is a pole-zero cancellation at $\omega_I = \omega_3$. In this situation the closed-loop system is inherently unstable since there are two -180° phase changes in close succession associated with the two remaining poles at $\omega_L \sim 4.1 \text{rads}^{-1}$ and $\omega_U \sim 8.3 \text{rads}^{-1}$.

A way of achieving stability when feeding back to the intermediate mass alone ($H_2 = 0$) would be to introduce an artificial zero between the two natural poles, giving a +180° phase change and close to zero magnitude at the selected frequency in the open-loop transfer function. One way of doing this is by using a parallel-T-network in the feedback circuit [Hammond 1958]. This network (or notch) gives a high attenuation at a selected frequency and can be designed in such a way that it produces a +180° phase change at this frequency. Figures 4.6 and 4.7 show the gain and phase characteristics of such a notch derived using MATLAB.
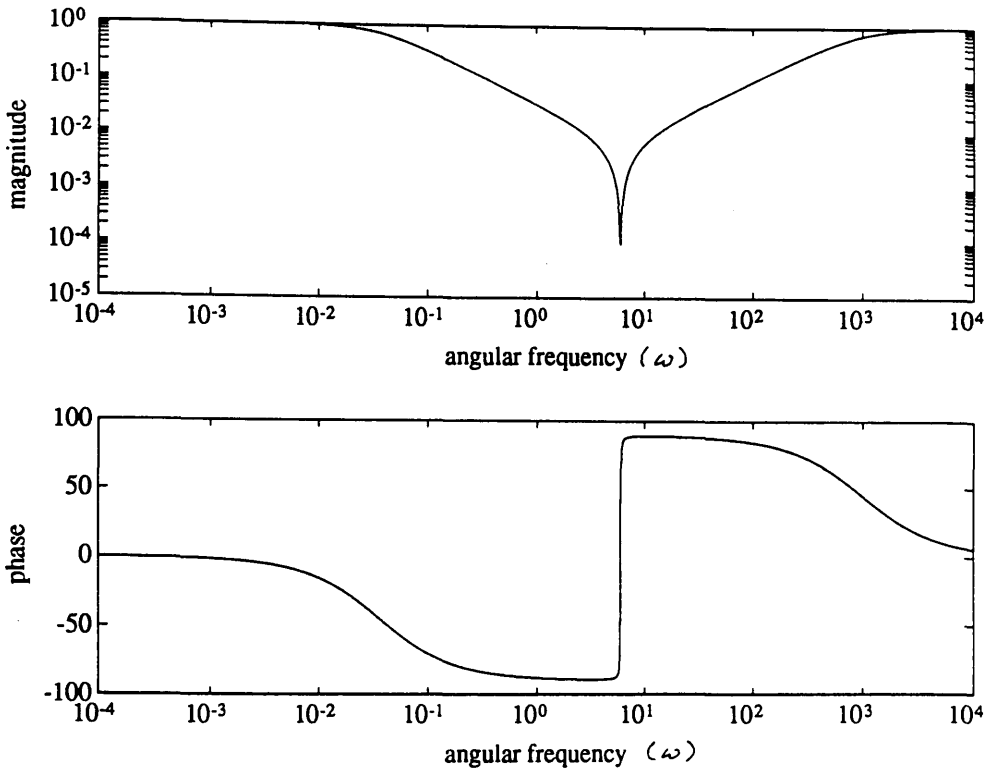
Figures 4.6 & 4.7   Bode magnitude and phase plots for a Parallel-T-Network.

The notch frequency in this example was designed to occur at $\omega_{notch}\sim 6\text{rads}^{-1}$. The desired null and associated $+180^\circ$ phase change are exhibited. However note that the phase on approaching the rejection frequency is -90°. If not compensated for, this negative phase introduced in the region of the first (lower) pendulum resonance would cause the feedback system for the double pendulum to become unstable.

4.4   Initial Experimental Investigations

The behaviour of the nested pendulum system with all of the position control feedback signals applied directly to the test mass *via* the feedback coils mounted on the reaction mass was investigated experimentally. This initial investigation was carried out prior to the installation of a split-feedback scheme to check that there were no obvious problems associated with the novel pendulum design or interaction of the shadow sensor damping loops with the main position control loop.

The rotational motions of the test mass about the y (tilt) and z -axes (see Figure 4.1) were damped electronically using two shadow sensor feedback systems (see Section 3.5.5) in each degree of freedom. The reaction mass was also damped to the ground using two such shadow sensor devices. The circuits used are shown in Figure 4.8. Note that these circuits are D.C. coupled. This means that each resonance would not only be damped but would be forced to slightly higher frequency depending on the gain in the relevant loop. Each of these shadow sensor feedback loops were observed to adequately damp their respective motions preserving the optical alignment of the interferometer.

With the above loops closed the position of the test mass was locked to the reference mirror with the aid of some gain in the auxiliary feedback loop (which controlled the position of the reference mirror) to initially slow down the rate of fringe passage (refer to Section 2.6.1). Once lock was achieved the gain in the auxiliary loop was reduced to zero. The circuit used for the test mass feedback loop is shown in Figure 4.9 with the damping capacitor having a value of C_{damp}=0.47μF. Three sets of open-loop gain data were obtained using the standard method described in Section 2.6. Sine wave signals of a single frequency $\overset{were}{\wedge}$ used to drive the PZT on which the reference mirror was mounted. The electronic gain setting was similar for each set of measurements. The open-loop gain curves obtained are shown in Figure 4.10.

From Figure 4.10 one can see that the three sets of data are consistent. To compare with experiment, the open-loop transfer function was modelled using equation (4.3) with H_1=0. The calibration for the displacement of the test mass per volt across the position control feedback coils was $\Delta x / \Delta V \sim 0.2$ mm/V with the photodiode calibration being $\Delta V / \Delta x \sim 6.4 \times 10^3$ V/mm. The model predicted the gradient of the open-loop gain curve to be 12dB/octave until approximately 60Hz where the presence of the damping capacitor C_{damp}=0.47μF caused a reduction in the gradient. This was observed. The predicted unity gain frequency was about 500Hz which agrees fairly well with the extrapolated value.

In order to search for the new upper resonant frequency with the loop closed, the damping capacitor was reduced to C_{damp}=0.1μF. The maximum observed upper resonant frequency was at f_{upper}~220Hz and had a Q of a few. Reducing the damping capacitor in this way caused a reduction in the unity gain frequency.
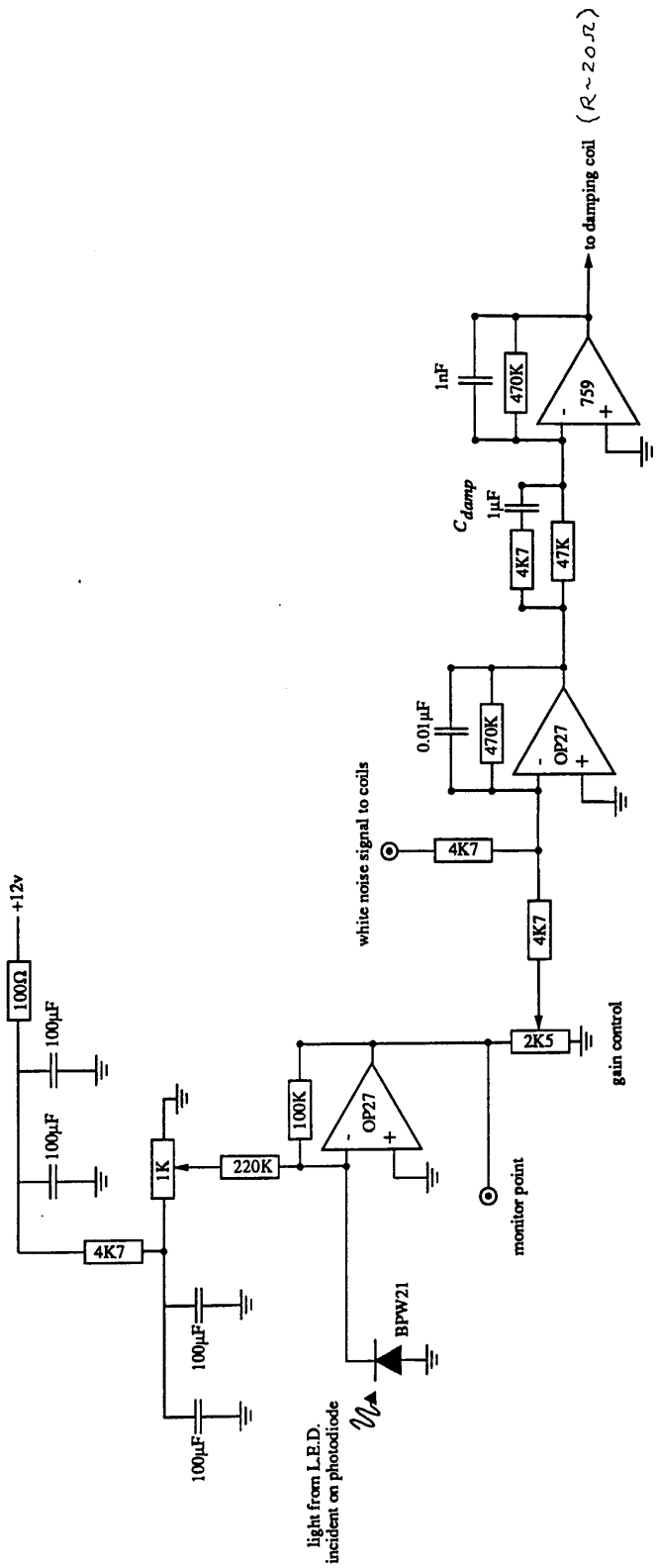
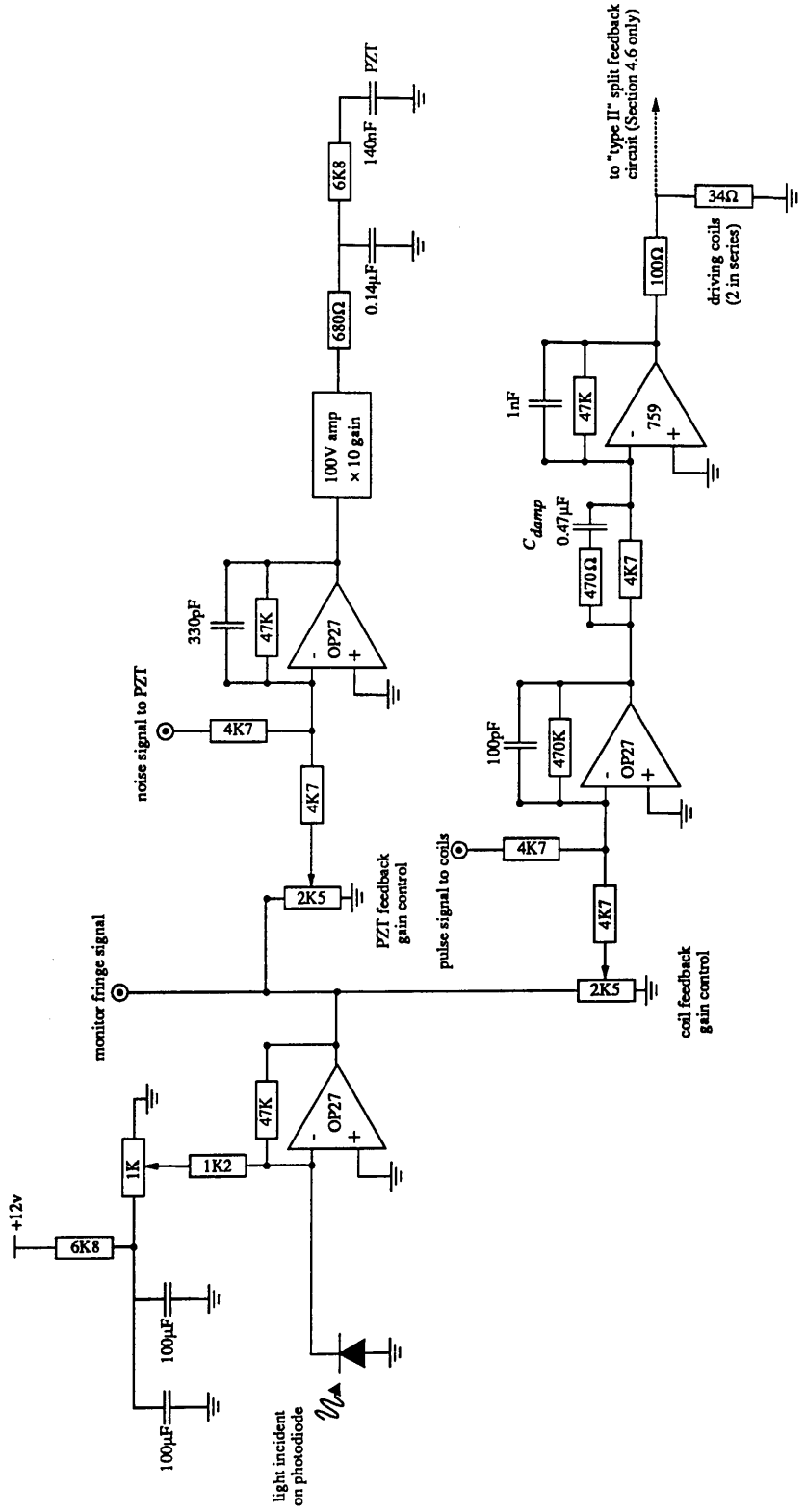*Figure 4.8 The circuit for the shadow sensor damping servos.*

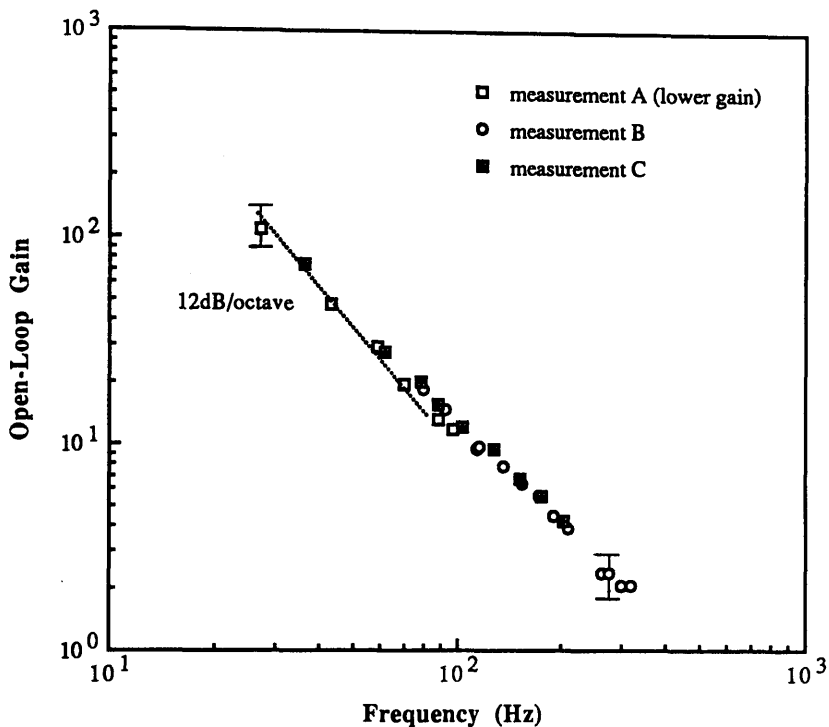*Figure 4.9 The circuit for the PZT and coil feedback loops.*

Figure 4.10 Open-loop gain data for the nested double pendulum system where all of the position control signals are applied directly to the test mass via coils mounted on the surrounding reaction mass.

These initial investigations were suitably encouraging since there were no obvious problems associated with the novel pendulum design or interaction of the shadow sensor damping loops with the main position control loop.

4.5 Split-Feedback System - "Type I"

4.5.1 Initial Design

The designed Type I split-feedback system used a parallel-T-network similar to that described in Section 4.3 to achieve stability in the intermediate mass feedback loop. The forms of H_1 (intermediate mass loop) and H_2 (test mass loop) used are described below

88

in terms of their filter corner frequencies:

$$H_1 \equiv \begin{bmatrix} \text{gain of} \\ \sim1\times10^4 \end{bmatrix} \cdot \begin{bmatrix} \text{minimum phase} \\ \text{notch with } \omega\sim6\text{rads}^{-1} \end{bmatrix} \cdot \begin{bmatrix} \text{two differentiations from} \\ \omega\sim0.45\text{rads}^{-1} \text{ to } \omega\sim310\text{rads}^{-1} \end{bmatrix} \cdot \begin{bmatrix} \text{two integrations} \\ \text{at } \omega\sim450\text{rads}^{-1} \end{bmatrix}$$

$$H_2 \equiv \begin{bmatrix} \text{gain of} \\ \sim8\times10^4 \end{bmatrix} \cdot \begin{bmatrix} \text{minimum} \\ \text{phase notch} \\ \text{with } \omega\sim6\text{rads}^{-1} \end{bmatrix} \cdot \begin{bmatrix} \text{differentiation from} \\ \omega\sim0\text{rads}^{-1} \text{ to } \omega\sim130\text{rads}^{-1} \end{bmatrix} \cdot \begin{bmatrix} \text{differentiation from} \\ \omega\sim450\text{rads}^{-1} \text{ to} \\ \omega\sim9.7\times10^3\text{rads}^{-1} \end{bmatrix} \cdot \begin{bmatrix} \text{one integration at} \\ \omega\sim3.1\times10^4\text{rads}^{-1} \end{bmatrix} \cdot$$

Note that H_2 is A.C. coupled.

The modelled Bode magnitude plots for the separate feedback loops (H_1G_1 and H_2G_2) are shown in Figure 4.11. The feedback signal to the intermediate mass dominates at low frequencies below a few tens of hertz. Figure 4.12 shows the Bode magnitude plot for the combined loop. The bump in the curve at about 30Hz marks the approximate cross-over frequency between the two loops. The unity gain frequency of the combined loop is at $\omega_{unity\ gain}\sim3\times10^3\text{rads}^{-1}$ ($f\sim480$Hz). The gain margin is ~14 with a phase margin of ~70° and therefore the system is stable (see Section 2.5.3).

The Nyquist plot for the Type I split-feedback system is shown in Figure 4.13. The system is stable since the Nyquist curve does not enclose the (-1,0) point (see Section 2.5.3). The two differentiations in H_1 at $\omega\sim0.45\text{rads}^{-1}$ provide sufficient phase lead to ensure that the first resonance loop at $\omega_L\sim4.1\text{rads}^{-1}$ lies in the 1st, 4th and 3rd quadrants. Two differentiations are necessary to compensate for the negative phase change ($\rightarrow$-90°) introduced by the notch at frequencies below the rejection frequency (see Figure 4.7) and to provide some phase lead (damping of the lower resonance). The intermediate resonance at $\omega_I\sim4.7\text{rads}^{-1}$ is not completely cancelled by the zero in H_1G_1 since H_2G_2 has large magnitude at this frequency (see Figure 4.11) and this causes the observed phase fluctuation in the Nyquist plot at $\sim\omega_I$. The notch at $\omega_{notch}\sim6\text{rads}^{-1}$ produces a minimum (with a +180° phase change) in the transfer function before the upper resonance at $\omega_U\sim8.3\text{rads}^{-1}$ ensuring that this resonance loop does not encircle the point (-1,0). Note that the notch is also present in H_2 to ensure that H_2G_2 does not dominate at the notch frequency reducing the effective depth of the null (see Figure 4.11). Differentiation is present in H_2 to establish the feedback cross-over frequency to be at about 30Hz. H_1 is then rolled-off (integrated) at a frequency higher than this cross-over between the two feedback loops to avoid saturation of the feedback amplifiers driving the intermediate mass. The differentiation in H_2 at ~450rads^{-1} maintains the phase lead necessary for stability at the higher frequencies. H_2 is then rolled-off above the unity
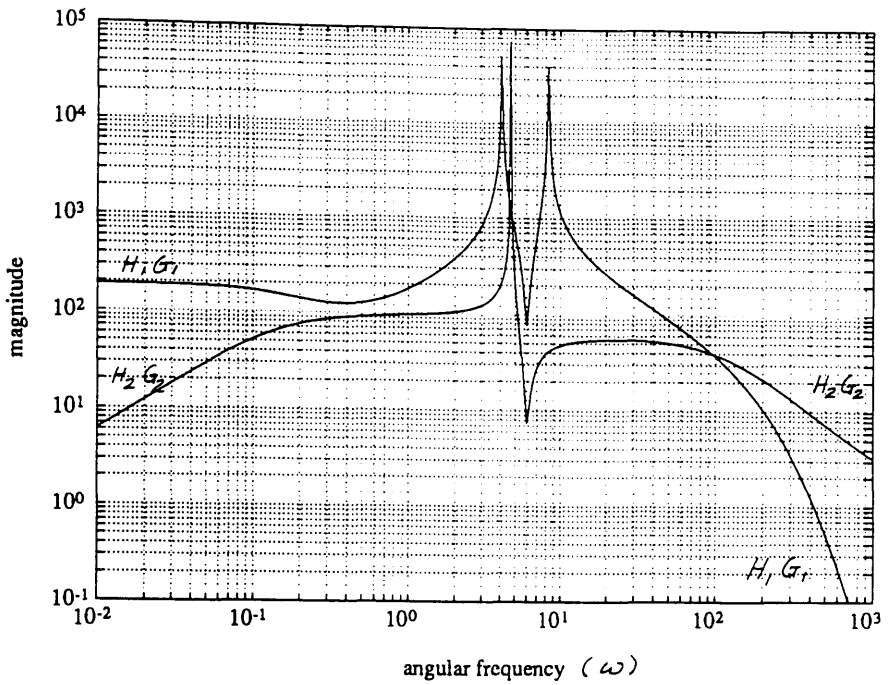
Figure 4.11 **Bode magnitude plots of the open-loop transfer functions H_1G_1 and H_2G_2 with the Type I split-feedback design.**
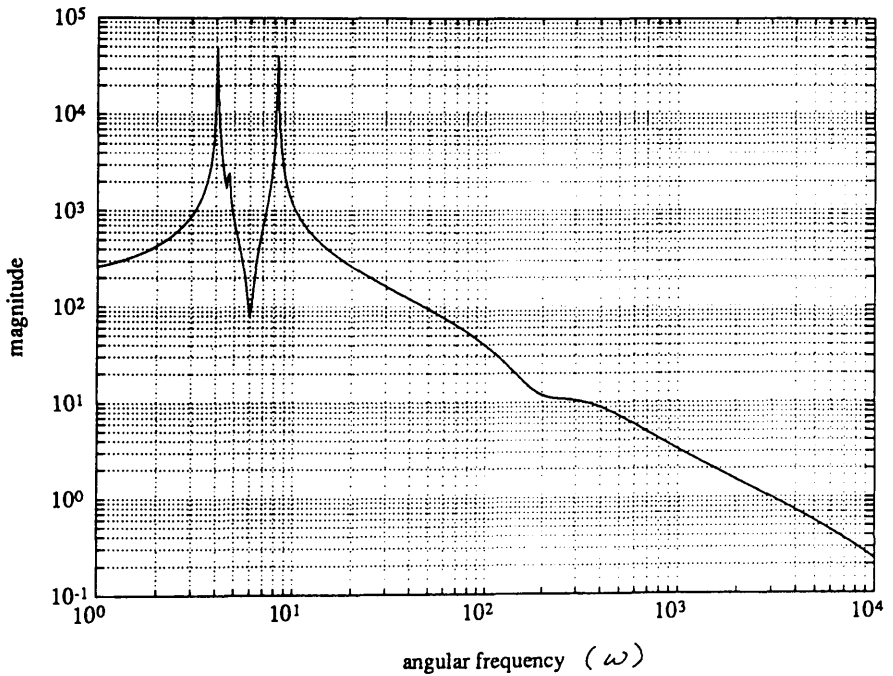

Figure 4.12 **Bode magnitude plot of the open-loop transfer function $(H_1G_1 + H_2G_2)$ with the Type I split-feedback design.**
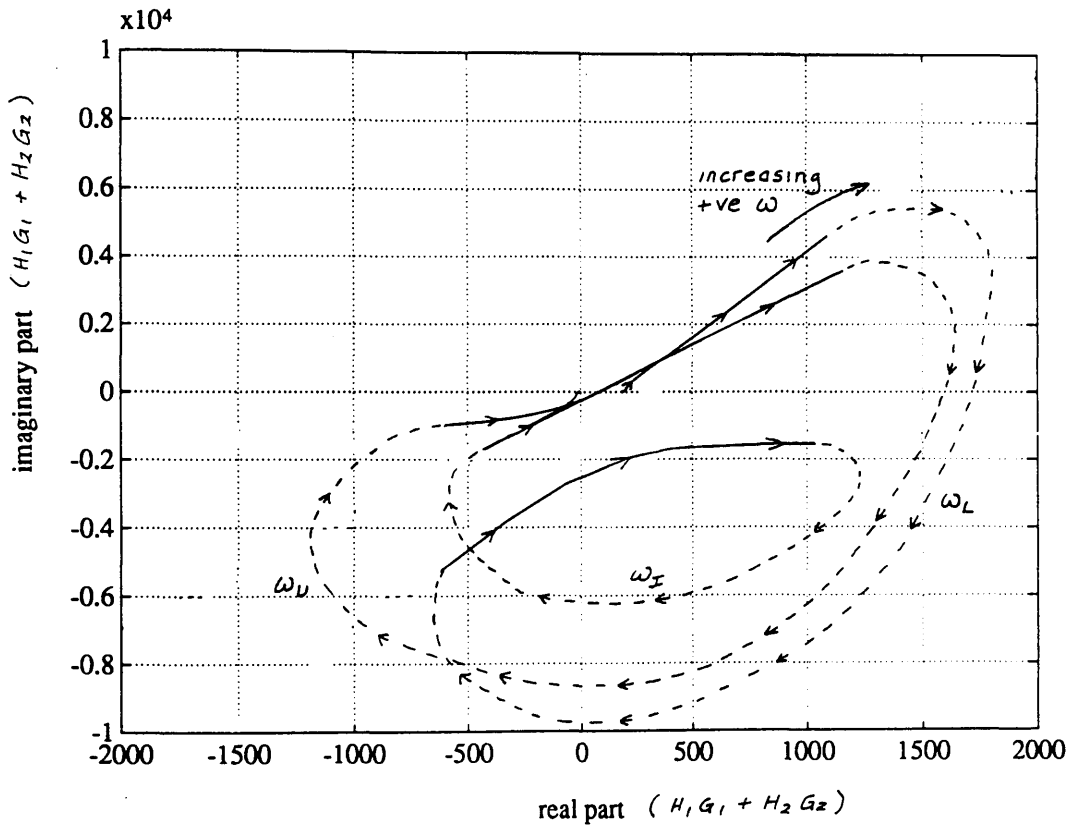
Figure 4.13 Nyquist plot for the Type I split-feedback system.

gain frequency of the split-feedback loop.

4.5.2 Performance

The transfer function of the notch was measured. An attenuation of ~55dB with a phase change of $+180^0$ at $\omega_{notch} \sim 6 \text{rads}^{-1}$ ($f \sim 0.96 \text{Hz}$) was obtained as desired. The rotational (about the z-axis) and tilting (about the y-axis) motions of the test mass were damped using the shadow sensor devices described in Section 4.4 (see Figure 4.1). The reaction mass was also damped to the ground here as in Section 4.4. Recall that the natural frequency of the reaction pendulum may have been forced to a higher frequency by the action of this loop since the feedback circuit used was D.C. coupled. However the gain in this loop was kept low and this effect should have been small. Furthermore it was shown theoretically that the effect of this shadow sensor feedback loop on the pole-zero configuration of the nested pendulum would not compromise the stability of the Type I split-feedback system even if the reaction pendulum frequency was forced up to a relatively high frequency *e.g.* 10Hz.

With the shadow sensor loops damping their respective motions the performance of the Type I split-feedback system was tested. The test mass feedback loop (high frequency feedback) was observed to operate satisfactorily. If the gain in this loop was turned too high it became unstable at ~800Hz (approximately the unity gain frequency). However the gain which could be used in the low frequency feedback loop was severely limited by various mechanical resonances which were excited by the application of feedback signals to the intermediate mass. These resonances, which were not accounted for in the loop design, caused the feedback signal to the intermediate mass to saturate at very low gain.

For example, two such troublesome resonances were at ~20Hz and ~30Hz. These were suspected to be tilting resonances of the intermediate mass and the top plate about the y-axis (see Figure 4.1). If the coil/magnet transducers were not acting exactly along the centre of mass of the intermediate mass it is feasible that such resonances could be excited since the intermediate mass was suspended using double wire loops. In order to investigate this further the test feedback loop was D.C. coupled and used to lock the position of the test mass to the reference mirror. The intermediate mass was then driven over a range of frequencies. Two peaks were observed in the residual fringe signal at the frequencies corresponding to these two resonances. This verified that these were indeed mechanical resonances and were not associated with the designed feedback loop. The

tilting motion of the intermediate mass was damped with respect to the support framework by connecting a vertical paddle immersed in an oil pot to each end of the mass.

Another troublesome resonance was at ~45Hz and this was suspected to be a tilting resonance of the reaction mass. Oil damping pots and vertical paddles were attached to each end of the reaction mass in such a way as to damp this tilting motion.

Another resonance which caused the intermediate mass feedback signal to saturate was at ~24Hz. A smaller peak at ~12Hz was also observed in the feedback signal. It was suspected that these peaks were associated with the stacks connecting the support plate of the pendulum to the support framework. A vertical accelerometer placed on the top support plate showed peaks at these frequencies. To try to improve the damping of the pendulum masses in the vertical direction thicker oil was used in the oil damping pots. On doing this the 12Hz peak was observed to be much better damped. However the 24Hz peak was still causing the feedback signal to saturate. The stacks were shorted out by clamping the top plate to the support frame and this reduced the amplitude of the 24Hz peak. However the gain which could be used in the intermediate mass feedback loop was once more limited by the 12Hz oscillation.

Since the clamps ruined the alignment of the shadow sensors which were used to damp the box to the ground they were removed. Instead the top support plate was damped to the support frame using vertical paddles attached to the ends and centre of the plate and immersed in pots containing very thick oil. An accelerometer on top plate showed that the peak at ~12Hz was well damped. The peak at ~24Hz was also damped to some degree. The intermediate mass feedback signal was now seen to saturate at ~24Hz. Smaller peaks were also present in the feedback signal at ~12Hz and ~48Hz.

Throughout these experimental investigations attempts were made to reduce the gain in the intermediate mass feedback loop at the frequencies where the resonance peaks were encountered. This was done by introducing lower frequency integrations in the electronics used in this feedback loop. However it was not possible to reduce the gain rapidly enough to avoid exciting these troublesome resonances.

4.5.3 Conclusions

The analysis presented here shows that it is possible in theory to control the position of a test mass suspended as a double pendulum using split-feedback, avoiding feeding the

large low frequency signals (below about 30Hz) directly to the test mass, without losing stability and without imposing unreasonable dynamic range requirements on the feedback amplifiers. Unfortunately it was not possible to demonstrate the operation of this split-feedback system experimentally since practical difficulties were encountered which were not intrinsically related to the designed feedback system. The designed feedback system accounted for the presence of the three fundamental pendulum resonances in the horizontal test direction (see Figure 4.5). However no account was taken of the effects of the pendulum resonances in the remaining degrees of freedom or the effects of the resonances of the isolation stacks and support structure which connected the pendulum to the ground. The excitation of such extraneous resonances by the application of feedback signals to the intermediate mass caused the feedback amplifiers in this loop to saturate at very low gain and a significant cross-over frequency was never achieved. However the performance of the Type I split-feedback system should be further investigated since there is no fundamental reason why it should not operate satisfactorily if care is taken in the construction and design of the isolation system and support framework to minimise the effects of these extraneous resonances.

4.6 Split-Feedback System - "Type II"

4.6.1 Initial Design

The Type II split-feedback system was less ambitious than the Type I system in that the feedback cross-over frequency between the two loops occurred at a much lower frequency (at a frequency below the first pendulum resonance). Despite this lower cross-over frequency, the Type II system should be capable of reducing the noise level at the test mass by a significant amount since the largest of the low frequency signals are applied to the intermediate mass (see Section 4.1).

This split-feedback system was based on the feedback system used to control the test mass *via* signals applied solely to the test mass, as described in Section 4.4. The output signal from the circuit in Figure 4.9 is applied directly to the test mass as previously. However this signal is then further amplified and filtered and fed to the transducers acting on the intermediate mass. The extra amplification is designed to be of a large enough magnitude that the intermediate mass feedback loop dominates at frequencies below the pendulum resonances. Above the resonances the system is

designed to behave similarly to the original test mass feedback loop.

The forms of H_1 (intermediate mass loop) and H_2 (test mass loop) used initially are described below in terms of their filter corner frequencies:

$$H_1 \equiv \begin{bmatrix} \text{gain of} \\ {\sim}4{\times}10^{12} \end{bmatrix} \cdot \begin{bmatrix} \text{one integration at} \\ \omega{\sim}7{\times}10^{-6}\text{rads}^{-1} \end{bmatrix} \cdot \begin{bmatrix} \text{one integration at} \\ \omega{\sim}1\text{rads}^{-1} \end{bmatrix} \cdot \begin{bmatrix} \text{differentiation from} \\ \omega{\sim}450\text{rads}^{-1}\text{ to} \\ \omega{\sim}4.5{\times}10^{3}\text{rads}^{-1} \end{bmatrix} \cdot \begin{bmatrix} \text{two integrations at} \\ \omega{\sim}2.1{\times}10^{4}\text{rads}^{-1} \end{bmatrix}$$

$$H_2 \equiv \begin{bmatrix} \text{gain of} \\ {\sim}3{\times}10^{6} \end{bmatrix} \cdot \begin{bmatrix} \text{differentiation from} \\ \omega{\sim}450\text{rads}^{-1}\text{ to} \\ \omega{\sim}4.5{\times}10^{3}\text{rads}^{-1} \end{bmatrix} \cdot \begin{bmatrix} \text{two integrations at} \\ \omega{\sim}2.1{\times}10^{4}\text{rads}^{-1} \end{bmatrix}$$

4.6.2 Performance

The Type II split-feedback system was observed to operate well. The shadow sensor loops were used to damp the test mass in tilt and rotation and also to damp the reaction mass with respect to the ground. The Type II feedback system was then used to lock the position of the test mass to the reference mirror (see Figure 2.7) with the aid of a small amount of gain in the auxiliary loop (which controlled the position of the reference mirror). The tilting motions of the intermediate and reaction masses about the y-axis (see Figure 4.1) were also being damped here using the oil pots and paddles implemented in Section 4.5. The circuit used for the test mass feedback loop is shown in Figure 4.9. The signal from this circuit was then further amplified and filtered using the circuit shown in Figure 4.14 and fed to the coil/magnet transducers acting between the intermediate mass and ground (see Figure 4.1). The open-loop gain was measured using the standard method described previously in Section 2.6.2 where the reference mirror of the interferometer (which was mounted on a PZT) was driven using sine wave signals of a single frequency. Figure 4.15 shows three sets of data of the open-loop gain as a function of frequency.

Measurements (A) and (C) were obtained without the 100K feedback resistor in place (see Figure 4.14). The gain setting for measurement (C) was slightly higher than for (A) and (B). Measurement (B) illustrates the effect on the low frequency gain of placing the 100K feedback resistor on the first amplifier stage causing the integration in H_1 to occur at a lower frequency. The two curves (A) and (B) merge at the predicted frequency.
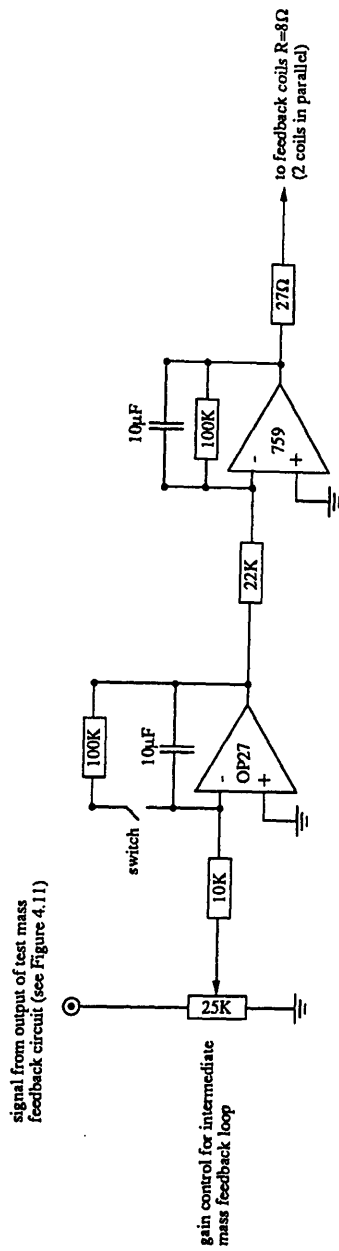
Figure 4.14 The extra electronics for the intermediate mass feedback loop. The output from circuit Figure 4.9 is input to this circuit. The signal obtained is then applied to the coils controlling the position of the intermediate mass.
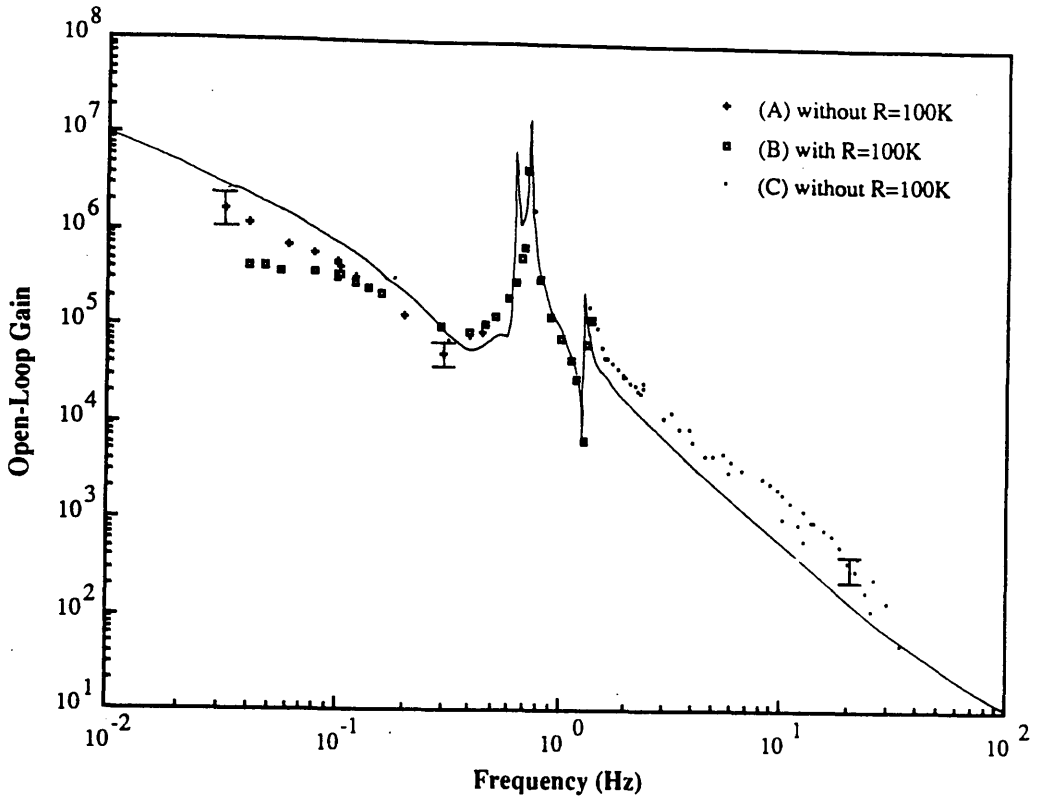
Figure 4.15 *Open-loop gain data for the "Type II" split-feedback scheme. Measurements (A) and (C) were taken without the R=100K feedback resistor in the circuit (see Figure 4.17). The electronic gain setting was slightly higher for measurement (C). The theoretical curve corresponding to measurement (A) is superimposed for comparison. The theoretically predicted open-loop gain at D.C. is ~ 9 × 10^{10}.*

The open-loop transfer function for the Type II split-feedback system was modelled using MATLAB. The calibration for the photodiode here was $\Delta V/_{\Delta x} \sim 2.3 \times 10^4$ V/mm (a more powerful laser was being used compared to Section 4.4). The calibrations for the displacement of the test mass per volt across the test/intermediate mass feedback coils were $\Delta x/_{\Delta V} \sim 0.2$ mm/v and $\Delta x/_{\Delta V} \sim 0.1$ mm/v respectively. The Bode magnitude plot obtained is superimposed in Figure 4.15 for comparison. The agreement is reasonably good. Recall from Section 4.5.2 that the shadow sensor loops used to

damp the reaction stage to the ground would cause the natural frequency of the reaction stage to be forced to a higher frequency depending on the gain used in these loops. If this reaction pendulum was forced upwards in frequency in this way the new upper resonant frequency of the nested pendulum would correspond closely to this new frequency. From Figure 4.15 one can see that the upper resonance of the pendulum is at ~1.3Hz as predicted by the model which does not take account of this effect. This strongly suggests that the effect of the shadow sensor loops on the resonant frequency of the reaction pendulum was indeed small.

The model was used to predict the approximate cross-over frequency of the two feedback loops (defined here as the frequency up to which the open-loop gain is increased by the additional feedback to the intermediate mass) and to assess the relative stability of the combined loop. The modelled Bode magnitude plots for the separate feedback loops are shown in Figure 4.16. Notice that the loop gain in the intermediate mass feedback loop dominates at the very low frequencies. Figure 4.17 shows the corresponding Bode magnitude plot for the combined loop. Superimposed on this is the plot for the test mass feedback loop alone (H_1=0). From this one can see that, according to the model, the open-loop gain up to about 0.2Hz is enhanced by the additional feedback to the intermediate mass. This was confirmed experimentally by measuring the open-loop gain of the test mass feedback loop alone in this frequency region. The behaviour of the split-feedback open-loop gain curve above the resonances is identical to that of the test mass feedback loop. However notice that by applying feedback to the intermediate mass, the exact pole-zero cancellations of the 1st and 3rd resonances which usually occur when the test mass feedback loop is operating alone do not occur (see Figure 4.15). This pole-zero cancellation is in fact compromised to such an extent that the split-feedback loop is theoretically unstable. The system was observed to be stable in practice probably due to the presence of 'natural' damping of the pendulum in the longitudinal test direction (*e.g.* brought about by the presence of the tilt damping oil pots incorporated in Section 4.5.2 or friction at the suspension breakaway points).

The model predicted the open-loop gain of the working split-feedback loop at zero frequency to be ~9×10^{10}. Assuming that the natural damping was maintaining stability at lower frequencies, the unity gain frequency of the working split-feedback loop was predicted to be $\omega_{unity\ gain}$~4×10^3 rads^{-1} (*f*~640Hz) with a corresponding gain margin of ~2 and phase margin ~18°. Note that the natural damping present in the pendulum might increase these margins in practice. If the overall gain in the split-feedback loop was

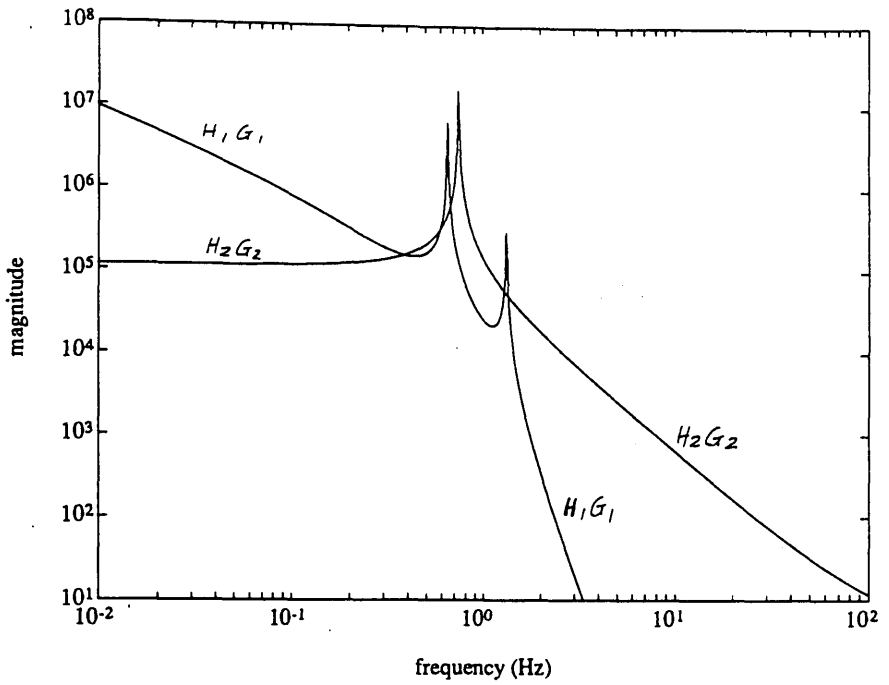**Figure 4.16** *Bode magnitude plots of H_1G_1 and H_2G_2 for the Type II split-feedback system.*
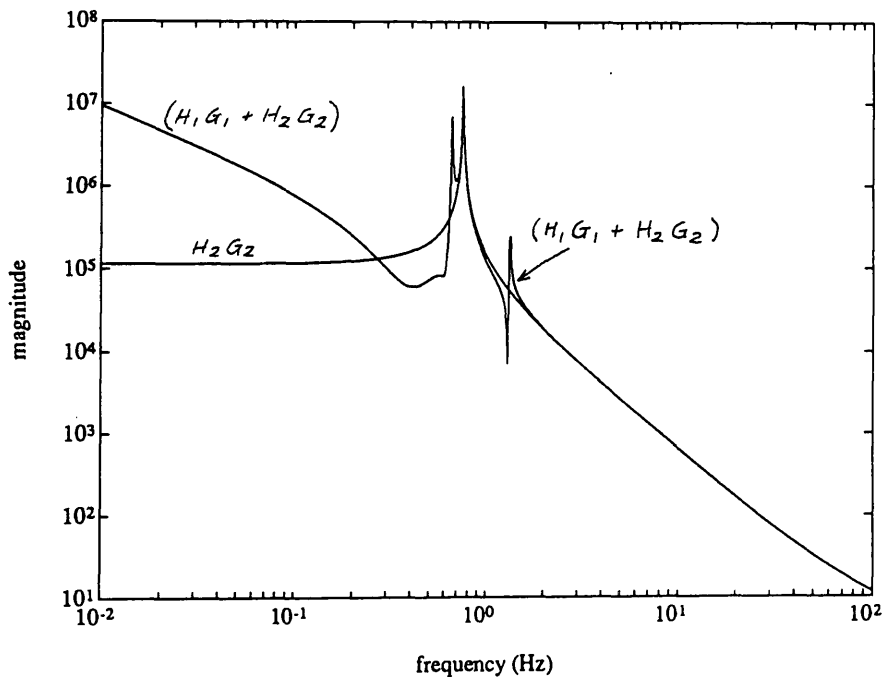

Figure 4.17 *Bode magnitude plot of $(H_1G_1 + H_2G_2)$ for the Type II split-feedback system. Superimposed is the corresponding plot for H_2G_2 (test mass feedback loop alone). From this one can see that the intermediate feedback loop increases the open-loop gain at frequencies below ~0.3Hz.*

turned too high the closed-loop system was observed to oscillate at ~790Hz (the unity gain frequency). This is consistent with the model.

The oil pots for damping the tilting motions of the intermediate and reaction masses were removed since these were probably giving rise to significant damping of the pendulum in the horizontal test direction. With the split-feedback loop closed a large peak at ~1.30Hz (corresponding to the upper pendulum resonance) with a smaller peak at ~0.66Hz (corresponding to the lower pendulum resonance) (see Figure 4.5) were present in the residual fringe signal implying that the system was verging on instability. These pendulum resonances, excited by the feedback to the intermediate mass, could not be controlled by the test mass feedback loop which was the dominant control loop in this frequency region.

4.6.3 Effect of Varying the Cross-Over Frequency

The effect of increasing the feedback cross-over frequency of the split-feedback loop was investigated. This was done by decreasing the values of the integration capacitors in the extra amplifier stages to the intermediate mass (see Figure 4.14) so that the first two integration corner frequencies in H_1 occurred at slightly higher frequencies. With the two capacitor values decreased from $C=10\mu F$ to $C=4.7\mu F$ the system was observed to oscillate at $\omega_U \sim 8.3 \text{rads}^{-1}$ (or $f \sim 1.32 \text{Hz}$, the upper pendulum resonance) and eventually become unstable. A smaller peak was also observed in the residual fringe signal at $\omega_L \sim 4.1 \text{rads}^{-1}$ (or $f \sim 0.66 \text{Hz}$, the lower pendulum resonance). In this case the gain in the intermediate mass feedback loop was too large in the region of the resonances and stability could not be maintained despite the natural damping present in the pendulum. Figures 4.18 and 4.19 show the Bode magnitude and phase plots for this system. The magnitude plot in Figure 4.18 clearly exhibits the three pendulum resonance peaks. From the phase plot of Figure 4.19 one can see that the phase 'jumps' discontinuously between the resonances because the test mass feedback loop temporarily dominates at the intermediate resonance ω_I. At frequencies above the upper resonance at ω_U the test mass feedback loop again dominates. The Nyquist plot for this split-feedback loop was sketched and is shown in Figure 4.20. This complicated plot shows that the loop is indeed unstable since the point (-1,0) lies to the right hand side of the contour marked 'A'.

The cross-over frequency of the split-feedback loop was then systematically
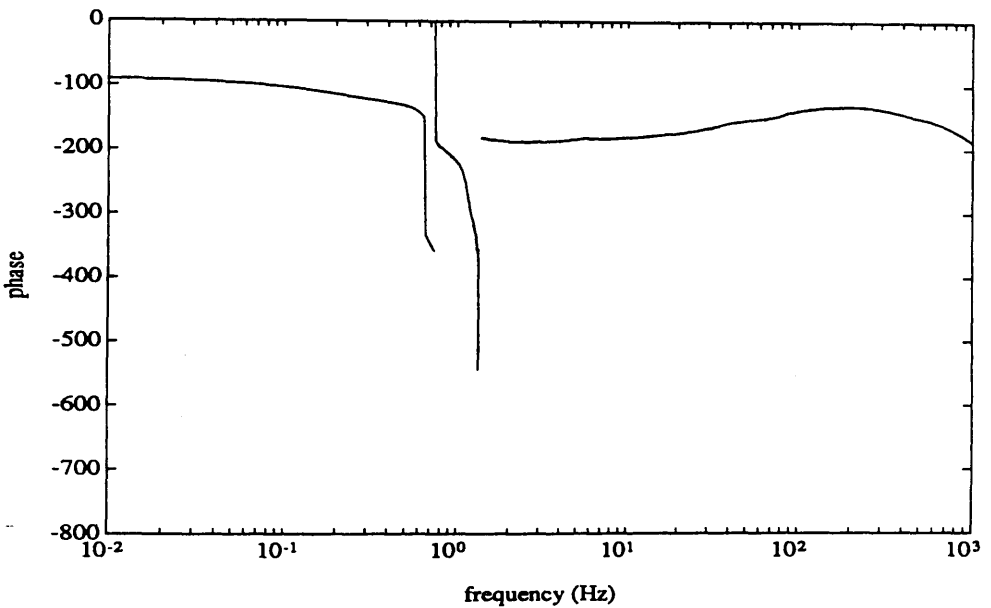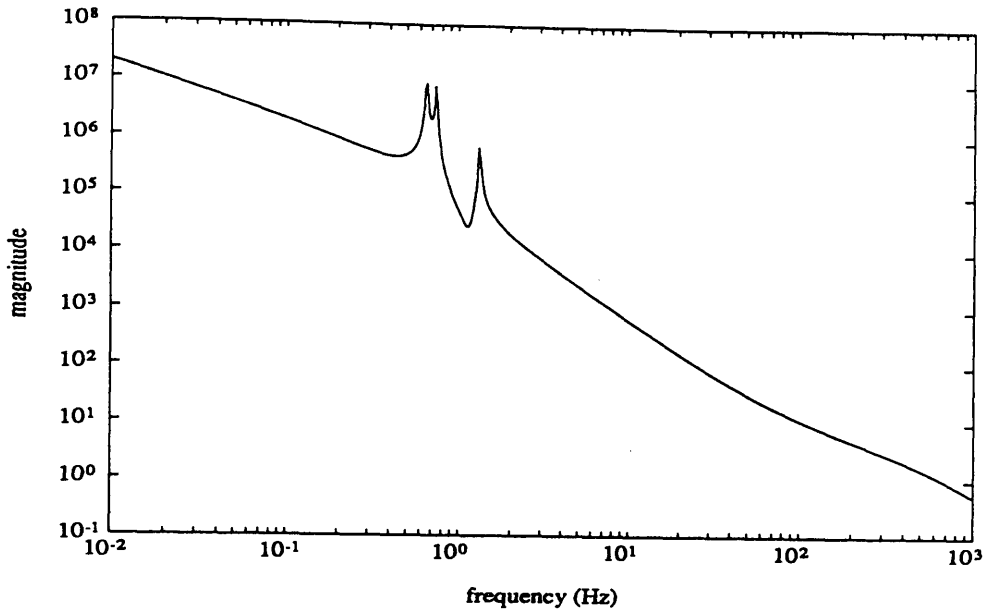
Figures 4.18 & 4.19
Bode magnitude and phase plots of $(H_1G_1+H_2G_2)$ for Type II split-
feedback with a relatively 'high' frequency cross-over between the two
feedback loops (see text). Three peaks corresponding to the three coupled
pendulum resonances are clearly visible in the magnitude plot. From the phase plot one
can see that the phase jumps discontinuously between the resonances since the test mass
feedback loop temporarily dominates at the intermediate resonance. At frequencies above
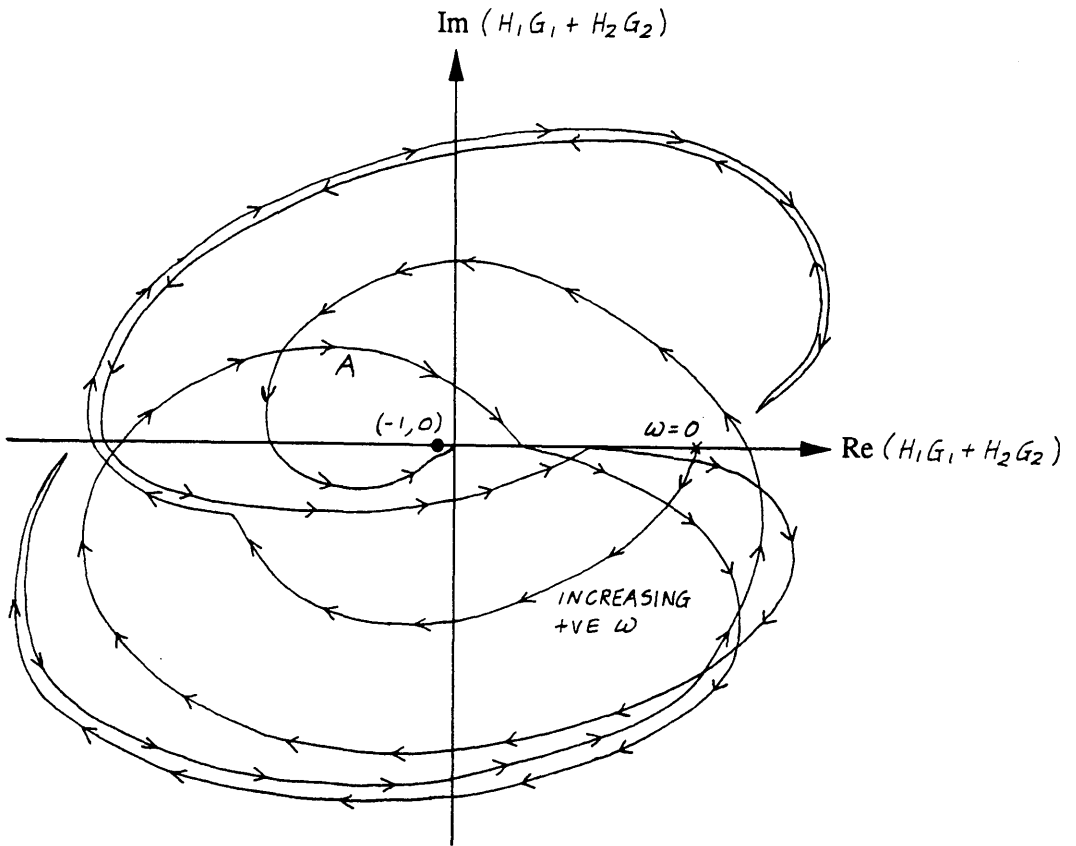the upper resonance the test mass feedback loop again dominates.

Figure 4.20 *Sketch of the Nyquist plot for the Type II split-feedback system with a relatively 'high cross-over frequency. Contour 'A' encloses the point (-1,0) and so the system is unstable.*

reduced. This was done by increasing the values of the integration capacitors in the extra amplifier stages to the intermediate mass (see Figure 4.14) so that the first two integration corner frequencies in H_1 occurred at slightly lower frequencies. The system was observed to become more stable, the stability increasing as the cross-over frequency decreased. For instance, with two integration capacitors of values $C=20\mu F$ the split-feedback loop is theoretically stable even for a pendulum with infinitely high Q stages. In this situation the cross-over frequency (frequency up to which the gain is increased by the extra feedback to the intermediate mass) between the two loops is at ~0.1Hz. Figures 4.21 and 4.22 show the Bode magnitude and phase plots for this system. From these Bode plots one can see that the lower and upper resonances are almost exactly cancelled by the zeros which exist in the test mass feedback loop. In actual fact the influence of the intermediate mass feedback loop is so small over the region of the resonances that the system behaviour is virtually identical to that for the test mass feedback loop operating alone. Figure 4.23 shows a sketch of the Nyquist plot for this stable system.

Since it is desirable to use very high Q pendulums (Q ~10^7 or 10^8 [Hough *et. al.* 1989]) in interferometric detectors, it seems likely that this type of split-feedback system for the position control of a test mass would have to be operated with the cross-over frequency well below the frequency of the lower pendulum resonance in order to maintain stability.

4.6.4 Electronic Damping of the Intermediate Mass to Ground

By electronically damping the intermediate mass to ground it was hoped that the lower (ω_L) and upper pendulum (ω_U) resonances could be sufficiently well damped that stability could be achieved with a Type II split-feedback loop having a higher cross-over (*i.e.* >0.1Hz).

Root-locus analysis similar to that of Section 3.3 was performed to see how well the two resonances could be damped simultaneously by applying feedback signals to the intermediate mass. For simplicity the nested system was modelled as a double pendulum whose lower mass was given the combined mass of the test and reaction masses of the nested system. The closed-loop transfer function was derived for the situation where a feedback force of the form $F_1 = b\left(\dot{x_1} - \dot{x_0}\right)$ was applied to the intermediate mass, where b is an 'electronic' damping co-efficient (see Figure 2.2). Here the pendulum is damped
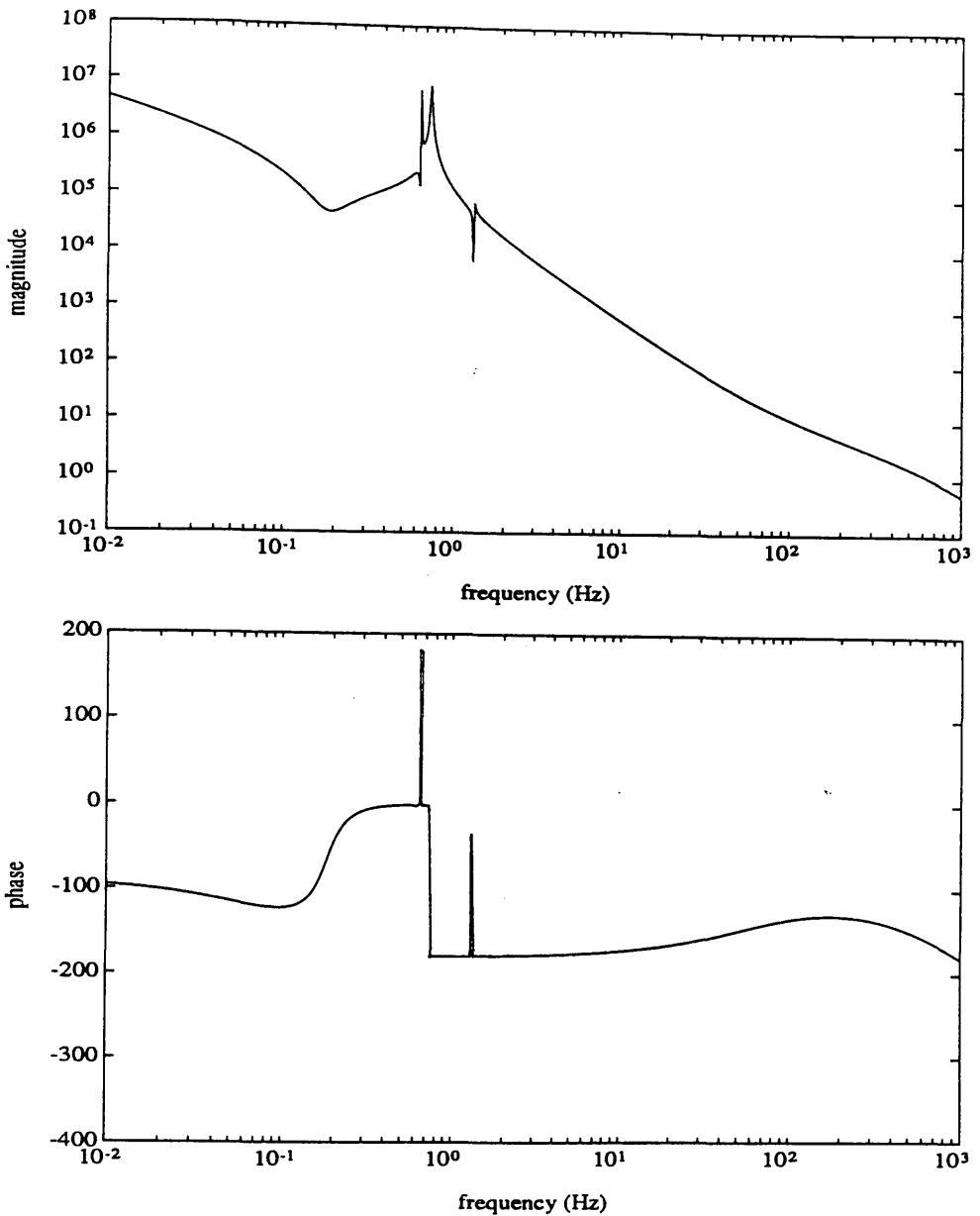
Figures 4.21 & 4.22

Bode magnitude and phase plots of $(H_1G_1+H_2G_2)$ for Type II split-feedback with a relatively 'low' frequency cross-over between the two feedback loops (see text). Three peaks corresponding to the three coupled pendulum resonances are clearly visible in the magnitude plot. Note however that the lower and upper peaks are very close in frequency to zeros. From the phase plot one can see that the phase changes due to the lower and upper resonances are cancelled by the phase changes due to the zeros. Therefore the behaviour from a frequency just below the first resonance onwards is identical to that of the test mass feedback loop (H_2G_2) (see text).
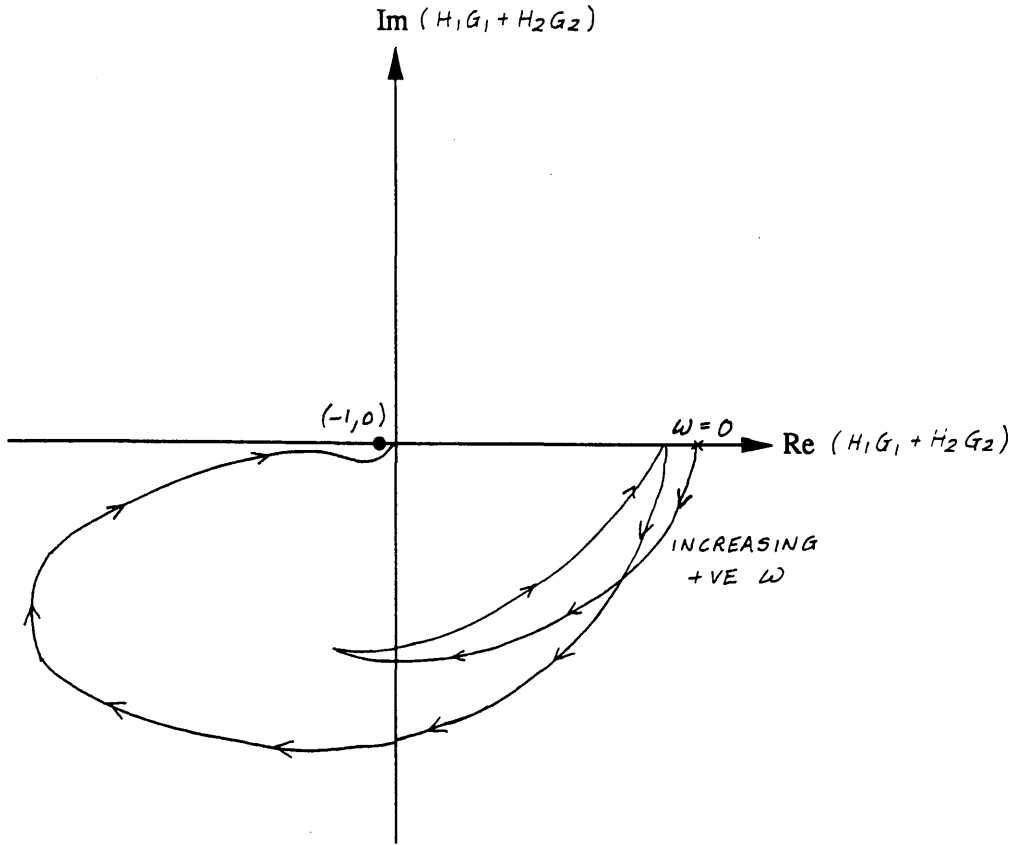
Figure 4.23   Sketch of the Nyquist plot for the Type II split-feedback system with a relatively 'low' cross-over frequency. The curve does not encircle the point (-1,0) and so the system is stable.

with respect to the ground, and not inertially as it was in the case considered in Section 3.3. However the open-loop transfer function (closed-loop pole behaviour) is identical in the two cases.

The pole positions were studied as a function of b (which is determined by both the value of damping capacitor used in the feedback electronics and the gain in the feedback loop (see Section 2.6.2)). A root-locus plot similar to that of Figure 3.10 was obtained where the upper mode at $\omega_U \sim 8.3 \text{rads}^{-1}$ could be critically damped and the lower mode at $\omega_L \sim 4.1 \text{rads}^{-1}$ (which tended towards the open-loop zero at $\omega_I = \omega_3 \sim 4.7 \text{rads}^{-1}$ with increasing gain) could be damped to an optimally high level.

Two shadow sensor devices (horizontally displaced along the y-axis) were used to sense the position of the intermediate mass (see Figure 4.1). In order to avoid locking the position of the intermediate mass to the ground the feedback circuits used were A.C. coupled as shown in Figure 4.24. In each damping loop the photodiode calibration was $\Delta V / \Delta x \sim 3.3 \text{ V/mm}$ and the coil/magnet transducer calibration was $\Delta x / \Delta V \sim 4.5 \times 10^{-2} \text{ mm/V}$. The analysis showed that to achieve optimum damping of the two modes a value of $C \sim 0.3 \mu F$ should be used in each circuit giving $Q_L \sim 7$ and $Q_U \sim 0.7$.

When the two shadow sensor loops were closed a rotational mode of the pendulum about the z-axis at $\sim 1.2 \text{Hz}$ (see Figure 4.1) appeared to be excited by the feedback rather than damped. If only one loop was closed this resonance could be damped stably. The reason why this particular resonance could not be damped by the combined action of the two feedback loops is not obvious. It is possible that poor alignment and gain imbalance of the shadow sensors caused this instability. However attempts were made to ensure that good alignment and balance were achieved. To circumvent this problem the signals from the two shadow sensors were summed as shown in Figure 4.24 and the derived signal applied to the coils connected in series. By independently varying the gain in each loop the peak at $\sim 1.2 \text{Hz}$ could be removed from the sensed signal. Figure 4.25 shows the output signal from the summed circuit of Figure 4.24 with the loop open and closed. The two pendulum resonances at $\sim 0.66 \text{Hz}$ and $\sim 1.32 \text{Hz}$ are damped to the predicted levels. The peak at $\sim 1.4 \text{Hz}$ is a coupled "stirring" mode of the pendulum about the z-axis. This was damped adequately by the feedback. The amplitude of this resonance could also be suppressed by placing constraining wires on the intermediate mass in the y-direction.
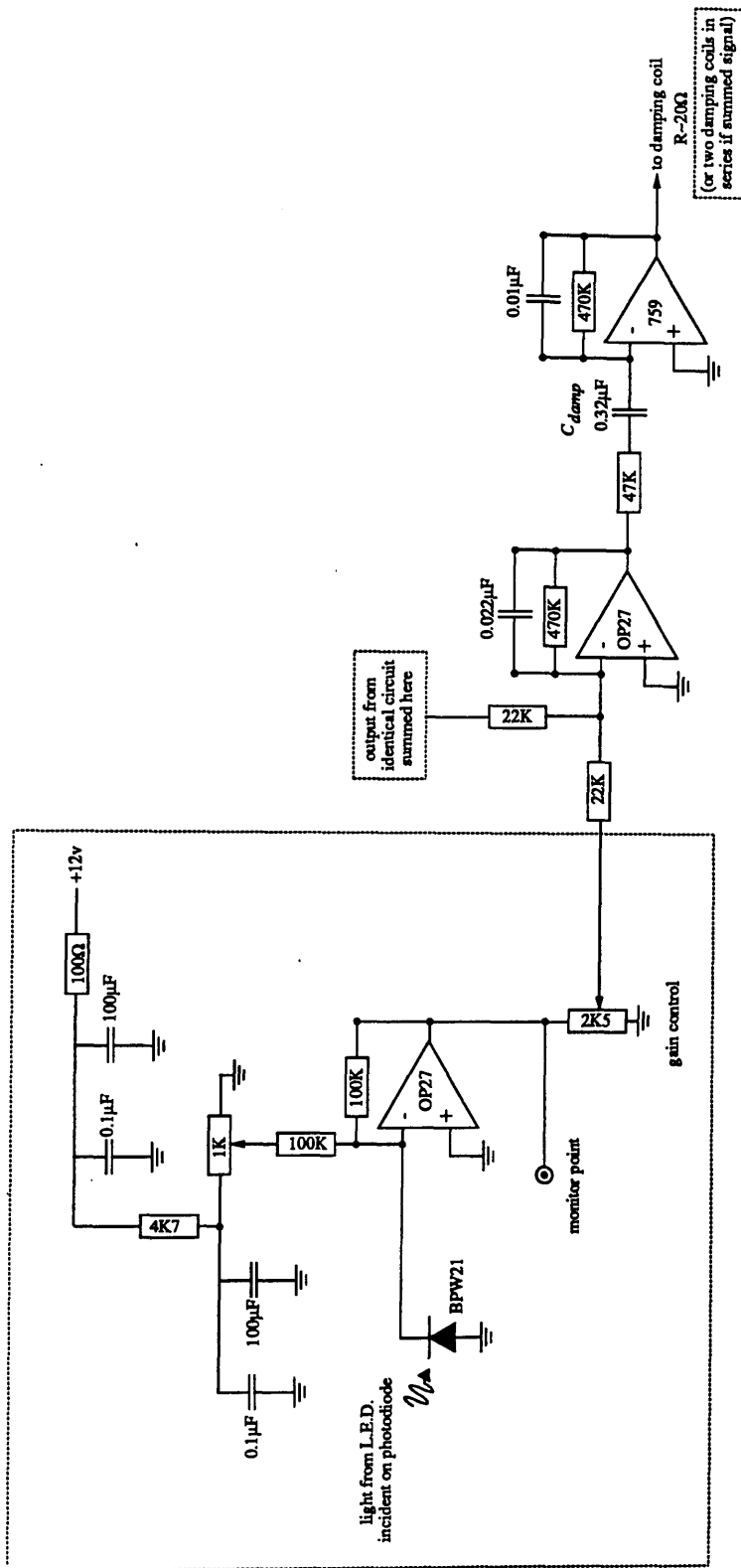
Figure 4.24 The circuit for the shadow sensor servos for damping the intermediate mass to ground. The boxed areas show how the signals from two such circuits are summed to cancel the sensed rotations.
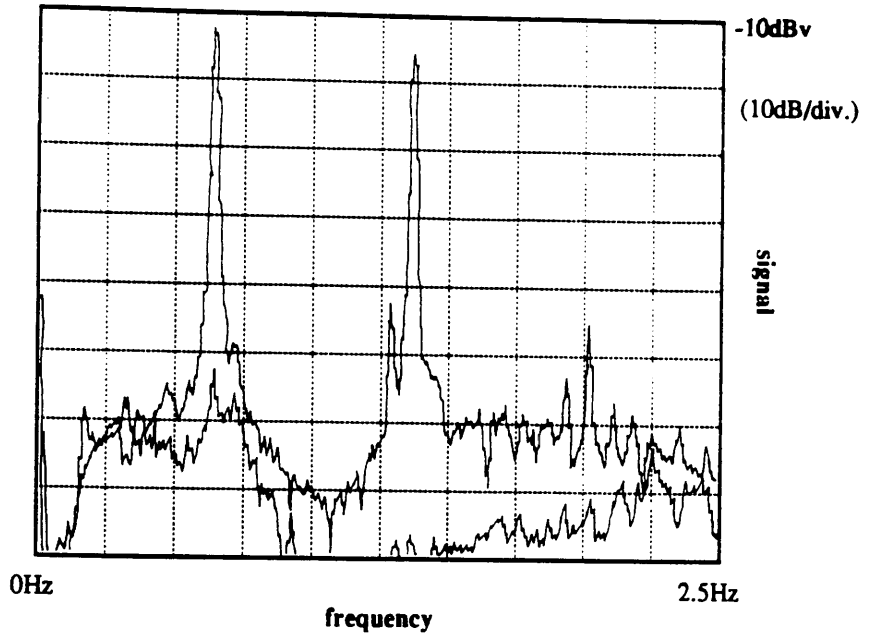
Figure 4.25 *Output signal from the summed circuit in Figure 4.24 with the coils connected and disconnected. The upper trace (open-loop) shows the peaks at 0.66Hz (1st pendulum resonance), 1.32Hz (3rd pendulum resonance) and 1.4Hz (coupled "stirring" resonance). The lower trace (closed-loop) shows how these peaks are damped by the feedback (see text).*

The Type II split-feedback was tested once more with the integration capacitors having values of $C=4.7\mu F$ (demonstrated previously to be experimentally unstable). With the intermediate mass damped to the ground in the way described above this split-feedback system could maintain lock. However if the gain was turned too high the closed-loop system was observed to oscillate at the first pendulum resonance ($\omega_L \sim 4.1 \text{rads}^{-1}$ or $f_L \sim 0.66\text{Hz}$) since this mode could not be critically damped by the shadow sensor transducers damping the intermediate mass. The additional position control feedback to the intermediate mass in this case increases the open-loop gain up to a frequency somewhere in the region of the pendulum resonances (though it is difficult to define a cross-over frequency precisely). When the electronic damping was removed the Type II control loop was observed to become unstable as demonstrated previously.

4.6.5 Conclusions

The Type II split-feedback system was demonstrated to operate satisfactorily if the cross-over frequency between the two feedback loops (the frequency up to which the intermediate mass feedback loop increases the overall open-loop gain) is at a frequency much lower than the first pendulum resonance e.g. ~0.1Hz. A higher cross-over frequency can be achieved by electronically damping the intermediate mass to the ground using shadow sensor devices. However it seems unlikely that this type of split-feedback system could ever be operated with a cross-over frequency any higher than the frequency of the lowest pendulum resonance. Nevertheless since the transfer function of the pendulum is unity below the first pendulum resonance and seismic noise is larger at the low frequencies (see Chapter 2), the largest feedback signals will be associated with correcting for these low frequency motions. By feeding back these low frequency position control signals to the intermediate mass, the potential for introducing higher frequency displacement noise to the test mass due to non-linear conversion in the feedback electronics or tranducers is reduced.

Chapter 5

Finite Element Analysis of the Nested Double Pendulum

5.1 Introduction

The degree of seismic isolation obtainable using the prototype nested double pendulum system described in Chapter 4 can be predicted using simple theory. However only an approximate estimate of the transmissibility could be made by multiplying the transmissibilities of the individual components. The precise figure could not be evaluated since cross-coupling between the different directions will inevitably take place and vibrations can be transmitted to the test mass *via* several routes. This effect is very important and has the consequence that in addition to a high level of isolation in the horizontal direction a high level of isolation in the vertical direction is likely to be required. Furthermore there could be some non-linear coupling between the various components of the system. The effects of the coupling of internal and external structural resonances to the test mass may also be significant.

A more realistic assessment of the passive isolation achievable with the nested double pendulum suspension system can be made using the finite element method of structural analysis. This yields information on the effects of internal structural resonances and illustrates the methods by which the various modes could couple giving a better understanding of the system behaviour.

The finite element program MSC/NASTRAN was used to determine the eigenvalues of the nested double pendulum and to predict the levels of horizontal and vertical isolation achievable. The horizontal transmissibility was then measured experimentally to compare with the theoretical prediction.

5.2 The Finite Element Method

This is a method of structural analysis in which a mathematical model of a real world structure is generated by dividing the structure into a finite number of small regions called elements. Grid points are generated to connect each element to its surrounding neighbours at a finite number of locations. Interactions between the neighbouring elements are then carried out by the forces exerted at the common grid points. In NASTRAN each grid point is assigned six degrees of freedom (3 translations and 3 rotations). The analyst defines constraints on the degrees of freedom of the various grid points as required. The manuals [Msc/Nastran 1983] and [Msc/Nastran 1985] contain further information.

5.3 Model Description

A schematic diagram of the nested pendulum is shown in Chapter 4, Figure 4.1. The finite element mesh generated to represent the system is shown in Figure 5.1. The positions of the suspension wires have been superimposed here by hand (dotted lines). In order to generate the mesh of grid points a reference origin was chosen at the intersection of the vertical symmetry axis of the pendulum with the rectangular support plate. This origin was in fact slightly offset in the y-direction from the centre of mass of the support plate. Plate elements were used throughout the model to represent the aluminium top support plate, the intermediate, test and surrounding reaction (box-shaped) mass. Two-dimensional elements were used since this reduces the complexity involved in the model generation and in the interpretation of the results obtained. The bar shaped intermediate mass and test mass were modelled as plates of identical cross-sectional area in the x-y plane and identical mass to their real-life counterparts. Triangular plate elements (in the y-z plane) were connected to the sides of the box-shaped reaction mass to represent the triangular platelets used to mount the wire breakaway points for the reaction mass suspension (see Figure 5.1).

Typically high Q test masses are used in interferometric detectors (internal $Q \sim 10^6$ or higher) [Hough et. al. 1989]. However the support structure (e.g. the top support plate) would be designed to have low internal Q to reduce the amplitude of its resonant motions since these motions might couple to the suspended masses. Each of the masses in the model were assigned an internal Q of 20 since this would be sufficiently large to

102
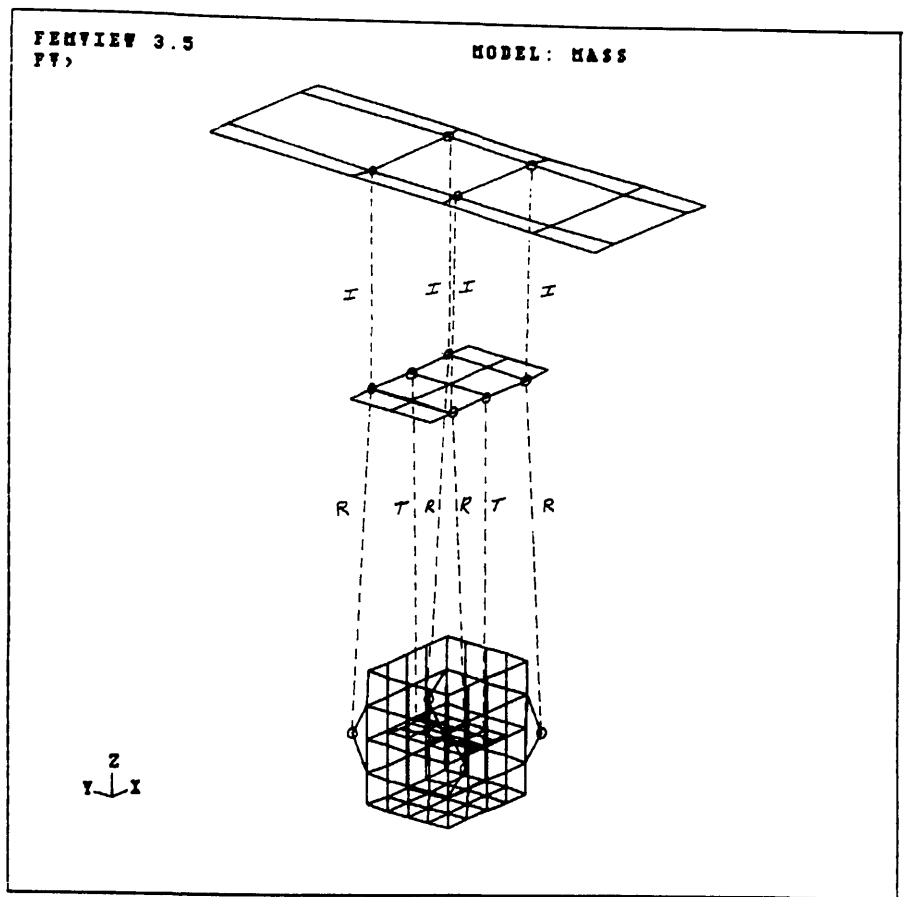
Figure 5.1 Finite element mesh for the nested double pendulum. The horizontal test direction is along the x-axis. The positions of the suspension wires have been superimposed (dotted lines) and the wire breakaway points have been circled. The intermediate mass is suspended with double-loops (marked I); the box-shaped reaction mass with double-loops (marked R), and the enclosed test mass with a single-loop (marked T).

enable observation of any coupling effects which took place.

The model was constrained to move only in two dimensions (the x-z plane) since we are primarily concerned with the level of isolation obtained in the horizontal test direction along the x-axis (see Figure 5.1).

Horizontal spring elements were used in the model to represent the horizontal restoring forces acting on the suspended masses when they are displaced sideways from their equilibrium positions. These were connected between the upper and lower

breakaway points of each suspension wire. The restoring forces acting in the vertical direction due to the stiffness of the suspension wires were modelled similarly using vertical spring elements connecting the breakaway points. Damping elements were connected in parallel with each of these horizontal and vertical spring elements to give each stage of pendulum suspension a $Q\sim10^6$. Note that in representing the suspension wires in this way the presence of the wire violin resonances were not accounted for. The effect that such resonances have on the isolation properties of a pendulum was discussed in Section 2.3.3.

In the model the test mass was constrained in rotations about the y-axis since the two breakaway points of the single loop suspension wire were collinear with the centre of mass of the test mass in the model and therefore there was no restoring force in this degree of freedom. In the real system a small vertical offset of the breakaway points and centre of mass would give rise to the restoring force. In the nested pendulum the tilting motion of the test mass is damped electronically using shadow sensor feedback systems (see Chapter 4).

5.4   Modes of the Suspension System

Real eigenvalue analysis [Msc/Nastran 1983] was carried out to compute the natural resonant frequencies of the modelled system. To enable identification, the mode shapes were viewed using the graphics package FEMVIEW.

The lowest frequency modes of the system were the three fundamental horizontal pendulum modes at 0.64Hz, 0.73Hz and 1.32Hz. These compare well with the values derived from the equations of motion *i.e.* 0.65Hz, 0.75Hz and 1.32Hz (Section 4.3, Figure 4.5). Three normal modes involving vertical motion of the suspended masses were observed at 14.3Hz, 21.4Hz and 33.5Hz. However only two normal modes were observed for rotation of the masses about the y -axis (18.6Hz and 32.2Hz) since the test mass was constrained in this degree of freedom in the model. Similarly only two normal modes involving rotation of the masses about the x-axis were observed (24.6Hz and 40.5Hz). This was a consequence of the side plates of the box in the x-z plane being constrained not to move in the y-direction. No information on the modes involving rotational motions of the masses about the z-axis was obtained since the model was constrained only to move in the x-z plane.

Internal resonances of the top support plate were observed at higher frequencies. The first few of these were the drum-like modes involving flexing of the plate in the vertical direction (z-axis) *e.g.* the first drum mode was at 256Hz. The first shear mode of the top plate (in the x-y plane) was at a much higher frequency *i.e.* 2120Hz.

The lowest frequency mode of the box-shaped reaction mass occurred at 1490Hz and involved oscillation of the opposite sides of the box in phase. Note however that in the real system there was a plate across the top of the box on which the tilt control coils were mounted. This was not included in the model. In reality this mode would occur at a slightly different frequency than the model suggests. A whole series of modes involving complicated motions of the box sides were observed at higher frequencies.

5.5   Frequency Response Analyses

The response of the pendulum to horizontal and vertical excitation at the corners of the top support plate (see Figure 5.1) was analysed to predict the level of isolation achievable in each dimension.

5.5.1   Horizontal Frequency Response

Figure 5.2 shows the transmissibility curves to the centres of mass of the intermediate and test masses in the horizontal direction (x-axis). Above the resonances the horizontal transmissibility to the intermediate mass decreases as 12dB/octave or $1/f^2$ as one would expect for one stage of high Q pendulum suspension. Above the resonances the horizontal transmissibility to the test mass decreases as 24dB/octave or $1/f^4$ as one would predict for a high Q double pendulum suspension.

The transfer function from motion of the suspension point to motion of the test mass can be approximated to that of a simple "two-stage" double pendulum (see equation (2.18)). Substituting for the natural frequency of the upper stage (f_1=0.94Hz or ω_1=5.9rads^{-1}) and lower stage (f_2=0.75Hz or ω_2=4.7rads^{-1}) (see Section 4.3) and using m_1=11Kg (the intermediate mass) and m_2=5.6Kg (the combined mass of the test and reaction mass) (see Figure 4.1) this formula yielded a value for the transmissibility at 100Hz of T~7.4 × 10^{-9}. This is in fact identical to the value derived in the finite element analysis.
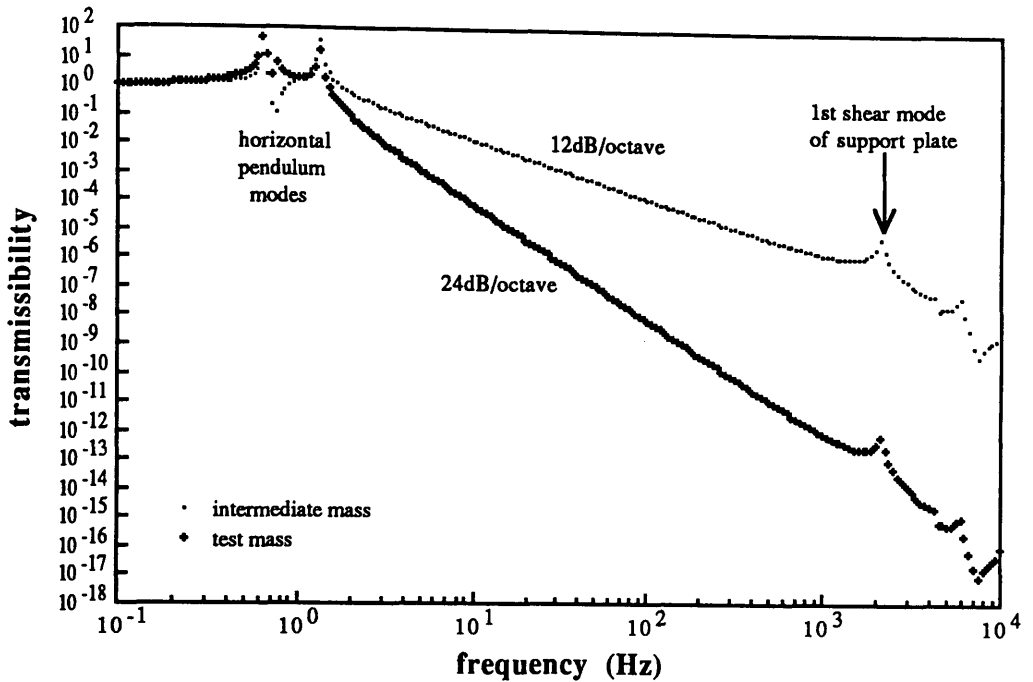
Figure 5.2 *Horizontal transmissibility curves from the support plate to the centres of mass of the intermediate and test masses. The shear modes of the support plate give rise to peaks in both curves.*

Notice however that at higher frequencies the isolation at both stages of the pendulum is degraded by coupling of the shear resonances of the support plate in the x-y plane. Figure 5.3 is a table summarising the first few modes giving rise to peaks in the horizontal transmissibility curve for the test mass. Sketches of the shear modes of the plate which couple to the pendulum are given in this table. The first of these shear modes is at a frequency of ~2.1kHz. Note that the second shear mode at ~4.3kHz gives rise to a relatively small peak in the transmissibility curve. The coupling of this mode directly to the horizontal direction could probably be avoided if the intermediate mass was suspended directly below the centre of mass of the support plate.

106

frequency (Hz)	brief description
0.64	1st horizontal pendulum mode (see Figure 4.5)
0.73	2nd horizontal pendulum mode (see Figure 4.5)
1.32	3rd horizontal pendulum mode (see Figure 4.5)
2120	1st shear mode of support plate $^y\!\llcorner_x$
4310	2nd shear mode of support plate $^y\!\llcorner_x$
5930	3rd shear mode of support plate $^y\!\llcorner_x$

Figure 5.3   The first few modes giving rise to peaks in the horizontal transmissibility curve for the test mass. Rough sketches of the shear modes of the plate in the x-y plane are shown.

In Figure 5.2 it is interesting to see that the gradients of the transmissibility curves appear to increase above the shear resonances indicating that the plate is providing some extra horizontal isolation above its resonant frequencies. However these resonance peaks occur in an important frequency region for the detection of gravitational waves and to avoid such large motions of the test mass at these frequencies the support plate for the pendulum should be critically damped.

5.5.2 Vertical Frequency Response

Figure 5.4 shows the transmissibility curves to the centre of mass of the test and intermediate masses in the vertical direction (z-axis). Above the resonances the vertical transmissibility to the intermediate mass decreases at 12dB/octave or $1/f^2$ as expected for a single pendulum. The vertical transmissibility to the test mass decreases as 24dB/octave or $1/f^4$ above the pendulum resonances as one would expect for a double pendulum suspension.
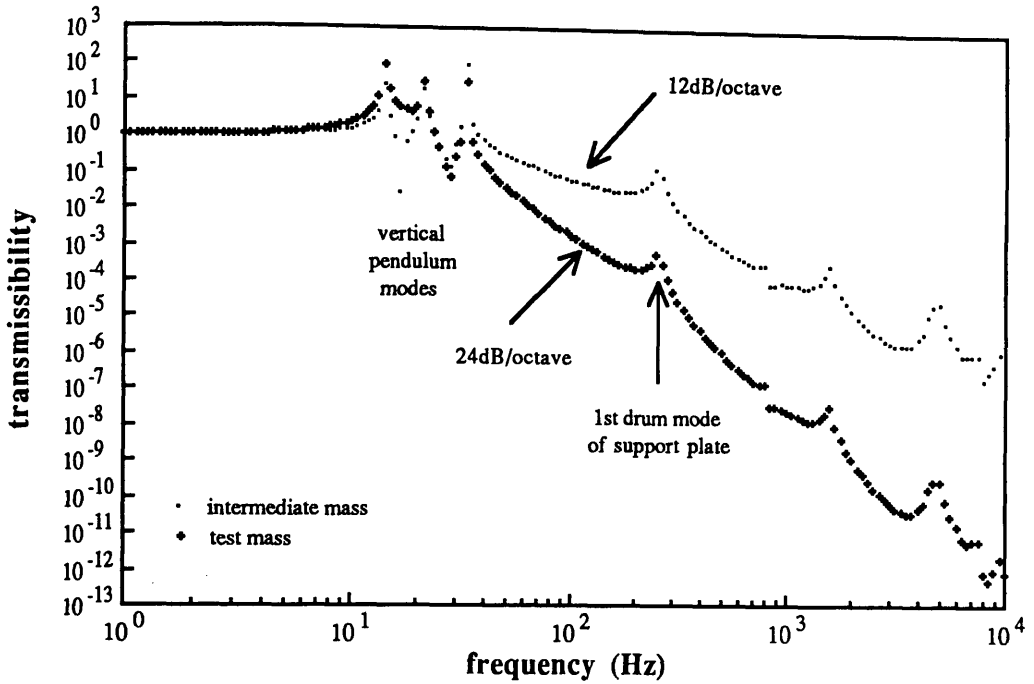
Figure 5.4 Vertical transmissibility curves from the support plate to the centres of mass of the intermediate and test masses. The drum modes of the support plate give rise to peaks in both curves.

Considering the system to be a simple two-stage double pendulum the vertical transmissibility to the test mass is approximately given by:

$$T \sim \frac{f_1^2 f_2^2}{f^4} \qquad (5.1)$$

where f_1, f_2 are the natural vertical frequencies of the upper and lower (test mass) stages respectively. These were calculated to be f_1=22.3Hz (or ω_1=140rads^{-1}) and f_2=16.8Hz (or ω_2=105rads^{-1}) giving $T \sim 1.4 \times 10^{-3}$ at 100Hz. The finite element analysis yielded a value of T=1.8 × 10^{-3}. The slight discrepancy is probably due to the fact that the reaction stage has a slightly different natural frequency from the test stage since the loading conditions on the suspension wires are different in each case.

108

From Figure 5.4 one can see that the isolation of both masses at higher frequencies is degraded by coupling of the drum modes of the support plate, the lowest of these occurring at ~260Hz. Notice that the gradients of the transmissibility curves appear to increase above each resonance indicating that the plate is providing some extra vertical isolation above its drum resonant frequencies. However these resonance peaks occur in an important frequency region for the detection of gravitational waves. Since it is possible that vertical motion of the test mass can cross-couple to horizontal motion it is desirable to avoid such large motions of the test mass at these frequencies. The support plate for the pendulum should therefore be critically damped if possible.

Figure 5.5 is a table summarising the first few modes giving rise to large vertical motions of the centre of mass of the test mass.
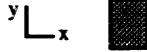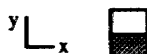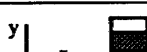
frequency (Hz)	brief description
14.3	1st vertical pendulum mode
21.4	2nd vertical pendulum mode
33.5	3rd vertical pendulum mode
256	1st drum mode of support plate $^y\llcorner_x$
812	3rd drum mode of support plate $^y\llcorner_x$
1580	5th drum mode of support plate $^y\llcorner_x$

Figure 5.5   The first few modes giving rise to peaks in the vertical transmissibility curve for the test mass. Rough sketches of the drum modes of the plate in the x-y plane are shown.

5.5.3 Conclusions

At 100Hz, the isolation level in both dimensions appears to be as simple theory would suggest. However at higher frequencies this analysis has shown that the internal modes of the support plate can couple to motions of the centre of mass of the test mass.

If the pendulum were suspended directly below the centre of mass of the support plate one could probably remove the direct coupling of certain shear modes to the horizontal direction (and certain drum modes to the vertical direction). However these shear modes would give rise to rotational motions of the mass about the z-axis which can non-linearly convert to horizontal motion at the mirrored surface of the test mass. The effects of coupling can be reduced if the support plate for the pendulum system is damped to a high level or is designed such that its lowest internal resonant frequency lies outwith the detection frequency range (say $f_{int.} \sim$ 5kHz or more).

The box shaped reaction mass in this system has a whole series of complicated internal modes at frequencies above about 1.5kHz. These modes could couple displacement noise to the test mass *via* the coil/magnet transducers if the unity gain frequency of the position control feedback loop were at a frequency approaching this lowest modal frequency. This problem could be alleviated by reinforcing the plates making up the reaction mass so that the lowest mode lay at a frequency outwith the frequency range of interest.

The isolation system used in an interferometric gravitational wave detector should be efficient enough to allow the photon noise limited design sensitivity for burst sources *i.e.* a limit to the sensitivity due to seismic noise of $h \sim 10^{-23}$, or better, for pulses at 100Hz [Hough *et. al.* 1989]. It was shown in Chapter 2 that the seismic displacement spectrum is approximately described by $\frac{10^{-7}}{f^2}$ $^m/\sqrt{Hz}$ in both the horizontal and vertical directions in a bandwidth from about 10Hz to a kilohertz [Hough *et. al.* 1986]. Using the horizontal transmissibility value given in Figure 5.2 for the double pendulum considered here, it can be shown that the resulting horizontal motion of the test mass in a bandwidth of $f/2$ at 100Hz will be $dx \sim 1.1 \times 10^{-18}$m. Assuming that the motions of the test masses in the detector are uncorrelated, the limiting gravitational wave amplitude from the residual horizontal motion (with a detector arm length of L=3km) is given by

$$h \sim \frac{2dx}{L} \sim 7.3 \times 10^{-22}. \qquad (5.2)$$

This is approaching the limit required.

Vertical motions transmitted to the test mass due to vertical seismic motions can cross-couple to the horizontal direction. Del Fabbro and colleagues have suggested a figure of 1% for this conversion based on experimental investigations carried out on their

'super-attenuator' [Del Fabbro *et. al.*1988b]. Using the vertical transmissibility value given in Figure 5.4 for the double pendulum considered here, it can be shown that the resulting vertical motion of the test mass in a bandwidth of $f/_2$ at 100Hz will be $dz \sim 2.6 \times 10^{-13}$m. Taking 1% of this value, the limiting gravitational wave amplitude from the residual vertical motion (with a detector arm length of 3km) is

$$h \sim \frac{2\,(0.01 \times dz)}{L} \sim 1.7 \times 10^{-18} \qquad (5.3)$$

(assuming that the motions of the test masses in the detector are uncorrelated). This value is more than a factor of 10^5 worse than the design sensitivity.

To meet the desired isolation requirements it is proposed to use five-layer vibration isolation stacks in conjunction with the two-stage pendulum suspensions for the test masses in the proposed 3km (GEO) detector [Hough *et. al.* 1989]. Chapter 6 presents some theoretical investigations carried out on the limitations to the performance of such multi-layer stacks. Air springs will also be used in the 3km detector to connect the stacks to the ground (these give an attenuation of $\sim10^2$ in each dimension at frequencies above $\sim$50Hz).

There are obvious limitations to the conclusions which can be drawn from these analyses. Since the resulting displacements of the centres of mass of the suspended masses were observed and the pendulum was modelled in such a way that each mass was suspended symmetrically about its centre of mass, the effects of the coupling of rotational modes of the pendulum were not apparent here. For instance, rotational motions of the test mass about the z-axis can give rise horizontal displacements at the mirrored surface leading to a reduction in the detector sensitivity. However the rotational motions of the test mass about the z and y-axes can be damped and controlled using feedback loops such as those described in Chapter 4. Cross-coupling effects (both linear and non-linear) due to asymmetries of the system have not been investigated fully here and these need to be taken into account. The effects of the internal resonances of the pendulum masses and the violin resonances of the suspension wires have not been accounted for in this model. The effects of the coupling of ground tilting motions to the pendulum have not been investigated here. In reality these might couple strongly to horizontal motion of the test mass if the intermediate mass is suspended using double wire loops as is the case for the nested pendulum system.

111

5.6 Experimentally Measured Horizontal Response

The horizontal frequency response of the pendulum was measured to compare it with the predicted response. The support plate (which was connected to the support frame *via* isolation stacks) was driven in the horizontal (x) direction (see Figure 5.1) over a range of frequencies using two high power loudspeaker cones mounted rigidly on an adjacent pillar. The loudspeakers were enclosed by a lead/rubber foam box to provide acoustic shielding. The displacement of the driven plate was evaluated at the various frequencies using the value of acceleration measured with a commercial accelerometer mounted on the edge of the plate. The corresponding displacement of the suspended test mass was monitored using the position control feedback loop described in previous chapters (see Section 2.6). The feedback loop was used to lock the position of the test mass to the reference mirror of the Michelson interferometer (see Figure 2.7). The residual displacement of the test mass at a given frequency was evaluated by observing the feedback signal to the coils (the coil calibration in terms of force per volt was $\sim 1.7 \times 10^{-2}$ N/v). It was assumed that the reference mirror of the interferometer was relatively stationary over the range of frequencies considered. Note that the shadow sensor loops for damping the test mass in tilt and rotation and the loops for damping the reaction mass to the ground were disconnected whilst these measurements were made.

Figure 5.6 is a graph showing the measured horizontal response compared to that predicted using the finite element model. The isolation of the test mass above a few hertz appears to be much worse than predicted though it does appear to improve towards higher frequencies. The oil pots for damping the tilting motions of the support plate, intermediate and reaction masses were removed to see if motions of the support framework were coupling to the pendulum masses *via* the damping pots. However no improvement in the isolation was observed.

To test whether the sensitivity of the interferometer was being limited by acoustic or mechanical pick-up from the driving signal a test mirror was mounted on the rigid base of the interferometer in front of the suspended test mass. The auxiliary feedback loop (refer to Section 2.6) was then used to lock the position of the reference mirror to the new test mirror. By observation of the feedback signal to the PZT and the acceleration of the driven plate, the overall magnitude of the transfer function from the driven plate to the interferometer (*via* all possible routes) could be calculated. At 115Hz the magnitude of

the transfer function was measured to be of the order of $\sim 5 \times 10^{-3}$. It was also measured using an accelerometer mounted on the rigid base of the interferometer and found to be $\sim 2 \times 10^{-3}$ at $\sim 85Hz$. Note that these values are of similar magnitude to those shown in Figure 5.6 for the measured transfer function from the driven plate to the suspended test mass. This means that the sensitivity of the interferometer was indeed being compromised by mechanical or acoustical coupling to the driving signal and the results shown in Figure 5.6 are therefore not a measurement of the transfer function of the pendulum *via* the suspension wires. Acoustic coupling of the drive signal to the interferometer was possible since the system was not under vacuum. Mechanical coupling between the driven plate and the interferometer was possible since both the support framework and the interferometer were mounted on the same bench.

An alternative set of frequency response measurements was made using an accelerometer to monitor the residual displacement of the reaction mass (the test mass was inaccessible due to the presence of the surrounding reaction mass). Both of the accelerometers used here were coated in lead/rubber foam to provide some acoustic isolation. Figure 5.7 shows the transmissibility curve measured in air. The curve is similar in magnitude to that obtained using the interferometer.

It was suspected that the vibrations of the support frame induced by the driven support plate might have been coupling either mechanically (*via* the thin coiled wires supplying current to the control coils which were connected to the reaction mass *via* the intermediate mass) or acoustically to the suspended masses reducing the isolation. Since it would have been impractical to place the whole system under vacuum, a polythene tent was constructed around the system and filled with helium gas (which has a lower density than air). Whilst the tent was being filled with helium gas the test signal from a loudspeaker was monitored using a microphone. The test signal measured by the microphone was observed to decrease by a factor of ~ 2.2 at $\sim 90Hz$ in the helium environment.

The horizontal response curve measured in helium is shown in Figure 5.7. The isolation appears to have improved by a factor of a few up to about 60Hz. This suggests that acoustic coupling of some sort was indeed taking place in this frequency region. It is possible that mechanical resonances of the support frame were acoustically coupling to the pendulum masses in this frequency region. From about 60Hz to about 100Hz there is no obvious difference between the measurements taken in air and in helium. This
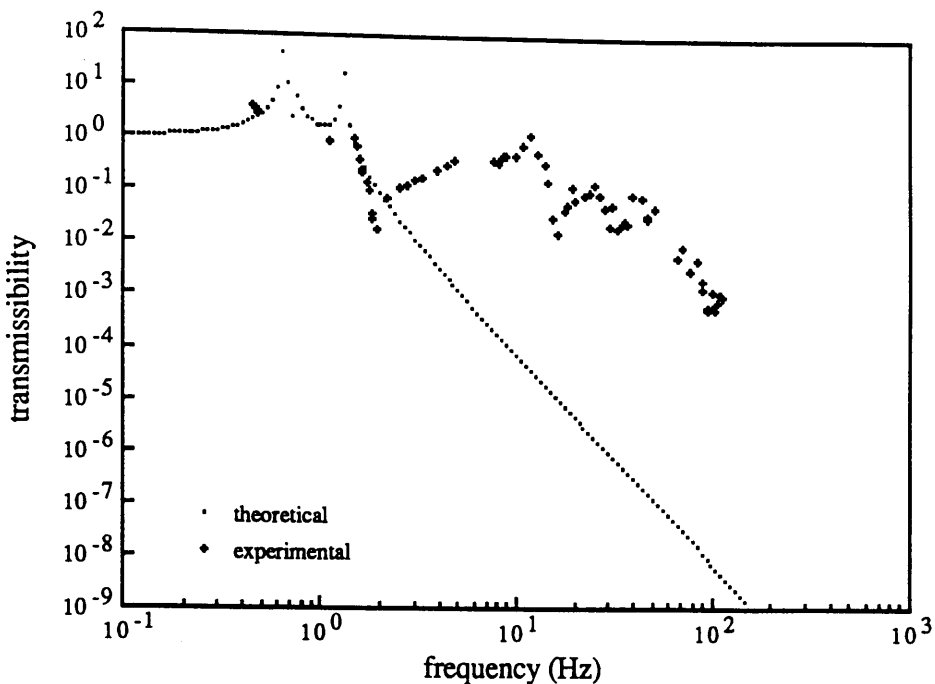
Figure 5.6 Horizontal transmissibility of the nested double pendulum measured using the position control feedback loop to monitor the displacement of the test mass. The theoretical curve is superimposed for comparison (see text).
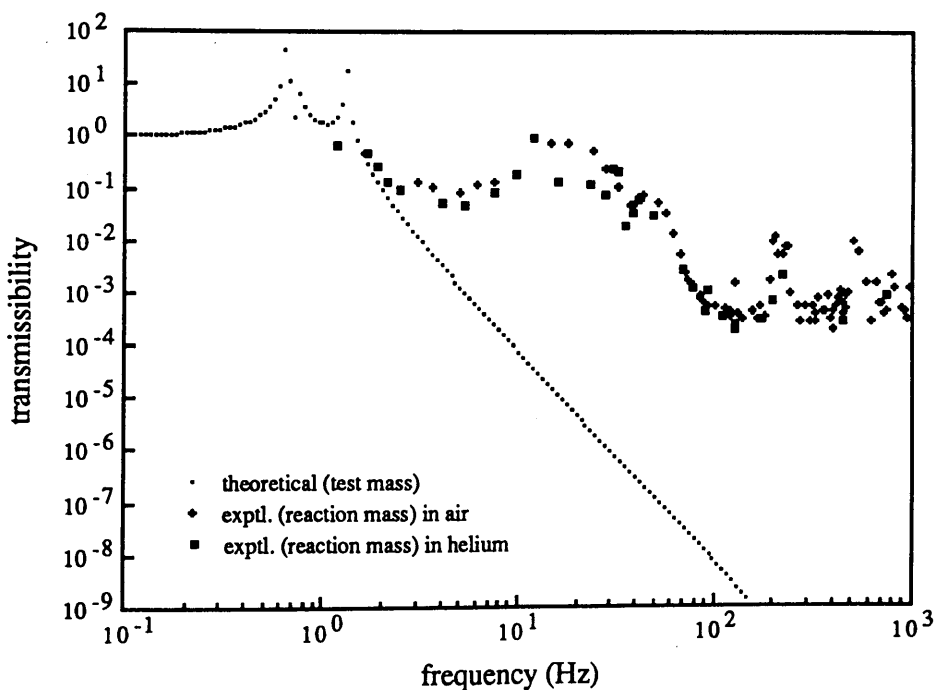

Figure 5.7 Horizontal transmissibility of the nested double pendulum measured in both air and in helium using an accelerometer to monitor the displacement of the reaction mass. The theoretical curve is superimposed for comparison (see text).

suggests that a negligibly small level of acoustic coupling was taking place in this frequency region. Note that this is the frequency region where the isolation appears to have begun to improve. This is consistent with the deduction that no acoustic coupling was taking place in this region. Both curves shown in Figure 5.7 tend to flatten at about 100Hz with peaks appearing at various higher frequencies (possibly due to wire violin resonances). This flattening is probably due to direct acoustic coupling between the loudspeaker drivers and the pendulum masses/accelerometers. The helium data may be of a slightly lower magnitude than the air data in this region but there is not a very significant difference.

It is interesting to note that some of the peaks observed in the transmissibility curves shown in Figures 5.6 and 5.7 are at the same frequencies as those at which the type I split feedback system was found to become unstable (*e.g.* at ~12Hz, ~24Hz and ~45Hz). This suggests that the peaks in the transmissibility curves were due to the coupling of resonances of the stacks or support frame to the pendulum in some way.

In conclusion, it appears that resonances of the support system (*i.e.* support frame or stacks) were coupling either acoustically directly through the air (or helium) to the pendulum or mechanically to the pendulum and limiting the isolation obtained. In order to properly assess the isolation performance of the pendulum the measurements should be made under vacuum. It would also be better to use a more massive structure to support the pendulum to reduce the possibility of coupling of the resonances of the structure to the pendulum.

Chapter 6

An Investigation of the Performance of Vibration Isolation Stacks Using the Finite Element Method

6.1 Introduction

In Earth-borne laser interferometric gravitational wave detectors the continuous background of seismic motions at the Earth's surface can lead to displacement noise of the test masses and other optical components. The magnitude of this noise can be reduced to such a level that it does not limit the sensitivity of the detector if a vibration isolation system of high enough performance is used to connect the test masses and other vital components to the Earth.

It is particularly important that the designed isolation system can provide a high degree of horizontal isolation. However the seismic background against which we are trying to provide isolation produces not only horizontal motions of the Earth's surface but also vertical and rotational motions. These rotational motions can be categorized as those involving rotation about an axis perpendicular to the Earth's surface and those involving rotation about axes coplanar with the Earth's surface (more commonly referred to as ground tilts). Therefore the isolation system must also provide adequate isolation to vertical and rotational ground motions since cross-coupling effects of a significant magnitude will possibly take place.

Vibration isolation stacks are widely used as part of the isolation systems for gravitational wave detectors. These multiple stacked arrangements consisting of alternating layers of a heavy metal and an elastic material such as rubber provide isolation from horizontal, vertical and rotational motions. They are most commonly used in conjunction with pendulum suspensions for the test masses and are placed somewhere between the ground and the top of the pendulum.

Using simple dynamical theory the transmissibility of unidirectional motion at the

base of a stack to the corresponding displacement at the centre of mass of the top plate of the stack as a function of frequency can be readily estimated (refer to Section 2.3.4). However this type of analysis where the stack system is treated as a simple system of point masses connected with damped springs does not account for the possibility of cross-coupling effects in the three dimensions. It is therefore important to gain some insight into the magnitude of cross-coupling of vertical and rotational motion to horizontal motion in vibration isolation stacks by some other means. This would enable a realistic assessment of the magnitude of horizontal noise at the top of any pendulum system suspended from the top of the stack. Furthermore, information on the resulting rotation of the top plate of the stack about its centre of mass induced by ground tilts or other means is important for any situation where the pendulum suspension point is not positioned exactly at the centre of mass of the plate. It is also of interest to investigate the ramifications of these rotational, horizontal and vertical ground motions for the situation where there is an imbalance in the stiffness of the rubber on each side of the stack.

In order to investigate some of these effects a finite element model representing an aluminium plate supported by four rubber corner pieces was generated and the finite element program MSC/NASTRAN was used to carry out various analyses. For a description of the finite element method refer to Section 5.2. The model was based on the design of the suspension support plate of the nested double pendulum suspension system discussed in Chapter 4. By choosing these particular dimensions the information obtained here could then be used to infer any isolation degradation which might occur in the nested pendulum system due to both cross-coupling mechanisms in the stack system and internal resonances in the plate.

A series of initial investigations were conducted using a one-layer stack model, both with homogeneous rubber elements and with a 10% imbalance between the stiffness of the rubber on either side of the stack. The first of these were eigenvalue analyses of the free undamped vibrations of the stack to predict the eigenfrequencies and mode shapes (Section 6.4). The next stage was to look at the transmissibility of horizontal motion at the base of the stack to horizontal motion at the centre of mass of the supported plate, and similarly for vertical and tilting motion (Direct Transmissibility Investigations, Section 6.5). Finally coupled transmission effects were investigated where the base of the stack was driven in the horizontal, vertical or rotational (tilting) sense and the resulting motions of the centre of mass of the plate were observed in the complementary senses (Indirect Transmissibility Investigations, Section 6.6).

Additionally the effects of varying the intrinsic quality factor of the supported plate were investigated in each of the above analyses to observe any reduction in the isolation achieved at frequencies on and above the resonant frequencies of the plate. Furthermore since stacks are seldom used in one layer form in gravitational wave detectors the above analyses were extended to a two layer stack system (Sections 6.7 and 6.8). Information could then be gained on the critical transmission mechanisms between neighbouring layers of stack and the effects of excitation and cross-coupling of the various stack modes could be observed. From the information obtained in these analyses one could then infer the consequences for a five-layer stack system which is typically the size used in laser interferometric gravitational radiation detectors (refer to Section 6.9).

6.2   Generation of the Finite Element Model

It was decided to represent the three-dimensional system with what was essentially a 'two-dimensional' cross-sectional slice through it in the x-z plane (see Figure 6.1). This was done since using only two dimensional finite elements (where the third dimension is compressed) in general reduces the overall complexity involved in the model generation and in the interpretation of the results obtained. In modelling the stack in this way, the investigations involving rotational motion were restricted to those where the axis of rotation was parallel to the y-axis (tilting motions).

One way of modelling the isolation stack would be to use the simple spring/damper model shown in Figure 6.2. However in order to reproduce the physical system more accurately the rubber supports were instead modelled as extended rubber meshes. The structure was discretized by generating a mesh of grid points (nodes) and then by connecting these nodes with quadrilateral elements having the desired physical properties (see Figure 6.3). Some of the physical properties of the materials used in the model had to be scaled so that the two dimensional finite element model exhibited behaviour analogous to its three dimensional counterpart.

'Neoprene' is a synthetic rubber used extensively in the ten metre prototype gravitational radiation detector at Glasgow University (refer to Chapter 1) as well as in the prototype nested double pendulum isolation system (refer to Chapter 4). The horizontal and vertical resonant frequencies (f_h and f_v) of the plate (mass m) on four pieces of 'neoprene' rubber were determined experimentally.   Corresponding quality
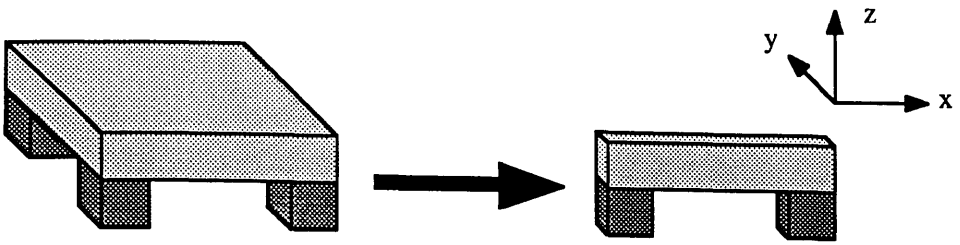
Figure 6.1 *Two-dimensional representation of a three-dimensional stack. The model is constrained to move only in the x-z plane.*
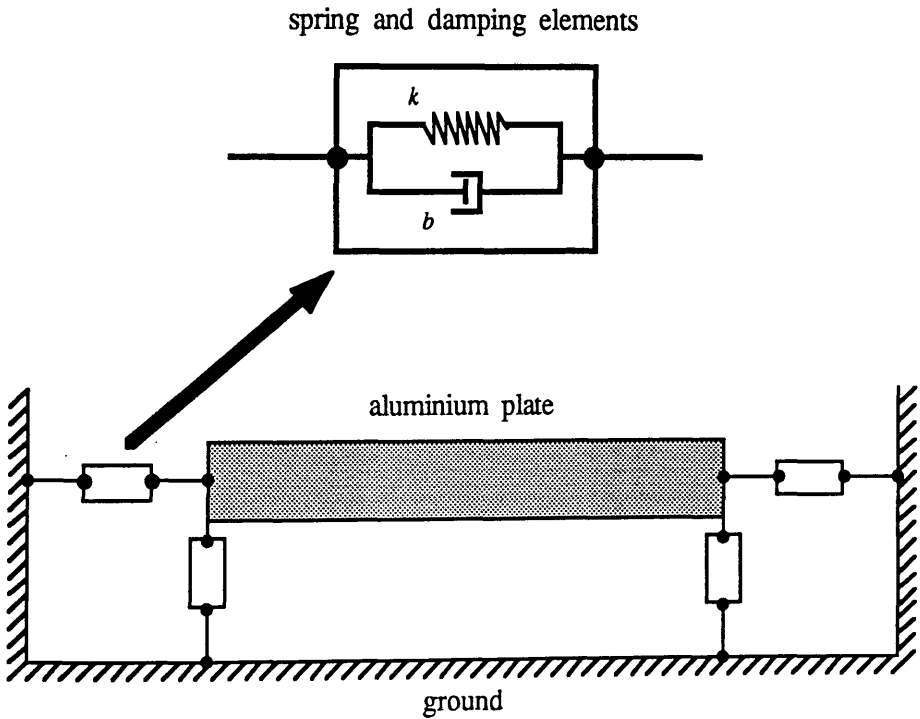

Figure 6.2 *Spring/damper model for vibration isolation stack. The plate is connected to the ground via horizontal and vertical spring/damping elements .*

factors (Q_h and Q_v) were assumed.[*] The value of f_h was used to calculate the horizontal stiffness (k_h) of the loaded rubber using the equation

$$k_h = m\ (2\pi f_h)^2 . \qquad (6.1)$$

Since the finite element model is a thin slice through the real system, a fictitious density had to be assigned to the supported aluminium plate to give the correct loading conditions per unit area of rubber support. Accordingly the shear modulus (G) and the Young's modulus (E) of the aluminium had to be scaled up by the same factor as the density in order to maintain the stiffness properties of the plate. The damping of the internal modes of the plate was controlled using a 'structural element damping coefficient' facility in the NASTRAN package [MSC/Nastran 1983].

In a similar way since one slice-like rubber support in the model represents two block-like supports in the real system it was necessary to scale the moduli of the rubber to give the stack realistic stiffness properties. The shear modulus of the rubber was determined using the equation

$$G = \frac{k_h\,h}{A} \qquad (6.2)$$

where,

$h =$ height of the rubber supports

$A =$ total top surface area of the rubber

and was scaled appropriately.

There is approximately no volume change when rubber undergoes tension or compression [Snowdon 1979] hence

$$Poisson's\ ratio\ \nu = \frac{contractile\ strain}{linear\ strain} \sim 0.5 . \qquad (6.3)$$

This is the largest value for ν that is allowable in the NASTRAN data card describing the material properties of the rubber, since any value larger than 0.5 implies that the material has increased in volume under compression. Consequently the value of the Young's modulus for the rubber was calculated by the finite element program according to the relationship [Snowdon 1979]:

$$E = 2G\ (1 + \nu) \qquad (6.4)$$

[*]Refer to Chapter 2, Section 2.3.4.

giving $$E = 3\,G \qquad\qquad (6.5)$$

and hence $$f_v = \sqrt{3}\,f_h\,. \qquad\qquad (6.6)$$

It is important to note that the ratio between the vertical and horizontal resonant frequencies of stacks is typically larger than $\sqrt{3}$ as a consequence of the effects of loading on the rubber *e.g.* a ratio of ~2.4 was observed experimentally. When loaded, the stiffness in each dimension increases by a varying amount depending on the load applied and the composition and shape of the rubber supports. This illustrates one of the disadvantages of using meshes to represent the rubber supports since the upper limit to the size of f_v was predetermined by the maximum allowed value of v. By the same argument the modelled frequency of the tilting resonance will also be lower by the same factor.

A structural damping coefficient was assigned to the rubber so that the internal modes of the rubber supports were damped to give an internal Q of ~5, this being a typical value [Greenhalgh 1989]. However this internal damping did not provide the viscous damping for the fundamental stack resonances. This was implemented by connecting the nodes at the bases and tops of the rubber supports with orthogonally connected[†] damping elements in the horizontal and vertical directions (see Figure 6.4).

The size of the damping factor b_h was established using knowledge of the quality factor Q_h of the resonance peak (angular frequency ω_h) and the equation

$$b_h = \frac{m\,\omega_h}{Q_h}\,. \qquad\qquad (6.7)$$

The size of the damping factor b_v was calculated in a similar way using the corresponding values for Q_v and ω_v. Note that the value of b_v for the vertically connected damping elements (see Figure 6.4) determines the amount of damping for both the vertical and the tilting modes of the stack. It can be shown by deriving the rotational

---

[†] The horizontal and vertical damping elements were connected orthogonally using a massless 'fictitious node'. Using 'multipoint constraints' this node was instructed to follow the vertical motions of the horizontal element and the horizontal motions of the vertical element. In this way the levels of damping in the two directions are independently defined (refer to Appendix B).

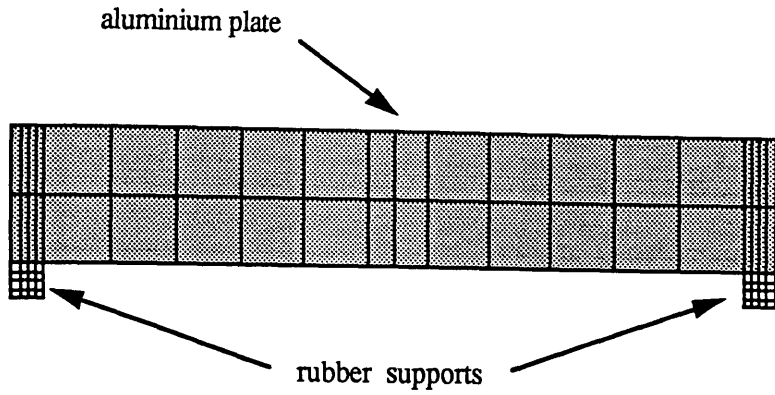**Figure 6.3** *Finite element mesh model of vibration isolation stack. The model is divided into a number of elements having the prescribed physical properties.*
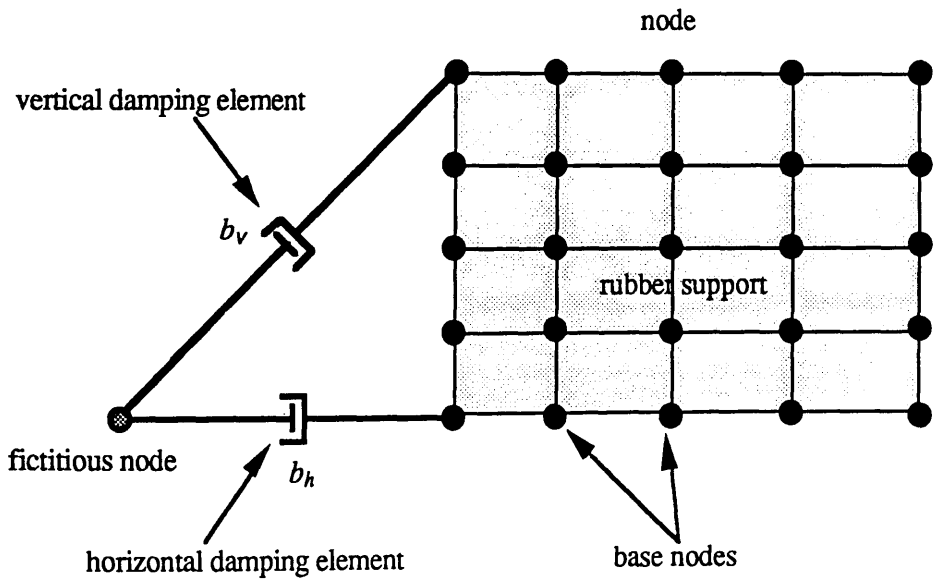

Figure 6.4 *Damping elements connected across rubber supports. A fictitious node is used to connect the two damping elements orthogonally. These provide damping of the supported plate to the ground in both the horizontal and vertical directions.*

equation of motion for the one-layer stack system modelled here that:

$$b_t \sim 3 \, b_v. \tag{6.8}$$

For reference a summary of the physical properties of the modelled system is shown in Figure 6.5.

Despite the approximate nature of this model it incorporates the essential properties of the observed one-layer system and should give a reasonable indication of the cross-coupling mechanisms which take place in vibration isolation stacks.

6.3 Methods of Analysis

Eigenvalue analyses were carried out on the various models described in Section 6.1 to compute the free vibrational modes in each case. These analyses not only eased the interpretation of the frequency response analyses that followed but also provided a way of choosing the frequencies of interest at which to sample, and checking that the mesh had been correctly generated. The various models studied are illustrated in Figure 6.6.

The horizontal to horizontal frequency response analyses for each model were executed by driving the base nodes of the rubber supports (see Figure 6.4) sinusoidally in the horizontal direction with unit amplitude displacement at all frequencies in the range considered. Similarly in the vertical to vertical frequency response analyses the base nodes were driven with unit vertical input. In each case the resulting amplitude of motion of the centre of masses of the supported plates in the appropriate directions were observed. When investigating the rotational isolation behaviour however the base nodes were driven in a stepped manner with reference to a unit vertical input at the end nodes of the base of the rubber supports and with consecutively decreasing displacement drive towards the centre of the plate as illustrated in Figure 6.7. For each plate the relative vertical displacement of an end node and the centre of mass node was observed. This value was then compared to the unit amplitude displacement of the driven end nodes at the base of the rubber supports to give a value for the transmissibility. In evaluating the transmissibility in this way it was assumed that the plates were perfectly rigid at the frequencies considered. This assumption becomes invalid at the modal frequencies of the plates. However the eigenvalue analyses conducted prior to this yield information on the frequencies at which these modes occur.

Investigations into the cross-coupling of tilting ground motion to horizontal and
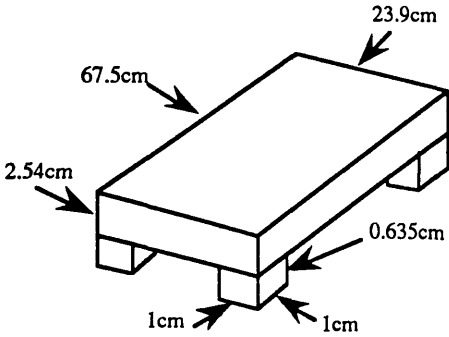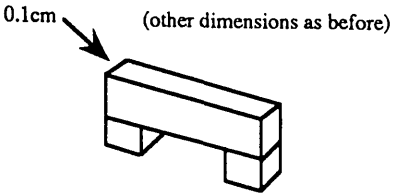
THREE-DIMENSIONAL STACK	TWO-DIMENSIONAL MODEL

23.9cm

67.5cm

2.54cm

0.635cm

1cm   1cm

0.1cm   (other dimensions as before)

aluminium plate	
mass (m) = 11.1Kg	mass (m) = 11.1Kg
density (ρ)=2.7×10^{3}Kgm^{-3}	density (ρ')=1.8×10^{6}Kgm^{-3}
shear modulus (G)=2.8×10^{10}Nm^{-2}	shear modulus (G')=1.9×10^{13}Nm^{-2}
Young's modulus (E)=7.0×10^{10}Nm^{-2}	Young's modulus (E')=4.7×10^{13}Nm^{-2}
Poisson's ratio (ν) = 0.27	Poisson's ratio (ν) = 0.27
internal Q = 0.5 or 20	internal Q = 0.5 or 20
rubber supports	
density (ρ)=1.1×10^{3}Kgm^{-3}	† density (ρ)=1.1×10^{3}Kgm^{-3}
shear modulus (G)=3.6×10^{5}Nm^{-2}	shear modulus (G')=7.3×10^{6}Nm^{-2}
*Young's modulus (E)=1.1×10^{6}Nm^{-2}	* Young's modulus (E')=2.2×10^{7}Nm^{-2}
Poisson's ratio (ν) = 0.5	Poisson's ratio (ν) = 0.5
internal Q = 5	internal Q = 5
KEY	

† this parameter was unscaled (see text Section 6.4)

* determined using the value of the shear modulus and the Poisson ratio (see Section 6.2)

Figure 6.5   *Summary table of the parameters used in the model compared to the three-dimensional system.*

ONE - LAYER STACK MODEL
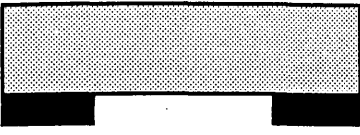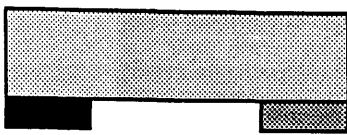
balanced rubber

imbalanced rubber

TWO - LAYER STACK MODEL

balanced rubber

symmetrically imbalanced rubber

10% less stiff than

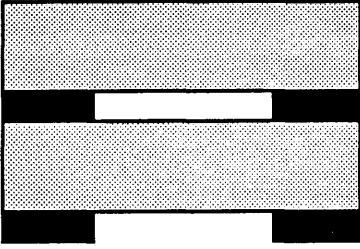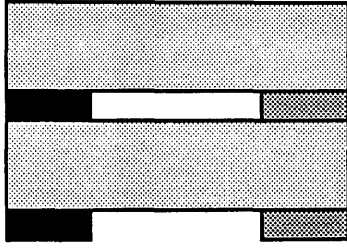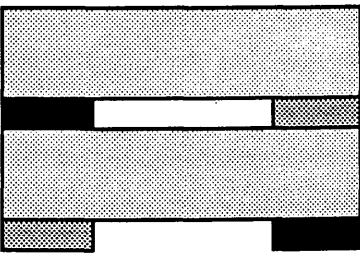asymmetrically imbalanced rubber

Figure 6.6 The various stack systems investigated.

vertical motion of the centres of mass of the plates were carried out using the same stepped driving mechanism described above. The amplitude of the horizontal or vertical motion of the centres of mass of the plates were compared to the unit amplitude displacement of the driven end nodes to give a value for the transmissibility in each case.

In the analyses of the remaining cross-coupling effects, unit vertical or horizontal input at the driven base nodes was used and the orthogonal directional components at the centre of mass nodes of the plates were observed. The amplitude of rotational motion of the plates about their centres of mass were also evaluated in each case by observing the vertical displacements of the end and centre nodes of the plates.

Since the rotational (tilting) motions were measured in this way, the transmissibility graphs for cross-couplings involving rotational motion are presented in terms of a dimensionless transmissibility. These figures can be easily converted to units of $^m/_{rad}$ or $^{rad}/_m$ where appropriate using the conversion factors which are given beside the relevant graphs.

Appendix B gives an example of an input data deck for the horizontal to horizontal frequency response analysis of the one layer stack with imbalanced rubber stiffness properties.

6.4 Eigenvalue Analyses

The one-layer stack model was constrained to move in the x-z plane. Therefore only two of the three possible translational degrees of freedom were accounted for. Similarly only one rotational degree of freedom remained unconstrained, this being rotation about the y-axis (tilt) (refer to Figure 6.1). As a consequence of these constraints the modelled stack had only three fundamental modes of oscillation, namely the horizontal, vertical and tilting modes. With rubber of identical stiffness properties on each side of the stack the observed fundamental frequencies were at $f_h \sim 6.7$Hz, $f_v \sim 13.4$Hz and $f_r \sim 22.1$Hz. These values agreed reasonably well with those predicted using simple theory (see Figure 6.8).

With the introduction of a second layer the number of eigenvalues increased by a factor of two since the number of degrees of freedom of the system increased by a factor of two. (It follows that an n-layer stack modelled in this way would have $3n$ eigenvalues). The normal modes of the two-layer stack occurred in pairs of symmetric and anti-symmetric modes corresponding to the oscillations in the separate layers being in or out of phase with each other.

121
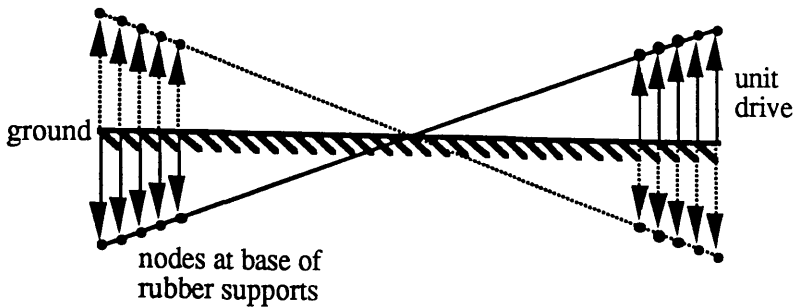
Figure 6.7 *Stepped driving mechanism for investigations of isolation from ground tilt. The nodes are driven with increasing amplitude as one moves further out from the position directly below the centre of mass of the plate. Unit amplitude vertical drive is applied to the end nodes. This is used as a reference value for the evaluation of transmissibilities involving rotational input (refer to Section 6.3).*

horizontal mode	vertical mode	tilting mode
$k_{horiz} \sim 2\,G\,A\,/\,h$	$k_{vert} \sim 2\,E\,A\,/\,h$	$\ddot{\Phi} \sim 6\,E\,A\,\Phi\,/\,m\,h$
$\omega_{horiz}^2 \sim 2\,G\,A\,/\,m\,h$	$\omega_{vert}^2 \sim 2\,E\,A\,/\,m\,h$	$\omega_{tilt}^2 \sim 6\,E\,A\,/\,m\,h$
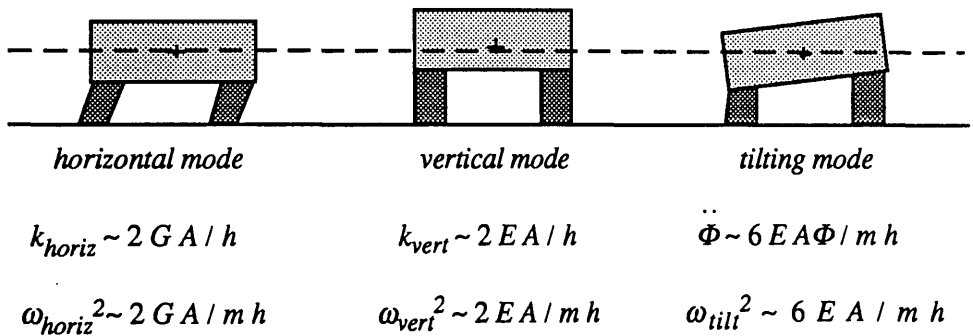
where

k = stiffness of the loaded rubber in the defined direction
G = scaled shear modulus
E = scaled Young's modulus
A = area of one rubber surface in the model
h = height of rubber supports
m = mass of supported plate
Φ = angle the plate makes relative to the horizontal

giving

$$f_{horiz} \sim 7.3\text{Hz} \qquad f_{vert} \sim 12.6\text{Hz} \qquad f_{tilt} \sim 21.7\text{Hz}$$

Figure 6.8 *The three fundamental modes of oscillation of a one-layer stack. Simple theory is used to predict the frequency at which each mode occurs (assuming massless springs and point masses - except for the tilting mode where the mass distribution is approximated to that of a rod).*

At much higher frequencies a series of internal modes of the stack components occurred, *i.e.* transverse modes of the aluminium plates or rubber supports. The first plate mode observed here (at a frequency of ~ 2.2kHz) was the transverse (bending) mode of the plate in the z-direction. With increasing frequency there followed a whole series of higher order transverse plate modes. As shown in Section 5.5.2, the presence of these transverse plate modes are significant in causing a reduction in the vertical isolation of any pendulum suspension supported by the plate. However it should be emphasized here that since this is only a two-dimensional model, the observed modes of the plate will not be identical to the modes occurring in the real three-dimensional system. The analysis of the nested double pendulum system in Chapter 5 yielded more accurate information on the first few modes occurring in such a plate (refer to Section 5.4). In this case the first mode of the plate was in fact the fundamental drum-like resonance where the centre of the plate moved in the vertical direction relative to the corners of the plate. This occurred at the much lower frequency of ~260Hz. Using the same philosophy, the computed internal modes of the rubber supports would not be identical to those of the real three-dimensional system. Furthermore, the density of the rubber in the model was not scaled up to compensate for the conversion from three dimensions to two dimensions (a factor of 20 necessary) and this introduced further discrepancy between the observed modal frequencies and the true modal frequencies. In the model the first internal mode for the rubber supports was the shear mode in the x-direction. This was at a frequency of ~6.1kHz. (With the rubber density scaled up it is predicted that this mode would in fact lie at a lower frequency of ~1.4kHz.) However, despite the fact that the internal modal frequencies of the components of the stack in the model are not identical to those which would occur in the real three-dimensional system, it is still reasonable to observe their effects on the isolation properties of the stack system with confidence.

To illustrate some of the concepts introduced here the first eight normal modes present in the two layer stack with balanced rubber properties are shown in Figure 6.9. The dotted lines represent the undisturbed position of the mesh for reference. These diagrams were generated using the MSC/NASTRAN graphics facility FEMVIEW.

With a 10% reduction in the stiffness of the rubber on one side of the stack, the computed fundamental stack frequencies were slightly lower in value as one would expect and the mode shapes were asymmetrical about the y-z plane.

Symmetric Horizontal Mode   4.1Hz
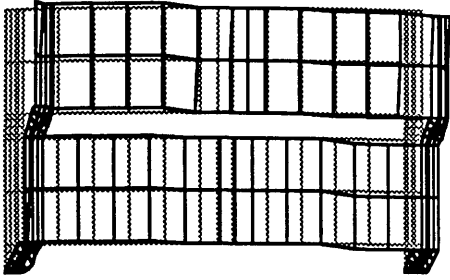
Antisymmetric Horizontal Mode 10.8Hz
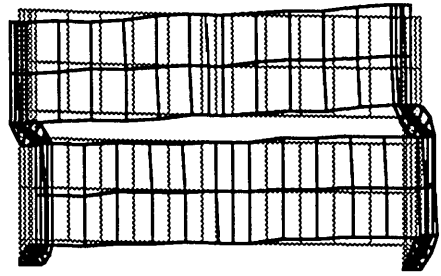
Symmetric Vertical Mode   8.3Hz
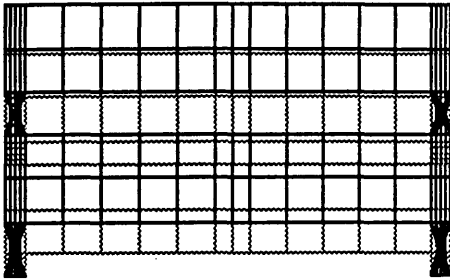
Antisymmetric Vertical Mode   21.7Hz
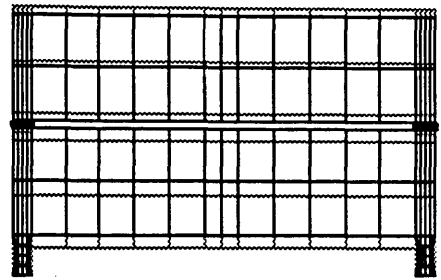
Symmetric Tilting Mode   13.9Hz
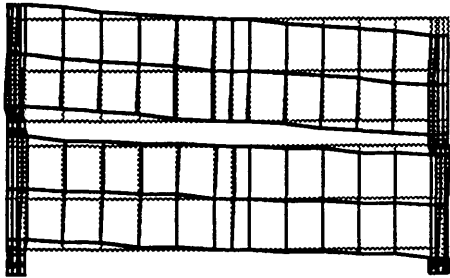
Antisymmetric Tilting Mode   35.6Hz
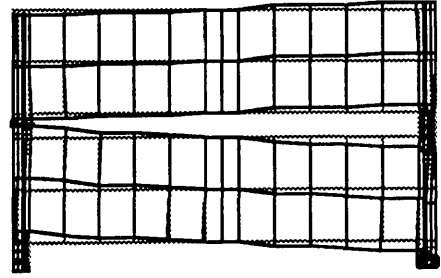
Symmetric Bending Mode   2.21kHz
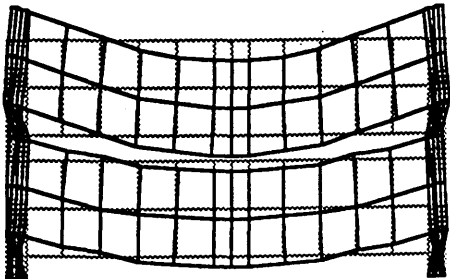
Antisymmetric Bending Mode 2.21kHz
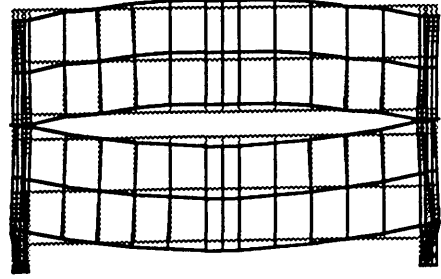
Figure 6.9   Modes present in the two-layer stack with balanced rubber properties. The modes occur in pairs corresponding to the oscillations in the two layers being in or out of phase with each other.

A complete summary of the fundamental frequencies obtained for the various stack models analysed is given in Figure 6.10.

6.5 Direct Transmissibility Investigations in a One-Layer Stack

Horizontal to Horizontal Transmissibility

The horizontal to horizontal frequency response was analysed in the way described in Section 6.3. The base of the stack was driven sinusoidally with unit amplitude and the resulting amplitude of horizontal motion of the centre of mass of the plate was observed. Figure 6.11 shows the transmissibility curve obtained for the case where the rubber on each side of the stack had identical stiffness properties.

Below the horizontal resonant frequency the transmissibility is unity *i.e.* no isolation of the supported plate is achieved. The low Q peak ($Q_h \sim 5$) corresponding to this resonance is seen clearly at $f_h \sim 6.7$Hz. At frequencies higher than this isolation begins to take place. The curve initially falls at ~12dB/octave as one would predict from simple dynamical analysis (refer to Chapter 2, Section 2.3.4). At the corner frequency f_{hc} where

$$f_{hc} = f_h Q_h \qquad (6.9)$$

the effects of the damping of this resonance become apparent and the gradient of the curve reduces to ~6dB/octave.

The transverse resonances of the plate had no observed adverse effect on the horizontal isolation characteristics of the stack. However, since this is only a two-dimensional representation of a three-dimensional system one must adopt a degree of caution when interpreting the results obtained here. Since the model is constrained to the x-z plane no account is taken of the shear modes of the plate in the x-y plane. In a real three-dimensional system these would give rise to peaks in the horizontal transmissibility curve if there was insufficient internal damping in the plate. This concept has already been illustrated in Chapter 5 when considering the effect of the shear modes of the top support plate of the nested double pendulum system (refer to Section 5.5.1).

When a 10% reduction of the stiffness of the rubber was introduced on one side of the stack, the form of the curve was not altered in any unexpected way except that the

ONE - LAYER STACK			
MODEL	f_h	f_v	f_t
balanced	6.7	13.4	22.1
imbalanced	6.6	13.1	21.5

TWO - LAYER STACK						
MODEL	f_h^{s}	f_h^{a}	f_v^{s}	f_v^{a}	f_t^{s}	f_t^{a}
balanced	4.1	10.8	8.3	21.7	13.9	35.6
symmetrically imbalanced	4.0	10.5	8.1	21.1	13.6	34.7
asymmetrically imbalanced	4.0	10.5	8.1	21.2	13.5	34.7

NOTES
All frequencies given in hertz.
Superscripts denote whether symmetric or antisymmetric mode.
Imbalanced figures given for a 10% reduction in the rubber stiffness.

Figure 6.10 Summary of the fundamental resonant frequencies for the various stack systems investigated (see Figure 6.6 and Figure 6.9).

resonant and corner frequencies were shifted to slightly lower values as one would predict.

In conclusion, the observed behaviour agreed well with that predicted using simple dynamical theory.

Vertical to Vertical Transmissibility

The vertical to vertical frequency response of the one-layer stack was analysed in a similar way to the horizontal response. Figure 6.12 shows the transmissibility curves obtained with identical rubber stiffness properties at each end of the stack for the two cases where the top plate had an internal Q of 20 and 0.5 (critical damping). Both curves exhibit the same general behaviour as described for the horizontal to horizontal transmissibility. However since we are now dealing with vertical excitation, the resonance peak is at $f_v \sim 13.4$Hz and the corner frequency is at $f_{vc} = f_v Q_v \sim 200$Hz corresponding to a vertical quality factor of $Q_v \sim 15$.

It is interesting to note the reduction in isolation that occurs when the top plate is not critically damped (refer to $Q=20$ curve in Figure 6.12). The first bending resonance of the plate clearly gives rise to a large peak in the transmissibility curve at about 2.2kHz with a resulting reduction in isolation at and above this frequency. A whole family of these peaks would occur at higher frequencies corresponding to the higher order modes which have an antinode at the centre of mass of the plate.

As in the case of the horizontal transmissibility, the presence of a 10% stiffness imbalance in the rubber did not alter the form of the curves in any unexpected way except for shifting the resonant and corner frequencies to slightly lower values.

In conclusion the observed behaviour agreed well with that predicted using simple dynamical theory at frequencies below the first transverse resonance of the plate. If the plate was not critically damped significant isolation degradation occurred at frequencies on and above the first transverse resonant frequency of the plate. This problem can be alleviated by careful design of the plate to attempt to ensure that these modes lie at frequencies high enough that the isolation degradation which occurs is relatively insignificant. Alternatively some form of damping compound can be used to critically damp the oscillations.
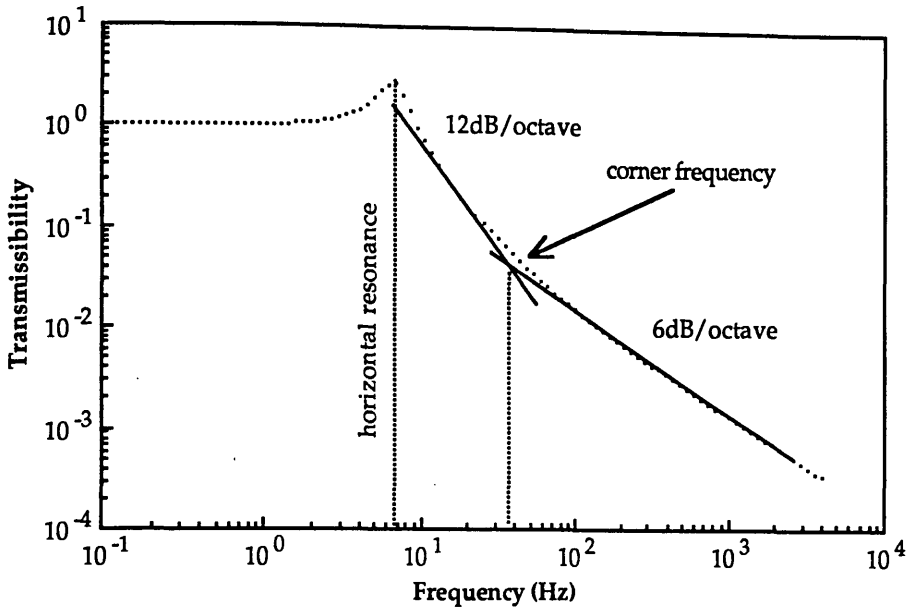
Figure 6.11 *Horizontal to horizontal transmissibility of a one-layer stack with balanced rubber properties.*
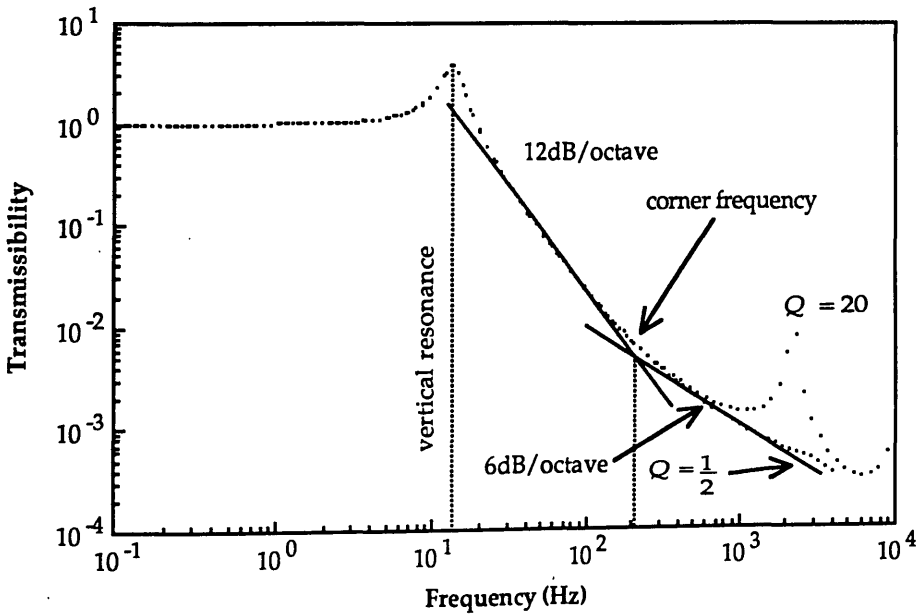
Figure 6.12 *Vertical to vertical transmissibility of a one-layer stack with balanced rubber properties.*

Rotational to Rotational Transmissibility

The rotational to rotational transmissibility was investigated using the stepped driving mechanism described in Section 6.3 (see Figure 6.7). The curves obtained for the various cases examined with a top plate $Q = 0.5$ exhibited behaviour similar to those obtained in the other direct transmissibility investigations already discussed in this section. For the case with identical rubber stiffness properties at each end of the stack the tilting resonance peak was observed at $ft \sim 22.1$Hz. The corner frequency at which the gradient reduced from ~12dB/octave to ~6dB/octave was observed at $ftc \sim 190$Hz corresponding to a Qt ~ 9. In the cases examined where the top plate was less than critically damped the measured rotation figures were invalid at the transverse modal frequencies of the plate.

In conclusion the observed behaviour in each case agreed well with that predicted using simple dynamical theory if the components of the stack had sufficient internal damping. It was also shown here that the presence of a stiffness imbalance does not affect the direct transmissibility characteristics of the one-layer stack in any unexpected way.

6.6 Indirect Transmissibility Investigations in a One-Layer Stack

This section examines the cross-coupling mechanisms which take place in a one-layer stack. For convenience these have been divided into two categories; those mechanisms which do not depend on the presence of a stiffness variation between the rubber at opposite ends of the stack (Section 6.6.1) and those mechanisms which arise only if a variation in the rubber stiffness is present (Section 6.6.2).

6.6.1 Indirect Transmissions Independent of the Presence of a Stiffness Variation in the Rubber

The transmission routes observed to be in this category were those of horizontal to rotational motion and conversely of rotational to horizontal motion. These coupling mechanisms can be visualized by considerations of the geometry of the system. Furthermore, in each case, the magnitude of the variation in coupling due to the presence of a stiffness variation between the rubber at either end of the stack is relatively

125

insignificant.

Horizontal to Rotational Transmissibility

Figure 6.13 shows the horizontal to rotational transmissibility curve for the one-layer stack system with identical rubber stiffness properties. The base of the stack was driven with unit amplitude in the horizontal direction and the resulting rotation of the plate about its centre of mass was observed in the manner described in Section 6.3. The curve rises at ~12dB/octave at low frequency. This can be explained by referring to Figure 6.14. The system is essentially rigid at low frequencies. One can see from this diagram that the plate is subject to   torques which force the plate to undergo rotation about its centre of mass. Now since the base is driven in such a way as to give unit displacement of the base nodes at all frequencies, the driving force must increase with angular frequency (ω) squared according to the equation

$$|F| = m\,\omega^2\,|x| \qquad\qquad (6.10)$$

where,

    $|F|$ = magnitude of the driving force

    m = the sum of the masses assigned to the nodes being driven [†]

    $|x|$ = magnitude of the displacement = 1.

Since the net couple has the same frequency dependence as the driving force this means that the resulting rotation increases with the frequency squared at frequencies below the horizontal resonance.

Two resonance peaks are visible on the curve at f_h and f_t. The higher frequency isolation characteristics are those of a one resonance system with the curve initially falling at ~12dB/octave and eventually tending to ~6dB/octave. The tilting resonance is directly excited by the applied torque. Above this frequency isolation takes place. A peak occurs at f_h because the horizontal motion of the plate becomes large at this frequency and this effectively increases the torque. It is important to note that if there were no vertical offset between the centre of mass of the supported plate and the centres of the rubber supports then the mechanism for cross-coupling of this type would no longer exist.

[†] A fictitious mass is assigned to any driven node. This mass is usually of the order of 10^5 or 10^6 times the mass of the whole system [MSC/Nastran 1983].

Figure 6.13 *Horizontal to rotational transmissibility[†] of a one-layer stack with balanced rubber properties. To convert to units of $^{rad}/_m$ divide the transmissibility value by the half plate length ($\sim 1.2 \times 10^{-1}$m). ([†]as defined in Section 6.3)*

Figure 6.14 *Mechanism for the cross-coupling of horizontal to rotational motion in a one-layer stack. The plate is subject to torques which force it to rotate about its centre of mass (c.o.m.).[*]*

Rotational to Horizontal Transmissibility

Figure 6.15 shows the rotational to horizontal transmissibility curve obtained. In comparison with the above case, the transmissibility at low frequencies has a constant value the magnitude of which depends directly on the physical dimensions of the stack. The system is essentially rigid at low frequencies and rotation at the base converts linearly to horizontal motion of the centre of mass of the plate since the axis of rotation is vertically offset from the centre of mass. This is illustrated in Figure 6.16. Hence the centre of mass is effectively driven at the same frequency in the horizontal direction with constant amplitude at low frequencies giving a flat response curve. Both the horizontal and tilting modes are excited directly by the rotational drive at the base giving rise to peaks at f_h and f_t. At higher frequency the motion of the plate is complicated with components in both the rotational and horizontal senses. The two motions are coupled together and therefore the transmissibility curve initially falls at ~24dB/octave tending to ~12dB/octave at higher frequencies.

6.6.2 Indirect Transmissions Dependent on the Presence of a Stiffness Variation in the Rubber

The transmission routes observed to be in this category include rotational to vertical transmissibility, vertical to rotational and horizontal transmissibility and horizontal to vertical transmissibility. The coupling mechanisms involved here originate due to the presence of a stiffness variation between the rubber supports at either end of the stack. Further, the magnitude of the cross-coupling effects were observed to scale linearly with the percentage stiffness imbalance.

Rotational to Vertical Transmissibility

At low frequency, rotational motion at the base of the stack converts to vertical motion of the centre of mass of the plate. However this is a non-linear conversion with the induced vertical motion occurring at twice the driving frequency. Since NASTRAN does not account for such non-linear effects there was no observed vertical motion for the case where the rubber stiffness at either end of the stack was identical. However, as described in Section 6.5, rotational drive will give rise to rotational motion of the plate. In the presence of a vertical stiffness imbalance between the rubber supports at either end of the stack the axis of the induced rotation will not be about the centre of mass of the plate.
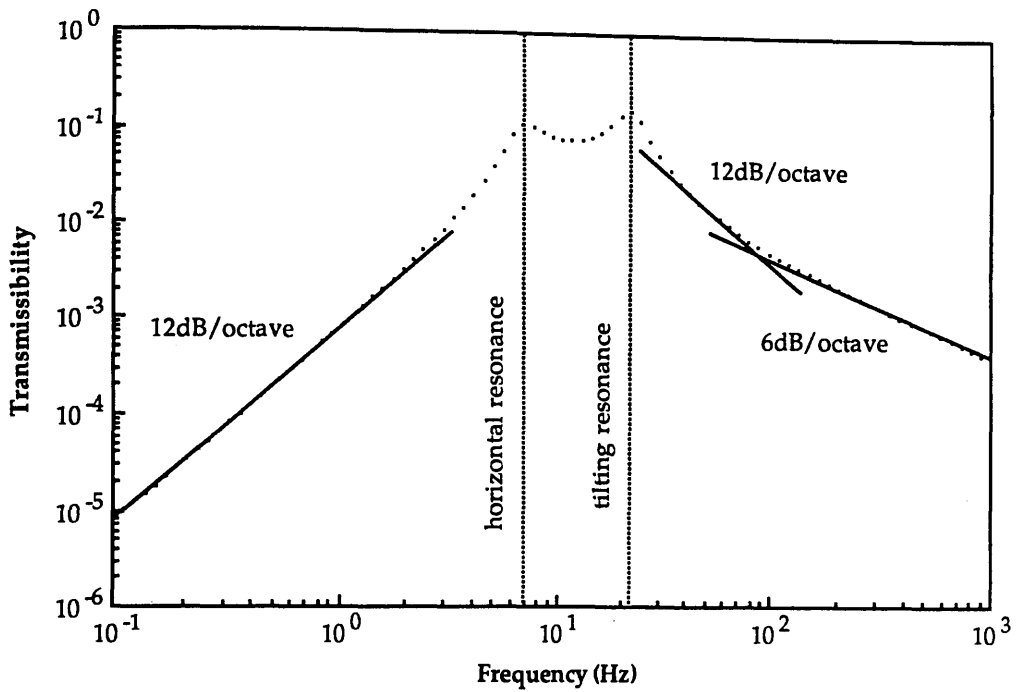
127
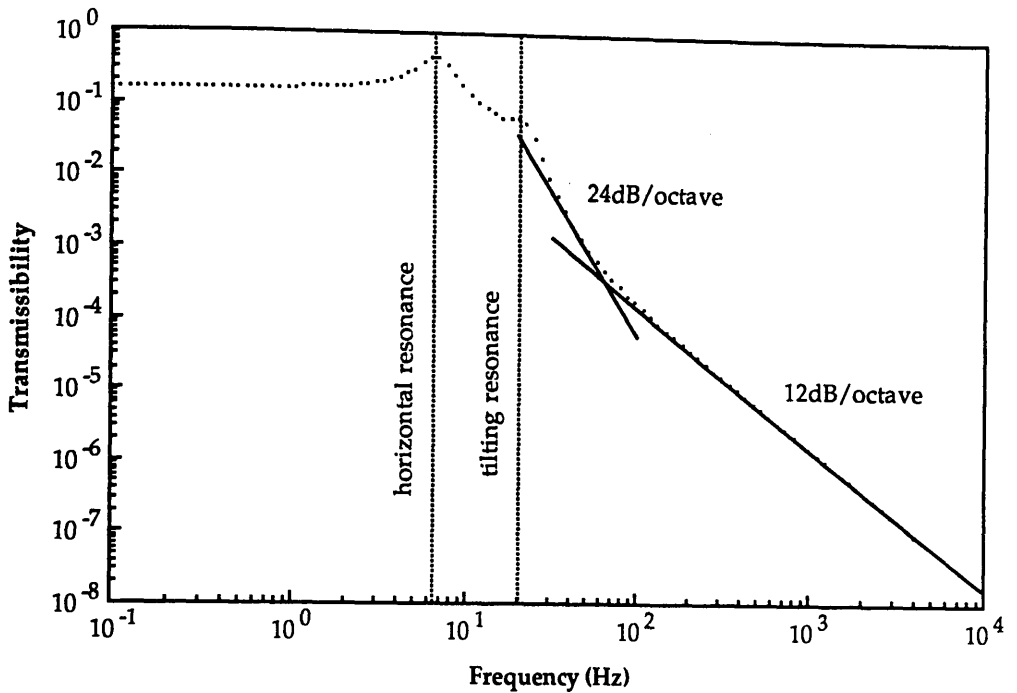
Figure 6.15 *Rotational to horizontal transmissibility[†] of a one-layer stack with balanced rubber properties. To convert to units of $m/_{rad}$ multiply the transmissibility value by the half plate length ($\sim1.2\times10^{-1}$m). ([†] as defined in Section 6.3)*
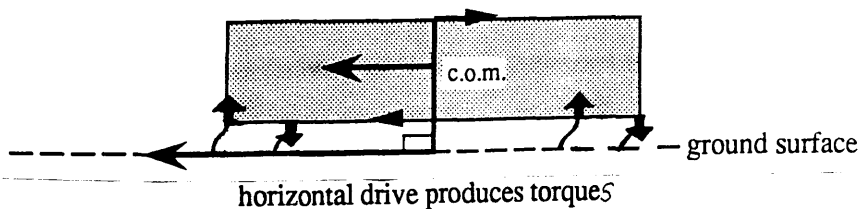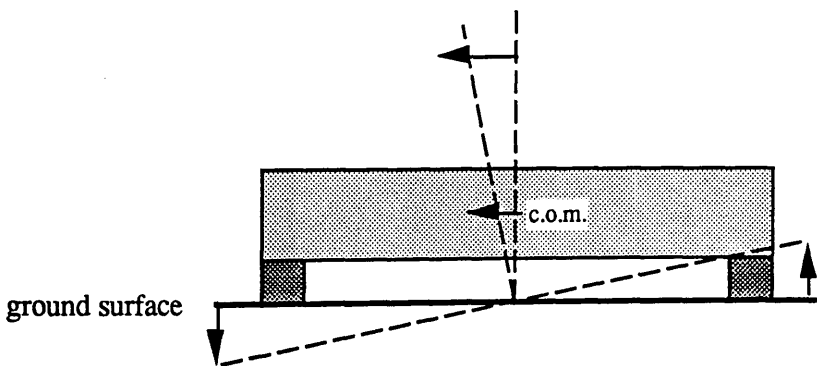

Figure 6.16 *Mechanism for the cross-coupling of rotational to horizontal motion in a one-layer stack. At low frequencies the system is essentially rigid and the centre of mass (c.o.m.) of the plate is effectively driven linearly in the horizontal direction. The larger the vertical offset the larger this effect.*

This gives rise to some component of vertical motion at the centre of mass of the plate. Figure 6.17 shows the response curve obtained. The curve rises at ~12dB/octave since the effective torque increases as the frequency squared (see equation (6.10)). The vertical and tilting modes are coupled and hence the transmissibility falls at a rate of ~12dB/octave at higher frequencies.

Vertical to Rotational Transmissibility

When applying a displacement vertically in the presence of a vertical stiffness imbalance the plate will tend to rotate since it is effectively subject to a torque. The curve for vertical to rotational transmissibility is shown in Figure 6.18. This curve rises at ~12dB/octave since the effective torque increases as the frequency squared (see equation (6.10)). The vertical and tilting modes are coupled and hence the curve tends to fall-off at ~12dB/octave at higher frequencies. The flattening of the curve at frequencies above a few hundred hertz is believed to be due to computational rounding errors.

Vertical to Horizontal Transmissibility

As discussed in the previous example, if a vertical stiffness imbalance exists between the rubber at opposite ends of the stack, when the plate is driven in the vertical sense it will tend to rotate. Since in the one-layer stack there is horizontally stiff rubber along the lower surface of the supported plate but not along the upper surface, the induced rotation will not be about the centre of mass of the plate. This results in some horizontal component of motion of the centre of mass. The transmissibility curve obtained in this case is shown in Figure 6.19. The curve rises at ~12dB/octave since the base is being driven with unit vertical displacement and this is equivalent to a frequency dependent torque being applied (see equation (6.10)). Three peaks corresponding to the fundamental stack resonances are observed in the curve. These resonances are coupled and hence the curve tends to fall at ~18dB/octave at higher frequencies. Again the curve flattens off at a few hundred hertz due to computational rounding errors.

Horizontal to Vertical Transmissibility

If no stiffness variation were present, horizontal motion at the base of the stack would not linearly convert to vertical motion of the centre of mass of the supported plate. Some non-linear conversion would probably take place. However as mentioned earlier NASTRAN cannot account for such non-linear effects.

Figure 6.17 *Rotational to vertical transmissibility[†] in a one-layer stack with a 10% stiffness variation present in the rubber. To convert to units of $^m/_{rad}$ multiply the transmissibility value by the half plate length (~1.2×10^{-1}m).*
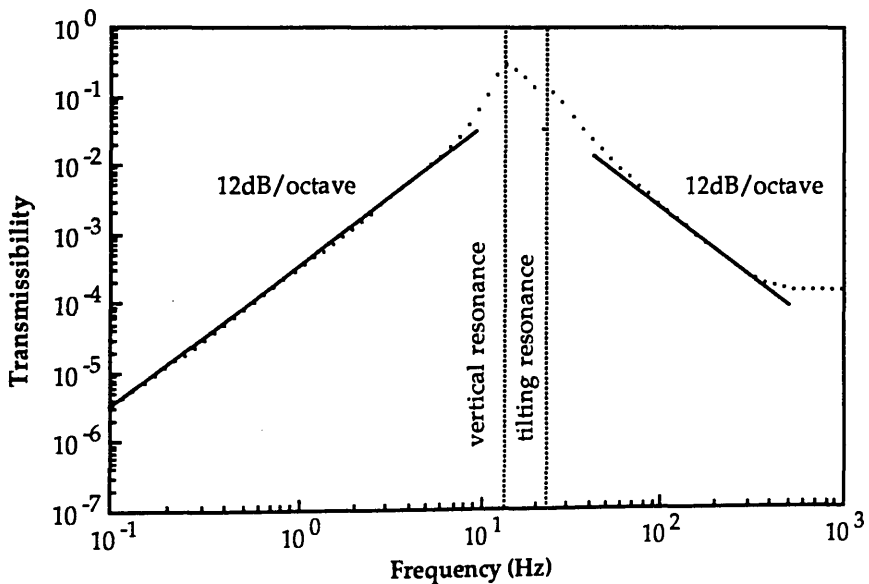
Figure 6.18 *Vertical to rotational transmissibility[†] in a one-layer stack with a 10% stiffness variation present in the rubber. To convert to units of $^{rad}/_m$ divide the transmissibility value by the half plate length (~1.2×10^{-1}m).*

(*[†] as defined in Section 6.3*)

It has already been shown in Section 6.6.1 that if the base is driven horizontally some rotational motion of the plate about its centre of mass will be induced (refer to Figure 6.14). As a consequence of the presence of a vertical stiffness imbalance between the rubbers at opposite ends of the stack the axis of this induced rotation will not be at the centre of mass of the plate. This results in the centre of mass of the plate having some vertical component of motion. The response curve is shown in Figure 6.20. At low frequency the curve rises at a rate of ~12dB/octave since the induced rotation rises with frequency squared (see equation (6.10)). Three resonance peaks are observed at the three fundamental stack resonances. The gradient of the curve tends to ~18dB/octave at high frequency since these three resonances are coupled. At a few hundred hertz the curve is seen to dip slightly and then flatten. Again this is believed to be due to rounding errors in the calculations performed by the computer.

In conclusion, the four types of cross-couplings described here originate due to the presence of a stiffness variation in the rubber properties across the stack. Furthermore, for vertical to horizontal and horizontal to vertical coupling to take place *it is thought that* there must also be a vertical offset between the centre of mass of the supported plate and the *centres* ^ of the rubber supports.

For convenience a summary table of the transmissibility values (both direct and indirect) obtained for the one-layer stack at a frequency of 100Hz is given in Figure 6.21.

6.7 Direct Transmissibility Investigations in a Two-Layer Stack

Each of the direct transmissibility investigations with the various combinations of parameters discussed in Section 6.3 were repeated for the case of a two-layer stack.

Horizontal to Horizontal Transmissibility
The horizontal to horizontal transmissibility curves for the transmission of motion at the base of the stack to the centre of mass of each plate in the stack with the plates critically damped and identical rubber stiffness properties is shown in Figure 6.22. The curve obtained for layer one is almost identical to that shown in Figure 6.11 for the one layer stack model except that in this case there are two fundamental horizontal resonant frequencies of the stack as shown in Figure 6.9. Two peaks are therefore present in the
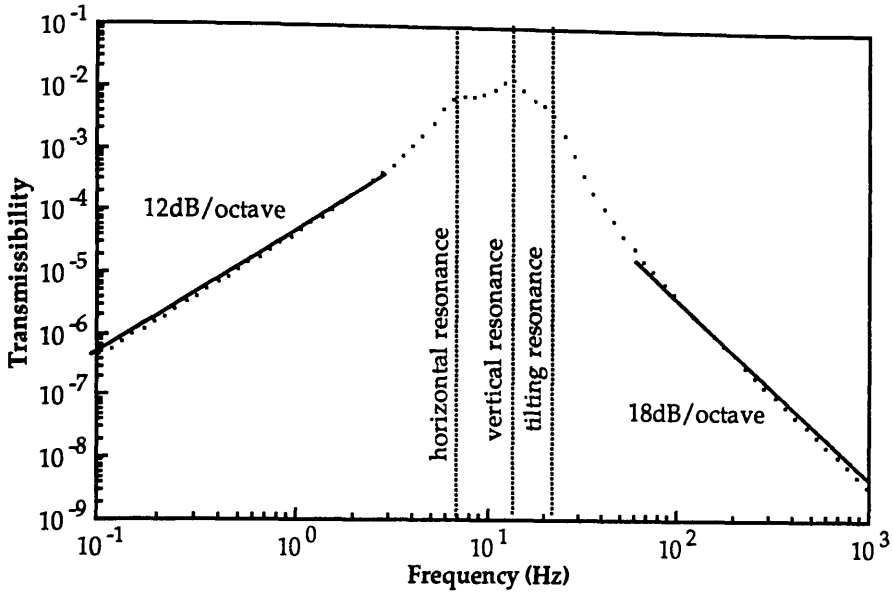
Figure 6.19 *Vertical to horizontal transmissibility in a one-layer stack with a 10% stiffness variation present in the rubber.*

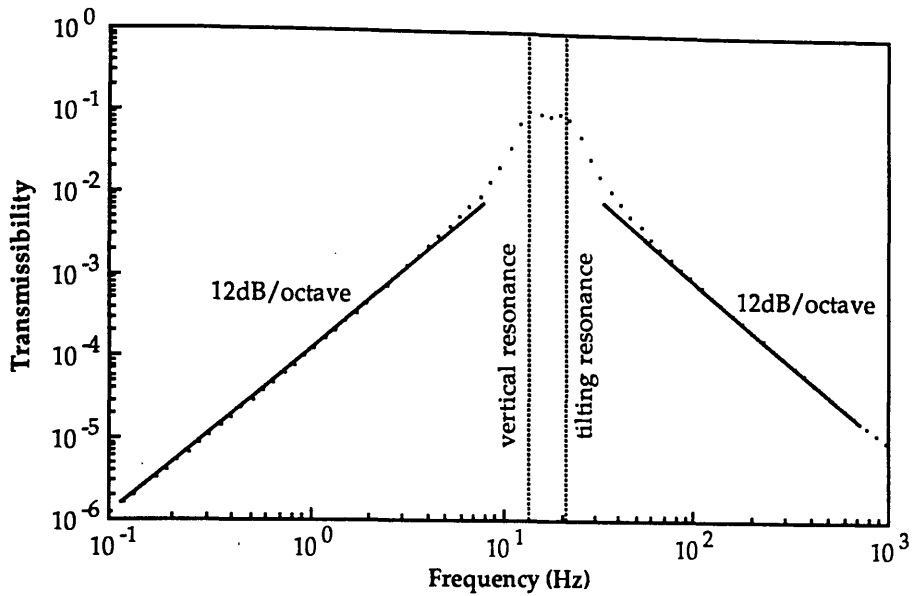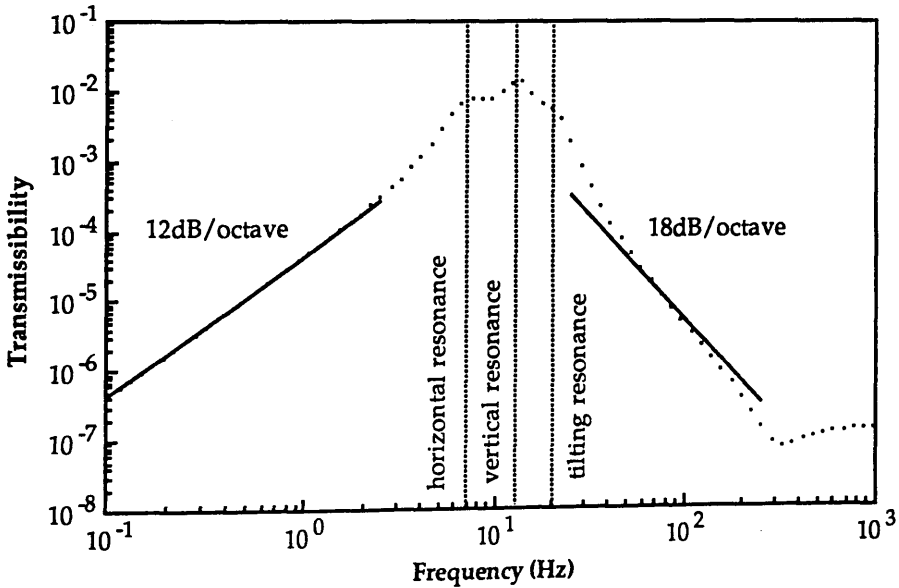**Figure 6.20** *Horizontal to vertical transmissibility in a one-layer stack with a 10% stiffness variation present in the rubber.*

OUT IN	HORIZONTAL	VERTICAL	ROTATIONAL
HORIZONTAL	~1.6 × 10^{-2}	~5.0 × 10^{-6}	~4.4 × 10^{-2} rad/$_m$
VERTICAL	~5.1 × 10^{-6}	~2.3 × 10^{-2}	~2.3 × 10^{-2} rad/$_m$
ROTATIONAL	~2.1 × 10^{-5} m/$_{rad}$	~1.2 × 10^{-4} m/$_{rad}$	~6.4 × 10^{-2}

☐ Independent of a stiffness variation in the rubber across the stack.

▨ Dependent on the presence of a stiffness variation in the rubber. Values given for the case of a 10% variation.

Figure 6.21 Summary table of the transmissibility values for the one-layer stack at 100Hz.
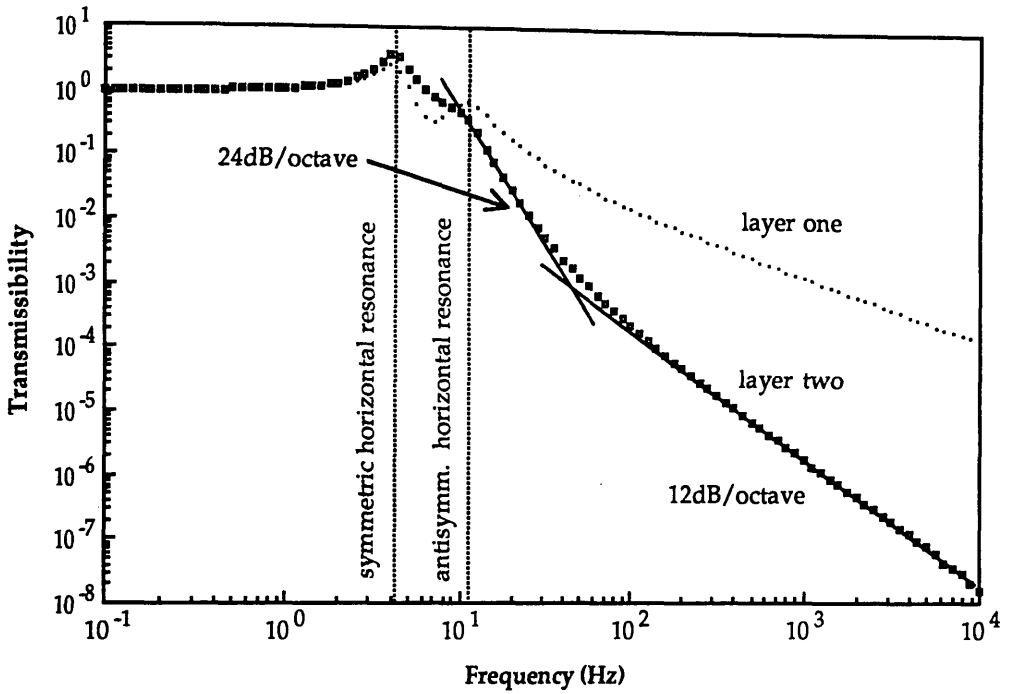
Figure 6.22 *Horizontal to horizontal transmissibility of a two-layer stack with balanced rubber properties. The isolation at layer two becomes improved over that at layer one at frequencies above the second horizontal resonance of the system.*

curve as opposed to one. However the isolation characteristics of layer one are the same as for the one-layer model. The second layer has improved isolation above the second horizontal resonant frequency of the stack with the curve initially falling at ~24dB/octave and reducing to ~12dB/octave above the new corner frequency.

Vertical to Vertical & Rotational to Rotational Transmissibility
The vertical to vertical and rotational to rotational transmissibility curves exhibited similar general characteristics to the horizontal to horizontal curves with improved isolation at the second layer at frequencies above the second coupled resonance peak.

In conclusion, improved isolation is obtained with an increasing number of layers in terms of direct transmissibility. The observed isolation agrees well with that predicted using simple dynamical theory if the components of the stack have sufficient internal damping. Furthermore it was observed that the presence of a stiffness imbalance in the rubber whether it is symmetrical or asymmetrical about the y-z plane (see Figure 6.6) does not affect the direct transmissibility characteristics of the two-layer stack in any unexpected way.

6.8 Indirect Transmissibility Investigations in a Two-Layer Stack

These mechanisms occur in a similar way to those described for the one-layer stack system in Section 6.6. However there are some interesting results as a consequence of the presence of more than one layer.

6.8.1 Indirect Transmissions Independent of the Presence of a Stiffness Variation in the Rubber

Horizontal to Rotational Transmissibility
The curves obtained for the two-layer stack are shown in Figure 6.23. The general shape of the curve for layer one has already been explained in Section 6.6.1. A damped null is observed between the two tilting resonances (labelled no.5). This occurs due to the phase change in the motion of the plate with respect to the driving force which takes place between the symmetric and antisymmetric tilting resonances. Layer two exhibits similar

low frequency behaviour with essentially the same magnitude of transmission because the rotational motions induced at layer one have unit transfer to layer two at these low frequencies. However layer two has improved isolation at higher frequencies above the various resonances. Horizontal motion at the base is converted to rotational motion at layer two mainly *via* induced rotational and horizontal motions at layer one. Thus the principal transmission routes at 100Hz are:

$$horizontal_{base} \text{ - } rotational_{c.o.m.1} \text{ - } rotational_{c.o.m.2} \quad \text{giving } T \sim 2.8 \times 10^{-3} \text{ rad}/_m$$
and
$$horizontal_{base} \text{ - } horizontal_{c.o.m.1} \text{ - } rotational_{c.o.m.2} \quad \text{giving } T \sim {\sim}7.0 \times 10^{-4} \text{ rad}/_m.$$

The subscripts describe the position at which the motion is taking place[†]. The transmissibility (*T*) in each case was evaluated by taking the product of the relevant transmissibility values obtained from the one-layer analyses as given in Figure 6.21. The curve initially falls at about 24dB/octave tending to ~12dB/octave at higher frequencies. In conclusion horizontal motion at the base of the stack converts to rotational motion at the top of the stack mainly *via* rotational motion induced at the intermediate stage.

Rotational to Horizontal Transmissibility

Figure 6.24 shows the transmissibility curves from the rotationally driven base to the horizontal motions of the centres of mass of the two plates. At low frequencies there is greater transmission to layer two than to layer one. This is understandable since the stack behaves rigidly at low frequencies and layer two has a larger vertical offset from the axis of rotation. Figure 6.16 illustrates this idea. Both curves fall at approximately 12dB/octave at high frequency; the isolation at layer two is not much improved over that at layer one. This is a surprising result since it somewhat disagrees with what one would intuitively think. One might assume that the rotational motion at the base would be converted to horizontal motion at layer two either *via* rotational or horizontal motion at layer one. Using these assumptions one would then predict the transmissibility at layer two, at say 100Hz, to be the product of the two transmissibility figures obtained from the one-layer case (refer to Figure 6.21) *i.e.*

[†]   base   =   the ground surface on which the base nodes lie

  c.o.m.1 =   centre of mass of plate one

  c.o.m.2 =   centre of mass of plate two
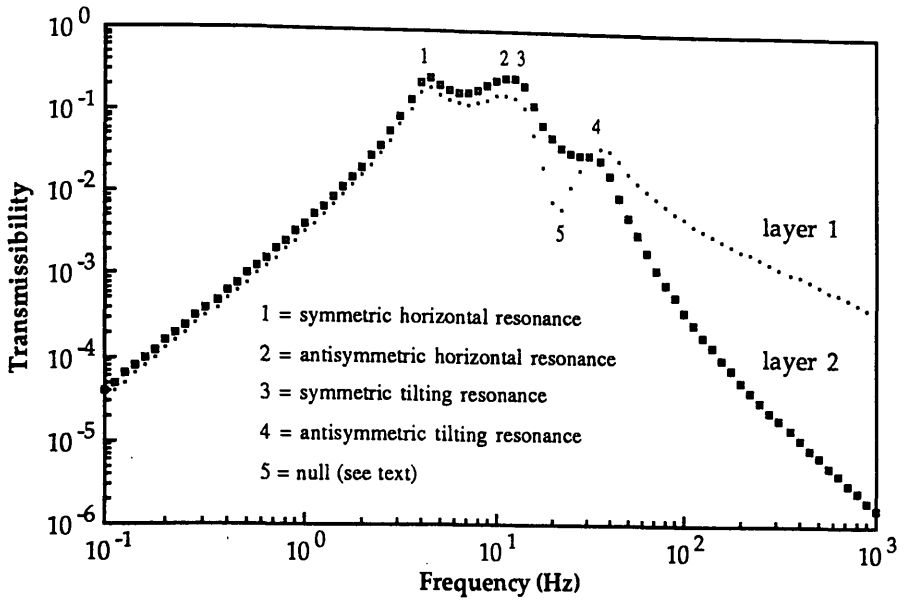
Figure 6.23 *Horizontal to rotational transmissibility[†] in a two-layer stack with balanced rubber properties. To convert to units of $^{rad}/_m$ divide the transmissibility value by the half plate length (~1.2×10⁻¹m).*
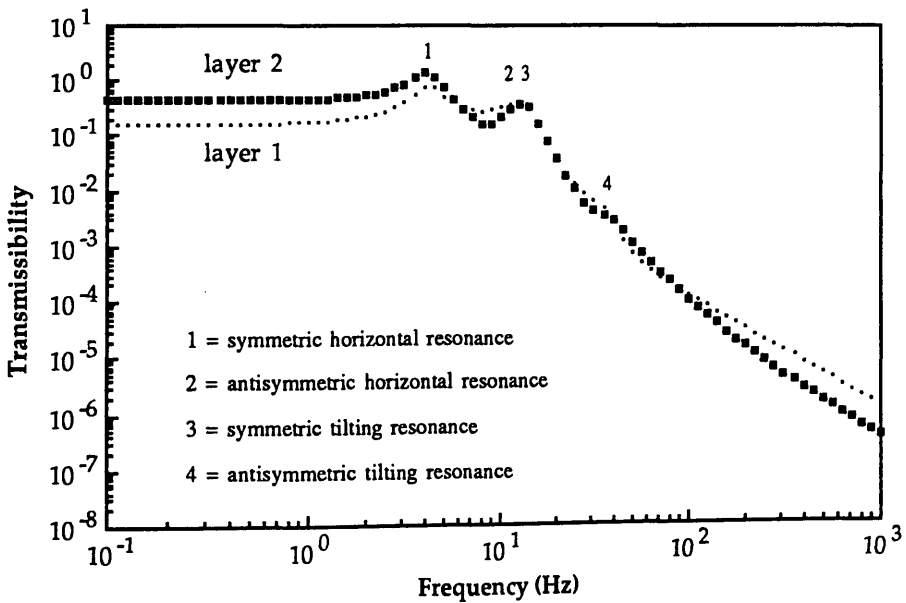
Figure 6.24 *Rotational to horizontal transmissibility[†] in a two-layer stack with balanced rubber properties. To convert to units of $^m/_{rad}$ multiply the transmissibility value by the half plate length (~1.2×10⁻¹m).*

(*[†] as defined in Section 6.3*)

rotational $_{base}$ - *rotational* $_{c.o.m.1}$ - *horizontal* $_{c.o.m.2}$ giving $T \sim 1.3 \times 10^{-6}$ m/$_{rad}$

or

rotational $_{base}$ - *horizontal* $_{c.o.m.1}$ - *horizontal* $_{c.o.m.2}$ giving $T \sim 3.4 \times 10^{-7}$ m/$_{rad}$.

However neither of these factors account for the large magnitude of transmissibility observed at layer two. The solution to this puzzle lies in the fact that since the intermediate plate in the stack has a finite thickness and the rubber supports for layer two are connected to the plate in layer one along its top surface, there exists a vertical offset between the bases of the rubber supports and the centre of mass of the underlying plate. Therefore any rotation of the plate in layer one about its centre of mass gives rise to an effective horizontal motion at the top surface of this plate. Hence the bases of the rubber supports for layer two are subject to a horizontal motion which is much larger than the horizontal motion observed directly at the centre of mass of the underlying plate. Therefore the principal transmission route is in fact

rotational $_{base}$ - (*rotational* $_{c.o.m.1}$ - *horizontal* $_{top1}$) - *horizontal* $_{c.o.m.2}$

giving $T \sim 1.3 \times 10^{-5}$ m/$_{rad}$ at 100Hz.

Again the subscripts describe the position at which the motion is taking place [†]. Note that the size of the bracketed term is directly proportional to the size of the vertical offset. This bracketed term which describes intra-plate conversion of rotational to horizontal motion is responsible for the isolation at layer two being much poorer than expected.

In conclusion the vertical offset between the centre of mass of plate one and the base level of the rubber supports in layer two determines the extent to which ground tilts couple to horizontal motion at the top plate of the two-layer stack.

6.8.2 Indirect Transmissions Dependent on the Presence of a Stiffness Variation in the Rubber

Rotational to Vertical Transmissibility

The curves obtained for the transmission to the plates in the two layers are shown in

---

[†] $_{top1}$ = top surface of plate one (equivalent to base line of rubber supports for layer two).

Figure 6.25. As one might expect, improved isolation is observed at layer two, the transmission curve falling at ~18dB/octave at high frequency. There are two principal transmission routes to the second layer at 100Hz *i.e.*

$rotational_{base}$ - $rotational_{c.o.m.1}$ - $vertical_{c.o.m.2}$ giving $T \sim 7.7 \times 10^{-6}$ $^m/_{rad}$
    and

$rotational_{base}$ - $vertical_{c.o.m.1}$ - $vertical_{c.o.m.2}$ giving $T \sim 2.8 \times 10^{-6}$ $^m/_{rad}$.

Vertical to Rotational Transmissibility

Figure 6.26 shows the curves obtained for the vertical to rotational transmissibility at each layer. Improved isolation is observed at layer two, the transmission curve falling at ~18dB/octave at high frequency. Again the principal transmission route to layer two at 100Hz is *via* rotation at the intermediate layer *i.e.*

$vertical_{base}$ - $rotational_{c.o.m.1}$ - $rotational_{c.o.m.2}$ giving $T \sim 1.5 \times 10^{-3}$ $^{rad}/_m$.

Vertical to Horizontal Transmissibility

Figure 6.27 shows the transmissibility curves obtained for this case. The isolation at layer two is poorer than at layer one at frequencies above the resonances. The larger than expected transmission to layer two can again be explained *via* rotation at layer one being introduced and intra-plate conversion of rotational to horizontal motion taking place. The principal transmission route to layer two is:

$vertical_{base}$ - $(rotational_{c.o.m.1}$ - $horizontal_{top1})$ - $horizontal_{c.o.m.2}$

giving $T \sim 4.7 \times 10^{-6}$ at 100Hz.

Perhaps of even greater interest is the form of the curve for layer one of this two-layer model. The curve falls at ~30dB/octave and flattens off at high frequencies due to computational rounding errors. In Section 6.6.2 it was shown that the corresponding transmissibility curve for the one-layer model had a gradient of ~ 18dB/octave (refer to Figure 6.19). In other words, it appears that the presence of the overlying layer has reduced the coupling of vertical ground motion to horizontal motion at layer one. This effect can be explained by considering the changes in the dynamics of layer one which
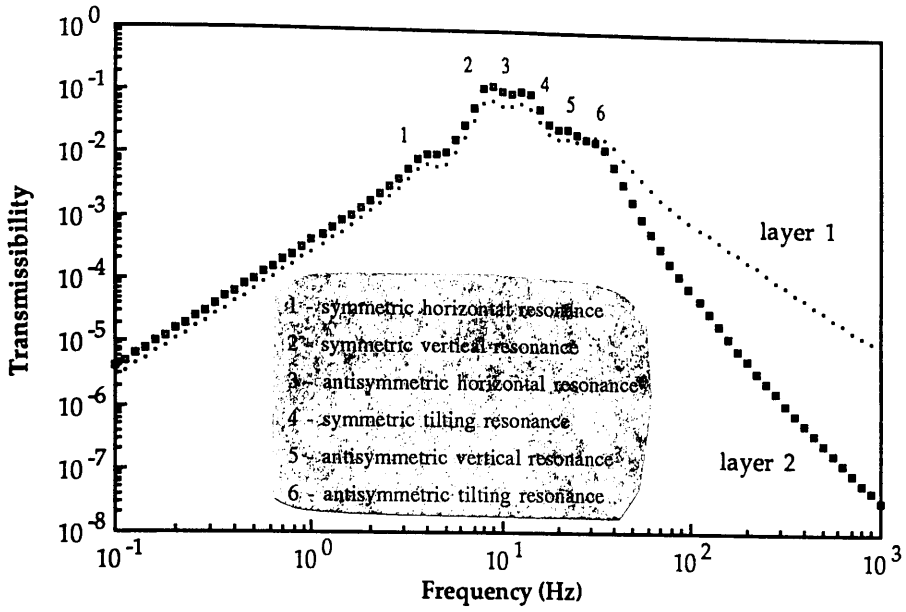
Figure 6.25 *Rotational to vertical transmissibility[†] in a two-layer stack with a 10% stiffness variation. To convert to units of $^m/_{rad}$ multiply the transmissibility value by the half plate length ($\sim 1.2 \times 10^{-1}$m).*
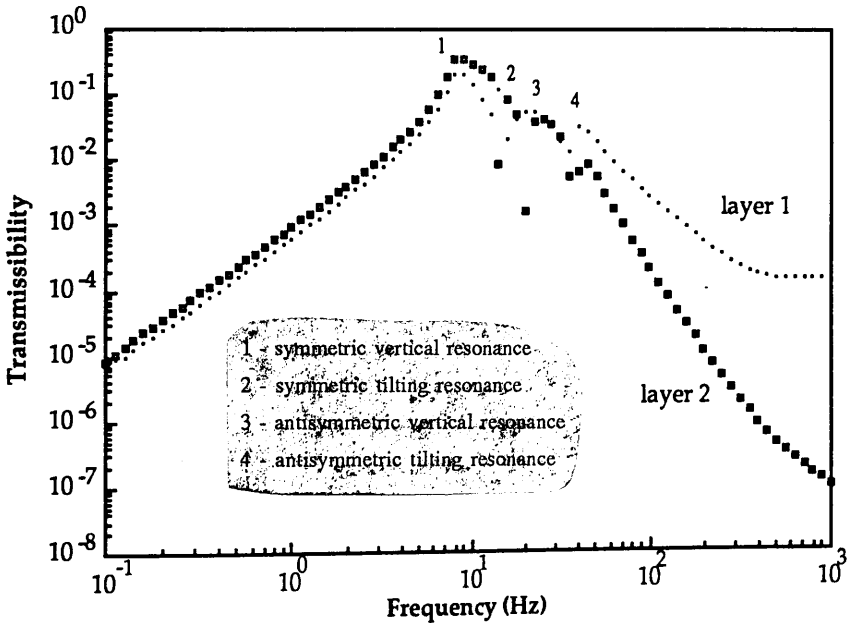
Figure 6.26 *Vertical to rotational transmissibility[†] in a two-layer stack with a 10% stiffness variation. To convert to units of $^{rad}/_m$ divide the transmissibility value by the half plate length ($\sim 1.2 \times 10^{-1}$m).*

([†] *as defined in Section 6.3*)

have been brought about by the presence of the overlying layer. Recall from Section 6.6.2 that the transmission of vertical to horizontal motion in the one-layer stack only takes place because the induced rotations of the plate are subject to a horizontal restoring force along the lower surface of the plate which is larger than those along the upper surface. If however the restoring forces at the upper and lower surfaces of the plate are balanced, the induced rotation will be symmetrical and there will be no component of horizontal motion at the centre of mass of the plate. This is the situation for the two-layer stack where plate one is sandwiched by rubber along both its lower and upper surfaces. Furthermore the same effect is observed whether the two-layer stack is symmetrically or asymmetrically imbalanced (see Figure 6.6). This is because in both cases the net horizontal stiffness at the upper and lower surfaces of plate one are equal.

However there is some horizontal motion observed at plate one due to a downward transmission from layer two. The various induced motions at plate two drive plate one horizontally. Having effectively undergone three stages of isolation these are of relatively small magnitude as shown in Figure 6.27.

In conclusion the conversion of vertical ground motion to horizontal motion is much worse at layer two of the stack than at layer one. The magnitude of the transmissibility at layer two depends crucially on the vertical offset between the centre of mass of plate one and the base level of the rubber supports for layer two. Note that if this vertical offset were zero the most significant transmission route to layer two would be:

$$vertical_{base} - rotational_{c.o.m.1} - horizontal_{c.o.m.2} \quad \text{giving } T \sim 4.8 \times 10^{-7} \text{ at 100Hz.}$$

Furthermore, the isolation at layer one is improved with the presence of layer two since the mechanism whereby vertical ground motions directly drive layer one horizontally is removed.

Horizontal to Vertical Transmissibility

The curves obtained for the transmission to the plates in the two layers are shown in Figure 6.28. Both curves tend to fall at ~18dB/octave at high frequency. The layer one curve dips and flattens at high frequencies due to computational rounding errors. The isolation at layer two at high frequencies is only marginally better than at layer one. This unexpected result can be explained by the fact that the principal transmission route to layer two of the stack is *via* rotation at layer one *i.e.*

134
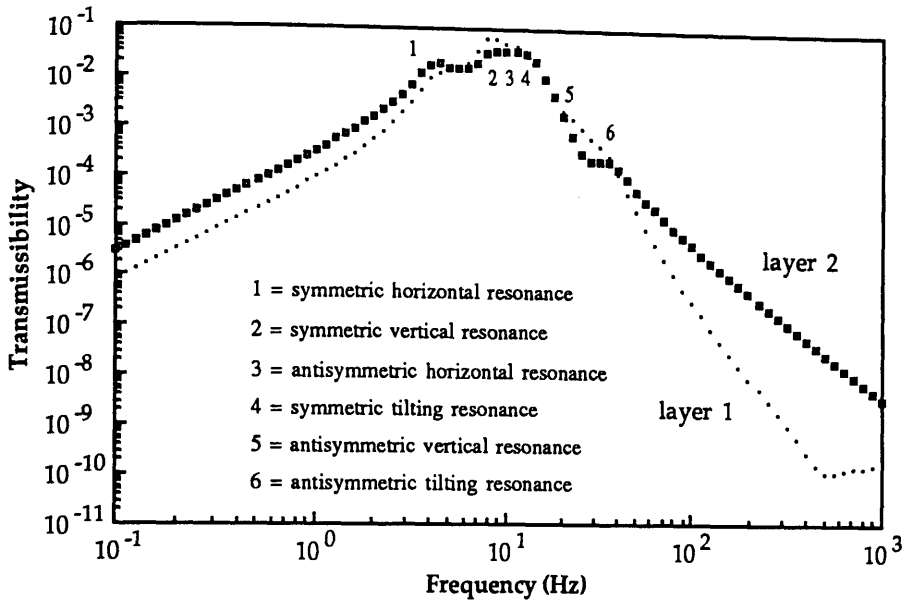
Figure 6.27 *Vertical to horizontal transmissibility in a two-layer stack with a 10% stiffness variation.*
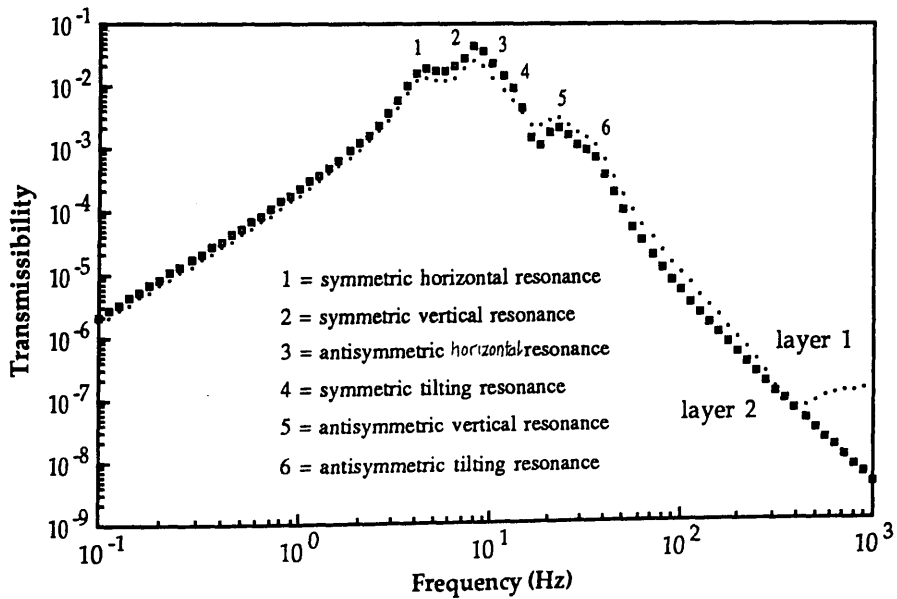
Figure 6.28 *Horizontal to vertical transmissibility in a two-layer stack with a 10% stiffness variation.*

horizontal $_{base}$ - *rotational $_{c.o.m.1}$* - *vertical $_{c.o.m.2}$*   giving $T \sim 5.3 \times 10^{-6}$ at 100Hz.

Since horizontal to rotational transmissibility tends to ~6dB/octave and rotational to vertical to ~12dB/octave in a one-layer stack, this means that the horizontal to vertical transmissibility curve for the two-layer stack falls as ~18dB/octave at high frequency.

However in contrast to the previous example of vertical to horizontal coupling, the isolation observed at layer one does in this case depend on whether the imbalance in the rubber stiffness of the two-layer stack is symmetrical or asymmetrical (see Figure 6.6). The curve shown in Figure 6.28 is for the case of symmetrically imbalanced rubber. In this situation there is no reduction in the transmissibility to layer one due to the presence of layer two. This is because even with the presence of the overlying layer there remains a difference in the vertical stiffness at each end of plate one. Its induced rotational motion will therefore remain asymmetrical with respect to its centre of mass. However, if the stiffness imbalance is changed in polarity (giving the asymmetrically imbalanced stack shown in Figure 6.6), then a reduction in the transfer to layer one is indeed observed, the curve falling at ~30dB/octave. In this situation the net vertical stiffness which plate one is subject to is identical at each end. Therefore the induced rotation is symmetrical about its centre of mass and no vertical motion occurs by this mechanism. However, in a similar way to the previous example described in this section, there will be some vertical motion induced at plate one *via* downward transmission from plate two.

In conclusion, the coupling of horizontal ground motions to vertical motions at layer two of the two-layer stack are at least comparable in size to those at layer one. Reduced coupling can be achieved at layer one if the imbalance in rubber stiffness properties of layer two are of the opposite polarity.

6.9   Implications for a Five-Layer Vibration Isolation Stack

6.9.1 Introduction

As mentioned in Section 6.1 the stacks used in gravitational radiation detectors are commonly of multi-layer form. It has been suggested that five-layer isolation stacks are used as part of the isolation system for test masses in the proposed 3km German-British gravitational radiation detector (GEO) [Hough *et. al.* 1989]. This isolation system

contains various components, the five-layer stacks playing a crucial role in attaining the desired isolation level. It is proposed that double pendulum suspensions for the test masses will be attached to the top of the stack systems. In choosing this number of layers for the stack it was assumed that the principal transmission routes resulting in horizontal and vertical motions at the top of the stack were the direct transmissions described below:

$$horiz._{base} - horiz._{c.o.m.1} - horiz._{c.o.m.2} - horiz._{c.o.m.3} - horiz._{c.o.m.4} - horiz._{c.o.m.5}$$
$$and$$
$$vert._{base} - vert._{c.o.m.1} - vert._{c.o.m.2} - vert._{c.o.m.3} - vert._{c.o.m.4} - vert._{c.o.m.5}.$$

In series with the isolation provided by the double pendulums and the air springs connecting the stacks to ground this provided, in theory, more than adequate isolation in both the horizontal and the vertical directions [Hough *et. al.* 1989]. However it has already been shown in this chapter that alternative indirect transmission routes of a significant magnitude can exist in a two-layer stack system. This strongly suggests that significant alternative routes may exist in a five-layer stack system also.

Using the information obtained in the two-layer analyses discussed in Sections 6.7 and 6.8, the implications for a five-layer stack with components of the same dimensions have been assessed. Here the principal transmission routes resulting in horizontal, vertical and rotational (tilting) motion at the top of the stack and the conditions under which they occur are described and transmissibility figures for each case quoted. These calculations are based on the values for the various transmissibilities in a one-layer stack given in Figure 6.21. Obviously the absolute displacement at the top plate of the stack in the respective directions will depend critically on the magnitude of the input motion at the base of the stack. Therefore typical magnitudes for horizontal, vertical and rotational (tilting) seismic motion have been presented here also. Finally an evaluation has been made of the resulting horizontal motion at the top of a pendulum suspension attached to the top plate of the stack for the various situations discussed.

6.9.2 Horizontal Motion at the Top of a Five-Layer Stack

Direct horizontal transmission up the stack as shown by the route described below:

$$horiz._{base} - horiz._{c.o.m.1} - horiz._{c.o.m.2} - horiz._{c.o.m.3} - horiz._{c.o.m.4} - horiz._{c.o.m.5}$$

gives a value of transmissibility $T \sim 1.0 \times 10^{-9}$ at 100Hz. This is independent of the presence of a stiffness variation. If one assumes a horizontal seismic noise spectrum of $1 \times 10^{-7}/f^2$ $^{m}/\sqrt{Hz}$ [Hough *et. al.* 1986], then at 100Hz this would give a horizontal displacement amplitude of $dx \sim 1.0 \times 10^{-20}$ $^{m}/\sqrt{Hz}$ at the top of the stack/pendulum suspension. However the analyses carried out previously on the two-layer stack have indicated that the principal transmission mechanism will in fact be:

$rotn._{base}$ - $rotn._{c.o.m.1}$ - $rotn._{c.o.m.2}$ - $rotn._{c.o.m.3}$ - $(rotn._{c.o.m.4}$ - $horiz._{top4})$ - $horiz._{c.o.m.5}$

which gives a transmissibility of

$$T \sim 3.5 \times 10^{-9} \times \left[\frac{a}{1.3 \times 10^{-2}m} \right] \ ^{m}/_{rad}$$

at 100Hz independent of a stiffness variation being present. As shown in Figure 6.29, a is the vertical offset between the centre of mass of layer four and the base level of the rubber supports for layer five. From the experimental ground tilt data in Appendix C (refer to Figure C.4), the ground tilt at 100Hz is $\Phi \sim 2 \times 10^{-11}$ $^{rad}/\sqrt{Hz}$. This will be valid over a length of $\sim \lambda/2$ where λ is the wavelength of a surface seismic wave giving rise to the tilts *i.e.* Rayleigh waves. Assuming a lower limit to the velocity of Rayleigh waves in the surface sediments of $v_R \sim 500ms^{-1}$ then at 100Hz the half-wavelength $\lambda/2$ will be at least $\sim 2.5m$ which is much greater than the length of the stack ($\sim 0.24m$). Hence the resulting horizontal motion at the top of the pendulum *via* this route would be

$$dx \sim 7.0 \times 10^{-20} \times \left[\frac{a}{1.3 \times 10^{-2}m} \right] \ ^{m}/\sqrt{Hz}.$$

It should be noted that the conversion of rotational motion about the centre of mass of any given layer to horizontal motion at the bases of the rubbers in a layer immediately above can occur at various stages up the stack. For instance, if one considers the conversion taking place at one stage lower than in the previous example *i.e.* at layer three

$rotn._{base}$ - $rotn._{c.o.m.1}$ - $rotn._{c.o.m.2}$ - $(rotn._{c.o.m.3}$ - $horiz._{top4})$ - $horiz._{c.o.m.4}$ - $horiz._{c.o.m.5}$
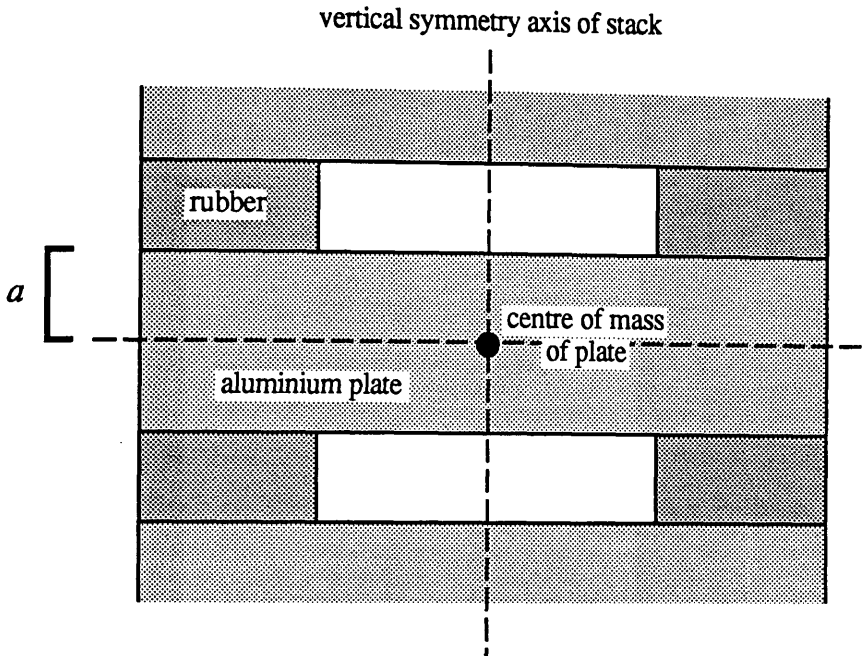
a = the vertical offset between the centre of mass of some intermediate plate and the base level of the overlying rubber supports

Figure 6.29 *Portion of the multi-layer stack showing the parameter 'a'. Intra-plate conversion of rotational to horizontal motion can occur giving rise to unexpectedly large horizontal motion at the overlying layer as detailed in Sections 6.8 and 6.9. If a=0 this conversion will not take place.*

then the transmissibility at 100Hz is

$$T \sim 8.7 \times 10^{-10} \times \left[\frac{a}{1.3 \times 10^{-2}\text{m}} \right] \; \text{m}/_{\text{rad}}$$

independent of a stiffness variation being present. Again assuming that the length of the stack is much shorter than the half-wavelength of the surface waves, this would result in a horizontal motion at the top of the pendulum of magnitude

$$dx \sim 1.7 \times 10^{-20} \times \left[\frac{a}{1.3 \times 10^{-2}\text{m}} \right] \; \text{m}/_{\sqrt{\text{Hz}}}.$$

Note that this value of horizontal motion is still comparable with the reference value derived *via* the direct conversion of horizontal motion at the base to horizontal motion at the top stage ($dx \sim 1.0 \times 10^{-20} \; \text{m}/_{\sqrt{\text{Hz}}}$). Going one step further, if the same calculation is performed with the conversion taking place at layer two then the corresponding horizontal motion is

$$dx \sim 4.4 \times 10^{-21} \times \left[\frac{a}{1.3 \times 10^{-2}\text{m}} \right] \; \text{m}/_{\sqrt{\text{Hz}}},$$

which is more than a factor of two smaller than the directly transmitted horizontal motion. Hence for a stack of these particular dimensions this is the critical level at which this type of cross-coupling becomes less significant than the direct coupling of horizontal to horizontal motion.

Another significant route whereby horizontal motion at the base of the stack couples to horizontal motion at the top layer is:

$$horiz._{base} - rotn._{c.o.m.1} - rotn._{c.o.m.2} - rotn._{c.o.m.3} - (rotn._{c.o.m.4} - horiz._{top4}) - horiz._{c.o.m.5}$$

which gives a transmissibility of

$$T \sim 2.4 \times 10^{-9} \times \left[\frac{a}{1.3 \times 10^{-2}\text{m}} \right]$$

at 100Hz. This route does not depend on the presence of a stiffness variation. However it does depend on the presence of the offset between the ∧ of the rubber supports and
                                              vertical   centres

138

centre of mass of the plate in layer one. Using the figure for the horizontal seismic noise spectrum of $1 \times 10^{-7}/f^2 \ \mathrm{m}/\sqrt{\mathrm{Hz}}$ [Hough et. al. 1986] then at 100Hz this would give a horizontal displacement amplitude of

$$dx \sim 2.4 \times 10^{-20} \times \left[\frac{a}{1.3 \times 10^{-2} \mathrm{m}} \right] \ \mathrm{m}/\sqrt{\mathrm{Hz}}.$$

If the conversion of rotational to horizontal motion takes place at one stage lower *i.e.*

$horiz._{base}$ - $rotn._{c.o.m.1}$ - $rotn._{c.o.m.2}$ - $(rotn._{c.o.m.3}$ - $horiz._{top3})$ - $horiz._{c.o.m.4}$ - $horiz._{c.o.m.5}$

this gives a transmissibility of

$$T \sim 6.0 \times 10^{-10} \times \left[\frac{a}{1.3 \times 10^{-2} \mathrm{m}} \right]$$

at 100Hz. This would give a horizontal displacement amplitude of

$$dx \sim 6.0 \times 10^{-21} \times \left[\frac{a}{1.3 \times 10^{-2} \mathrm{m}} \right] \ \mathrm{m}/\sqrt{\mathrm{Hz}}.$$

Hence for a stack of these particular dimensions this is the critical level at which this type of cross-coupling becomes less significant than the direct coupling of horizontal to horizontal motion.

Furthermore if a stiffness variation exists in the rubber in the stack then vertical motion at the base couples to horizontal motion at the top of the stack *via* the route:

$vert._{base}$ - $rotn._{c.o.m.1}$ - $rotn._{c.o.m.2}$ - $rotn._{c.o.m.3}$ - $(rotn._{c.o.m.4}$ - $horiz._{top4})$ - $horiz._{c.o.m.5}.$

For instance, with a 10% reduction in the stiffness of the rubber on one side of the stack, this gives a transmissibility of

$$T \sim 1.3 \times 10^{-9} \times \left[\frac{a}{1.3 \times 10^{-2} \mathrm{m}} \right]$$

139

at 100Hz. Again assuming a vertical seismic noise spectrum of $1 \times 10^{-7}/f^2 \ \text{m}/\sqrt{\text{Hz}}$ [Hough *et. al.* 1986] then at 100Hz this would give a horizontal displacement amplitude of:

$$dx \sim 1.3 \times 10^{-20} \times \left[\frac{a}{1.3 \times 10^{-2} \text{m}} \right] \ \text{m}/\sqrt{\text{Hz}}.$$

6.9.3 Vertical Motion at the Top of a Five-Layer Stack

Direct vertical transmission up the stack where vertical motion at the base of the stack couples directly through from layer to layer *i.e.*

$$\text{vert.}_{base} - \text{vert.}_{c.o.m.1} - \text{vert.}_{c.o.m.2} - \text{vert.}_{c.o.m.3} - \text{vert.}_{c.o.m.4} - \text{vert.}_{c.o.m.5}$$

gives $T \sim 6.4 \times 10^{-9}$ at 100Hz independent of the presence of a stiffness variation in the rubber in the stack. If one assumes the vertical seismic displacement spectrum to have an amplitude of $1 \times 10^{-7}/f^2 \ \text{m}/\sqrt{\text{Hz}}$ [Hough *et. al.* 1986] then at 100Hz this would give a vertical displacement amplitude of $dz \sim 6.4 \times 10^{-20} \ \text{m}/\sqrt{\text{Hz}}$ at the top of the pendulum. In the presence of a 10% stiffness variation in the rubber then rotational motion at the base couples to vertical motion at the top *via* the route

$$\text{rotn.}_{base} - \text{rotn.}_{c.o.m.1} - \text{rotn.}_{c.o.m.2} - \text{rotn.}_{c.o.m.3} - \text{rotn.}_{c.o.m.4} - \text{vert.}_{c.o.m.5}.$$

This gives a transmissibility of $T \sim 2.0 \times 10^{-9} \ \text{m}/\text{rad}$ at 100Hz. Again using the figure for the ground tilt at 100Hz of $\Phi \sim 2 \times 10^{-11} \ \text{rad}/\sqrt{\text{Hz}}$ (Appendix C, Figure C.4) and assuming that the half-wavelength of the surface waves is much longer than the length of the stack, this would give rise to a vertical displacement of the centre of mass of the top plate of the stack of $dz \sim 4.0 \times 10^{-20} \ \text{m}/\sqrt{\text{Hz}}$. This is smaller than the value obtained by the direct coupling of vertical ground motions as described above. It is important to note here that vertical motion at the top of a stack system supporting a pendulum may give rise to horizontal motion at the bottom of the pendulum *via* cross-coupling. The magnitude of the cross coupling of vertical to horizontal motion in a pendulum is not easily predictable since it will vary from system to system depending on how much care was taken in the pendulum design and construction to minimise the magnitude of such effects. However a

figure of ~1% of the vertical to vertical transmissibility has been predicted based on experimental evidence obtained using a seven-stage pendulum [Del Fabbro *et. al.* 1988b].

6.9.4 Rotational Motion at the Top of a Five-Layer Stack

Direct transmission of rotational motion up the stack where rotational motion at the base of the stack couples directly through from layer to layer *i.e.*

$$rotn._{base} - rotn._{c.o.m.1} - rotn._{c.o.m.2} - rotn._{c.o.m.3} - rotn._{c.o.m.4} - rotn._{c.o.m.5}$$

gives $T \sim 1.1 \times 10^{-6}$ at 100Hz. This is the principal transmission route resulting in rotational motion at the top of the stack independent of whether or not there is a stiffness variation present.

Consider the situation where the pendulum suspension point is vertically offset from the centre of mass of the top plate of the stack by a distance z. This can be described by the route:

$$rotn._{base} - rotn._{c.o.m.1} - rotn._{c.o.m.2} - rotn._{c.o.m.3} - rotn._{c.o.m.4} - (rotn._{c.o.m.5} - horiz._{susp.pt.})$$

The rotation of the top plate about its centre of mass will linearly convert to horizontal motion at the suspension point. For instance, if the offset is $z = 1 \times 10^{-3}$ m then the resulting horizontal motion of the suspension point at 100Hz, using a ground tilt value of $\Phi \sim 2 \times 10^{-11}\ \mathrm{rad}/\sqrt{\mathrm{Hz}}$ (Appendix C, Figure C.4) is then

$$dx \sim 2.2 \times 10^{-20} \times \left[\frac{z}{1 \times 10^{-3}\mathrm{m}} \right]\ \mathrm{m}/\sqrt{\mathrm{Hz}} .$$

This value is greater than the corresponding figure obtained in Section 6.9.2 for the case where horizontal ground motion coupled directly to horizontal motion at the top of the stack. Recall that this gave an amplitude of horizontal motion of $dx \sim 1.0 \times 10^{-20}\ \mathrm{m}/\sqrt{\mathrm{Hz}}$ at 100Hz.

Another route giving rise to significant rotational motion of the top plate of the stack resulting in horizontal motion of the suspension point is described by:

horiz. $_{base}$ - *rotn.* $_{c.o.m.1}$ - *rotn.* $_{c.o.m.2}$ - *rotn.* $_{c.o.m.3}$ - *rotn.* $_{c.o.m.4}$ - (*rotn.* $_{c.o.m.5}$ - *horiz.* $_{susp.pt.}$)

Assuming a horizontal seismic displacement spectrum of $1 \times 10^{-7}/f^2$ $^m/\sqrt{Hz}$ [Hough *et. al.* 1986] and a vertical offset of the suspension point with respect to the centre of mass of the top plate of $z = 1 \times 10^{-3}$ m, then the resulting horizontal motion of the suspension point at 100Hz is given by:

$$dx \sim 7.4 \times 10^{-21} \times \left[\frac{z}{1 \times 10^{-3} m} \right] \ ^m/\sqrt{Hz} \ .$$

This value is comparable to the value derived *via* the direct conversion of horizontal motion at the base to horizontal motion at the top plate ($dx \sim 1.0 \times 10^{-20}$ $^m/\sqrt{Hz}$). Note however that the conversion of horizontal to rotational motion at the first stage would reduce to zero if there were no vertical offset between the $\underset{\vee}{centres}$ of the rubber supports and the centre of mass of the plate in layer one.

In a similar way vertical ground motion can lead to horizontal motion of the suspension point in the presence of a vertical positioning error of the suspension point. However this route described by:

vert. $_{base}$ - *rotn.* $_{c.o.m.1}$ - *rotn.* $_{c.o.m.2}$ - *rotn.* $_{c.o.m.3}$ - *rotn.* $_{c.o.m.4}$ - (*rotn.* $_{c.o.m.5}$ - *horiz.* $_{susp.pt.}$)

depends on the presence of a stiffness variation between the rubber supports in the first stage of the stack. Assuming a vertical seismic displacement spectrum of $1 \times 10^{-7}/f^2$ $^m/\sqrt{Hz}$ [Hough *et. al.* 1986] and a vertical positioning error of the suspension point of $z = 1 \times 10^{-3}$ m, then the resulting horizontal motion of the suspension point at 100Hz is given by:

$$dx \sim 3.9 \times 10^{-21} \times \left[\frac{z}{1 \times 10^{-3} m} \right] \ ^m/\sqrt{Hz} \ .$$

This value is more than a factor of two smaller than the reference value derived *via* the direct conversion of horizontal motion at the base to horizontal motion at the top plate ($dx \sim 1.0 \times 10^{-20}$ $^m/\sqrt{Hz}$).

6.10 Conclusions

It has been shown in this chapter that the frequency response characteristics of isolation stacks are much more complicated than one would initially predict using simple dynamical theory. In Section 6.5 it was shown that simple theory is fairly accurate in predicting the degree of attenuation which unidirectional motion at the base of a one-layer stack undergoes in its passage up the stack. However this is true only if the components of the stack are adequately damped. In reality the internal resonances of the components can lead to a reduction in the predicted isolation at frequencies on and above the frequencies at which these modes occur. For instance Figure 6.12 illustrates how the underdamped transverse resonances ($Q=20$) of the supported plate can significantly reduce the vertical isolation achieved. It was also shown in Section 6.5 that the presence of an asymmetry in the stiffness properties of the rubber across the stack did not affect the direct transmission characteristics of the stack in any unpredictable way.

These analyses were extended to a two-layer stack system in Section 6.7. It was shown here that improved isolation was obtained at layer two of the stack in each of the direct transmissibility cases investigated. The observed isolation agreed well with that predicted using simple theory if the components of the stack were sufficiently well damped. Furthermore, the presence of a stiffness variation in the rubber, whether it was symmetrically or asymmetrical imbalanced (refer to Figure 6.6), did not affect the direct transmissibility characteristics of the two-layer stack in any unexpected way.

The cross-coupling mechanisms which occur in a one-layer stack were examined in Section 6.6. Some of these were observed to originate due to the extended geometry of the system, other mechanisms took place only in the presence of an asymmetry in the stiffness properties of the rubber across the stack. Furthermore, the magnitudes of the cross-couplings of this type were directly proportional to the percentage stiffness imbalance between the rubber at either end of the stack. It was interesting to note here that ∧ It is believed that the coupling of vertical to horizontal and horizontal to vertical motion in a one-layer stack can only occur if there is both a stiffness variation present and a vertical offset between the mid level of the rubber supports and the centre of mass of the supported plate.

The cross-coupling mechanisms in a two-layer stack were investigated in Section 6.8. Some interesting results were observed here as a consequence of the presence of an intermediate plate in the stack. In Section 6.8.1 it was shown that ground tilt can couple very strongly to horizontal motions at the second layer of the stack *via*

rotational motions induced at the intermediate layer. If the bases of the rubber supports for the second layer were vertically offset from the centre of mass of the intermediate plate (see Figure 6.29) then intra-plate conversion of rotational to horizontal motion took place leading to an unexpectedly high magnitude of horizontal motion at the top of the stack.

Horizontal and rotational (tilting) motions at the base of the stack can give rise to rotational motions at the intermediate plate leading to significant vertical motions at the top of the stack if a stiffness imbalance exists in the rubber across the stack. This effect was discussed in Section 6.8.2. Similarly vertical motions at the base can couple to rotational motions at the top *via* rotations being induced at the intermediate stage.

When examining the coupling of vertical to horizontal motion in the two-layer stack (in the presence of a stiffness imbalance in the rubber across the stack) it was shown that the isolation at layer two was much worse than one would have initially predicted. Again this was due to intra-plate conversion of rotational to horizontal motion at the intermediate stage (layer one). However of even greater interest was the observed reduction in the transmission of vertical to horizontal motion at layer one with the presence of a second layer in the stack. The presence of the over-lying layer removed the mechanism by which this type of coupling could take place between the ground and layer one of the stack.

Using the information obtained from the two-layer analyses the implications for a five-layer stack were then assessed, this being the typical order of stack in the vibration isolation systems used for laser interferometric gravitational wave detectors. In Section 6.9 the principal transmission mechanisms leading to horizontal, vertical and rotational (tilting) motions at the top of a five-layer stack of the prescribed dimensions were discussed. The resulting amplitude of motion at the top of the stack under various conditions in each case was evaluated at a frequency of 100Hz using typical magnitudes for the various components of seismic motion at that frequency. For reference Figure 6.30 shows a table summarising the main routes leading to horizontal motion at the top of a five-layer stack. The resulting amplitude of horizontal motion at the top of a pendulum suspension system connected to the top plate of the stack is also given in each case. It should be noted here that it is more common for a heavier metal such as lead to be used as the plate material in such stack systems. This would result in relatively lower resonant frequencies f_h, f_v and f_t (for the same stiffness of rubber) and improved isolation properties in each direction. However since it is the relative isolation level in each direction which is important, the conclusions which are drawn here will apply in a

144

KEY

a = vertical offset between the centre of mass (c.o.m.) of the plate where intra-plate conversion takes place and the base level of the rubber supports for the layer above (see Figure 6.29).

z = vertical offset between the pendulum suspension point (s.p.) and the centre of mass (c.o.m.) of the top plate of the stack

† with a 10% rubber stiffness variation

	transmission route	transmissibility (T) at 100Hz	horizontal motion (dx) of suspension point at 100Hz
1	$h_{base}-h_{com1}-h_{com2}-h_{com3}-h_{com4}-h_{com5}$	$\sim 1.0 \times 10^{-9}$	$\sim 1.0 \times 10^{-20}\ \mathrm{m}/\sqrt{\mathrm{Hz}}$
2	$r_{base}-r_{com1}-r_{com2}-r_{com3}-(r_{com4}-h_{top4})-h_{com5}$	$\sim 3.5 \times 10^{-9} \cdot \left[\dfrac{a}{1.3 \times 10^{-2}}\right]\ \mathrm{m/rad}$	$\sim 7.0 \times 10^{-20} \cdot \left[\dfrac{a}{1.3 \times 10^{-2}}\right]\ \mathrm{m}/\sqrt{\mathrm{Hz}}$
3	$r_{base}-r_{com1}-r_{com2}-(r_{com3}-h_{top3})-h_{com4}-h_{com5}$	$\sim 8.7 \times 10^{-10} \cdot \left[\dfrac{a}{1.3 \times 10^{-2}}\right]\ \mathrm{m/rad}$	$\sim 1.7 \times 10^{-20} \cdot \left[\dfrac{a}{1.3 \times 10^{-2}}\right]\ \mathrm{m}/\sqrt{\mathrm{Hz}}$
4	$h_{base}-r_{com1}-r_{com2}-r_{com3}-(r_{com4}-h_{top4})-h_{com5}$	$\sim 2.4 \times 10^{-9} \cdot \left[\dfrac{a}{1.3 \times 10^{-2}}\right]$	$\sim 2.4 \times 10^{-20} \cdot \left[\dfrac{a}{1.3 \times 10^{-2}}\right]\ \mathrm{m}/\sqrt{\mathrm{Hz}}$
5†	$v_{base}-r_{com1}-r_{com2}-r_{com3}-(r_{com4}-h_{top4})-h_{com5}$	$\sim 1.3 \times 10^{-9} \cdot \left[\dfrac{a}{1.3 \times 10^{-2}}\right]$	$\sim 1.3 \times 10^{-20} \cdot \left[\dfrac{a}{1.3 \times 10^{-2}}\right]\ \mathrm{m}/\sqrt{\mathrm{Hz}}$
6	$r_{base}-r_{com1}-r_{com2}-r_{com3}-r_{com4}-r_{com5}-h_{s.p.}$	$\sim 1.1 \times 10^{-9} \cdot \left[\dfrac{z}{1.0 \times 10^{-3}}\right]\ \mathrm{m/rad}$	$\sim 2.2 \times 10^{-20} \cdot \left[\dfrac{z}{1.0 \times 10^{-3}}\right]\ \mathrm{m}/\sqrt{\mathrm{Hz}}$

Figure 6.30 Table summarising the main routes leading to horizontal motion at the top of a five-layer stack.

similar way to such lead/rubber stack systems.

Referring to Figure 6.30, transmission route 1 describes the direct coupling of horizontal motion at the base of the stack to horizontal motion at the top plate of the stack giving a resulting horizontal motion of $dx \sim 1.0 \times 10^{-20}\ ^m/_{\sqrt{Hz}}$ at 100Hz. The corresponding values for dx produced by the remaining routes (2 to 6) given in Figure 6.30 should be compared to this reference value in order to assess the relative isolation degradation which is taking place in this particular stack.

Potentially the most significant transmission route for introducing excess noise at the top of a pendulum suspended from the stack is route 6 where the direct transmission of ground tilt results in rotational motion of the top plate about its centre of mass (as discussed in Section 6.9.4). If any vertical offset exists between the centre of mass of the top plate and the breakaway point of the pendulum suspension wire then rotational motion of the plate linearly converts to horizontal motion of the suspension point (basically the same effect as the intra-plate conversion of rotational to horizontal motions already discussed). Using the values shown in Figure 6.30 the critical offset at which this mechanism degrades the anticipated horizontal isolation (as shown in route 1) is $z \geq \sim 5 \times 10^{-4}$m. Positioning of the suspension point to this high degree of accuracy would be difficult to achieve in practice and hence the coupling of ground tilts to horizontal motion in this way might be a severe limitation to the isolation achievable in such a multi-component system. Further, one should be aware that the magnitude of this problem depends on both the relative magnitudes of horizontal and tilting seismic motions and also the relative isolation obtained in the horizontal and rotational (tilting) senses. It should be noted here that in the modelled stack the degree of isolation to ground tilts relative to the horizontal isolation is much better than is typical of most stack systems. This is due to the fact that the ratio of f_t to f_h is ~ 3 in the model and in a typical stack system this factor is larger (see Section 6.2). Therefore relatively speaking the isolation degradation which occurs in this way might be even more severe in a real system. One possible way of alleviating this problem is to ensure that the foundation on which the isolation system is mounted is particularly quiet with respect to seismic tilting motions. This can be attempted using an active tilt isolation platform as the first stage of the test mass isolation system placing less stringent constraints on the positioning error of the pendulum suspension point at the top of the stack.

Another mechanism by which the coupling of ground tilt can reduce the horizontal isolation achieved is a consequence of intra-plate conversion of rotational to horizontal

145

motion taking place. Routes **2** and **3** show this type of cross-coupling with the intra-plate conversion taking place at consecutively lower stages of the stack. The transmissibility is largest with the intra-plate conversion at layer four of this stack since rotational to rotational coupling is more efficient than horizontal to horizontal coupling between contiguous layers (this is a direct consequence of the fact that $f_h < f_t$ in a stack). The further down the stack the intra-plate conversion takes place the less significant this route becomes. An obvious way of avoiding this problem is to design the stack with the rubber supports embedded in the plates ensuring that the bases   of the rubber supports   are collinear with the plate centres of mass. The number of stages down the stack at which this action is necessary will depend on the particular stack system in question as well as the relative size of the seismic tilting motion compared to the horizontal motion.

Since horizontal motion at the base of a one-layer stack can couple to rotational motion of the supported plate, this gives rise to another route whereby horizontal motion is induced at the top of the five-layer stack *via* rotations being introduced at intermediate layers (as shown by route **4**). This route is similar to routes **2** and **3** except that horizontal motion is input at the base and not rotational motion. This route can be removed by ensuring that there is no vertical offset between the *mid* level of the rubber supports and the centre of mass of the supported plate in layer one, or by removing the mechanism by which intra-plate conversion of rotational to horizontal motion at layer four takes place. The latter effect can be achieved by ensuring that there is no vertical offset between the base level of the rubber supports for layer five and the centre of mass of the plate in layer four. This route would then no longer be the principal route for the coupling of horizontal ground motions to horizontal motion at the top plate of the stack.

If a stiffness variation exists between the rubber on either side of the stack then vertical motion may lead to significant horizontal motion at the top of the stack *via* rotational motions being introduced at intermediate layers (as shown in route **5**). The magnitude of the cross-coupling of vertical to rotational motion at the first layer will vary linearly with the percentage stiffness imbalance between the rubber supports. The horizontal motion induced at the top of the stack *via* this type of route again depends on intra-plate conversion occurring and therefore can be avoided by careful design.

Furthermore as stated previously, vertical motion of the top of a stack may lead to horizontal motion of a test mass suspended from the top plate *via* cross-coupling taking place in the pendulum. Two significant routes resulting in vertical motion at the top plate

146

of the stack were discussed in Section 6.9.3. The magnitude of the direct coupling of vertical seismic motion to vertical motion at the top of the stack is easily predictable from simple theory. The second route involves the coupling of ground tilt to vertical motion at the top *via* rotations induced in the intermediate layers. However the cross-coupling of rotational to vertical motion between layers four and five depends on the presence of a stiffness imbalance in the rubber in the stack. Again the effect this has on the horizontal isolation of the test mass will depend on the magnitude of cross-coupling of vertical to horizontal motion in the pendulum as well as the relative magnitude of ground tilt at the Earth's surface.

It should be emphasized that all of the calculations performed here were at a frequency of 100Hz, this being the lower limit of detection frequency initially aimed for in the proposed 3km detector (GEO). The relative significance of each of the transmission mechanisms discussed here may change at higher frequencies depending on the frequency characteristics of both the various seismic spectra involved and the transmission mechanisms occurring. It is commonly assumed that the seismic displacement spectra in the horizontal and vertical directions have similar magnitude and frequency characteristics, falling at ~12dB/octave in the region of 100Hz [Robertson N.A. 1991]. The seismic tilt spectrum however appears to fall somewhere between ~12dB/octave and ~18dB/octave (Appendix C). This suggests that the horizontal isolation degradation in stacks which transpires due to ground tilting motions may become relatively less significant at higher frequencies. The frequency characteristics of the relevant transmission mechanisms described in routes 1-4 and route 6 are roughly similar, each curve falling at ~12dB/octave initially and tending to ~6dB/octave at higher frequencies. However in the case of route 5, vertical to rotational coupling falls at ~12dB/octave and therefore this route might become less important at higher frequencies.

In conclusion the analyses carried here have shown that various cross-coupling effects in multi-layer vibration isolation stacks can degrade the predicted horizontal isolation of any test mass suspended from the top of the stack. These cross-coupling effects can be minimised if great care is taken when designing and constructing the stack. Care must be taken that the rubber used throughout the stack has uniform stiffness properties since it has been shown here that mechanisms for cross-coupling can be introduced which would not occur in a stack of uniform rubber stiffness. The magnitude of this cross-coupling varies linearly with the stiffness variation and it is relatively unimportant whether this stiffness variation is symmetrical or asymmetrical about the

147

vertical symmetry axis of the stack. However by far the most important criterion for good stack design is to ensure that the rubber supports in each layer of stack are positioned so that the base *Levels* are collinear with the centres of mass of the under -lying plates. Otherwise the introduction of horizontal motion *via* the cross-coupling of rotations introduced *via* ground tilts or other means can limit the horizontal isolation obtained. Further having taken care to design a high performance stack system, it is essential that the breakaway point for any pendulum suspension supported by the stack is coincident with the centre of mass of the top plate of the stack to a fairly high degree of accuracy.

It should be emphasized here that there are limitations in the conclusions which can be drawn from these analyses. For instance, the finite element program used here did not account for the possibility of non-linear cross-coupling mechanisms which in reality will be very important in determining the overall isolation achievable in stack systems. Consider as an example the case where a horizontal offset exists (along the x-axis) between the centre of mass of the top plate of the stack and the pendulum suspension point (see Figure 6.1). Rotational (tilting) motion of the plate will then non-linearly convert to horizontal motion at the top of the pendulum, the induced motion occurring at twice the frequency of the rotational motion. However if one is aware of the possibilities of such non-linear couplings the effects can be kept to a minimum by careful design.

In reality the cross-coupling effects which occur in three-dimensional stack systems will be more complicated. Using this model it was not possible to investigate the isolation properties of the stack to rotational motions about the z-axis (see Figure 6.1). For instance, if a horizontal offset exists (along the y-axis) between the suspension point and centre of mass of the top plate of the stack, induced rotational motions will result in horizontal motion of the suspension point. Also if a stiffness variation exists between the rubber on either side of the first layer of stack, such rotational ground motions will possibly induce horizontal motions of the supported plate. The possibility of these effects occurring should be taken into consideration when designing the stack system.

As described in Section 6.2, the effects of loading on the relative horizontal and vertical stiffness of the rubber have not been incorporated in the model.*Also in such a multi-layer stack, since these loading effects will be larger at the bottom of the stack, the behaviour of contiguous layers will not be identical as suggested for the model.

However, despite these limitations, the analyses carried out here have provided valuable information giving insight to the detailed dynamical behaviour of vibration

isolation stacks. As illustrated here for a five-layer stack system, this information is essential in order to attempt to accurately predict the main transmission routes giving rise to horizontal displacement noise at the top of multi-layer stacks. Various design criteria to achieve high vibration isolation performance have been established as a consequence of these investigations.

Chapter 7

Conclusions and Future Prospects

The potential wide bandwidth operation of an Earth-borne laser interferometric gravitational radiation detector could be severely compromised at low frequencies unless adequate isolation is provided from the effects of seismic noise. To achieve the required level of seismic isolation in the proposed 3km interferometric detector (GEO) we aim to use double pendulum suspensions for the test masses in conjunction with five-layer vibration isolation stacks and air mounts.

In addition to providing a high level of seismic isolation, it is also necessary to control the position and orientation of each test mass in an interferometric detector to a high degree of accuracy using feedback control. Various theoretical and experimental investigations into the feedback control of a test mass suspended as a double pendulum have been described in this thesis. It has been shown that it is possible to control the position of a test mass suspended as a double pendulum over a relatively large bandwidth (up to about a kilohertz or more) by sensing the position of, and applying feedback signals directly to, the test mass. The large motions of the test mass at the pendulum resonant frequencies can also be electronically damped to a low level using feedback signals applied to both masses of the pendulum simultaneously.

A novel design of double pendulum system for the vibration isolation and feedback control of a test mass has been developed. This nested double pendulum system was designed specifically in such a way as to attempt to reduce the level of any displacement noise re-introduced to the test mass due to the application of feedback control and damping signals.

To reduce the possibility of re-introducing displacement noise to an isolated test mass it would be desirable to avoid applying any position control signals directly to the mass. However it seems that it would not be possible in practice to control the position of the lower mass of a double pendulum system over a large enough bandwidth by applying feedback signals solely to the intermediate mass. A reasonable compromise is to consider a split-feedback loop arrangement where the low frequency position control is carried out

by feeding signals to the intermediate mass with the higher frequency signals being applied to the test mass. Such an arrangement should significantly reduce the potential for re-introducing displacement noise to the test mass since the largest control signals are associated with correcting for the large low frequency excursions of the test mass. This is due to a combination of the fact that seismic noise is larger at low frequencies and passive isolation is poorer.

Two split-feedback systems (which involved different feedback bandwidths to the two masses) were designed for application to the nested double pendulum system. The first of these systems was designed so that the motions of the test mass up to about 30Hz were controlled by feeding signals to the intermediate mass. Unfortunately it was not possible to demonstrate the operation of this split-feedback system experimentally due to practical difficulties which were encountered (*i.e.* the unanticipated excitation of mechanical resonances which were not accounted for in the feedback loop design). The performance of this type of split-feedback control system requires further experimental investigation since it is believed that the difficulties encountered were not intrinsically related to the designed feedback system. The second design of split-feedback system was less ambitious in that the cross-over frequency between the two feedback loops was chosen to occur at a much lower frequency (below the first pendulum resonant frequency). This system was demonstrated to operate well with very high gain at low frequency achieved.

Using the finite element method it has also been shown in this thesis that the frequency response characteristics of multi-layer stacks are much more complicated than one would initially have predicted using simple dynamical theory. Cross-coupling effects can take place between contiguous layers of the stack and consequently the horizontal isolation obtained at the top of such a multi-layer stack may not be as high as one might expect. However it is believed that these cross-coupling effects can be reduced if care is taken over the design and construction of the stacks. Various design criteria for multi-layer stacks which increase the likelihood of achieving high vibration isolation performance have been established as a consequence of the investigations carried out here.

The required level of seismic isolation for the test masses in an interferometric detector (at frequencies above ~100Hz) should be obtainable using passive isolation *e.g.* double pendulum suspensions in series with multi-layer stacks and air mounts. However it is possible that cross-coupling effects might take place within the isolation system and

these might lead to a reduction in the level of isolation achieved. Furthermore when implementing feedback control of the test masses one must be aware that it is possible that the resonances of the isolation system and support structure connecting the pendulum to the ground might be excited and that this may jeopardise the stability of the control loop. However both of these effects can be avoided if care is taken when designing and constructing the multi-component isolation system.

The development of interferometric detectors with high enough sensitivity to detect the levels of gravitational radiation predicted to be generated by astrophysical sources presents many demanding scientific and technical challenges. However these challenges are surmountable and it is believed that the first generation long-baseline detectors which have recently been designed and await construction will have sensitivity levels approaching those required. The scientific community involved in research and development towards the detection of gravitational waves is optimistic that by the year 2000 a worldwide network of three or more long-baseline interferometric detectors will be successfully operating. It is hoped these detectors will observe the gravitational waves from stellar collapses, coalescing compact binary systems and other types of interesting astrophysical sources some of which we may never have imagined.

Appendix A

Unwanted Magnetic Damping of a Pendulum Suspension

If coil/magnet transducers are used to control the position and orientation of a test mass it is possible that motions of the magnets in the region of the feedback coils will induce currents which might damp the quality factor of a test mass suspension to an undesirably low level. A simple calculation was performed to quantify this effect.

Consider the magnet to be a dipole of moment P which is aligned with the axis of a feedback coil of N turns, radius a and of negligible length, similar to that shown in Figure 3.14. Recall from Section 3.5.3 (equation (3.17)) that the magnetic field produced along the axis of the coil as a function of the current I passing through the coil is given by

$$B_c = \frac{\mu_0 N a^2 I}{2 \left(a^2 + r^2\right)^{3/2}}.$$ (A.1)

The force on the dipole (magnet) at a distance r along the axis of the coil will then be

$$F = P \left(\frac{dB_c}{dr}\right).$$ (A.2)

Substituting equation (A.1) gives

$$F = -\frac{3 \mu_0 N P a^2 r I}{2 \left(a^2 + r^2\right)^{5/2}}.$$ (A.3)

Now, motions of the magnet (dipole) in the region of the coil will induce a voltage (e.m.f.) in the coil giving rise to a force which will oppose the motion. The induced e.m.f. (ε) will be equal to the rate of change of magnetic flux (ϕ) through the coil as shown below

153

$$\varepsilon = -\left(\frac{d\phi}{dt}\right). \tag{A.4}$$

If the coil has cross-sectional area $A(=\pi a^2)$ then equation (A.4) can be re-written as

$$\varepsilon = -NA\left(\frac{dB_m}{dt}\right) \tag{A.5}$$

which gives

$$\varepsilon = -NA\left(\frac{dB_m}{dr}\right)\left(\frac{dr}{dt}\right) \tag{A.6}$$

or

$$\varepsilon = -NA\left(\frac{dB_m}{dr}\right)v \tag{A.7}$$

where B_m is the magnetic field of the dipole (magnet) along the axis of the coil and v is the relative velocity of the coil and magnet.

Now for a dipole of moment P, the magnetic field at a distance r along the axis is given by

$$B_m = \frac{\mu_0 P}{2\pi r^3} \tag{A.8}$$

and hence

$$\left(\frac{dB_m}{dr}\right) = -\frac{3\mu_0 P}{2\pi r^4}. \tag{A.9}$$

Therefore from equation (A.7) the e.m.f. (ε) induced in the coil due to motion of the magnet will be

$$\varepsilon = \frac{3\mu_0 NPAv}{2\pi r^4}. \tag{A.10}$$

Assuming that the coil has inductance L and is connected in series with a voltage source of high output impedance R (where $R \gg r_{coil}$) then the induced current I in the coil will be

$$I = \frac{\varepsilon}{R + sL} \tag{A.11}$$

where s is the complex frequency (*i.e.* $s = j\omega$). Therefore from equation (A.10) the current induced in the coil will be

$$I = \frac{3\mu_0 NPAv}{2\pi r^4 (R + sL)}. \tag{A.12}$$

Substituting this into equation (A.3) gives the force between the coil and the magnet as a function of the relative velocity v (with the cross-sectional area of the coil $A=\pi a^2$)

$$F = -\frac{9\left(\mu_0 N P\right)^2 a^4 v}{4\, r^3 \left(a^2 + r^2\right)^{5/2} (R + sL)} \tag{A.13}$$

the real part of which is equivalent to the damping force

$$F = -b\, v. \tag{A.14}$$

The damping coefficient b is therefore given by

$$b = \frac{9\left(\mu_0 N P\right)^2 a^4 R}{4\, r^3 \left(a^2 + r^2\right)^{5/2} \left(R^2 + \omega^2 L^2\right)}. \tag{A.15}$$

If the magnet is mounted on a mass m suspended as a simple pendulum of natural resonant angular frequency ω_0, then the Q factor of the pendulum will be (assuming that the pendulum has negligible natural damping)

$$Q = \frac{\omega_0\, m}{b} \tag{A.16}$$

where b is evaluated at the angular frequency ω_0.
Substituting equation (A.15) into equation (A.16) gives

$$Q = \frac{4\, \omega_0\, m\, r^3 \left(a^2 + r^2\right)^{5/2} \left(R^2 + \omega_0^2 L^2\right)}{9\left(\mu_0 N P\right)^2 a^4 R}. \tag{A.17}$$

Now using typical values for the various parameters $e.g.$

a	= 1 cm		μ_0	= $4\pi \times 10^{-7}$ Hm^{-1}
r	= 0.5 cm		NP	= 140 Am^2
ω_0	= 6 rads^{-1}		R	= 1 MΩ
m	= 3 Kg		L	= 10 mH

yields a value for the quality factor of the pendulum of $Q \sim 6 \times 10^5$.

Since very high Q's of the order of 10^7 or 10^8 [Hough *et. al.* 1989] are required for the pendulum suspensions used in interferometric detectors, it appears that this magnetic damping effect might reduce the Q of the pendulum suspension to an unacceptably low level. Note however from equation (A.17) that the magnitude of this effect can be reduced if R is increased *i.e.* if a very large output impedance driving amplifier is used for the coil. The effect can also be reduced by decreasing the coil/magnet coupling *e.g.* by reducing the number of turns N of the coil and/or reducing the strength of the magnets used *i.e.* making P smaller.

Obviously it is necessary to use more than one coil/magnet transducer to control both the position and orientation a test mass. Therefore the resulting Q might be even lower than this simple calculation suggests. However, if the coil/magnet transducers for the orientation control of the test mass are placed with their axes perpendicular to the horizontal test direction (as for the nested pendulum of Chapter 4), the flux-linkage will be effectively reduced and the damping effect in the test direction will be minimised.

This calculation is only approximate since it was assumed that the magnet was a point sized dipole, producing uniform flux through the coil (which was assumed to be of negligible length). Subsequent to this, a more detailed calculation has been performed where the finite dimensions of the coil were taken into account and the magnetic flux from a dipole source was integrated over the area of the coil [Logan 1990]. The Q formula obtained in this case reduced to the simplified version of equation (A.17) in the limit where the dimensions of the coil were assumed to be small compared to the coil/magnet separation. Using the typical values already defined, with a coil length of 0.5cm, this more rigorous formula yields a Q value of $Q \sim 2 \times 10^7$ which is much higher than the value obtained using equation (A.17). However the true Q value due to this effect probably lies somewhere between these two estimates since the bar magnets used in these feedback transducers are usually of similar cross-sectional area to the coils. In this situation the dipole approximation breaks down and it would be more accurate to take account of the finite dimensions of the magnet also.

Appendix B

Example of an MSC/Nastran Input Data Deck for Frequency Response Analysis

Horizontal Frequency Response Analysis of a One-Layer Vibration Isolation Stack

Introductory Notes

This appendix gives an example of an MSC/NASTRAN data deck used for the horizontal frequency response analysis of the one-layer vibration isolation stack described in Chapter 6. The example shown is for the case where the rubber stiffness has been reduced by 10% on one side of the stack. The contents of the deck can be fairly easily modified to perform the vertical and rotational frequency response analyses as well as the eigenvalue analysis [MSC/Nastran 1983].

Brief comments incorporated in the data deck have a $ sign preceding them (this ensures that they are invisible to the program) and are shown in italicized letters. Supplementary comments given in bold italicized letters have been added for the information of the reader. Further information on the various cards used in the deck can be obtained in the various users manuals *e.g.* [MSC/Nastran 1985] and [MSC/Nastran 1983]. The data deck is constructed in the following order:

EXECUTIVE CONTROL DECK	Identifies the job, the type of solution to be performed and the general conditions under which the job is to be executed *e.g.* the maximum time allowed for the job.
CASE CONTROL DECK	Defines the output requests. Also the boundary conditions and loading cases are selected *via* key words in the case control deck.
BULK DATA DECK	Contains the data necessary to describe the structural model, its constraint conditions and loading conditions.

.

Example:

NASTRAN DATA DECK

---

id cantley, horizontal transmissibility with top plate critically damped

sol 26	*The solution sequence for performing the*
time 1000	*frequency response analysis.*
$	
cend	*CASE CONTROL DECK*

title=frequency response with top plate (Q=0.5) supported by rubber with stiffness imbalance

subtitle=log h0012

label=rubber supports represented by meshed rubber plates

echo=unsort	*Refers to format of echo of data deck in the output file.*
set 999=1,25,62,72,82	*Selected nodes for which output data are requested.*
disp(sort2,print,phase)=999	*The type of output data requested.*
spc=100	*Identification number for single point constraint set.*
mpc=400	*Identification number for multi - point constraint set.*
method=1500	*Set identification number for frequency response analysis.*
freq=99	*Frequency set identification number.*
dload=88	*Dynamic load set identification number.*
$	
begin bulk	*BULK DATA DECK*
$*frequency set*	*Defines a set of excitation frequencies to be used by*
freq2,99,0.05,10000.0,100	*specification of a starting frequency, final frequency*
$	*and no. of logarithmic increments desired.*
rload2,88,44,,,66	*Defines a frequency dependent dynamic load.*
$	
darea,44,21,1,1.0,22,1,1.0	*Defines the nodes at which a dynamic load is*
darea,44,23,1,1.0,24,1,1.0	*to be applied, the direction and the scale factor*
darea,44,25,1,1.0,1,1,1.0	*e.g. node 21 in the x-direction with a scale factor of 1.0.*
darea,44,2,1,1.0,3,1,1.0	
darea,44,4,1,1.0,5,1,1.0	
$	
tabled4,66,0.0,1.0,0.05,10000.0,	*Defines the coefficients of a power*
0.0,0.0,4.37e8,endt	*series for use in generating a frequency*
$	*dependent dynamic load.*
$*used in frequency response analysis*	
eigr,1500,inv,0.05,10000.0,8,,,,+eig	*Defines data needed to perform the real*
+eig,max	*eigenvalue analysis.*

$

$ *coordinates of nodes for left hand rubber support*

grid,1,,0.0,0.0,0.0

grid,2,,0.0025,0.0,0.0

grid,3,,0.005,0.0,0.0

grid,4,,0.0075,0.0,0.0

grid,5,,0.01,0.0,0.0

grid,6,,0.0,0.0,0.00159

grid,7,,0.0025,0.0,0.00159

grid,8,,0.005,0.0,0.00159

grid,9,,0.0075,0.0,0.00159

grid,10,,0.01,0.0,0.00159

grid,11,,0.0,0.0,0.00318

grid,12,,0.0025,0.0,0.00318

grid,13,,0.005,0.0,0.00318

grid,14,,0.0075,0.0,0.00318

grid,15,,0.01,0.0,0.00318

grid,16,,0.0,0.0,0.00476

grid,17,,0.0025,0.0,0.00476

grid,18,,0.005,0.0,0.00476

grid,19,,0.0075,0.0,0.00476

grid,20,,0.01,0.0,0.00476

$

$ *coordinates of nodes for right hand rubber support*

grid,21,,0.229,0.0,0.0

grid,22,,0.2315,0.0,0.0

grid,23,,0.234,0.0,0.0

grid,24,,0.2365,0.0,0.0

grid,25,,0.239,0.0,0.0

grid,26,,0.229,0.0,0.00159

grid,27,,0.2315,0.0,0.00159

grid,28,,0.234,0.0,0.00159

grid,29,,0.2365,0.0,0.00159

grid,30,,0.239,0.0,0.00159

grid,31,,0.229,0.0,0.00318

grid,32,,0.2315,0.0,0.00318

grid,33,,0.234,0.0,0.00318

grid,34,,0.2365,0.0,0.00318

grid,35,,0.239,0.0,0.00318

grid,36,,0.229,0.0,0.00476

grid,37,,0.2315,0.0,0.00476

grid,38,,0.234,0.0,0.00476

Defines the location of a node (refer to Figure B.1) e.g. node number 7 at coordinates (0.0025,0.0,0.00159).

159

grid,39,,0.2365,0.0,0.00476
grid,40,,0.239,0.0,0.00476
$
$ *coordinates of nodes for supported plate*
grid,41,,0.0,0.0,0.00635
grid,42,,0.0025,0.0,0.00635
grid,43,,0.005,0.0,0.00635
grid,44,,0.0075,0.0,0.00635
grid,45,,0.01,0.0,0.00635
grid,46,,0.03,0.0,0.00635
grid,47,,0.05,0.0,0.00635
grid,48,,0.07,0.0,0.00635
grid,49,,0.09,0.0,0.00635
grid,50,,0.11,0.0,0.00635
grid,51,,0.1195,0.0,0.00635
grid,52,,0.129,0.0,0.00635
grid,53,,0.149,0.0,0.00635
grid,54,,0.169,0.0,0.00635
grid,55,,0.189,0.0,0.00635
grid,56,,0.209,0.0,0.00635
grid,57,,0.229,0.0,0.00635
grid,58,,0.2315,0.0,0.00635
grid,59,,0.234,0.0,0.00635
grid,60,,0.2365,0.0,0.00635
grid,61,,0.239,0.0,0.00635
grid,62,,0.0,0.0,0.01905
grid,63,,0.0025,0.0,0.01905
grid,64,,0.005,0.0,0.01905

....
etc

....
grid,100,,0.2315,0.0,0.03175
grid,101,,0.234,0.0,0.03175
grid,102,,0.2365,0.0,0.03175
grid,103,,0.239,0.0,0.03175
$
$*quadrilateral elements for left hand rubber support*
cquad4,1,1,6,7,2,1
cquad4,2,1,7,8,3,2
cquad4,3,1,8,9,4,3
cquad4,4,1,9,10,5,4

....
etc

Defines a quadrilateral plate element connection e.g. element number 1 of material 1 with corner nodes 6,7,2,1 (refer to Figure B.1).

```
......................
cquad4,15,1,43,44,19,18
cquad4,16,1,44,45,20,19
$
$quadrilateral elements for right hand rubber supports
cquad4,17,3,26,27,22,21
cquad4,18,3,27,28,23,22
cquad4,19,3,28,29,24,23
cquad4,20,3,29,30,25,24

......................
etc
......................
cquad4,30,3,58,59,38,37
cquad4,31,3,59,60,39,38
cquad4,32,3,60,61,40,39
$
$ quadrilateral elements for supported plate
cquad4,33,2,62,63,42,41
cquad4,34,2,63,64,43,42
cquad4,35,2,64,65,44,43
cquad4,36,2,65,66,45,44

......................
etc
......................
cquad4,70,2,100,101,80,79
cquad4,71,2,101,102,81,80
cquad4,72,2,102,103,82,81
$
$dimensions and material properties of left hand rubber elements
pshell,1,1,0.001,1                          Shell  element  property.
mat1,1,,7.29e6,0.5,1100.0,,,0.2             Defines  the  material  properties.
$
$dimensions and material properties of supported plate elements
pshell,2,2,0.001,2
mat1,2,4.7e13,,0.27,1.81e6,,,2.0
$
$dimensions and material properties of right hand rubber elements
pshell,3,3,0.001,3
mat1,3,,6.561e6,0.5,1100.0,,,0.2
$
$constrain all remaining nodes in y-direction and rotation about y
spc1,100,25,1,thru,103
```

161

$
$constrain driven base nodes in z direction
spc1,100,3,21,thru,25
spc1,100,3,1,thru,5
$
$fictitious supports for base nodes being driven
suport,21,1,22,1,23,1,24,1   *Defines coordinates at which the user*
suport,25,1,1,1,2,1,3,1   *desires determinate reactions to be*
suport,4,1,5,1   *applied to a free body during analysis*
$ *e.g. node 21 in the x-direction.*
$scalar mass property at base nodes being driven
cmass2,33,1.11e7,21,1   *Scalar mass property and connection.*
cmass2,34,1.11e7,22,1
cmass2,35,1.11e7,23,1
cmass2,36,1.11e7,24,1
cmass2,37,1.11e7,25,1
cmass2,38,1.11e7,1,1
cmass2,39,1.11e7,2,1
cmass2,40,1.11e7,3,1
cmass2,41,1.11e7,4,1
cmass2,42,1.11e7,5,1
$
$fictitious nodes for connecting damping elements across rubber supports
grid,290,,0.0,0.0,0.0   *Fictitious nodes used to connect*
grid,291,,0.0025,0.0,0.0   *orthogonal damping elements.*
grid,292,,0.005,0.0,0.0
grid,293,,0.0075,0.0,0.0
grid,294,,0.01,0.0,0.0
grid,295,,0.229,0.0,0.0
grid,296,,0.2315,0.0,0.0
grid,297,,0.234,0.0,0.0
grid,298,,0.2365,0.0,0.0
grid,299,,0.239,0.0,0.0
$
$multipoint constraints for fictitious nodes
mpc,400,41,1,1.0,290,1,-1.0
mpc,400,290,3,1.0,1,3,-1.0
mpc,400,42,1,1.0,291,1,-1.0
mpc,400,291,3,1.0,2,3,-1.0
mpc,400,43,1,1.0,292,1,-1.0
mpc,400,292,3,1.0,3,3,-1.0
mpc,400,44,1,1.0,293,1,-1.0
mpc,400,293,3,1.0,4,3,-1.0

162

```
mpc,400,45,1,1.0,294,1,-1.0
mpc,400,294,3,1.0,5,3,-1.0
mpc,400,57,1,1.0,295,1,-1.0
mpc,400,295,3,1.0,21,3,-1.0
mpc,400,58,1,1.0,296,1,-1.0
mpc,400,296,3,1.0,22,3,-1.0
mpc,400,59,1,1.0,297,1,-1.0
mpc,400,297,3,1.0,23,3,-1.0
mpc,400,60,1,1.0,298,1,-1.0
mpc,400,298,3,1.0,24,3,-1.0
mpc,400,61,1,1.0,299,1,-1.0
mpc,400,299,3,1.0,25,3,-1.0
$
```

$ensures fictitious nodes constrained in remaining degrees of freedom

```
spc1,100,2456,290,thru,299
$
```

$damping of node 290 to node 1 in the horizontal

```
cdamp2,45,9.35,290,1,1,1
$
```

Defines a scalar damping element.

$damping of node 41 to node 290 in the vertical

```
cdamp2,46,6.23,41,3,290,3
$
```

$damping of node 291 to node 2 in the horizontal

```
cdamp2,47,9.35,291,1,2,1
$
```

$damping of node 42 to node 291 in the vertical

```
cdamp2,48,6.23,42,3,291,3
$
```

$damping of node 292 to node 3 in the horizontal

```
cdamp2,49,9.35,292,1,3,1
$
```

$damping of node 43 to node 292 in the vertical

```
cdamp2,50,6.23,43,3,292,3
$
```

$damping of node 293 to node 4 in the horizontal

```
cdamp2,51,9.35,293,1,4,1
$
```

$damping of node 44 to node 293 in the vertical

```
cdamp2,52,6.23,44,3,293,3
$
```

$damping of node 294 to node 5 in the horizontal

```
cdamp2,53,9.35,294,1,5,1
```

$

$damping of node 45 to node 294 in the vertical

cdamp2,54,6.23,45,3,294,3

$

$damping of node 295 to node 21 in the horizontal

cdamp2,55,9.35,295,1,21,1

$

$damping of node 57 to node 295 in the vertical

cdamp2,56,6.23,57,3,295,3

$

$damping of node 296 to node 22 in the horizontal

cdamp2,57,9.35,296,1,22,1

$

$damping of node 58 to node 296 in the vertical

cdamp2,58,6.23,58,3,296,3

$

$damping of node 297 to node 23 in the horizontal

cdamp2,59,9.35,297,1,23,1

$

$damping of node 59 to node 297 in the vertical

cdamp2,60,6.23,59,3,297,3

$

$damping of node 298 to node 24 in the horizontal

cdamp2,61,9.35,298,1,24,1

$

$damping of node 60 to node 298 in the vertical

cdamp2,62,6.23,60,3,298,3

$

$damping of node 299 to node 25 in the horizontal

cdamp2,63,9.35,299,1,25,1

$

$damping of node 61 to node 299 in the vertical

cdamp2,64,6.23,61,3,299,3

$

enddata   *Signifies the end of the data deck.*

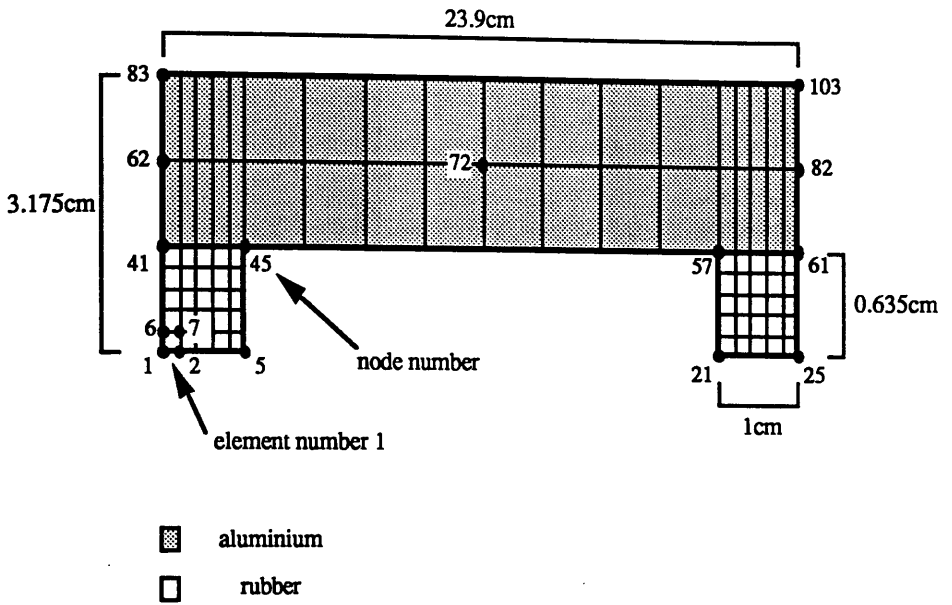--

Figure B.1 *Dimensions and node positions for the one-layer stack finite element model. One of the elements and its surrounding nodes are shown.*

Appendix C

The Ground Tilt Spectrum in an Urban Environment

Introduction

It was shown in Chapter 6 that ground tilting motions might couple strongly to horizontal motion at the top of the vibration isolation stacks used in gravitational radiation detectors. Since relatively little information on the magnitude of ground tilt at the Earth's surface is available it seemed important to make a measurement of the ground tilt spectrum at a typical detector site.

A series of measurements of the ground tilt spectrum were made at an outdoor site a few tens of metres from the 10m prototype detector which is based on campus at Glasgow University. Measurements were also taken indoors in the laboratory containing the prototype detector. Two different methods were used. The first set of measurements were taken using two horizontally sensitive accelerometers mounted at different heights on a 'rigid' pole which was embedded in the ground to a depth of ~0.5m. The second set of measurements were taken using two vertically sensitive accelerometers which were separated horizontally and rigidly mounted on the ground surface.

Determination of the Ground Tilt Spectrum Using Horizontal Accelerometers

Consider two accelerometers rigidly mounted on a pole at different heights h_1 and h_2 above the Earth's surface as shown in Figure C.1. It is assumed that the axis of rotation lies coplanar with the surface and is directly below the pole (here shown as the y-axis). Furthermore it is assumed that the pole has no internal resonances in the frequency range considered.
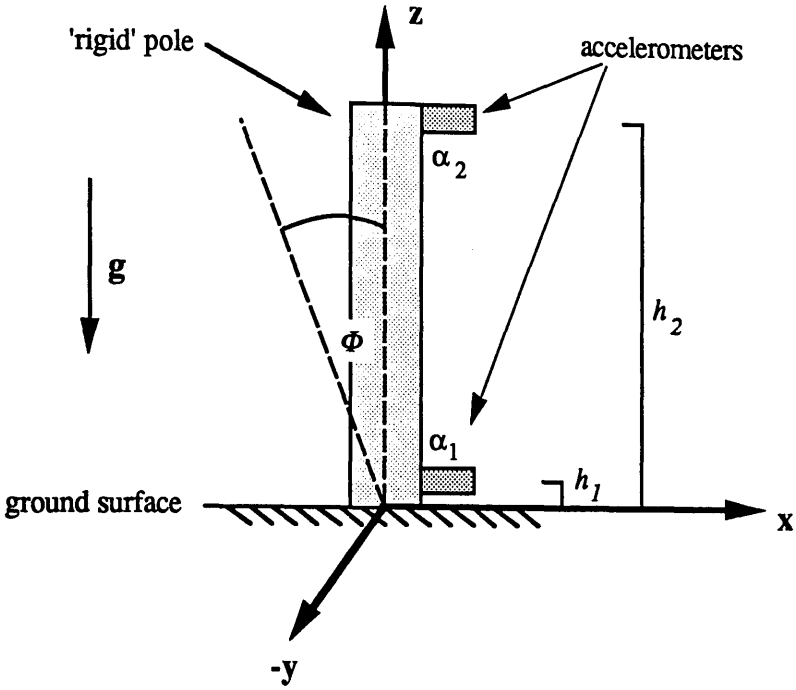
Figure C.1 Arrangement for measuring the ground tilt spectrum using horizontal accelerometers.

By deriving the equations of motion of the accelerometers (in the frequency domain), the acceleration outputs α_1 and α_2 are found to be [Reichle and Bradner 1972] :

$$\alpha_1 = s^2x + (s^2h_1 + g)\Phi \qquad (C.1)$$

$$\alpha_2 = s^2x + (s^2h_2 + g)\Phi \qquad (C.2)$$

where

$$s = j\omega$$

and g = acceleration due to gravity

Solving these equations for Φ gives:

$$\Phi = \frac{(\alpha_1 - \alpha_2)}{s^2(h_1 - h_2)} \qquad\qquad (C.3)$$

Therefore if the outputs from the two accelerometers are subtracted and recorded, the ground tilt Φ can be measured as a function of frequency.

The outputs from two such accelerometers mounted on a rigid pole (as shown in Figure C.1) at the outdoor site were differentially amplified and several spectra were recorded both with the accelerometers vertically separated by 1m and with them placed at the same height above the ground. This enabled a check to be made on whether the observed tilt signal was above the noise signal. Since the measurements were taken out of doors direct coupling of the wind noise to the measuring instruments was a problem, in particular the movement induced in the connecting cables. To minimise this effect care was taken to shield the connecting cables as much as possible and the readings were taken when the wind was subdued.

Figure C.2 shows four sets of data of the measured ground tilt Φ as a function of frequency. The ground tilt appears to fall at ~12dB/octave at frequencies below about 20Hz or 30Hz, tending to a gradient of ~18dB/octave at higher frequencies.

Superimposed on this graph is the ground tilt spectrum estimated by Weinstock from consideration of the vertical acceleration spectrum in a laboratory environment assuming an elastic surface wave model [Weinstock 1966]. The magnitude of the ground tilt at 10Hz measured in a laboratory environment by Speake and Newell [Speake and Newell 1990] is also shown on Figure C.2. At 10Hz the experimental data obtained with the accelerometers on the pole lie between these two reference values.

It should be noted however that the pole had two internal resonances at ~30Hz and at ~110Hz (Q's ~ 5). These resonances undoubtedly played some role in determining the shape of the measured spectrum above about 30Hz. However it would be difficult to predict their precise effects. Nevertheless it is interesting to note that the general shape of the measured spectrum is similar to that predicted by Weinstock.
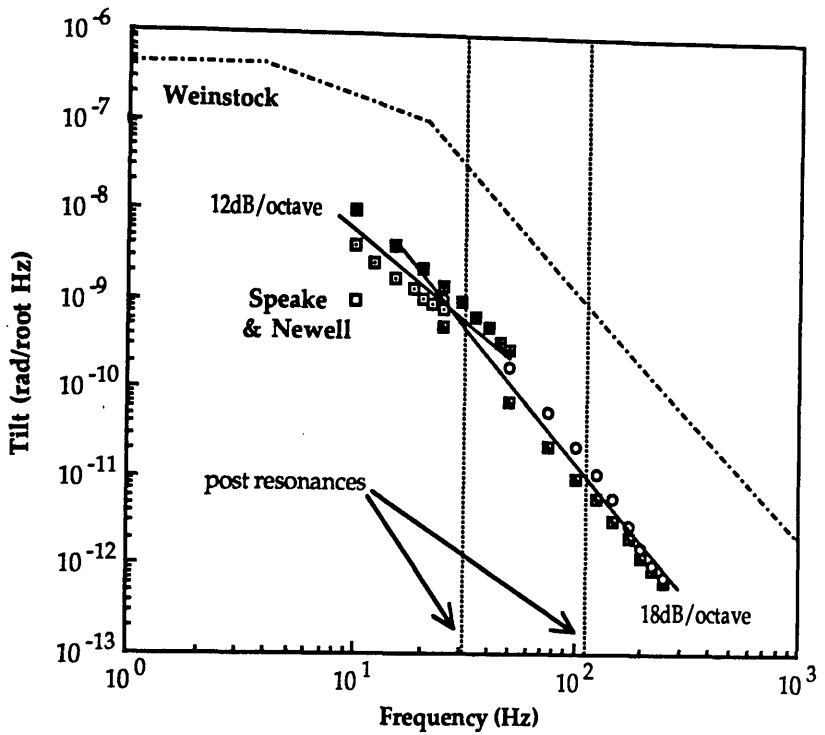
Figure C.2 Apparent ground tilt spectrum measured with horizontal accelerometers compared with quoted values (the sources are as detailed in the text).

Determination of the Ground Tilt Spectrum Using Vertical Accelerometers

Since the results shown in Figure C.2 were perhaps unreliable above about 30Hz due to the presence of internal resonances of the pole, an alternative method of measuring the ground tilt was used.

Consider two vertically sensitive accelerometers mounted rigidly on the ground surface and placed a distance d apart as shown in Figure C.3.
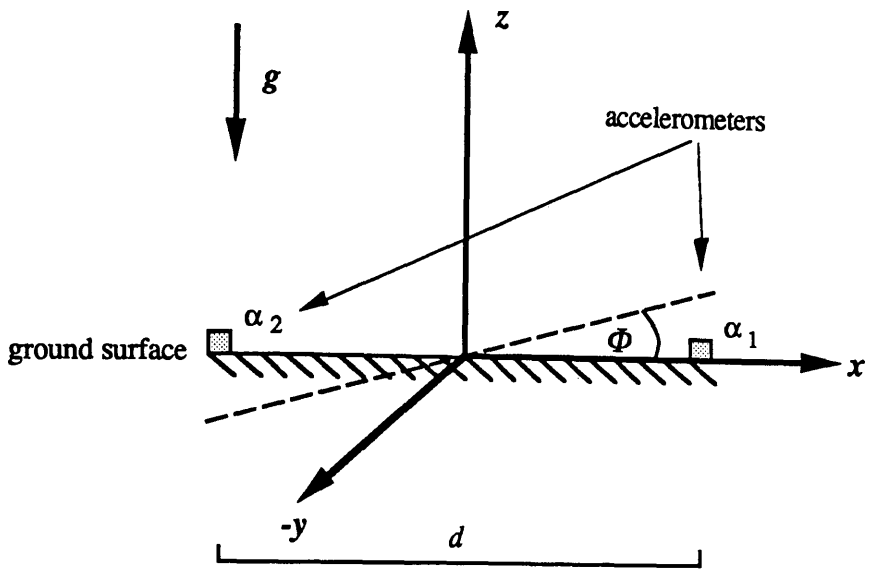
169

Figure C.3 Arrangement for measuring the ground tilt spectrum using vertical accelerometers.

It is assumed here that the axis of rotation is coplanar with the ground surface and lies between the two accelerometers (the y-axis here). By deriving the equations of motion of the accelerometers (in the frequency domain), the acceleration outputs α_1 and α_2 are found to be:

$$\alpha_1 = s^2 z_1 \qquad\qquad (C.4)$$

$$\alpha_2 = s^2 z_2 \qquad\qquad (C.5)$$

Note that the accelerometers are not sensitive to the constant gravitational acceleration g and so this term is not included in these equations. Using the small angle approximation and solving these for $\Phi = (z_1 - z_2)/d$ gives:

$$\Phi = \frac{(\alpha_1 - \alpha_2)}{s^2 d} \qquad\qquad (C.6)$$

So if the accelerometer outputs are subtracted and recorded, the ground tilt Φ as a function of frequency can be evaluated.

In the laboratory containing the prototype gravitational wave detector each accelerometer was magnetically clamped to a heavy iron block. The two accelerometers were then arranged as shown in Figure C.3 and the outputs differentially amplified. Several spectra were recorded both with the accelerometers separated by 1m and with the accelerometers coincident. This enabled a check to be made on whether the observed tilt signal was larger than the noise signal.

The experiment was repeated at the outdoor site with the accelerometers separated by a distance of $d \sim 0.2$m. Graphs of the ground tilt Φ versus frequency for the two sites are shown in Figure C.4.
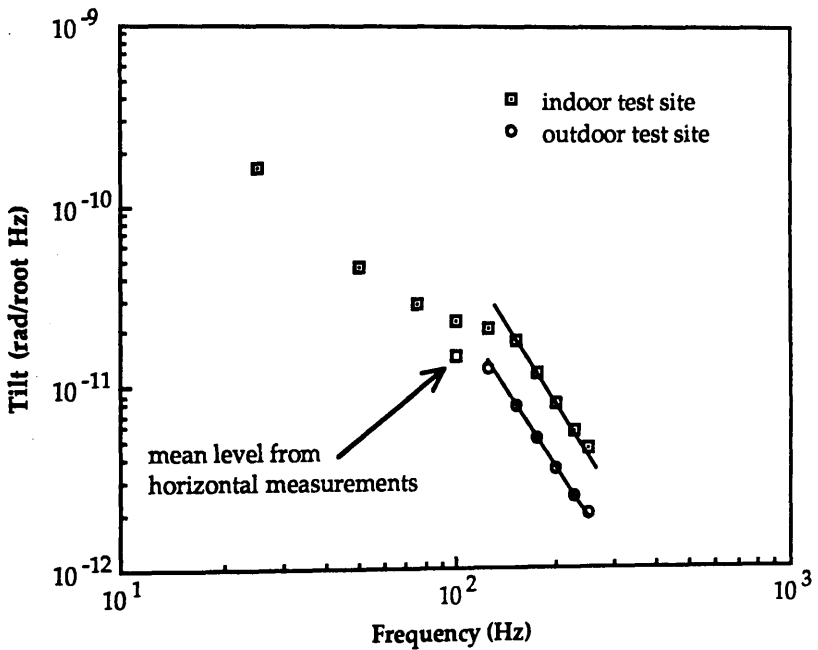

Figure C.4   *Ground tilt spectra measured with vertical accelerometers. The mean level at 100Hz from the horizontal accelerometer measurements (Figure C.2) is superimposed for comparison.*

The curves have similar shapes with a gradient of ~18dB/octave above about 100Hz. The indoor measurements have slightly larger magnitude and this may have been due to the

171

vacuum pumps and other equipment operating at the time of measurement. It is interesting to note that the magnitude and gradient of the spectrum above about 100Hz is similar to that obtained using the pole method.

Conclusions

The ground tilt spectrum measured on the 1m pole structure gave a value for the tilt at 10Hz of about 5×10^{-9} $rad/\sqrt{Hz}$. It is encouraging to see that this value lies between the value predicted by Weinstock [Weinstock 1966] and that measured by Speake and Newell [Speake and Newell 1990]. However the data shown in Figure C.2 are not a reliable measure of the true tilt at the Earth's surface at frequencies above about 30Hz since the pole had an internal resonance at this frequency and one also at about 110Hz. The precise effect that these resonances had on the measured tilt is difficult to predict. Nevertheless it is interesting to note that the ground tilt spectrum in Figure C.2 has a similar shape to that predicted by Weinstock.

The ground tilt spectrum measured using vertically sensitive accelerometers is a more reliable indication of the true tilt of the ground surface. From Figure C.4 the ground tilt spectrum has a value of $\sim 2 \times 10^{-11}$ $rad/\sqrt{Hz}$ at 100Hz and falls at ~18dB/octave above this frequency. It is interesting to notice that the magnitude of the tilt at 100Hz is approximately the same as that measured using the horizontal accelerometers on the pole. This perhaps suggests that the internal resonances of the pole were having very little effect on the measurements shown in Figure C.2.

References

Blair 1991

    D. Blair, editor. *The Detection of Gravitational Radiation.* Cambridge University Press, Cambridge, England, 1991 (in press).

Blair *et. al.* 1989

    D. Blair, J. Ferreirinho, P.J. Veitch, R.J. Sandeman, H.A. Bachor, D. McClelland and A. Wrightson. *Proposal for the Australian International Gravitational Observatory*, 1989.

Caves 1981

    C.M. Caves. Quantum-mechanical noise in an interferometer. *Physical review D*, vol. 23, no. 8, (1693-1708), 1981.

D'Azzo and Houpis 1982

    J.J. D'Azzo and C.H. Houpis. *Feedback Control System Analysis & Synthesis.* McGraw-Hill, 1982. (Tokyo)

Del Fabbro *et. al.* 1988a

    R. Del Fabbro, A. Di Virgilio, A. Giazotto, H. Kautzky, V. Montelatici and D. Passuello. First results from the Pisa seismic noise super-attenuator for low frequency gravitational wave detection. *Physics Letters A*, vol. 132, no.5, 1988. (p 237 - 240)

Del Fabbro *et. al.* 1988b

    R. Del Fabbro, A. Di Virgilio, A. Giazotto, H. Kautzky, V. Montelatici and D. Passuello. Low frequency behaviour of the Pisa seismic noise super-attenuator for gravitational wave detection. *Physics Letters A*, vol. 133, no.9, 1988. (p 471 - 475)

Drever *et. al.* 1983

    R.W.P. Drever, J. Hough, A.J. Munley, S.A. Lee, R. Spero, S.E. Whitcomb, H. Ward, G.M. Ford, M. Hereld, N.A. Robertson, G.A. Kerr, J.R. Pugh, G.P. Newton, B.J. Meers, E.D. Brooks III and Y. Gursel. Gravitational wave detectors using laser interferometers and optical cavities: Ideas, principles and prospects. In P. Meystre and M.O. Scully, editors, *Quantum Optics, Experimental Gravitation and Measurement Theory* (503-514). Plenum Press, New York, 1983.

Edelstein *et. al.* 1978

W.A. Edelstein, J. Hough, J.R. Pugh and W. Martin. Limits to the measurement of displacement in an interferometric gravitational radiation detector. *J. Phys. E: Sci. Instrum*, vol. 11, 1978. (p 710 - 712)

Forward 1978

R.L. Forward. Wideband laser-interferometer gravitational-radiation experiment. *Physical Review D*, vol. 17, no. 2, (379-390), 1978.

Giazotto 1987

A. Giazotto. The seismic noise challenge to the detection of low frequency gravitational waves. *Proceedings of 7th Conference on General Relativity and Gravitational Physics*. In U. Bruzzo, R. Cianci and E. Massa, editors. World Scientific, 449-463, 1987. (Chicago)

Giazotto *et. al.* 1989

A. Giazotto, A. Brillet and colleagues. *The VIRGO Project*, 1989.

Greenhalgh 1989

R.J.S. Greenhalgh. Rutherford Appleton Laboratory, Chilton, Oxfordshire. *Private communication*, 1989.

Hammond 1958

P.H. Hammond. *Feedback Theory and its Applications.* The English Universities Press Ltd., London, 1958.

Hough *et. al.* 1986

J. Hough, B.J. Meers, G.P.Newton, N.A. Robertson, H. Ward, B.F. Schutz, R.W.P. Drever, R. Mason, C. Pollard, R. Tolcher, D.W. Bellenger, J.R.J. Bennett, I.F. Corbett and M.D. *A British Long Baseline Gravitational Wave Observatory (Design Study Report)*. Technical Report GWD/RAL/86-001, May, 1986.

Hough *et. al.* 1987

J. Hough, B.J. Meers, G.P.Newton, N.A. Robertson, H. Ward, B.F. Schutz, I.F. Corbett and R.W.P. Drever. Gravitational wave astronomy - potential and possible realisation. *Vistas in Astronomy*, vol.30, (109-134), 1987.

Hough *et. al.* 1989

    J. Hough, B.J. Meers, G.P.Newton, N.A. Robertson, H. Ward, G. Leuchs, T.M. Niebauer, A. Rudiger, R. Schilling, L. Schnupp, H. Walther, W. Winkler, B.F. Schutz, J. Ehlers, P. Kafka, G. Schafer, M.W. Hamilton, I. Schutz, H. Welling, J.R.J. Bennet, I.F. Corbett, B.H.W. Edwards, R.J.S. Greenhalgh and V. Kose. *Proposal for a Joint German-British Interferometric Gravitational Wave Detector*. Technical report MPQ 147 and GWD/137/JH(89), September, 1989.

Isacks and Oliver 1964

    B. Isacks and J. Oliver. *Bull. Seismol. Soc. Am.*, 54,(1941), 1964.

Logan 1990

    J.E. Logan, University of Glasgow. *Private communication*, 1990.

Mackenzie 1989

    N.L. Mackenzie. *Experiments Relevant to the Development of Laser Interferometric Gravitational Wave detectors*. Ph.D. Thesis, Glasgow University, Glasgow, 1989.

MSC/Nastran 1983

    The MacNeal-Schwendler Corporation. *Handbook for Dynamic Analysis*. MSC/Nastran Version 63. California, 1983.

MSC/Nastran 1985

    The MacNeal-Schwendler Corporation. *Handbook for Linear Analysis*. MSC/Nastran Version 64. California, 1985.

Reichle and Bradner 1972

    M. Reichle and H. Bradner. *Use of Accelerometers to Determine Tilts and Displacements*. AIAA, Paper no. 72-818, American Institute of Aeronautics and Astronautics, New York, 1972.

Robertson D.I. 1990

    D.I. Robertson. *Investigations and Developments Relevant to a Prototype Laser Interferometric Gravitational Wave Detector*. Ph.D. Thesis, Glasgow University, Glasgow, 1990.

Robertson N.A. 1981

> N.A. Robertson. *Experiments Relating to the Detection of Gravitational Radiation and to the Suppression of Seismic Noise in Sensitive Measurements*. Ph.D. Thesis, Glasgow University, Glasgow, 1981.

Robertson N.A. 1991

> N.A. Robertson. Vibration isolation for the test masses in interferometric gravitational wave detectors. In D. Blair, editor, *The Detection of Gravitational Radiation*. Cambridge University Press, Cambridge, England, 1991 (in press).

Saenz and Shapiro 1981

> R.A. Saenz and S.L. Shapiro. Gravitational radiation from stellar collapse. III. Damped ellipsoidal oscillations. *The Astrophysical Journal*, 244 (1033-1038), 1981.

Schutz 1986

> B.F. Schutz. Determining the Hubble constant from gravitational wave observations. *Nature*, 323: (310-311), 1986.

Schutz 1989

> B.F. Schutz. Sources of gravitational radiation. In B.F. Schutz, editor, *Gravitational Wave Data Analysis*. NATO ASI series. Series C. Mathematical and Physical Sciences, vol. 253, (3-17), Kluwer Academic Publishers, 1989.
> (Dordrecht)

Shoemaker 1987

> D. Shoemaker. *Contributions à l'Étude de la Détection Interférométrique des Ondes de Gravitation*. Ph.D. Thesis, University of Paris, Paris, 1987.

Shoemaker *et. al.* 1988

> D. Shoemaker, R. Schilling, L. Schnupp, W. Winkler, K. Maischberger and A. Rudiger. Noise behaviour of the Garching 30m prototype gravitational wave detector. *Physical Review D*, vol. 38, no. 2: (423-432), 1988.

Snowdon 1979

> J.C. Snowdon. Vibration isolation: use and characterization. *NBS Handbook 128*. US Department of Commerce/National Bureau of Standards, 1979.
> (Washington DC)

Speake and Newell 1990

C.C. Speake and D.B. Newell. The design and application of a novel high-frequency tiltmeter. *Rev. Sci. Instrum.* 61(5),1990. (p 1500 - 1503)

Stephens *et. al.* 1991

M. Stephens, P. Saulson and J. Kovalik. A double pendulum vibration isolation system for a laser interferometric gravitational wave antenna. *Review of Scientific Instruments*, 1991 (in press).

Taylor *et. al.* 1979

J.H. Taylor, L.A. Fowler and P.M. McCulloch. Measurements of general relativistic effects in the binary pulsar PSR1913+16. *Nature*, 277 (437-440), 1979.

Thorne 1987

K.S. Thorne. Gravitational Radiation. In S.W. Hawking and W. Israel, editors, *300 Years of Gravitation*. Cambridge University Press, 1987.
                                             (Cambridge)

Thorne *et. al.* 1979

K.S. Thorne, C.M. Caves, V.D. Sandberg, M. Zimmerman and R.W.P. Drever. The quantum limit for gravitational wave detectors and methods of circumventing it. In L. Smarr, editor, *Sources of Gravitational Radiation*. Cambridge University Press, 1979. (p 49-68)
                                  (Cambridge)

Vachaspati and Vilenkin 1985

T. Vachaspati and A. Vilenkin. Gravitational radiation from cosmic strings. *Physical Review D*, vol. 31, no. 12, (3052-3058), 1985.

Vogt *et. al.* 1989

R.E. Vogt, R.W.P. Drever, K.S. Thorne, F.J. Raab and R. Weiss. *A Laser Interferometer Gravitational Wave Observatory*. California Institute of Technology and Massachusetts Institute of Technology, 1989.

Wagoner 1984

R.V. Wagoner. Gravitational radiation from accreting neutron stars. *The Astrophysical Journal*, 278: (345-348), 1984.

Weinstock 1966

H.Weinstock. *Limitations on Inertial Sensor Testing Produced by Test Platform Vibrations*. NASA Technical Note TND-3683, 1966.

Weiss 1972

R. Weiss. Electromagnetically coupled broadband gravitational antenna. *Quarterly Progress Report, Research Laboratory of Electronics, MIT*, 105: (54-76), 1972.

Winkler 1991

W. Winkler. A Michelson interferometer using delay lines. In D. Blair, editor, *The Detection of Gravitational Radiation*. Cambridge University Press, Cambridge, England, 1991 (in press).

Zimmerman 1978

M. Zimmerman. Revised estimate of gravitational radiation from Crab and Vela pulsars. *Nature*, 271 (524-525), 1978.